

NASA  
TP  
1051  
c.1

NASA Technical Paper 1051

LOAN COPY: RETURN  
AFWL TECHNICAL LIB  
KIRTLAND AFB, NM



**Behavior of Aircraft Antiskid Braking  
Systems on Dry and Wet Runway Surfaces**  
**A Slip-Velocity-Controlled,  
Pressure-Bias-Modulated System**

Sandy M. Stubbs, John A. Tanner,  
and Eunice G. Smith

DECEMBER 1979

**NASA**



NASA Technical Paper 1051

**Behavior of Aircraft Antiskid Braking  
Systems on Dry and Wet Runway Surfaces**  
**A Slip-Velocity-Controlled,  
Pressure-Bias-Modulated System**

Sandy M. Stubbs, John A. Tanner,  
and Eunice G. Smith  
*Langley Research Center  
Hampton, Virginia*

**NASA**

National Aeronautics  
and Space Administration

**Scientific and Technical  
Information Branch**

1979

## SUMMARY

An experimental investigation was conducted at the Langley aircraft landing loads and traction facility to study the braking and cornering response of a slip-velocity-controlled, pressure-bias-modulated aircraft antiskid braking system. The investigation, conducted on dry and wet runway surfaces, utilized one main gear wheel, brake, and tire assembly of a McDonnell Douglas DC-9 series 10 airplane. The landing gear strut was replaced by a dynamometer.

During maximum braking, average braking-behavior indexes based upon brake pressure, brake torque, and drag-force friction coefficient developed by the antiskid system were higher on dry surfaces than on damp and flooded surfaces. On the wet surfaces, these indexes were reduced with lighter vertical forces, increasing speeds, and when new tire treads were replaced by worn treads. The three braking-behavior indexes agreed with one another and may be used interchangeably as a measure of the braking behavior of this antiskid system. However, these braking-behavior indexes are based upon maximum values of pressure, torque, and drag-force friction coefficient, which may vary from system to system, and any comparisons between different antiskid systems based solely upon these indexes may be technically misleading. The average cornering-behavior index based upon the side-force friction coefficient developed by the tire under antiskid control was decreased on wet runway surfaces, with increasing yaw angle and carriage speed, and when new tire treads were replaced by worn treads. The interaction between braking and cornering forces indicated that during antiskid cycling on the dry runway surfaces, the side-force friction coefficient was significantly reduced during portions of the braking cycles. On the flooded runway surfaces, this coefficient was frequently reduced to negligible values. During the transition from a dry to a flooded surface under heavy braking, the wheel entered into a deep skid, but the antiskid system reacted quickly by reducing brake pressure and performed normally during the remainder of the run on the flooded surface. The time for brake-pressure recovery following the transition from flooded to dry was 4 sec and was controlled by the decay rate of the residual skid signal built up by the antiskid system during the initial skid cycles on the first runway surface.

## INTRODUCTION

Over the years, the number and variety of airplanes using antiskid braking systems have steadily increased until most current commercial and military jet airplanes are now equipped with various skid control devices. The earliest antiskid systems were generally designed to prevent wheel lockups and excessive tire wear on dry pavements. Modern skid control devices, however, are more sophisticated and are designed to provide maximum braking effort while maintaining full antiskid protection under all weather conditions. Operating statistics of modern jet airplanes indicate that these antiskid systems are both effective and dependable; the several million landings that are made each year in routine fashion with no serious operating problems attest to this fact.

However, it has also been well established, both from flight tests and from field experience, that the performance of these systems is subject to degradation on slippery runways; consequently, dangerously long roll-out distances and reduced steering capability can result during some airplane landing operations (refs. 1 to 5). There is a need to study different types of antiskid braking systems in order to find reasons for the degraded braking performance that occurs under adverse runway conditions; there is also a need to obtain data for the development of more advanced systems that will insure safe ground handling operations under all weather conditions.

In an effort to meet these needs, an experimental research program has been undertaken to study the single-wheel behavior of several different airplane antiskid braking systems under the controlled conditions afforded by the Langley aircraft landing loads and traction facility (formerly called the Langley landing loads track). The types of skid control devices undergoing study in this program include a velocity-rate-controlled system (ref. 6); a slip-ratio-controlled system with ground speed reference from an unbraked nose wheel (ref. 7); the present, a slip-velocity-controlled system; and others. The investigation of all these systems is being conducted with a single main wheel, brake, and tire assembly of a McDonnell Douglas DC-9 series 10 airplane.

The purpose of this paper is to present the results from a study of the behavior of a slip-velocity-controlled, pressure-bias-modulated aircraft antiskid braking system under maximum braking effort. The parameters varied in the study included carriage speed, tire loading, yaw angle, tire tread condition, brake-system operating pressure, and runway wetness conditions. A discussion of the effects of each of these parameters on the behavior of the skid control system is presented. In addition, comparisons are made between data obtained with the skid control system and data obtained from single-cycle braking tests without antiskid protection.

Hydro-Aire Division of Crane Company provided the antiskid-system hardware for this investigation, and the Federal Aviation Administration (FAA) provided the wheels, brakes, and tires.

#### SYMBOLS

Values are given in both SI and U.S. Customary Units. The measurements and calculations were made in U.S. Customary Units. Factors relating the two systems are given in reference 8.

$d$	position of footprint center of pressure
$F_v$	tire vertical force
$F_x$	drag force parallel to plane of wheel
$F_y$	side force perpendicular to plane of wheel
$h$	axle height

I	moment of inertia
P	power
p	pressure
r	tire rolling radius
S	wheel slip ratio
T	torque
t	time
V	carriage speed
$\alpha$	angular acceleration
$\beta$	behavior index
$\mu$	friction coefficient
$\psi$	yaw angle
$\omega$	test wheel angular velocity

Subscripts:

b	braking
c	cornering
d	drag
F	friction
f	final value
g	gross
max	maximum value
o	initial value
p	pressure
r	free rolling
s	side

T torque

t tire

A bar over a symbol denotes an average value.

## APPARATUS AND TEST PROCEDURE

### Test Tires

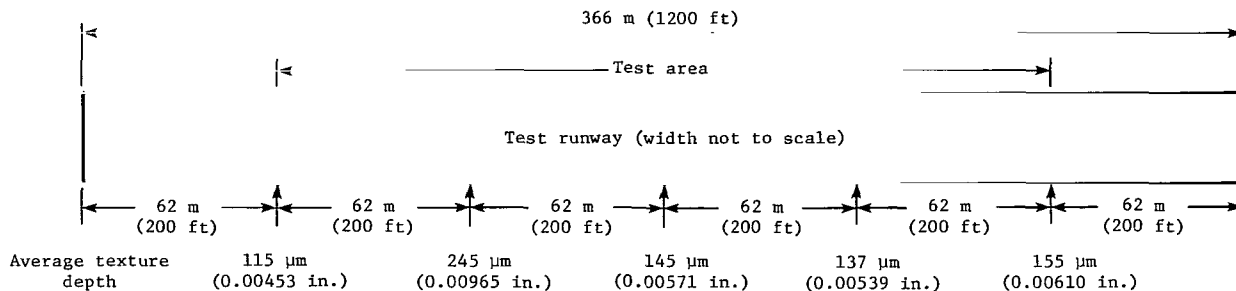
The tires used in this investigation were 40 × 14, type VII, bias-ply aircraft tires of 22 ply rating with a rated maximum speed of 200 knots (1 knot = 0.5144 m/sec). The tires were stock retreads with a six-groove tread pattern, and the study included both new and worn tread configurations. A photograph of the two test tires having new and worn treads is presented in figure 1. The new tread had a groove depth of 0.71 cm (0.28 in.) and was considered new until the groove depth decreased to 0.36 cm (0.14 in.). To generate worn tires, a commercially available tire grinding machine was employed to remove tread rubber uniformly from the retreaded tire until a groove depth of 0.05 cm (0.02 in.) remained. This simulated worn tire was probably in a worse wear condition than is normally experienced in airplane operations. Throughout this investigation, the tire inflation pressure was maintained at the normal airline operational pressure of 0.97 MPa (140 psi).

### Test Facility

The investigation was performed on a 4800-kg (106 000 lbm) test carriage at the Langley aircraft landing loads and traction facility described in reference 9. Figure 2 is a photograph of the carriage with the test wheel assembly installed; figure 3 is a close-up view of the wheel and other components. An instrumented dynamometer was used instead of a landing-gear strut to support the wheel and brake assembly because it provided an accurate measurement of the tire-ground forces.

For the tests described in this paper, approximately 244 m (800 ft) of the available 366 m (1200 ft) of the flat concrete test runway were used to provide braking and cornering data on a dry surface, on an artificially damp surface, on an artificially flooded surface, and on a natural rain wet surface. With the exception of transient runway friction tests, the entire runway had a uniform surface wetness condition, and antiskid cycling occurred for the entire 244 m (800 ft). The 61 m (200 ft) of runway preceding the test section were used for the initial wheel spin-up and brake actuation, and the 61 m (200 ft) beyond the test section were retained for brake release. To obtain a damp condition, the test surface was lightly wetted with no standing water. For the flooded runway condition, the test section was surrounded by a flexible dam and flooded to a depth of approximately 1.0 cm (0.4 in.). For the natural rain surface condition, the flexible dam was removed and no measurement of water depth was made.

The concrete surface in the test area had a light broom finish in a transverse direction, and the surface texture was not completely uniform, as shown by the texture depth measurements in the following sketch:



Details of the texture depth measurement technique are presented in reference 10. The average texture depth of the test runway was 159 μm (0.00626 in.), which is slightly less than that of a typical operational runway. (See ref. 11, for example.) The test runway was quite level compared with airport runways and had no crown. During the course of testing on the dry surface, particularly with a yawed tire, rubber was deposited on the runway and it was necessary to clean the surface periodically.

### Skid Control System

A slip-velocity-controlled, pressure-bias-modulated skid control system was used in this investigation. The system was configured to simulate a braking system that had the correct electronic and hydraulic components, including line lengths and sizes, for a single main wheel of a DC-9 series 10 airplane. Figure 4 is a photograph of the major hydraulic components of the simulated braking system installed on the test carriage; figure 5 is a schematic of the system. The brake system is activated by opening the pilot metering valve (fig. 5), which allows brake fluid to flow from a high-pressure reservoir and brake selector valve, through the normally open antiskid control valve and hydraulic fuse, to the brake. The sole function of the brake selector valve and hydraulic fuse was to duplicate the DC-9 hydraulic system. A pneumatic piston shown in figure 4 was used to open the pilot metering valve to its full stroke; thus, maximum braking effort for all tests was provided.

During antiskid braking, an ac signal proportional to instantaneous wheel speed is generated by a wheel-driven alternator. In the control box, this signal is converted to a dc voltage and compared with a reference wheel speed that is also derived electronically from the braked wheel. The difference between the braked-wheel speed and the reference speed is defined as the wheel slip velocity; thus, a freely rolling wheel has, by definition, zero slip velocity. When this slip velocity is greater than a certain threshold value, a skid signal is generated which is transmitted to the antiskid control valve to reduce brake pressure. When the wheel recovers from the skid and the slip velocity

once again drops below the threshold value, the skid signal is reduced to a level established by the magnitude, duration, and number of preceding skid signals that are retained in the pressure-bias-modulation memory circuit which controls the rate of brake-pressure reapplication. The initial threshold slip velocity is approximately 3 m/sec (10 ft/sec), but during the course of anti-skid braking, this threshold value may vary according to the adaptive correction in the control circuit. A more detailed discussion of the antiskid system operation can be found in reference 3.

The slip velocity data shown in this report were not obtained from the control box but were obtained from two dc generators, one measuring test wheel speed and the other measuring carriage speed. Typical time histories of wheel speed, slip velocity, skid signal, brake pressure, and the resulting drag-force friction coefficient  $\mu_d$  are presented in figure 6 to help describe the system operation. The points labeled (A) to (K) are used to highlight events which occur during antiskid cycling. In the figure, the brake pressure is first applied rapidly ((A) to (B)) and results in a decrease in wheel speed ((C)); consequently, an increase in slip velocity ((D)) occurs above the threshold (dashed line in fig. 6) and thereby produces a small skid signal ((E)). The threshold slip velocity shown in figure 6 is an initial value; the threshold is a variable that is dependent upon an adaptive correction in the control circuit. The skid signal partially closes the antiskid control valve, which causes a leveling pause in brake-pressure application ((F)). The slip velocity becomes almost constant ((D) to (G)), and the pressure-bias-modulation circuit permits the skid signal to be gradually reduced ((E) to (H)); this reduction allows a slight rise in brake pressure ((F) to (I)) and a corresponding increase in the developed friction level ((J) to (K)). At about 3 sec, the slip velocity again increases above the apparent threshold value and the brake release cycle is repeated.

#### Instrumentation

The tire friction forces were measured with the dynamometer shown in figure 3 and illustrated schematically in figure 7. Strain gages were mounted on the five dynamometer support beams: two of the beams were used for measuring vertical forces, two were used for measuring drag forces parallel to the wheel plane, and a single beam was used for measuring side force perpendicular to the wheel plane. Three accelerometers on the test wheel axle provided information for inertia corrections to the force data. The brake torque was measured with

torque links which were independent of the drag-force beams. Transducers were installed in the hydraulic system (fig. 5) to measure pressures at the pilot metering valve, at the antiskid control valve, at the hydraulic fuse, at the brake, and in the return line between the brake and the hydraulic reservoir. A pressure relief valve in the return line maintained a back pressure of 448 kPa (65 psi) in the hydraulic lines, and all the pressure transducers were calibrated to read zero at this pressure. A steel-reinforced, cogged, rubber timing belt was driven by the test wheel to run an auxiliary axle which drove the pulse (ac) alternators and dc generators that were used to obtain a measure of the test wheel angular velocity. Signals from one of the ac alternators supplied wheel-speed information to the antiskid system. This signal and the skid signal produced by the antiskid system were recorded for an examination of their characteristics. A lightweight trailing wheel was mounted on the side of the test carriage (as shown in fig. 8), and the output from a dc generator mounted on its axle recorded the carriage speed and was combined with the output from the test wheel dc generator to compute slip velocity and slip ratio. Due to small shaft misalignments of the two dc generators, a small ac ripple was induced on the recorded time histories of wheel speed, slip velocity, and slip ratio. A recording infrared thermometer was used for one test run to obtain a measure of the tire tread temperature. All data outputs were fed into signal conditioning equipment and then into two frequency-modulated tape recorders. A time code was transmitted to both recorders to provide synchronization of the two sets of data.

#### Test Procedure

The technique for the braking tests with and without antiskid protection consisted of rotating the yoke holding the dynamometer and tire assembly to the chosen yaw angle, propelling the test carriage to the desired speed, applying a preselected vertical load on the tire, and recording the outputs from the onboard instrumentation. For antiskid tests, the brake was actuated by a pneumatic piston at the pilot metering valve, which gave full pedal deflection or maximum braking, and the antiskid system modulated the braking effort. The runway surface condition was essentially uniform over the entire length; the brake was applied the full distance and was released prior to carriage arrestment.

In addition to antiskid braking tests, single-cycle braking tests were made without antiskid protection. These single brake cycles consisted of applying sufficient brake pressure to bring the tire from a free-rolling condition to a locked-wheel skid and then releasing the brake to allow full tire spin-up prior to the next cycle. For single-cycle braking, the runway surface was divided into three sections (dry, damp, and flooded), and brake pressure was applied by triggering devices at each section along the test track.

The nominal carriage speeds for both types of tests ranged from 40 to 100 knots and were measured approximately midway along the runway where, after initial acceleration, the carriage was coasting through the test section, with some speed decay due to carriage wheel friction, air drag, and the braking of the test tire. Tire vertical loading was maintained hydraulically and ranged from approximately 58 kN (13 000 lbf) to 120 kN (27 000 lbf), which represented

a nominal landing weight and a refused take-off weight, respectively, for a single main wheel of the DC-9. Tests were run at tire yaw angles from  $0^\circ$  to  $12^\circ$ . For most test runs, nominal brake-system pressure was the normal airplane system pressure of 21 MPa (3000 psi), but some tests were made at system pressures of 14 MPa (2000 psi) and 10 MPa (1500 psi).

### Data Reduction

All data were recorded on analog magnetic tape filtered to 1000 Hz. Except for the ac alternator signals, all analog data were then filtered through a low pass filter (cutoff frequency of 60 Hz) and digitized at 250 samples/sec. Time-history plots used in the data analysis and those in the appendix are plotted at 50 samples/sec. From these digitized data, direct measurements were obtained of the carriage speed, the braked-wheel angular velocity, the skid signal generated by the antiskid system, the brake pressure and torque, the drag force  $F_x$  (sum of two beams), the side force  $F_y$ , the vertical force applied to the tire  $F_v$  (sum of two beams), and the accelerations of the dynamometer. The instantaneous vertical-, drag-, and side-force data were corrected for acceleration effects and were combined to compute both the instantaneous drag-force friction coefficient  $\mu_d$  parallel to the direction of motion and the side-force friction coefficient  $\mu_s$  perpendicular to the direction of motion. The load transfer between the two drag-force beams (fig. 7) provided a measure of the alining torque about the vertical or steering axis of the wheel. The braked-wheel dc generator signal was converted to wheel speed, which was combined with carriage speed to yield wheel slip velocity and slip ratio. Time histories of some of the measured parameters for a typical antiskid braking test are presented in figure 9(a). These plots start just prior to wheel spin-up and end approximately 2 sec after the release of brake pressure. To minimize tire wear on some dry runs, especially at the higher yaw angles, the runway was flooded from the brake-pressure release point for the remainder of the test, as is noted in figure 9. Data acquired when the tire operated on this flooded section were not used in this report. As previously mentioned, the vertical and drag forces are each a summation of two data channels, with corrections made for acceleration effects. The time histories of figure 9(b) are the parameters calculated from the data of figure 9(a). Although brake pressure is a measured parameter, it is included in figure 9(b) to serve as a reference.

In most cases, the friction-coefficient traces were not as smooth as the pressure and torque traces, and a study was made to determine whether the traces should be faired prior to obtaining values of  $\mu_{d,max}$ . A run in which a known abrupt change in  $\mu_d$  occurred was chosen for this study to determine the maximum frequency response requirement. Figure 10 shows the drag-coefficient trace from a run in which the tire experienced an abrupt change in friction coefficient during transition from a dry to a flooded surface. Figure 10(a) is the raw data showing all the 250 digitized points/sec ( $\Delta t = 0.004$ ). Figure 10(b) is the same raw data, but only every fifth point is plotted ( $\Delta t = 0.02$ ). A least-squares fairing technique was used on the raw data digitized at 250 points/sec, and the effects of four different order polynomials are shown in figures 10(c) to 10(f). The least-squares fairing technique used in reference 12 to smooth acceleration data was employed. As can be

seen in figures 10(c) to 10(f), different frequency responses can be obtained by varying the polynomial order of the least-squares fairing (i.e., from 4 Hz in fig. 10(c) to 24 Hz in fig. 10(f)). Data in the vicinity of the transition from a dry to a flooded surface in figure 10 (see circled area in fig. 10(f)) are expanded and presented in figure 11. When no fairing is made, the data in figure 11(a) at  $\Delta t = 0.004$  sec indicate that the friction transition occurs over a 0.03-sec interval, and the data at  $\Delta t = 0.02$  sec show a 0.05-sec interval. It is believed that the abrupt friction changes shown in this run actually occur, and any fairing that might be used must be able to respond to this abrupt friction change. The least-squares fairing of first-, third-, and fifth-order polynomials gave intervals of 0.12 sec, 0.09 sec, and 0.06 sec, respectively (figs. 11(c), 11(d), and 11(e)). Only when a seventh-order polynomial was used did the interval of the friction transition (0.04 sec) approach the response that occurred when no fairing was used. Since the seventh-order trace has characteristics very similar to the unfaired trace at  $\Delta t = 0.02$  sec, it was deemed unnecessary to fair the data; consequently, none of the time-history data appearing in this report have been faired.

#### DEFINITIONS

An assessment of the behavior of an antiskid braking system subjected to a wide variety of operational conditions requires careful consideration of many variables. Four methods are used in this paper to analyze the behavior of this antiskid braking system, and these methods are based upon the following parameters: brake pressure, brake torque, tire friction coefficient, and the stopping and cornering power generated by the antiskid system. The development of the parameters used to describe the antiskid-system behavior is discussed in the following paragraphs.

#### Brake Pressure

One method of determining antiskid-system behavior is to compare the average brake pressure  $\bar{p}$  to the maximum brake pressure  $\bar{p}_{\max}$  developed by the system. This method is defined in references 13, 14, and 15 as a comparison of the area under the brake-pressure time history with the area beneath a pressure profile obtained from the envelope defined by the peaks in the brake-pressure time history. It is noted in reference 13 that an examination of the wheel-speed time history must show sufficient variations in both magnitude and frequency to demonstrate that the brake is not torque limited. According to reference 14, this method of study may be open to objection, especially for rate threshold systems, because the threshold rate may be lower than the maximum attainable deceleration, or the pressure may continue to increase while the wheel is spinning down. Furthermore, mechanical lags in the brake may not allow the brake-pressure time history to coincide with the drag-force-friction-coefficient time history. However, this process can be applied to the analysis of airplane test data and may prove helpful for comparison purposes (ref. 14).

Typical examples of the relatively smooth brake-pressure trace are shown in figure 12. The average pressure  $\bar{p}$  developed by the antiskid system during a given test is defined by the expression

$$\bar{p} = \frac{1}{t_f - t_o} \int_{t_o}^{t_f} p \, dt \quad (1)$$

where  $t_o$  and  $t_f$ , identified in figure 12, enclose the time interval over which  $\bar{p}$  is measured. The time  $t_o$  represents the point at which the brake pressure neared the maximum system pressure or the point where the first skid occurs. The time  $t_f$  is taken just prior to brake release at the end of the test section. The average pressure is computed for each braking test by numerical integration techniques. The maximum pressure  $\bar{P}_{max}$  is derived in much the same way as  $\bar{p}$ , except that the dashed curves in figure 12 that are formed by joining the straight line segments between the pressure peaks are used.

The slope of the least-squares line through the origin, which fairns the data when  $\bar{p}$  is plotted as a function of  $\bar{P}_{max}$ , is defined as the pressure braking-behavior index  $\bar{\beta}_{b,p}$ .

#### Brake Torque

A second indication of antiskid-system behavior is the ratio of the average brake torque  $\bar{T}$  to the maximum torque  $\bar{T}_{max}$  developed during a test (refs. 13 and 15). In many test programs, it is difficult to measure the brake torque; hence, torque is not commonly used to study antiskid-system behavior. Fortunately, the instrumented dynamometer used in this investigation gives a direct and independent measure of brake torque. According to reference 16, the relationship between brake torque and friction forces is more easily defined than the relationship between brake pressure and friction forces. This relationship, described fully in reference 2, is

$$\text{Torque} = F_x h + F_y d - I \alpha \quad (2)$$

and indicates that brake torque is defined by a linear combination of moments and thus cannot be uniquely defined by the product of drag force  $F_x$  and its moment arm  $h$ . When the tire operates at a fixed slip velocity such that  $\alpha$  becomes negligible and  $d$  is relatively small, then the torque may more closely reflect the drag-force friction coefficient. In most cases, however, antiskid cycling results in rapid wheel-speed changes and significant shifts  $d$  in the fore and aft position of the tire footprint center of pressure. Thus, peaks in the brake-torque time histories may not coincide with the peaks in the  $\mu_d$  time histories; however, the brake-torque time histories for this antiskid system are relatively smooth (see fig. 12), and the torque ratios are presented as an independent method to study antiskid behavior.

The average brake torque  $\bar{T}$  developed by the antiskid system during a given test is defined by an expression similar to that for  $\bar{p}$ . This expression

$$\bar{T} = \frac{1}{t_f - t_0} \int_{t_0}^{t_f} T dt \quad (3)$$

was also computed from measured torque time histories by numerical integration techniques. The maximum torque  $\bar{T}_{\max}$  was derived in the same way as the average torque except that the dashed curves in figure 12 that are formed by joining straight line segments between the torque peaks are used.

The slope of the least-squares line through the origin, which fairns the data when  $\bar{T}$  is plotted as a function of  $\bar{T}_{\max}$ , is defined as the torque braking-behavior index  $\beta_{b,T}$ .

### Friction Coefficients

Drag-force friction coefficients.- Many references acknowledge the existence of a peak or maximum value of drag-force friction coefficient. (See refs. 16 to 26 for examples.) Most antiskid systems actively seek this peak friction coefficient or are designed to operate within a relatively narrow range of slip velocities or slip ratios in which this peak is assumed to occur, thus providing maximum airplane deceleration (ref. 27). Accordingly, reference 13 defines the brake-pressure and torque ratios as indirect indications of antiskid-system behavior and regards the ratio of average developed to maximum achieved ground reaction forces due to braking effort as a direct indication of the antiskid-system braking behavior. However, friction data can be more difficult to analyze.

During this investigation, the antiskid system exhibited two distinct response modes. Response mode A is defined as antiskid cycling with well-defined incipient skid points, as shown in figure 12(a). Response mode B is defined as antiskid cycling without well-defined incipient skid points, as shown in figure 12(b). Mode A response has been reported frequently in the literature. (See refs. 1, 2, and 6 for examples.) In this study, response mode A is generally associated with the new tires at yaw angles of 0° and 3° and represents approximately 50 percent of the data. When response mode A was observed, values of  $\mu_{d,\max}$ , denoted by the circles in figure 12(a), were measured near the incipient skid points. Using incipient skid points for obtaining  $\mu_{d,\max}$  (see refs. 1, 13, 15, 22, and 25 for examples) is a well-established and accepted method.

Mode B response was reported previously in reference 7. In this investigation, response mode B is associated with the worn tire and with the higher yaw angles. This type response is probably the result of the interaction between the antiskid cycling frequency and the tire mechanical properties. The possible effect that this interaction may have on the shape of the  $\mu$  vs slip curve and hence the  $\mu_{d,\max}$  incipient skid relationship is shown in references 1, 6, and 7 and is discussed in some detail in reference 28. Since response mode B generally precluded determination of  $\mu_{d,\max}$  from incipient skid points, an alternate approach was employed based upon fixed time increments. For this method, the  $\mu_d$  time history was divided into uniform time increments and the apparent  $\mu_{d,\max}$  value nearest each time line was measured

(the last seven circled points in fig. 12(b)). These  $\mu_{d,max}$  values were occasionally supplemented by data from well-defined incipient skids within the time history. (See, for example, the first circled data point in fig. 12(b).)

It should be noted that the distinction between response modes A and B is only made with respect to the friction-coefficient data. The pressure and torque data were always treated as mode A data.

The magnitude of  $\mu_{d,max}$  during a test depends upon the local runway surface texture and the wetness condition, both of which can vary along the length of the test section. The temperature of the tire tread may also be a contributing factor. To assess the system braking behavior, it was necessary to assign a single value to the maximum achieved drag-force friction coefficient for each run (in light of all the differences observed, for example, in fig. 12). The values of  $\mu_{d,max}$  developed by the braking system throughout an individual run were averaged, and this value is denoted by  $\bar{\mu}_{d,max}$  in figure 12. This averaging procedure differs slightly from the integrated averaging techniques used for the pressure and torque data (refs. 13, 15, and 29); however, it will be subsequently shown that there is good agreement among the three sets of data. Values of  $\bar{\mu}_{d,max}$  are not available for torque-limited braking tests because, in those cases, the maximum friction level could not be confirmed. (Torque limited in this investigation refers to a situation where, for a given supply pressure, the brake torque is insufficient to cause a spin-down of the tire.) It is apparent that no antiskid cycling occurs when the brake is torque limited.

The average drag-force friction coefficient  $\mu_d$  developed by the antiskid system during a given test is defined by the expression

$$\bar{\mu}_d = \frac{1}{t_f - t_o} \int_{t_o}^{t_f} \mu_d dt \quad (4)$$

and was computed for each braking test with the use of numerical integration techniques.

The drag-force friction coefficient that is observed when there is no braking results from the tire rolling resistance and is assumed to remain constant throughout a test run; this coefficient is labeled  $\mu_r$  in figure 12. For those tests on flooded surfaces,  $\mu_r$  also includes the resistance attributed to fluid drag (ref. 2). When the ratio is computed of average developed  $\bar{\mu}_d$  to maximum achieved drag-force friction coefficient  $\bar{\mu}_{d,max}$ ,  $\mu_r$  is subtracted from both the numerator and denominator to isolate the friction coefficient attributed to the braking effort.

The slope of the least-squares line through the origin, which fits the data when  $\bar{\mu}_d - \mu_r$  is plotted as a function of  $\bar{\mu}_{d,max} - \mu_r$ , is defined as the braking-friction behavior index  $\beta_{b,F}$ .

Side-force friction coefficients.- Usually the maximum side-force friction

coefficient  $\bar{\mu}_{s,max}$  for a yawed-wheel braking test was obtained when the yawed wheel was freely rolling prior to brake application but after spin-up transients, as shown in figure 12(a). (See refs. 23 and 30 for examples.) Occasionally, however, the variability of  $\mu_s$  during a run was so great that an alternate method, illustrated in figure 12(b), was used. For this method, a number of  $\mu_{s,max}$  values were obtained during the braking portion of the run near points of full wheel-speed recovery, which indicated a momentary relaxation of the braking effort (five circled points in fig. 12(b)). These  $\mu_{s,max}$  values were averaged, and this value is denoted by  $\bar{\mu}_{s,max}$  in the figure. The expression for the average side-force friction coefficient developed during braking

$$\bar{\mu}_s = \frac{1}{t_f - t_0} \int_{t_0}^{t_f} \mu_s dt \quad (5)$$

was computed by numerical integration techniques for each yawed-wheel braking test.

The slope of the least-squares line through the origin, which fair's the data when  $\bar{\mu}_s$  is plotted as a function of  $\bar{\mu}_{s,max}$ , is defined as the cornering-friction behavior index  $\beta_{c,F}$ .

#### Power Terms

As noted in reference 6, the behavior of an antiskid system can also be expressed in terms of the gross stopping power developed by the braking system and by the stopping and cornering power dissipated by the tire. These various power terms are defined in reference 6 in terms of the carriage speed  $V$ , the total drag force  $F_x$  parallel to the wheel plane, the side force  $F_y$  perpendicular to the wheel plane, the yaw angle  $\psi$ , and the slip ratio  $S$ . Time histories of some of these variables during a typical antiskid braking test are presented in figure 13. Slip ratio is the instantaneous ratio of slip velocity of the braked wheel ( $V - \omega r$ ) to the carriage speed  $V$  and is given by the following equation:

$$S = \frac{V - \omega r}{V} \quad (6)$$

where  $r$  for the test tire was computed from the unbraked rolling distance and wheel-revolution count for each run. The value of  $r$  varied from 0.466 to 0.488 m (1.53 to 1.60 ft), depending upon the various combinations of tire vertical load and speed. The following expressions are defined over the interval between  $t_0$  and  $t_f$  in the figure.

Gross stopping power.- The gross stopping power  $P_{d,g}$  developed by the antiskid system during a braking test is derived from forces opposing the direction of motion and is a measure of the overall braking effort. The expression for that power is

$$P_{d,g} = \frac{1}{t_f - t_0} \int_{t_0}^{t_f} (F_x \cos \psi + F_y \sin \psi) V dt \quad (7)$$

where  $F_x \cos \psi + F_y \sin \psi$  converts the measured drag and side forces noted in figure 13 to a single drag force opposing carriage motion. The product of velocity and time yields the distance through which the force acts and completes the work equation. Dividing the work by the duration provides a measure of the power being generated.

Tire stopping power.- A measure of the stopping power dissipated by the tire  $P_{d,t}$  is given by

$$P_{d,t} = \frac{1}{t_f - t_0} \int_{t_0}^{t_f} [(F_x \cos \psi + F_y \sin \psi) VS + F_y \sin \psi (1 - S) V] dt \quad (8)$$

where the carriage speed is multiplied by the slip ratio to obtain the slip velocity (relative speed between tire and pavement). The last term in equation (8),  $\int_{t_0}^{t_f} F_y \sin \psi (1 - S) V dt$ , is an estimate of the work dissipated by the rolling resistance, which is attributed to a yawed rolling tire. The value of  $P_{d,t}$  is thus an indicator of the tread wear associated with the braking effort.

Tire cornering power.- The cornering power dissipated by the tire  $P_{c,t}$  can be closely approximated by the expression

$$P_{c,t} = \frac{1}{t_f - t_0} \int_{t_0}^{t_f} (F_y \cos \psi - F_x \sin \psi) (1 - S) V \sin \psi dt \quad (9)$$

where  $F_y \cos \psi - F_x \sin \psi$  converts the measured side and drag forces to a single side force perpendicular to the direction of motion and where  $(1 - S)V$  is the braked wheel speed which, when multiplied by  $\sin \psi$ , yields the tire lateral velocity. The value of  $P_{c,t}$  is an indicator of the tread wear associated with the cornering effort.

## RESULTS AND DISCUSSION

Pertinent data obtained from all the antiskid braking tests are presented in table I, together with parameters which describe each test condition. In addition, time histories of key parameters from all the tests are presented in the appendix. The tabular data and the appendix time histories are given for the convenience of the user in plotting the data in ways other than those presented in this report. The following sections describe the braking-system behavior, the tire frictional behavior under skid control, and the antiskid-system behavior under a variety of operating conditions.

### Braking-System Behavior

To study the behavior of the antiskid system, it is first necessary to establish the response characteristics of the braking system and its components. The following paragraphs describe the pressure-torque response, the antiskid-system electronic and hydraulic response, and the braking-system response to transient runway friction conditions.

Pressure-torque response.- The relationship between brake pressure and brake torque is shown in figure 14(a) where arrowheads are used to indicate whether pressure is increasing or decreasing for the initial braking cycles. The figure clearly shows that the hysteretic nature of the pressure-torque relationship for this friction condition results in substantial variations in the brake torque for a given brake pressure. This characteristic is most notable during the first brake cycle when the temperature of the brake is essentially the ambient temperature and would suggest that the temperature of the brake has a significant influence on its ability to develop torque. For the test shown, most of the cycling occurred at brake pressures between 10 and 14 MPa (1500 and 2000 psi), but an occasional wheel spin-down caused large fluctuations in both the brake pressure and torque.

The large hysteresis loop associated with the initial brake cycle may weigh more heavily in the determination of the antiskid-system braking behavior during these track tests than during an actual airplane braking stop. During the track tests, several runs are necessary to cover a representative speed range and this large initial hysteresis cycle is repeated for each run; however, during an airplane braking stop, this initial cycle might appear only once.

Large hysteresis loops are also noted during normal antiskid cycling when the brake pressure is presented as a function of the skid signal (fig. 14(b)). The data presented in figure 14 illustrate typical dynamic behavior of the braking system during antiskid operation and provide some insight into the difficulties of designing efficient antiskid braking systems.

Electronic and hydraulic response.- Time histories from run 34 are presented in figure 15 to illustrate the electronic and hydraulic response characteristics of the antiskid system. The electronic response can be described by examining both the test wheel-speed sensor (ac input signal) and the same signal after it passes through an ac-dc converter within the antiskid control box.

Plots of these signals and the corresponding skid-signal and brake-pressure traces are presented in the first four time histories of the figure. Data for this transition run from a dry to a flooded runway surface indicate essentially no time lag between the incipient skid point and the initiation of the skid signal and subsequent brake-pressure dump.

The hydraulic response characteristics of the antiskid system can be described by examining the hydraulic pressure at the antiskid control valve and at the brake. Typical time histories of these signals and the corresponding brake torque are also presented in figure 15. Although approximately 2.2 m (7.25 ft) of the hydraulic line (inside diameter of 0.810 cm (0.319 in.)) and a line fuse separate the two pressure transducers, no measurable hydraulic lags can be detected between them since the pressure response spikes of each occur at approximately the same time. However, approximately 50 msec is required for a complete pressure-torque dump. This duration closely corresponds to the time noted on the wheel-speed trace of figure 15 for the tire to lock up following transition from a dry to a flooded section of the runway.

Response to runway friction transition.- The adaptive characteristics of the antiskid system are illustrated by time histories of the wheel speed, skid signal, brake pressure, and drag-force friction coefficient as presented in figure 16 for two transient runway friction conditions. The response of the braking system to a single transition from a dry to a flooded runway is presented in figures 16(a) and 16(b) for nominal carriage speeds of 54 knots and 94 knots, respectively. At both test speeds, the brake pressure reached a nominal system operating pressure of 21 MPa (3000 psi) and was modulated by the antiskid system on the dry surface. Upon entering the flooded section, the wheel in both tests rapidly decelerated to a deep skid, as noted by the immediate reduction in wheel speed. At a carriage speed of 54 knots, the antiskid system reacted quickly to permit the wheel to recover from the skid, and the remainder of the braking test was conducted with proper antiskid protection. As shown in figure 16(b), at a carriage speed of 94 knots, the wheel did not recover but continued to skid even though the antiskid system responded properly and released all brake pressure. The predicted spin-up hydroplaning speed for the tire, based upon a tire inflation pressure of 0.97 MPa (140 psi), was 91 knots (ref. 5), which is equivalent to a wheel speed of approximately 15.6 rps; thus, once the tire had spun down, insufficient torque was being developed between the tire and the pavement to spin the tire up.

Time histories of test runs that were selected to illustrate the response of the braking system during the transition from a flooded to a dry runway surface are presented in figures 16(c) and 16(d), for nominal carriage speeds of 56 knots and 94 knots, respectively. In both tests, the wheel was spun up to carriage speed on a dry surface prior to entering the flooded test section, and the brakes were applied at or near the start of the flooded section. Figure 16(c) shows that, at 56 knots, the skid signal bleeds off after the initial skid to allow a reapplication of brake pressure until, at about 4 sec, the wheel speed again decreases to the point that the antiskid system modulates the brake pressure on the flooded portion of the runway. Upon reaching the dry section, the brake pressure increased almost linearly for approximately 4 sec at a rate commensurate with the skid-signal bleedoff, which is generated by the pressure-bias-modulation memory circuits. Just prior to the end of the test,

9.5 sec into the run, brake pressure was modulated due to a slight spin-down of the test wheel, which indicated cycling had recommenced.

For the test run at a nominal carriage speed of 94 knots (fig. 16(d)), the wheel commenced to spin down on the flooded section before brakes were applied due to dynamic tire hydroplaning. The calculated spin-down hydroplaning speed for the tire in this test, based on an inflation pressure of 0.97 MPa (140 psi), was 106 knots, which is equivalent to a wheel speed of approximately 18.2 rps (ref. 5). The antiskid system acted as designed and produced a saturated skid signal which prevented the application of pressure to the brake. Upon reaching the dry section, the wheel rapidly spun up to the carriage speed, and approximately 0.75 sec later, the brake pressure increased to 14 MPa (2000 psi). Beyond 3.8 sec, the brake pressure increased gradually for 1.25 sec toward 21 MPa (3000 psi) but was controlled again by the decay rate of the residual skid signal that is a function of the pressure-bias-modulation circuit of the antiskid system.

### Tire Frictional Behavior Under Skid Control

The runway/tire maximum drag- and side-force friction values are discussed here to provide a quantitative measure of the surface condition and for use in updating tire friction models with data from realistic antiskid operating conditions.

Effect of test parameters on maximum drag-force friction coefficient.- The average maximum drag-force friction coefficient  $\bar{\mu}_{d,max}$  as developed by the unyawed tire under dry, damp, flooded, and natural rain conditions is presented as a function of carriage speed in figure 17. The fairings in the figure are linear least-squares curve fits of the data. For these tests, the damp and natural rain wetness conditions provided similar friction characteristics. As expected, values of  $\bar{\mu}_{d,max}$  for the wet runways are substantially lower than those for the dry runway, and the difference is greater for the flooded surface than for the damp surface, particularly at the higher speeds. An extrapolation of the linear curve fit of  $\bar{\mu}_{d,max}$  for the flooded condition is seen to approach negligible values near the predicted tire spin-down hydroplaning speed of 106 knots (ref. 5). Also noted in the figure is the maximum value of the drag-force friction coefficient, 0.78, which was predicted from the empirical expression developed in reference 31 for the test tire operating at very low speeds. It is apparent from the fairings that the dry data for  $\bar{\mu}_{d,max}$  would fall below this prediction if extrapolated to zero speed. The reason for this difference can be explained by examining the data of figure 18, where values of  $\mu_{d,max}$  that were obtained solely during the first wheel spin-down at the initial brake application (for the tests that were not torque limited) are presented as a function of carriage test speed. These values represent the maximum friction coefficients developed from an unheated tire on a dry runway and are faired by a straight line that corresponds to a least-squares fit of the data. The faired line agrees closely with the value of  $\mu_{d,max}$  that was empirically determined from reference 31 for cold tires during a single braking cycle. For comparison purposes, the fairing of the average values of  $\bar{\mu}_{d,max}$  obtained over the entire duration of each of the five dry test runs (fig. 17,

solid line) is also presented in the figure. The maximum friction developed during the initial brake cycle exceeded the average maximum developed throughout each of the tests, particularly those conducted at speeds below 80 knots. This difference may be attributed to high tread temperatures that are generated as the antiskid system maintains the tire at a relatively constant slip ratio.

An example of the tire surface temperatures generated during antiskid cycling is shown in figure 19. An optical pyrometer was focused on the center of the tread in a region approximately one-sixth of a revolution aft of the tire-pavement contact area; thus, the temperature was measured as the hot footprint area rotated into the field of view of the pyrometer. Due to instrument damage, temperature data were obtained for only one run, and data below 110° C (230° F) are not plotted since the pyrometer did not respond to values below this level. The wheel speed and drag-force friction coefficient are presented in the figure to show their relationship with the tire surface temperature. During braking, the tire tread temperature experienced six distinct peaks which correspond to six skid cycles and, after one revolution of the tire following a skid cycle, which required roughly 0.1 sec, the tire had cooled appreciably.

The friction data of figure 17 were obtained at a yaw angle of 0°. The fairings of these data for dry, damp, and flooded surface conditions are reconstructed in figure 20, together with corresponding data obtained at yaw angles of 3°, 6°, 9°, and 12°, to show the effect of yaw angle on  $\bar{\mu}_{d,max}$ . The figure shows that the effect of yaw angle is dependent upon the surface condition and forward speed. With the introduction of yaw,  $\bar{\mu}_{d,max}$  is reduced on the dry and damp surfaces but is relatively unaffected when the surface was flooded.

The effect of tire tread wear on  $\bar{\mu}_{d,max}$  is presented in figure 21, in which the values of  $\bar{\mu}_{d,max}$  for tires having new and worn treads are plotted as a function of carriage speed for three test surface conditions. The new tread data were again obtained from the faired curves of figure 17. The data indicate that when the new tread is replaced by a worn tread, there is no degradation in  $\bar{\mu}_{d,max}$  on the dry surface, but there is a reduction on the damp and flooded runway surfaces. These trends are in reasonable agreement with similar trends noted in references 2, 6, and 7.

Effect of test parameters on maximum side-force friction coefficient.- The maximum side-force friction coefficients developed by the yawed rolling tire under dry, damp, and flooded conditions are plotted as a function of carriage speed in figure 22. The fairings in the figure are linear least-squares curve fits of the data. As discussed previously, these coefficients were generally measured during the free-rolling portion of the run and, for the wet runway surfaces, are lower than those for the dry runway, with the difference becoming greater with increasing water depth and speed. As expected, the values of  $\mu_{s,max}$  on the dry and damp runway surfaces generally increase with increasing yaw angle, at least for yaw angles up to 9°. On the flooded surface, however, this trend, although still present, was not as distinctive, and the values of  $\mu_{s,max}$  at yaw angles of 3° and 6° are shown to approach zero as the speed approaches the predicted tire spin-down hydroplaning speed of 106 knots (ref. 5).

The effect of tread wear on  $\mu_{S,max}$  is shown in figure 23 where the values of  $\mu_{S,max}$  at a yaw angle of  $6^\circ$  on dry, damp, and flooded runway surfaces are plotted as a function of carriage speed. The new tread data were obtained from the faired curves in figure 22 for a yaw angle of  $6^\circ$ . On the dry surface, the worn tread condition gave higher side-force friction coefficients than the new tread condition (a trend that was also noted in refs. 2, 6, and 7). On the flooded surface, however, there was a definite loss in side-force friction when the new tire tread was replaced by a worn one. For the damp surface, the data seem to indicate an increase in  $\mu_{S,max}$  with increasing speed for the worn tire, but this may be due to varying dampness conditions between runs.

Interaction between braking and cornering.- Typical tire friction response to antiskid braking on dry and flooded runway surfaces (interaction between braking and cornering) is presented in figure 24. The drag- and side-force friction coefficients  $\mu_d$  and  $\mu_s$  are plotted as a function of slip ratio for the tire yawed to  $6^\circ$  and operating at a nominal carriage speed of 77 knots. The data presented in the figure illustrate the irregular nature of the friction coefficient to which the antiskid braking system must respond. The apparently random perturbations may result from a combination of such factors as small fluctuations in the tire vertical load due to runway unevenness, flexibility in the wheel support which would be reflected in the measured drag and side forces, variations in the runway surface texture, tire and brake temperatures, and the spring coupling provided by the tire between the wheel and the pavement. Reference 28 discusses some of these factors in detail.

The data presented in figure 24 also illustrate the traction losses associated with flooded runway operations. For example, on the dry runway, the maximum value of  $\mu_d$  is approximately 0.55, but it never exceeds 0.18 on the flooded runway. A similar loss is noted in the maximum side-force friction coefficients. The figure also demonstrates the deterioration in tire cornering capability with increased braking effort (higher slip ratio). The value of  $\mu_s$  is reduced approximately 70 percent on the dry runway at a slip ratio of only 0.3 and is reduced from 0.1 to a negligible value at that same slip ratio on the flooded surface. These cornering reductions during the braking cycles are consistent with those noted for similar antiskid braking tests reported in references 1, 6, and 7 and further illustrate the cornering/braking dilemma faced by antiskid designers.

Effect of cyclic braking on maximum drag-force friction coefficients.- So far, the friction data presented herein were derived from cyclic brake operations. However, there is in the literature a large body of tire friction data available which were obtained under single-cycle conditions, and a discussion of the two data sets is appropriate. A comparison of values of  $\mu_{d,max}$  measured during single-cycle braking tests made without antiskid protection and the average of corresponding values measured under the same test conditions with the antiskid system operational is presented in figure 25. The single-cycle data were obtained approximately 2 yr prior to the present antiskid braking tests and were used previously in references 6 and 7. In figure 25, data are presented separately for dry, damp, and flooded test conditions and for all the test conditions combined. These data include coefficients for tests at similar speeds, yaw angles, vertical loads, and for worn as well as new tread configurations. The data for each test condition are faired by a

least-squares straight line through the plot origins. The data indicate that the maximum drag-force friction coefficients obtained from the single-cycle braking tests tend to be higher than the average maximum coefficients developed by the antiskid system on all the test surfaces, with the greatest difference occurring on the flooded surface. When the data for all three surface wetness conditions are compared simultaneously, the least-squares curve fit indicates that the single-cycle data are approximately 25 percent higher than the maximum drag-force friction coefficient developed by the antiskid system. There are several possible explanations for these trends, ranging from surface weathering and traffic polishing to tire heating associated with cyclic brake operations. However, the implication is quite clear that caution should be exercised in any estimate of antiskid-system braking behavior that is based solely upon  $\mu_{d,max}$  values obtained from single-cycle tests.

### Antiskid-System Behavior Analysis

Braking behavior.- In this section, four terms are used to describe the extent of the braking effort and to examine the antiskid behavior: (1) the brake-pressure behavior index  $\bar{\beta}_{b,p}$ , which assesses the ability of the system to control brake pressure; (2) the brake-torque behavior index  $\bar{\beta}_{b,T}$ , which assesses the system torque control; (3) the friction-behavior index  $\bar{\beta}_{b,F}$ , which measures the ability of the antiskid system to use the apparent maximum friction coefficient at the tire/runway interface; and (4) the total stopping power  $\bar{P}_{d,g}$  that is developed by the antiskid system.

Presented in figure 26 are plots of  $\bar{p}$  versus  $\bar{p}_{max}$ ,  $\bar{T}$  versus  $\bar{T}_{max}$ , and  $\bar{\mu}_d - \mu_r$  versus  $\bar{\mu}_{d,max} - \mu_r$ . Data are plotted for all braking tests except those which were torque limited throughout the entire run, those involving tire hydroplaning, and those performed to examine the effects of a runway friction transition. In each case, the dry data and the wet data are plotted separately. The different surface wetness conditions are denoted by different symbols, but no distinction is made for the various test parameters such as carriage speeds, yaw angles, and vertical forces. The solid line in each plot represents the line of perfect agreement between the average developed and maximum achieved behavior parameter and has a unit slope. The dashed line in each plot is the least-squares fit passing through the plot origin. The slope of each dashed line represents the average braking-behavior index for each data set. (See fig. 16 of ref. 26.)

On the dry runway surfaces, the average braking-behavior indexes  $\bar{\beta}_b$  determined from the pressure, torque, and friction ratios vary between 0.91 and 0.93, a difference of only 2 percent. On the wet runway surfaces, the variation in  $\bar{\beta}_b$  is between 0.68 and 0.71, a difference of approximately 4 percent. A comparison of the  $\bar{\beta}_b$  values for the wet runway surfaces with the  $\bar{\beta}_b$  values for the dry runway surfaces indicates a reduction of between 23 and 25 percent in the braking-behavior indexes. Thus, figure 26 shows that the antiskid braking system suffers a degraded braking-index level on the wet runway surfaces, in addition to the obvious reduction in friction coefficient. The data also indicate that the antiskid braking-behavior indexes derived from the three parameters give essentially the same results. This correlation may not be exhibited by other antiskid systems; however, it does indicate that, for

this antiskid system, the three indexes can be used interchangeably as a measure of the braking behavior. It should also be emphasized that the braking-behavior indexes are based upon maximum achieved values of pressure, torque, and friction which may vary from one antiskid system to another, and any comparisons between different antiskid systems based solely upon these indexes may be technically misleading since there is no common base for comparison.

To isolate the effect that various test parameters have on the pressure, torque, and friction indexes, data from figure 26 are plotted in figures 27 to 32. Each figure is divided into three parts: (a) pressure indexes, (b) torque indexes, and (c) friction indexes. Each plot includes the line of perfect agreement and the least-squares fit passing through the origin, from which the average braking-behavior index  $\bar{\beta}_b$  is determined. The trends observed for some test conditions may be influenced by a small sample size.

The effect of speed on braking-behavior indexes is shown in figure 27. On the dry runway surfaces, the indexes are higher at a speed of 100 knots than at the lower speeds. On the damp runway surfaces, the opposite trend is observed. On the flooded runway surfaces, the braking-behavior indexes are reduced when the carriage speed is increased from 50 to 75 knots, and no data are available at 100 knots due to tire hydroplaning.

Figure 28 presents the effect of yaw angle on the braking-behavior indexes. On the dry runway surfaces, these indexes are generally higher at a yaw angle of  $6^\circ$  than for the other yaw angles. No consistent trends were observed for the wet runway surfaces.

The effect of variations in the vertical force on the braking-behavior indexes is shown in figure 29. Insufficient data are available to discuss the effect of vertical-force variations on the dry runway surfaces and are not plotted. On the wet runway surfaces, however, the data indicate that the braking-behavior indexes are consistently lower for the light vertical forces.

Shown in figure 30 is the effect of tread wear on the braking-behavior indexes. On the dry runway surfaces, the indexes are slightly higher for the worn tire than for the new tire. The opposite trend is generally observed on the wet runway surfaces. The only exception occurs on the flooded runway when the braking-behavior index is obtained from the friction ratio (fig. 30(c)), but this may be due to the small sample number.

Figure 31 presents the effect of system operating pressure on the braking-behavior indexes. Insufficient brake torque was available to permit antiskid activity on the dry runway surfaces for the reduced system pressure; thus, only the wet runway data are presented. On the damp runway surfaces, the indexes are highest for a system pressure of 10 MPa (1500 psi) and lowest for a system pressure of 14 MPa (2000 psi). No consistent trends are observed for the flooded runway surfaces.

Presented in figure 32 is the effect of system response mode on the braking-behavior indexes. The data indicate that mode B system response produces significant increases in the pressure, torque, and friction indexes over

those obtained from mode A operation. This trend is observed for all three surface wetness conditions.

In summary, the data presented in figures 27 to 32 imply that the braking behavior of the antiskid system would not be adversely affected by cross-wind operations (yaw-angle effects), but might be degraded by excessive wing lift during the landing roll-out (vertical-force effects). These results also indicate that the antiskid-system braking behavior may be adversely affected by excessive tire wear on wet runway surfaces. Finally, the data indicate that the highest braking-behavior indexes are achieved when the antiskid system operates in response mode B.

The gross stopping power  $P_{d,g}$  (eq. (7)) developed by the antiskid system, which is a measure of the overall antiskid braking effort, is listed in table I for each test condition. Figure 33 presents bar graphs of these data in terms of  $\bar{P}_{d,g}$ , a numerical average of all the data for a given test condition. For example, the dry, 50-knot bar graph is the average of all dry runs at 50 knots, including the various yaw angles, vertical forces, tread configurations, and system pressures. Data from torque-limited tests and from tests involving tire hydroplaning are included in the figure, but no data are included from tests performed under transient runway friction conditions. As expected, because of higher available friction coefficients, the gross stopping power on the dry surface is much higher than that on the wet runway surfaces. On the dry surface,  $\bar{P}_{d,g}$  increases to a lesser extent with tire vertical force and with a worn tread configuration. The wheel yaw angle appears to have little effect. On the wet surfaces,  $\bar{P}_{d,g}$  increases with tire vertical force, decreases with tread wear, and exhibits no substantial change for variations in carriage speed, brake supply pressure, or yaw angle.

The stopping power dissipated by the tire alone  $P_{d,t}$  (eq. (8)) is only a small fraction of the gross stopping power, but it does provide an indication of the tread wear associated with the braking effort; thus, the ideal antiskid system would maximize  $P_{d,g}$  and minimize  $P_{d,t}$ . Values of  $P_{d,t}$  are listed in table I for each test condition. The data are averaged and plotted as bar graphs in figure 34 to show the effects attributed to test parameter variations. Data from all tests except those performed to study the effect of a runway friction transition are included in the figure. The figure shows that for corresponding conditions,  $\bar{P}_{d,t}$  is generally higher on the dry surface than on the wet surfaces except for the 10 MPa (1500 psi) brake supply pressure tests. On a dry surface,  $\bar{P}_{d,t}$  increases with carriage speed, yaw angle, brake supply pressure, and when a new tread is replaced by a worn tread. On the wet runway surfaces,  $\bar{P}_{d,t}$  increases with carriage speed, yaw angle, tire vertical force, and brake supply pressure but decreases when a worn tread is used. The data in figure 34 indicate that the most severe tread wear occurs during combined braking and cornering operations on a dry surface.

The ratio of tire stopping power to gross stopping power for each test is plotted as a function of  $\bar{\mu}_{d,max}$  in figure 35. Data are not included for torque-limited tests, for tests performed under transient runway friction conditions, or for tests involving tire hydroplaning. The curves which fair the data represent a least-squares fit and indicate that the ratio increases slightly as the surface friction level decreases, perhaps due to hydroplaning

effects. The figure also shows that the general effect of increasing the wheel yaw angle is to increase the percentage of the total stopping power dissipated by the tire and to increase tire wear (also suggested by the amount of rubber deposited on the runway during yawed rolling tests).

Cornering behavior.- Antiskid systems are not designed to maximize cornering performance since good cornering is not compatible with heavy braking, but cornering is important for directional control, especially when cross winds are present.

Presented in figures 36 to 38 are plots of  $\bar{\mu}_s$  versus  $\bar{\mu}_{s,max}$  to show the effect several test parameters have on the cornering-behavior indexes  $\beta_C$ . The test parameter levels and surface wetness conditions are plotted separately. Each plot includes the line of ideal behavior and the least-squares fit passing through the plot origin from which the average cornering-behavior index is obtained. It should again be emphasized that trends observed for some test conditions may be influenced by a small sample size.

The effect of yaw angle on the cornering-behavior indexes is shown in figure 36. Data are presented for all three wetness conditions at 3° and 6°. Data taken at yaw angles of 9° and 12° are shown for the damp runway surfaces only. In general, these indexes are somewhat higher on the dry runway surfaces than on the wet runway surfaces for yaw angles of 3° and 6°. The cornering-behavior indexes are shown to decrease when the yaw angle is increased from 3° to 6° for each wetness condition. Indexes from the 9° and 12° data are slightly higher than 0.5.

Figure 37 shows the effect of carriage speed on the cornering-behavior indexes. On the dry runway surfaces, the indexes are relatively insensitive to variations in carriage speed. On the wet runway surfaces, the indexes decrease with increasing carriage speed. At 100 knots on the flooded runway surfaces, hydroplaning effects have completely eliminated the tire cornering capability.

Presented in figure 38 is the effect of tread wear on the cornering-behavior indexes. All three surface wetness conditions show a decrease in the indexes when a new tire is replaced by a worn tire, and this decrease is much more pronounced on the wet runway surfaces.

The cornering power dissipated by the tire  $P_{C,t}$  (eq. (9)) not only is indicative of the overall cornering capability of the tire during the antiskid controlled braking, but also provides an indication of the increased tread wear associated with the steering effort. The effects of test parameter variations on  $\bar{P}_{C,t}$  are presented in figure 39 as bar graphs. The data indicate that  $\bar{P}_{C,t}$  values are, as expected, considerably higher on the dry surface than on the wet surfaces and increase with yaw angle and speed on both surfaces. The value of  $\bar{P}_{C,t}$  was higher for the worn tread conditions on the dry surface and was higher for the new tread condition on the wet surfaces. Although  $\beta_{C,F}$  decreased with increasing yaw angle (fig. 36), the values of  $\bar{P}_{C,t}$  increased substantially when the yaw angle was increased from 3° to 12° (fig. 39); thus, both power terms and behavior-index terms are needed when studying the characteristics of antiskid systems.

## CONCLUDING REMARKS

An experimental investigation was conducted at the Langley aircraft landing loads and traction facility to study the braking and cornering response of a slip-velocity-controlled, pressure-bias-modulated aircraft antiskid braking system. The investigation, conducted on dry and wet runway surfaces, utilized one main gear wheel, brake, and tire assembly of a McDonnell Douglas DC-9 series 10 airplane.

Results from the experimental investigation indicate that:

1. During maximum braking, average braking-behavior indexes based upon brake pressure, torque, and drag-force friction coefficient developed by the antiskid system were higher on the dry surfaces than on the damp and flooded surfaces.
2. On the wet surfaces, these indexes were reduced with lighter vertical forces, higher carriage speeds, and when new tire treads were replaced by worn treads.
3. The three braking-behavior indexes agreed with one another and can be used interchangeably as a measure of the braking behavior for this antiskid system.
4. These braking-behavior indexes are based upon maximum values of pressure, torque, and drag-force friction coefficient which may vary from system to system, and any comparisons between different antiskid systems based solely upon these indexes may be technically misleading.
5. The average gross stopping power generated by the brake system was considerably higher on the dry surfaces than on the wet surfaces.
6. That portion of the stopping power which was dissipated by the tire and which provided an indication of the tire wear was observed to be greatest during combined braking and cornering on a dry surface.
7. The average cornering-behavior index based upon the side-force friction coefficient developed by the tire under antiskid control was decreased on wet surfaces, with increasing yaw angle and carriage speed, and when tires with new treads were replaced by those with worn treads.
8. The interaction between braking and cornering forces indicated that, during antiskid cycling on the dry runway surfaces, the side-force friction coefficient was significantly reduced during portions of the braking cycles; on the flooded runway surfaces, this coefficient was frequently reduced to negligible values.
9. During the transition from a dry to a flooded surface under heavy braking, the wheel entered into a deep skid but the antiskid system reacted properly by quickly reducing brake pressure and performed normally during the remainder of the run on the flooded surface.

10. The brake-pressure recovery following transition from a flooded to a dry surface took 4 sec and was shown to be a function of the decay rate of the residual skid signal built up by the antiskid system during the initial skid cycles on the first surface.

Langley Research Center  
National Aeronautics and Space Administration  
Hampton, VA 23665  
September 12, 1979



## REFERENCES

1. Tanner, John A.: Performance of an Aircraft Tire Under Cycle Braking and of a Currently Operational Antiskid Braking System. NASA TN D-6755, 1972.
2. Horne, Walter B.; and Leland, Trafford J. W.: Influence of Tire Tread Pattern and Runway Surface Condition on Braking Friction and Rolling Resistance of a Modern Aircraft Tire. NASA TN D-1376, 1962.
3. Tracy, William V., Jr.: Wet Runway Aircraft Control Project (F-4 Rain Tire Project). ASD-TR-74-37, U.S. Air Force, Oct. 1974. (Available from DDC as AD A004 768.)
4. Danhof, Richard H.; and Gentry, Jerauld R.: RF-4C Wet Runway Performance Evaluation. FTC-TR-66-6, U.S. Air Force, May 1966. (Available from DDC as AD 486 049.)
5. Horne, Walter B.; McCarty, John L.; and Tanner, John A.: Some Effects of Adverse Weather Conditions on Performance of Airplane Antiskid Braking Systems. NASA TN D-8202, 1976.
6. Stubbs, Sandy M.; and Tanner, John A.: Behavior of Aircraft Antiskid Braking Systems on Dry and Wet Runway Surfaces - A Velocity-Rate-Controlled, Pressure-Bias-Modulated System. NASA TN D-8332, 1976.
7. Tanner, John A.; and Stubbs, Sandy M.: Behavior of Aircraft Antiskid Braking Systems on Dry and Wet Runway Surfaces - A Slip-Ratio-Controlled System With Ground Speed Reference From Unbraked Nose Wheel. NASA TN D-8455, 1977.
8. Metric Practice Guide. E 380-72, American Soc. Testing & Mater., June 1972.
9. Tanner, John A.: Fore-and-Aft Elastic Response Characteristics of 34 x 9.9, Type VII, 14 Ply-Rating Aircraft Tires of Bias-Ply, Bias-Belted, and Radial-Belted Design. NASA TN D-7449, 1974.
10. Leland, Trafford J. W.; Yager, Thomas J.; and Joyner, Upshur T.: Effects of Pavement Texture on Wet-Runway Braking Performance. NASA TN D-4323, 1968.
11. Yager, Thomas J.; Phillips, W. Pelham; Horne, Walter B.; and Sparks, Howard C. (appendix D by R. W. Sugg): A Comparison of Aircraft and Ground Vehicle Stopping Performance on Dry, Wet, Flooded, Slush-, Snow-, and Ice-Covered Runways. NASA TN D-6098, 1970.
12. Alfaro-Bou, Emilio; and Vaughan, Victor L., Jr.: Light Airplane Crash Tests at Impact Velocities of 13 and 27 m/sec. NASA TP-1042, 1977.
13. Skid Control Performance Evaluation. ARP 862, Soc. Automot. Eng., Mar. 1, 1968.

14. Lester, W. G. S.: Some Factors Influencing the Performance of Aircraft Anti-Skid Systems. Tech. Memo. EP 550, British R.A.E., July 1973.
15. Brake Control Systems, Antiskid, Aircraft Wheels, General Specifications for. Mil. Specif. MIL-B-8075D, Feb. 24, 1971.
16. Aircraft Stopping Systems. Aircr. Eng., vol. 47, no. 10, Oct. 1975, pp. 18-22.
17. Merritt, Leslie R.: Concorde Landing Requirement Evaluation Tests. Report No. FAA-FS-160-74-2, 1974.
18. Proceedings First International Skid Prevention Conference. Part I. Virginia Counc. Highway Invest. Res., Aug. 1959.
19. Flight Tests To Determine the Coefficient of Friction Between an Aircraft Tyre and Various Wet Runway Surfaces. Part 7: Trials on a Concrete Runway at Filton. S & T MEMO 3/62, British Minist. Aviat., May 1962.
20. Batterson, Sidney A.: Investigation of the Maximum Spin-up Coefficients of Friction Obtained During Tests of a Landing Gear Having a Static-Load Rating of 20,000 Pounds. NASA MEMO 12-20-58L, 1959.
21. Theisen, Jerome G.; and Edge, Philip M., Jr.: An Evaluation of an Accelerometer Method for Obtaining Landing-Gear Drag Loads. NACA TN 3247, 1954.
22. Sawyer, Richard H.; Batterson, Sidney A.; and Harrin, Eziaslav N.: Tire-to-Surface Friction Especially Under Wet Conditions. NASA MEMO 2-23-59L, 1959.
23. Dreher, Robert C.; and Yager, Thomas J.: Friction Characteristics of 20 x 4.4, Type VII, Aircraft Tires Constructed With Different Tread Rubber Compounds. NASA TN D-8252, 1976.
24. Batterson, Sidney A.: Braking and Landing Tests on Some New Types of Airplane Landing Mats and Membranes. NASA TN D-154, 1959.
25. Zalovcik, John A.: Ground Deceleration and Stopping of Large Aircraft. Presented at Thirteenth Meeting of the Flight Test Panel of AGARD (Copenhagen, Denmark), Oct. 20-29, 1958.
26. Frictional and Retarding Forces on Aircraft Tyres. Part II: Estimation of Braking Force. Eng. Sci. Data, Item No. 71026, R. Aeronaut. Soc., Oct. 1971.
27. Hirzel, E. A.: Antiskid and Modern Aircraft. [Preprint] 720868, Soc. Automot. Eng., Oct. 1972.
28. Batterson, Sidney A.: A Study of the Dynamics of Airplane Braking Systems as Affected by Tire Elasticity and Brake Response. NASA TN D-3081, 1965.

29. Frictional and Retarding Forces on Aircraft Tyres. Part I: Introduction. Eng. Sci. Data, Item No. 71025 With Amendment A, R. Aeronaut. Soc., Aug. 1972.
30. Yager, Thomas J.; and McCarty, John L.: Friction Characteristics of Three 30 x 11.5-14.5, Type VIII, Aircraft Tires With Various Tread Groove Patterns and Rubber Compounds. NASA TP-1080, 1977.
31. Smiley, Robert F.; and Horne, Walter B.: Mechanical Properties of Pneumatic Tires With Special Reference to Modern Aircraft Tires. NASA TR R-64, 1960. (Supersedes NACA TN 4110.)

TABLE I.- SUMMARY OF TEST

Run	Response mode	Tire-tread condition	Brake supply pressure		Yaw angle, deg	Surface condition	Vertical load		Nominal speed, knots	$\bar{\mu}_d$	$\bar{\mu}_{d,max}$	$\mu_r$	$\bar{p}$		$\bar{F}_{max}$	
			MPa	psi			kN	lbf					MPa	psi	MPa	psi
1	A	New	21	3000	0	(a)	60	13.4	54	0.50	0.66	0.03	11.2	1624	15.1	2205
2	A	New	21	3000	0	Dry	60	13.5	74	.58	.66	.03	15.7	2277	18.1	2625
3	A	New	21	3000	0	Dry	65	14.6	70	.58	.66	.02	11.3	1639	13.2	1914
4	B	New	21	3000	0	Dry	62	13.9	99	.57	.60	.05	13.8	2002	15.0	2176
5	A	New	20	2900	0	Dry	84	18.8	43	.54	.61	.04	16.5	2393	18.8	2727
6		New	19	2800	0	Dry	83	18.6	99	.45						
7		New	20	2900	0	Dry	97	21.8	94	.47						
8	A	New	21	3000	0	Damp	60	13.4	56	.20	.33	.03	4.1	595	8.2	1189
9	A	New	21	3000	0	Damp	60	13.4	77	.22	.28	.05	3.3	479	5.9	856
10	B	New	20	2900	0	Damp	59	13.3	101	.20	.28	.04	3.7	537	4.8	696
11	A	New	20	2900	0	Damp	82	18.5	60	.21	.32	.04	5.3	769	9.6	1392
12	A	New	21	3000	0	Damp	83	18.6	77	.24	.32	.04	5.1	740	6.4	928
13	B	New	21	3000	0	Damp	82	18.5	104	.22	.30	.04	4.9	711	6.3	914
14	A	New	21	3000	0	Damp	97	21.9	56	.24	.29	.03	6.9	1001	9.8	1421
15	A	New	21	3000	0	Damp	97	21.9	75	.21	.27	.02	6.3	914	7.9	1146
16	A	New	21	3000	0	Damp	97	21.9	101	.20	.35	.06	5.5	798	8.5	1233
17	A	New	21	3000	0	Damp	120	27.0	55	.26	.31	.02	9.3	1349	11.0	1595
18	B	New	20	2900	0	Damp	120	27.0	76	.22	.27	.03	6.8	986	8.2	1189
19	A	New	20	2900	0	Damp	120	27.0	102	.18	.26	.03	5.9	856	7.9	1146
20	A	New	20	2900	0	Flooded	59	13.2	53	.18	.26	.05	2.8	406	5.8	841
21	A	New	21	3000	0	Flooded	59	13.3	75	.10	.14	.06	1.2	174	3.7	537
22		New	21	3000	0	Flooded	59	13.2	93	.06						
23	A	New	21	3000	0	Flooded	78	17.5	53	.25	.19	.05	4.9	711	6.2	899
24	A	New	21	3000	0	Flooded	81	18.2	56	.21	.24	.04	4.1	595	5.3	769
25	B	New	21	3000	0	Flooded	81	18.2	76	.12	.14	.05	2.1	305	4.0	580
26		New	21	3000	0	Flooded	81	18.1	92	.07						
27	A	New	20	2900	0	Flooded	101	22.7	59	.17	.22	.04	4.3	624	8.0	1160
28	A	New	21	3000	0	Flooded	94	21.2	75	.13	.17	.06	2.4	348	4.4	638
29		New	21	3000	0	Flooded	93	20.9	91	.06						
30	B	New	20	2900	0	Flooded	128	28.7	53	.25	.29	.06	7.6	1102	8.7	1262
31	A	New	20	2900	0	Flooded	125	28.2	74	.13	.17	.06	3.2	464	6.0	870
32		New	20	2900	0	Flooded	117	26.2	93	.07						
33		New	21	3000	0	Dry/Flooded	84	18.8	54	.32	.58/.23					
34		New	21	3000	0	Dry/Flooded	84	18.8	76	.29	.57/.16					
35		New	21	3000	0	Dry/Flooded	83	18.7	94	.26	.53/					
36		New	21	3000	0	Flooded/Dry	84	18.8	56	.23	.19/					
37		New	20	2900	0	Flooded/Dry	83	18.7	77	.16	.13/					
38		New	20	2900	0	Flooded/Dry	83	18.7	94	.28						
39	A	New	20	2900	0	Rain	82	18.5	55	.18	.36	.03	5.4	783	11.4	1653
40	A	New	20	2900	0	Rain	82	18.5	76	.22	.28	.03	5.7	827	7.8	1131
41	B	New	20	2900	0	Rain	82	18.5	103	.18	.24	.04	4.3	624	5.8	841
42	A	New	21	3000	3	Dry	85	19.0	40	.54	.62	.04	15.0	2176	17.4	2524
43	A	New	20	2900	3	Dry	85	19.2	72	.51	.58	.03	16.4	2379	17.8	2582
44	A	New	21	3000	3	Dry	86	19.4	97	.47	.49	.03	18.5	2683	19.4	2814
45	A	New	20	2900	3	Damp	84	18.9	53	.27	.29	.04	6.0	870	7.6	1102
46	A	New	20	2900	3	Damp	83	18.7	77	.20	.25	.03	4.9	711	5.9	856
47	A	New	20	2900	3	Damp	84	18.9	102	.19	.31	.03	4.6	667	7.1	1030
48	A	New	20	2900	3	Flooded	83	18.7	52	.20	.27	.05	4.0	580	7.8	1131
49	B	New	20	2900	3	Flooded	83	18.6	79	.10	.13	.06	1.6	232	4.1	595
50		New	20	2900	3	Flooded	81	18.3	95	.06						
51	B	New	21	3000	6	Dry	85	19.1	47	.53	.56	.07	13.3	1929	14.2	2060

<sup>a</sup>One damp spot on otherwise dry runway.

CONDITIONS AND RESULTS

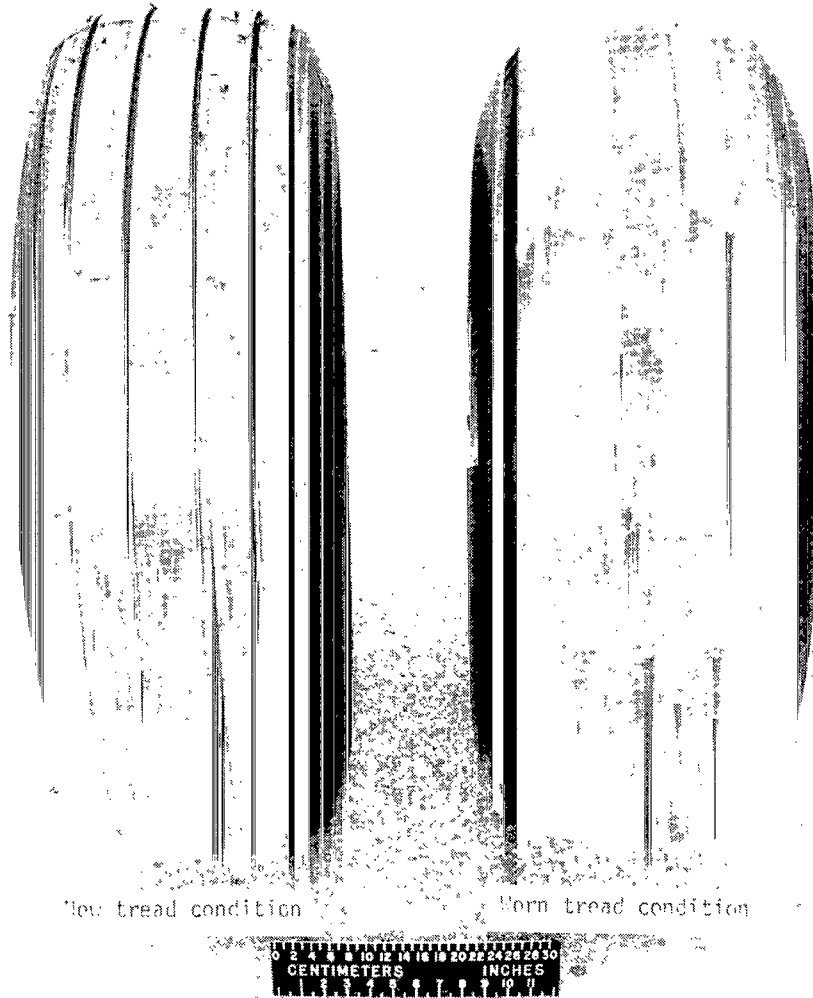
$\bar{T}$		$\bar{T}_{max}$		Torque limit, percent	$\bar{\mu}_s$	$\bar{\mu}_{s,max}$	Average slip ratio	Average slip velocity		Gross stopping power		Tire stopping power		Tire cornering power		Hydroplaning	Run		
kN-m	ft-lbf	kN-m	ft-lbf					m/sec	ft/sec	kW	hp	kW	hp	kW	hp				
14.1	10 415	19.3	14 256	31			0.11	3.04	9.96	835	1120	99	133			No	1		
17.0	12 557	19.5	14 404				.09	3.52	11.56	1342	1800	124	166			No	2		
18.8	13 887	21.0	15 512				.12	4.12	13.53	1342	1800	158	212			No	3		
17.3	12 779	18.6	13 739	28			.09	4.48	14.69	1767	2370	160	215			No	4		
20.4	15 068	23.3	17 211				.14	3.03	9.95	984	1320	131	176			No	5		
							.04	2.19	7.20	1864	2500	83	111			No	6		
				100			.06	3.01	9.89	2192	2940	138	185			No	7		
6.4	4 727	10.7	7 904				.08	2.18	7.15	350	469	25	33			No	8		
4.8	3 546	7.7	5 688				.06	2.47	8.11	530	711	39	52			No	9		
5.4	3 989	6.8	5 023	100			.05	2.70	8.87	612	821	40	53			No	10		
7.8	5 761	11.7	8 642				.08	2.30	7.56	530	711	40	54			No	11		
7.9	5 835	9.1	6 722				.06	2.37	7.78	776	1040	54	73			No	12		
7.0	5 171	9.0	6 648				.06	3.11	10.19	925	1240	64	86			No	13		
9.9	7 313	13.3	9 824				.07	2.05	6.71	656	880	49	66			No	14		
9.5	7 017	11.6	8 568				.07	2.66	8.74	805	1080	60	80			No	15		
6.5	4 801	12.5	9 233				.05	2.75	9.01	962	1290	75	100			No	16		
13.3	9 824	16.8	12 409				.07	1.97	6.45	872	1170	62	83			No	17		
11.2	8 273	12.6	9 307				.06	2.35	7.72	1037	1390	69	92			No	18		
8.7	6 426	11.2	8 273				.05	2.62	8.59	1104	1480	70	94			No	19		
3.7	2 733	6.9	5 097				.11	3.14	10.29	289	387	34	45			No	20		
.6	433	3.5	2 585				.33	12.71	41.71	239	320	79	106			No	21		
							.94	45.05	147.8	182	244	171	229			Yes	22		
8.1	5 983	9.3	6 869				.12	3.16	10.37	533	715	65	87			No	23		
6.5	4 801	8.9	1 291				.10	2.74	9.00	479	643	48	64			No	24		
2.5	1 847	4.6	3 398				.10	3.95	12.96	379	508	36	48			No	25		
							.93	44.19	144.98	276	370	259	347			Yes	26		
6.1	4 506	10.2	7 534				.08	2.49	8.16	511	685	49	61			No	27		
3.1	2 290	5.1	3 767				.12	4.50	14.77	467	626	57	77			No	28		
							.96	45.01	147.66	255	342	244	327			Yes	29		
11.6	8 568	13.7	10 120				.09	2.56	8.40	887	1190	84	113			No	30		
4.3	3 176	7.4	5 466	17			.07	2.76	9.05	611	820	50	67			No	31		
							.85	40.49	132.84	401	538	341	457			Yes	32		
							.14	4.02	13.19	783	1050	116	156			No	33		
							.21	8.06	26.46	977	1310	139	187			No	34		
							.58	28.34	92.97	1066	1430	230	308			No/Yes	35		
							.08	2.34	7.69	524	703	43	57			No	36		
							.18	7.26	23.82	507	680	51	68			No	37		
							.42	20.08	65.89	1111	1490	152	204			Yes/No	38		
							.08	2.29	7.51	428	574	42	56			No	39		
7.5	5 540	13.6	10 046	24	0.20	0.24	.07	2.67	8.75	729	977	57	76			No	40		
8.3	6 131	10.6	7 830				.04	2.38	7.80	753	1010	43	58			No	41		
5.4	3 989	7.3	5 392				.15	3.10	10.16	947	1270	157	211			16	21	No	42
20.6	15 216	23.2	17 137	13	.17	.22	.12	4.40	14.43	1603	2150	218	293			No	43		
20.0	14 773	21.2	15 659				.10	4.76	15.62	1998	2680	233	312			36	48	No	44
19.2	14 182	19.7	14 551				.11	3.00	9.84	610	818	88	118			16	22	No	45
9.0	6 648	10.8	7 977	85	.16	.18	.10	3.70	12.15	651	873	87	116			No	46		
6.9	5 097	8.4	6 205				.07	3.62	11.89	798	1070	97	130			30	40	No	47
6.4	4 727	8.0	5 909				.12	3.36	11.04	449	602	75	100			14	19	No	48
5.9	4 358	10.2	7 534		.13	.18	.25	10.17	33.35	347	466	79	106			No	49		
2.0	1 477	4.2	3 102				.98	47.77	156.71	247	331	242	325			0	0	Yes	50
							.18	4.17	13.67	1081	1450	251	337			51	68	No	51

TABLE I.-

Run	Response mode	Tire-tread condition	Brake supply pressure		Yaw angle, deg	Surface condition	Vertical load		Nominal speed, knots	$\bar{\mu}_d$	$\bar{\mu}_{d,max}$	$\mu_r$	$\bar{p}$		$\bar{P}_{max}$	
			MPa	psi			kN	lbf					MPa	psi	MPa	psi
52	B	New	20	2900	6	Dry	85	19.1	75	0.46	0.47	0.06	12.1	1755	13.5	1958
53	B	New	21	3000	6	Dry	85	19.1	103	.41	.42	.06	9.8	1421	11.2	1624
54	B	New	20	2900	6	Damp	61	13.8	77	.16	.22	.03	2.8	406	3.9	566
55	B	New	21	3000	6	Damp	86	19.3	57	.20	.23	.06	4.8	696	5.4	783
56	B	New	20	2900	6	Damp	84	18.9	77	.15	.19	.04	3.3	479	4.2	609
57	B	New	20	2900	6	Damp	78	17.5	106	.10	.17	.05	1.9	276	3.8	798
58	B	New	21	3000	6	Flooded	83	18.7	56	.22	.25	.06	4.2	609	5.5	798
59	B	New	21	3000	6	Flooded	80	17.9	80	.12	.13	.07	1.4	203	2.8	406
60		New	21	3000	6	Flooded	79	17.7	92	.06						
61	B	New	19	2800	9	Damp	86	19.3	55	.20	.27	.07	3.4	493	4.2	609
62	B	New	20	2900	9	Damp	86	19.3	78	.15	.20	.06	2.8	406	3.8	551
63	B	New	20	2900	9	Damp	84	18.9	104	.09	.13	.04	1.8	261	2.8	406
64	B	New	20	2900	12	Damp	85	19.1	76	.15	.21	.06	2.6	377	3.1	450
65	A	Worn	20	2900	0	Dry	72	16.2	49	.60	.67	.02	15.9	2306	18.2	2640
66	A	Worn	21	3000	0	Dry	77	17.2	73	.60	.65	.02	15.7	2277	17.7	2567
67	B	Worn	21	3000	0	Dry	77	17.2	101	.58	.63	.03	17.9	2596	18.6	2698
68	B	Worn	20	2900	0	Damp	71	16.0	54	.18	.23	.02	3.5	508	4.5	653
69	B	Worn	21	3000	0	Damp	89	20.0	53	.13	.16	.03	2.6	377	3.8	551
70	B	Worn	21	3000	0	Damp	88	19.7	72	.11	.21	.02	2.8	406	3.7	537
71	B	Worn	21	3000	0	Damp	88	19.7	104	.10	.21	.03	2.0	290	3.0	435
72	B	Worn	21	3000	0	Flooded	73	16.3	57	.11	.12	.05	2.0	290	3.0	435
73	B	Worn	20	2900	0	Flooded	73	16.3	72	.08	.09	.06	1.0	145	2.2	319
74		Worn	21	3000	0	Flooded	73	16.3	94	.06						
75	B	Worn	21	3000	6	Dry	84	18.9	51	.49	.50	.08	12.4	1798	13.4	1944
76	B	Worn	21	3000	6	Dry	84	18.9	75	.47	.49	.08	12.3	1784	13.4	1944
77	B	Worn	21	3000	6	Dry	86	19.3	99	.45	.47	.08	12.9	1871	14.0	2031
78	B	Worn	21	3000	6	Damp	59	13.2	77	.08	.16	.07	1.5	218	2.4	348
79	B	Worn	21	3000	6	Damp	88	19.7	54	.12	.16	.05	2.3	334	3.0	435
80	B	Worn	21	3000	6	Damp	80	17.9	58	.11	.15	.04	1.7	247	2.6	377
81	B	Worn	21	3000	6	Damp	81	18.3	76	.08	.12	.04	1.4	203	3.2	464
82	B	Worn	21	3000	6	Damp	80	17.9	105	.08	.15	.06	1.6	232	2.4	348
83	B	Worn	21	3000	6	Flooded	79	17.7	53	.10	.11	.04	1.9	276	3.7	537
84	B	Worn	20	2900	6	Flooded	78	17.5	75	.07	.08	.05	.7	102	2.1	305
85		Worn	21	3000	6	Flooded	78	17.6	93	.06						
86		New	14	2000	0	Dry	84	18.8	46	.49						
87		New	16	2300	0	Dry	84	18.9	71	.47						
88		New	13	1900	0	Dry	85	19.0	97	.36						
89	A	New	14	2000	0	Damp	82	18.5	54	.22	.40	.03	7.0	1015	11.5	1668
90	A	New	14	2000	0	Damp	82	18.4	76	.23	.31	.03	6.2	899	7.4	1073
91	A	New	13	1900	0	Damp	82	18.4	104	.18	.30	.04	4.5	653	6.1	885
92	A	New	14	2000	0	Flooded	82	18.5	53	.25	.30	.06	4.8	696	6.5	943
93	A	New	14	2000	0	Flooded	82	18.4	76	.12	.18	.06	1.9	276	3.9	566
94		New	14	2000	0	Flooded	81	18.1	93	.06						
95		New	10	1500	0	Dry	83	18.7	77	.28						
96	A	New	10	1500	0	Damp	82	18.4	55	.29	.33	.03	7.3	1059	7.6	1102
97	A	New	10	1500	0	Damp	82	18.5	75	.24	.29	.04	5.8	841	6.7	972
98	A	New	10	1500	0	Damp	83	18.7	102	.20	.28	.04	5.4	783	7.6	1102
99	A	New	10	1500	0	Flooded	82	18.5	56	.23	.27	.04	4.9	711	5.6	812
100	A	New	10	1500	0	Flooded	82	18.4	77	.11	.20	.05	1.5	218	3.3	479
101		New	10	1500	0	Flooded	82	18.4	104	.06						

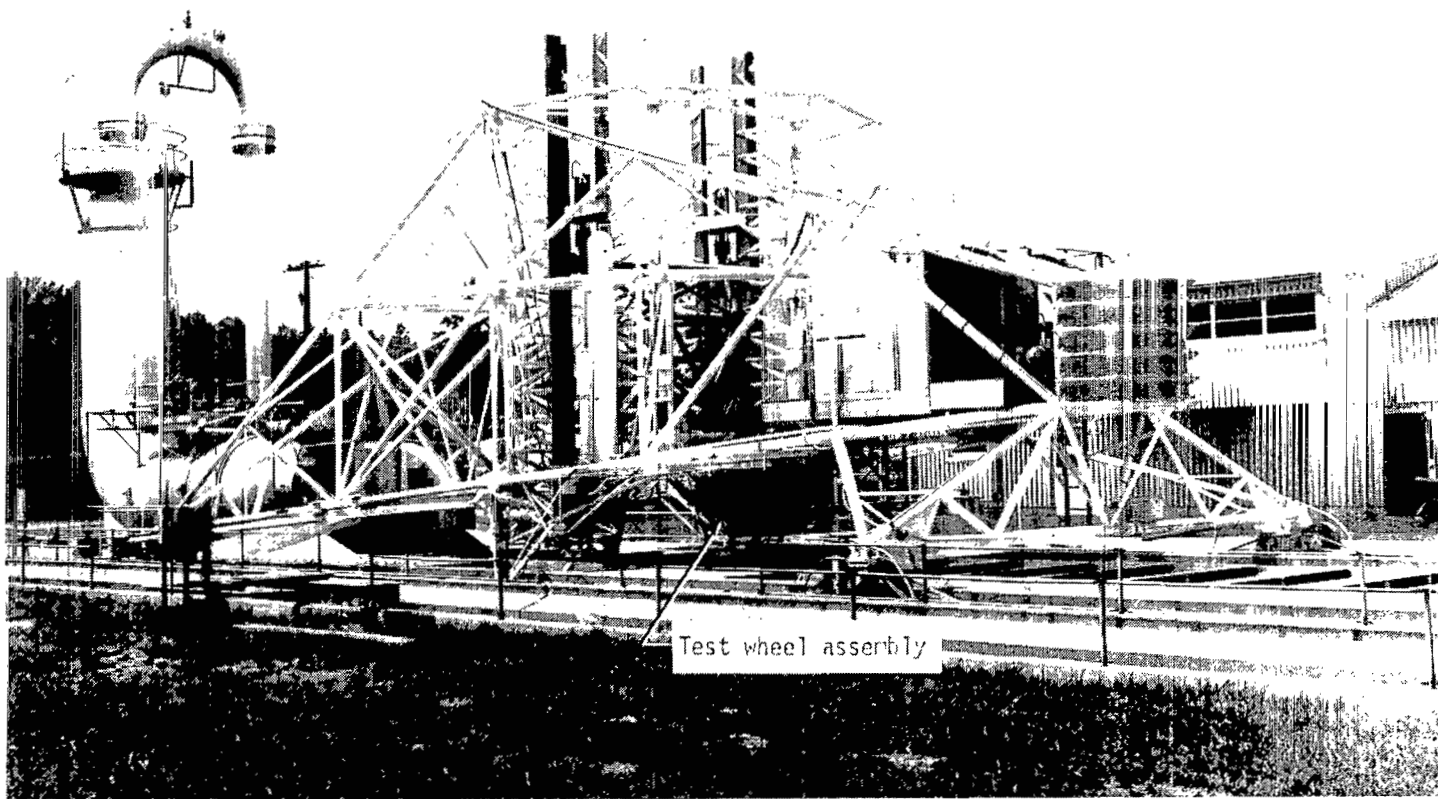
Concluded

$\bar{T}$		$\bar{T}_{max}$		Torque limit, percent	$\bar{\mu}_s$	$\bar{\mu}_{s,max}$	Average slip ratio	Average slip velocity		Gross stopping power		Tire stopping power		Tire cornering power		Hydroplaning	Run
kN-m	ft-lbf	kN-m	ft-lbf					m/sec	ft/sec	kW	hp	kW	hp	kW	hp		
16.9	12 483	18.3	13 517		0.24	0.41	0.18	7.06	23.17	1514	2030	357	479	69	93	No	52
16.1	11 892	16.4	12 114		.24	.39	.16	8.20	26.89	1775	2380	391	524	93	125	No	53
3.7	2 733	5.6	4 136		.18	.36	.12	4.41	14.48	385	516	90	121	41	55	No	54
6.4	4 727	7.7	5 688		.19	.28	.12	3.47	11.40	509	683	112	150	44	59	No	55
4.5	3 324	5.6	4 136		.14	.25	.11	4.17	13.69	510	684	107	143	45	60	No	56
2.7	1 994	5.4	3 989		.10	.29	.15	8.27	27.14	407	546	113	152	43	57	No	57
6.4	4 727	8.2	6 057		.12	.18	.18	5.04	16.55	520	698	124	166	25	33	No	58
1.4	1 034	3.5	2 585		.04	.06	.19	7.51	24.64	393	527	87	117	13	17	No	59
					0		.90	41.87	137.36	227	305	207	277	0	0	Yes	60
6.5	4 801	7.3	5 392		.28	.43	.16	4.38	14.36	492	660	177	238	89	120	No	61
4.5	3 324	6.7	4 949		.17	.37	.14	5.22	17.11	509	683	170	228	89	120	No	62
2.1	1 551	4.0	2 955		.12	.27	.09	4.88	16.02	396	531	130	174	81	109	No	63
4.5	3 324	5.1	3 767		.18	.34	.17	6.36	20.85	494	662	204	274	103	138	No	64
20.7	15 290	23.3	17 211	16			.11	2.73	8.95	1089	1460	118	158			No	65
23.0	16 989	25.0	18 466				.10	3.84	12.60	1737	2330	180	241			No	66
22.5	16 620	23.0	16 989				.07	3.84	12.59	2222	2980	176	236			No	67
5.3	3 915	6.8	5 023				.08	2.33	7.64	359	482	33	44			No	68
4.5	3 324	6.2	4 580				.08	2.19	7.19	319	428	27	36			No	69
4.2	3 102	5.9	4 358				.06	2.13	6.98	374	501	27	36			No	70
3.0	2 216	4.7	3 472				.05	2.78	9.11	450	604	28	38			No	71
2.2	1 625	3.1	2 290				.13	3.71	12.16	230	309	31	41			No	72
1.2	686	2.4	1 773				.10	3.72	12.20	220	295	23	31			No	73
							.97	47.02	154.27	204	274	199	267			Yes	74
18.1	13 370	18.9	13 961		.28	.46	.16	4.34	14.23	1081	1450	241	323	55	74	No	75
17.2	12 705	18.0	13 296		.24	.47	.17	6.68	21.90	1521	2040	344	461	71	95	No	76
17.3	12 779	17.8	13 148		.30	.45	.14	6.99	22.94	1939	2600	402	539	119	159	No	77
1.7	1 256	3.5	2 585		.08	.30	.10	4.04	13.25	192	258	42	56	20	27	No	78
3.8	2 807	4.6	3 398		.09	.22	.11	3.05	10.01	301	403	57	76	22	29	No	79
2.5	1 847	4.9	3 619		.10	.23	.11	3.20	10.51	252	338	51	69	22	30	No	80
1.8	1 330	4.9	3 619		.08	.26	.10	3.81	12.50	268	359	56	75	27	36	No	81
1.8	1 330	3.1	2 290		.10	.31	.08	4.37	14.35	349	468	78	105	44	59	No	82
1.5	1 108	3.9	2 881		.04	.08	.20	5.31	17.41	213	286	51	69	8	11	No	83
1.1	813	2.8	2 068		.04	.25	.28	10.86	35.64	215	288	69	92	4	5	No	84
					-0.01		.94	44.99	147.62	231	310	219	294	0	0	Yes	85
				100			.08	1.95	6.39	947	1270	78	105			No	86
				100			.07	2.53	8.31	1432	1920	99	133			No	87
				100			.04	2.25	7.39	1499	2010	70	94			No	88
8.0	5 909	13.5	9 972				.07	2.02	6.64	494	663	39	52			No	89
8.4	6 205	10.0	7 387				.05	2.11	6.93	740	992	46	62			No	90
5.6	4 136	7.9	5 835				.05	2.56	8.40	737	988	46	62			No	91
8.2	6 057	9.5	7 017				.09	2.42	7.95	573	769	53	71			No	92
2.2	1 625	3.8	2 807				.17	6.57	21.54	384	515	62	83			No	93
							.93	44.57	146.23	244	327	227	305			Yes	94
10.9	8 051	10.9	8 051	100			.03	1.11	3.65	917	1230	26	35			No	95
7.9	5 835	9.2	6 796				.06	1.58	5.17	661	887	37	50			No	96
7.0	5 171	10.1	7 460				.05	1.76	5.79	761	1020	38	51			No	97
6.8	5 023	8.5	6 279				.04	2.04	6.70	850	1140	36	48			No	98
2.0	1 477	4.4	3 250				.08	2.32	7.62	556	745	47	63			No	99
							.06	2.38	7.82	347	466	25	34			No	100
							.94	50.44	165.50	239	321	234	314			Yes	101



L-76-1704.1

Figure 1.- New and worn tread condition of six-groove, 40 x 14, type VII aircraft test tires.



Test wheel assembly

L-69-5860.2

Figure 2.- Test carriage.

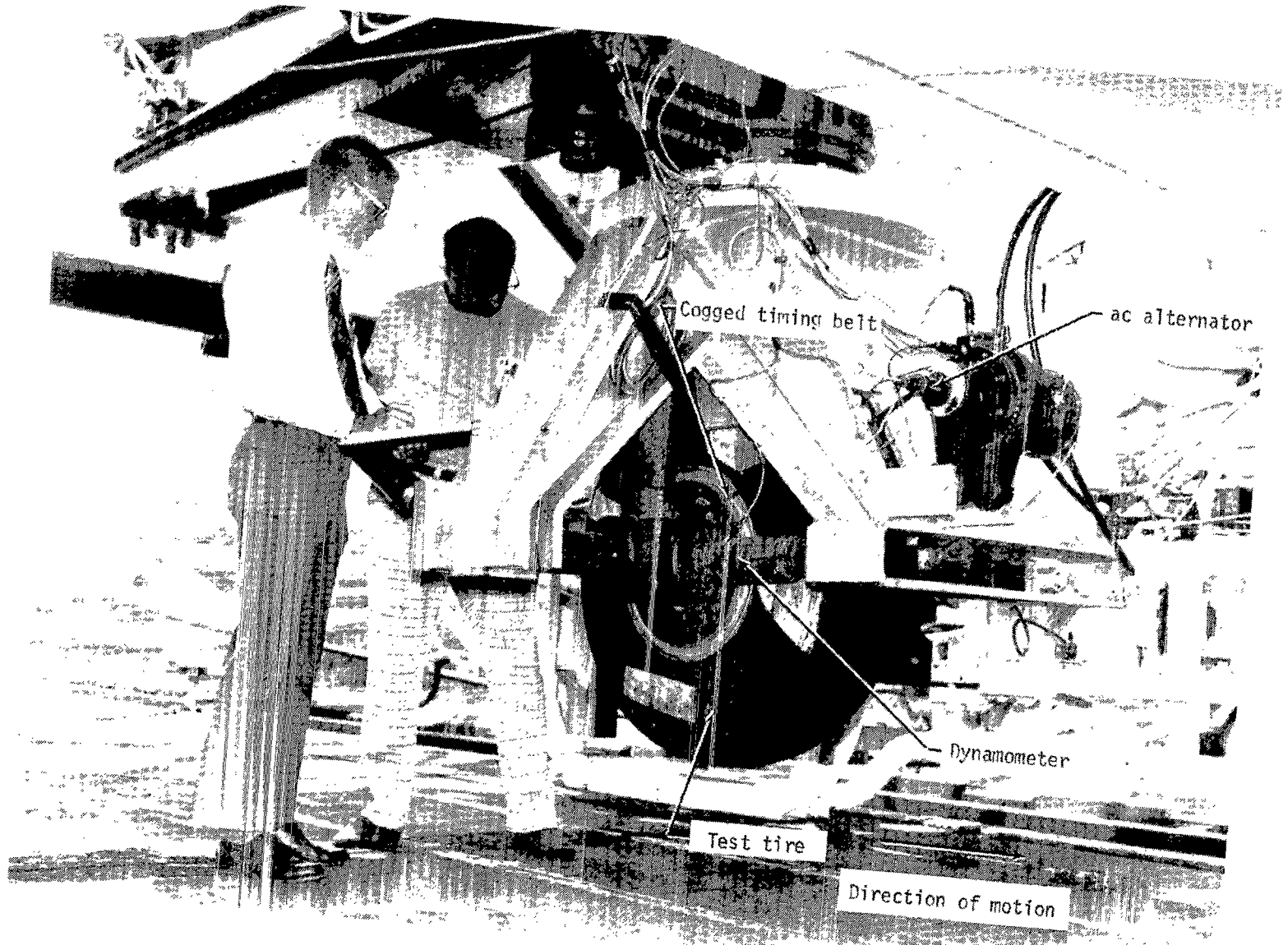
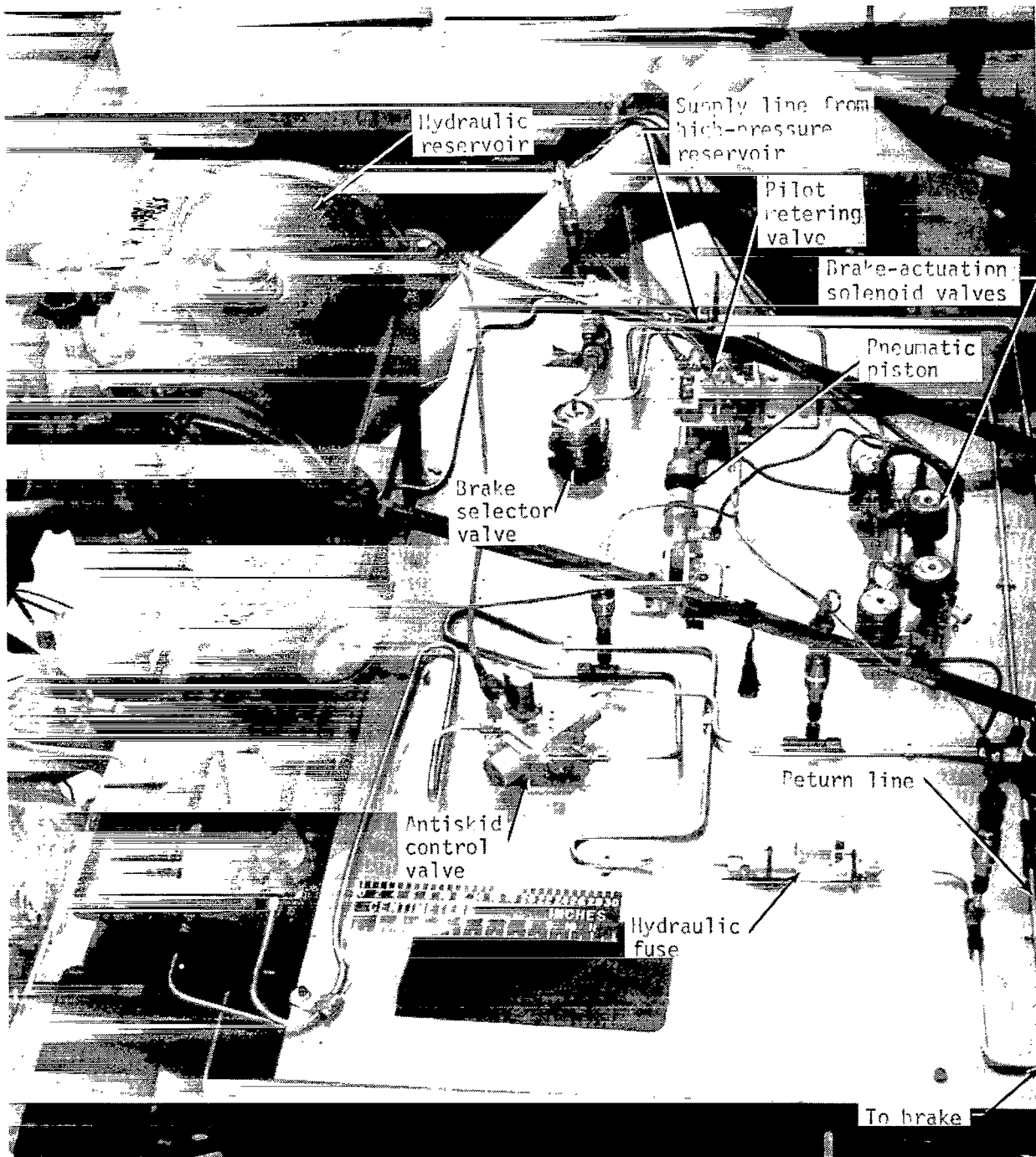


Figure 3.- Test tire and instrumented dynamometer.

L-75-3427.1



L-76-5905.1

Figure 4.- Layout of simulated braking system on test carriage.

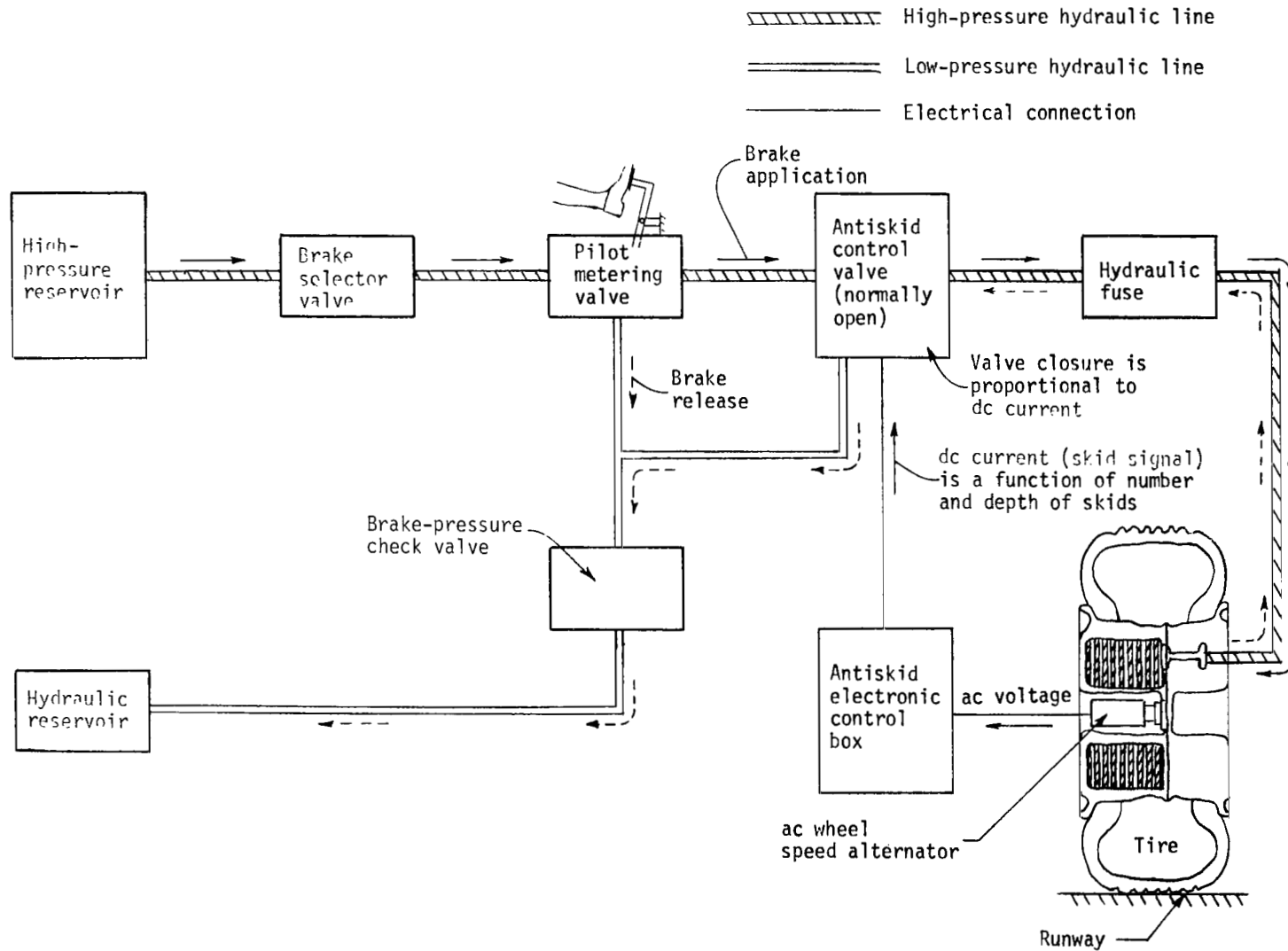


Figure 5.- Schematic of skid control system.

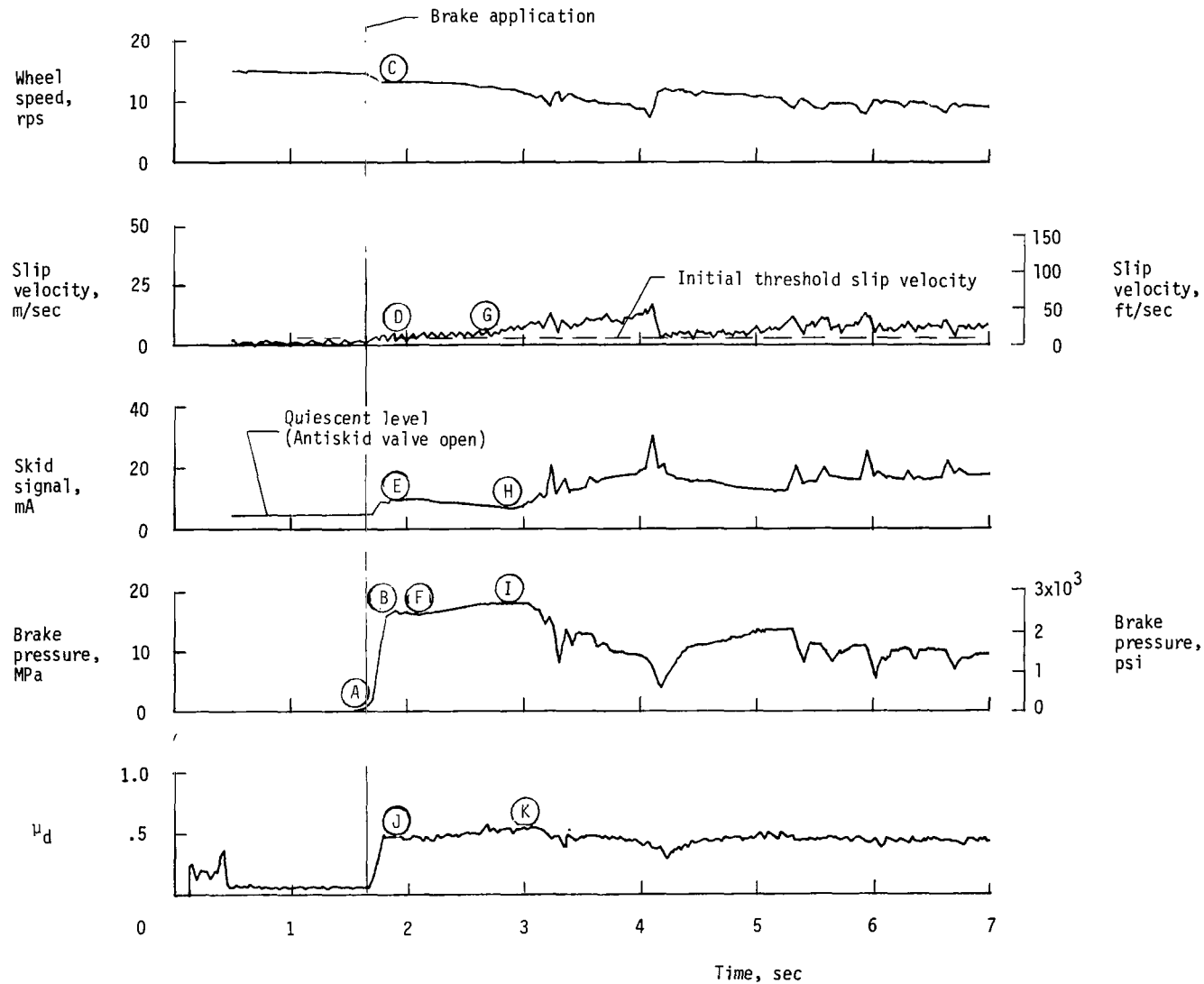


Figure 6.- Typical time histories of parameters to describe operation of antiskid system. Run 52. Nominal carriage speed, 75 knots; vertical load, 85 kN (19 100 lbf); yaw angle, 6°; brake supply pressure, 20 MPa (2900 psi); tire condition, new; surface condition, dry.

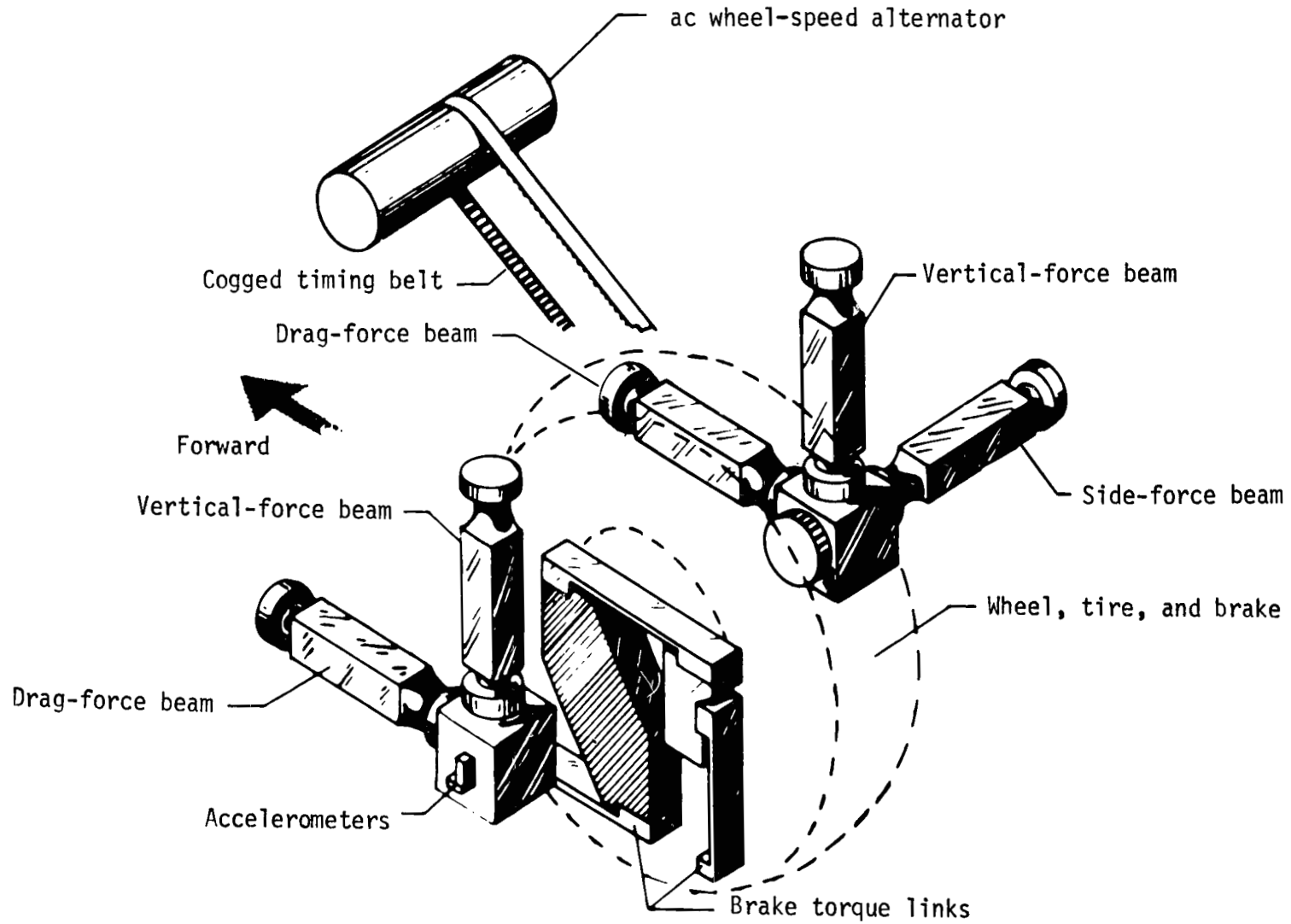
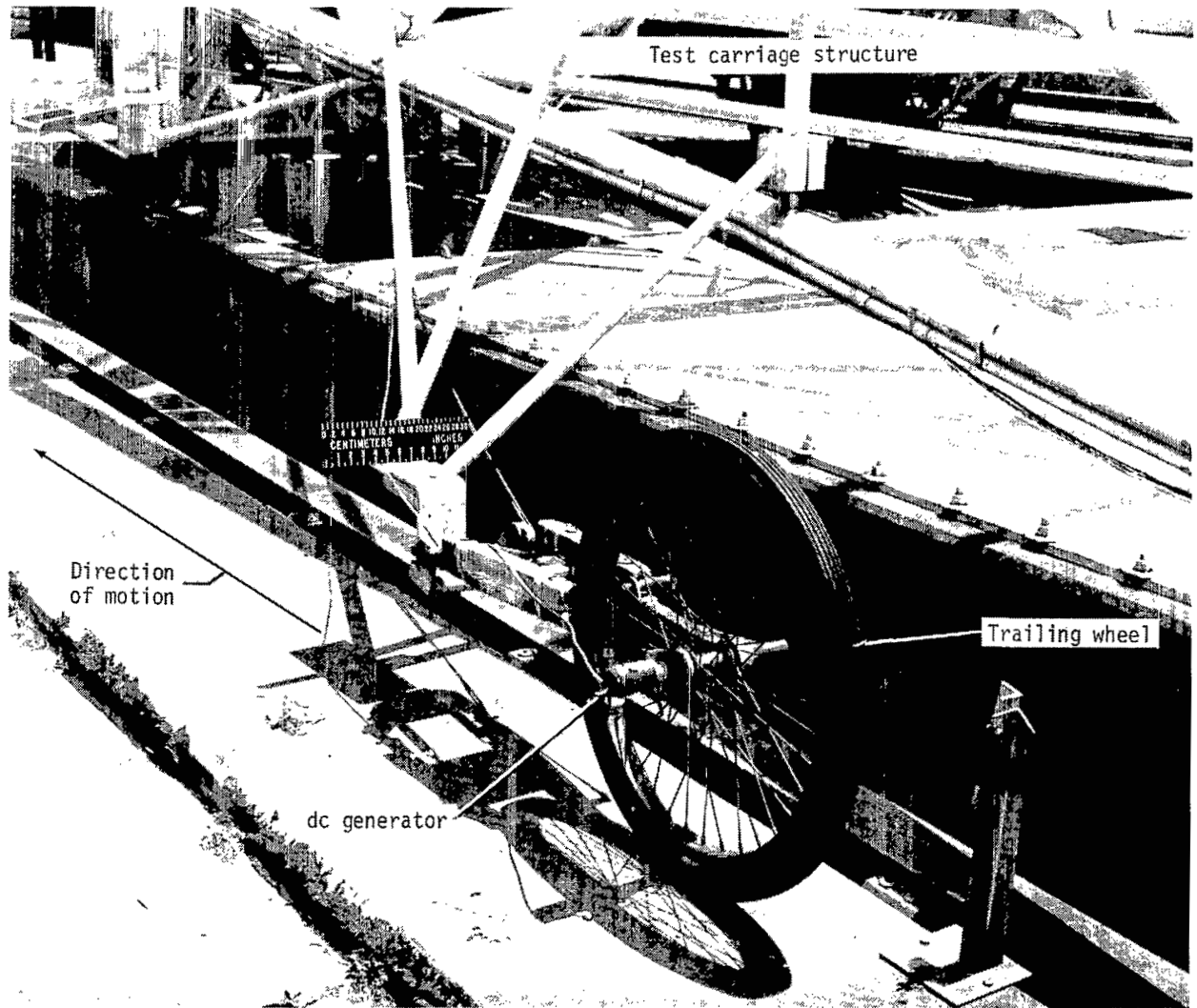
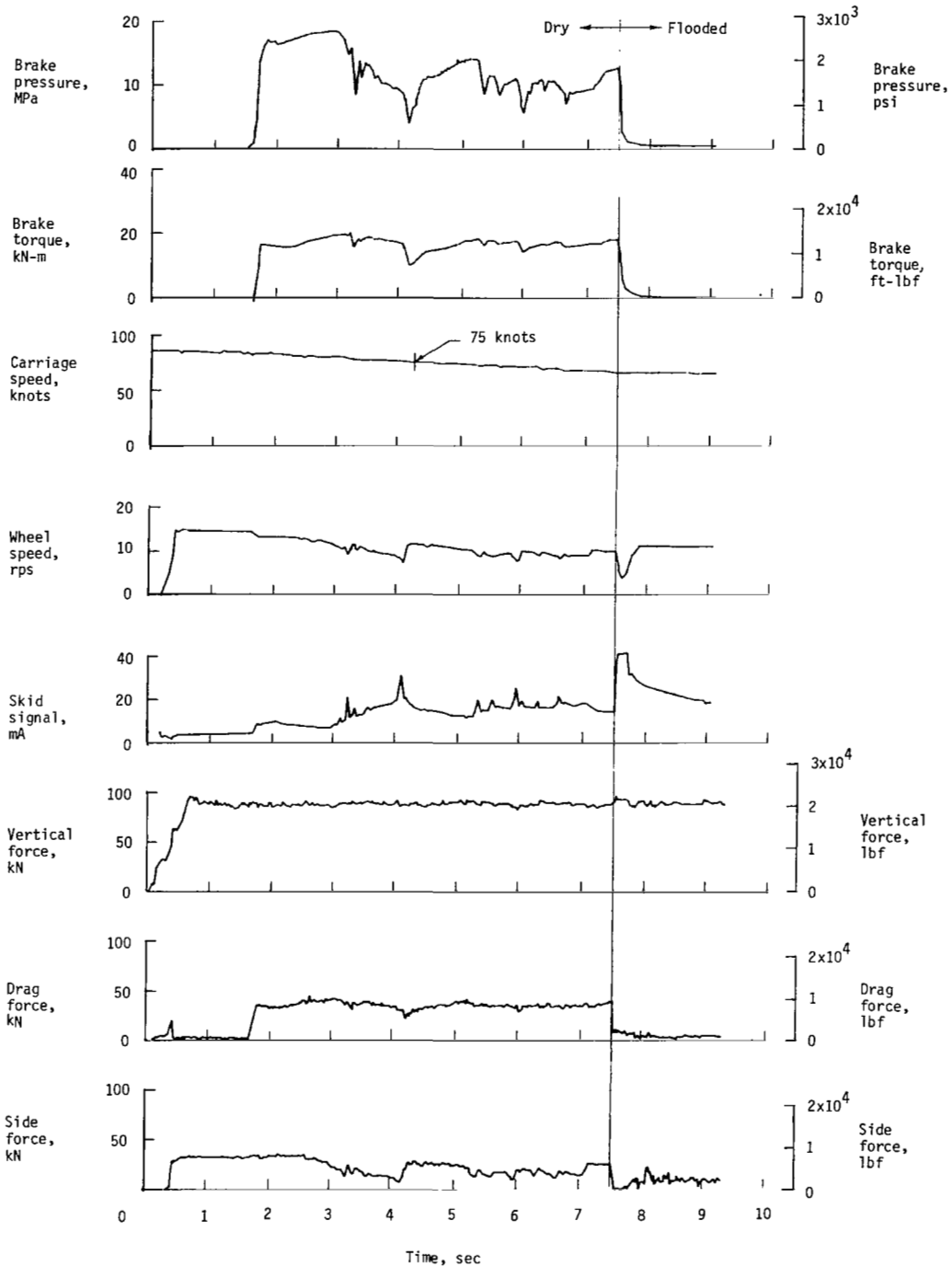


Figure 7.- Dynamometer details.



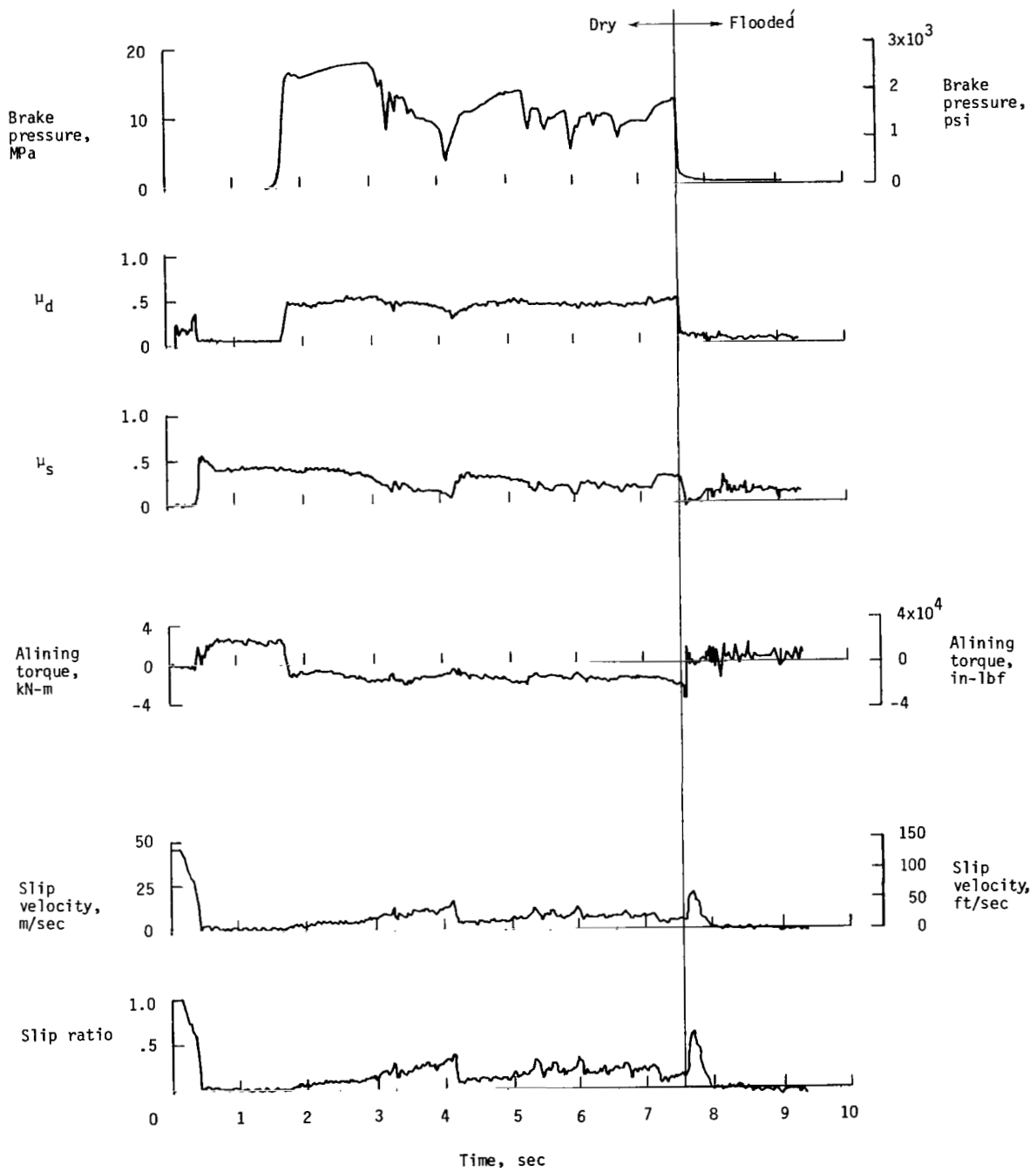
L-76-3786.1

Figure 8.- Lightweight trailing wheel used to obtain carriage speed.



(a) Measured parameters.

Figure 9.- Typical time-history plots of measured and calculated parameters. Run 52. Nominal carriage speed, 75 knots; vertical load, 85 kN (19 100 lbf); yaw angle,  $6^\circ$ ; brake supply pressure, 20 MPa (2900 psi); tire condition, new; surface condition, dry.



(b) Calculated parameters.

Figure 9.- Concluded.

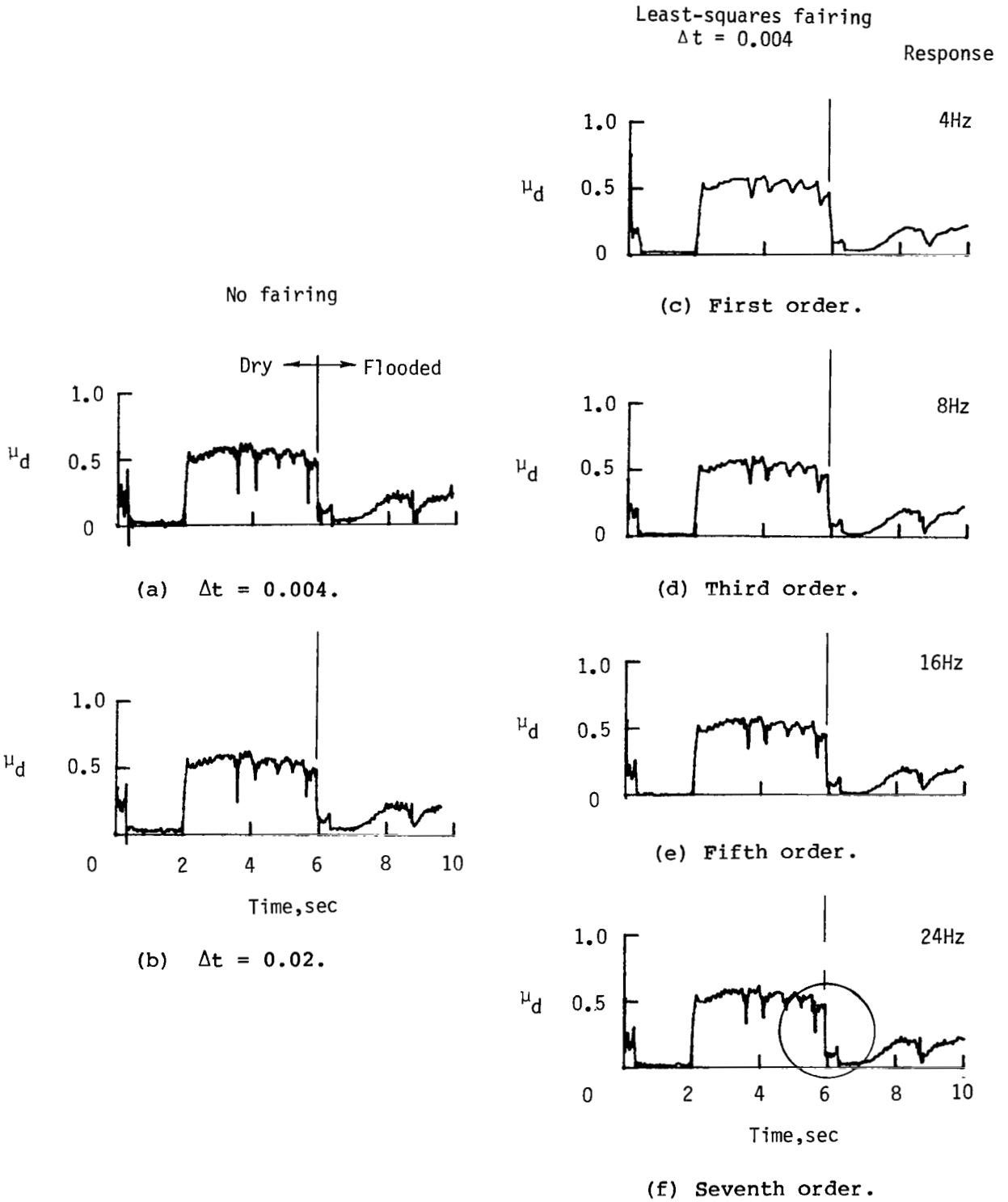


Figure 10.- Least-squares fairing of friction data from run 33.

Least-squares fairing  
 $\Delta t = 0.004$

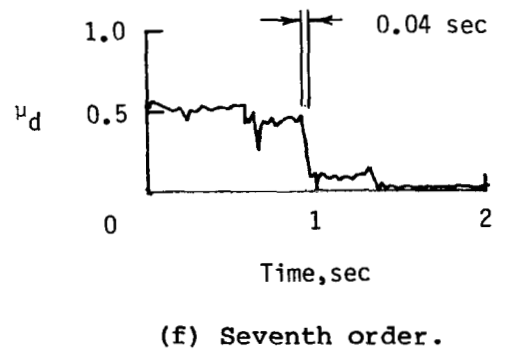
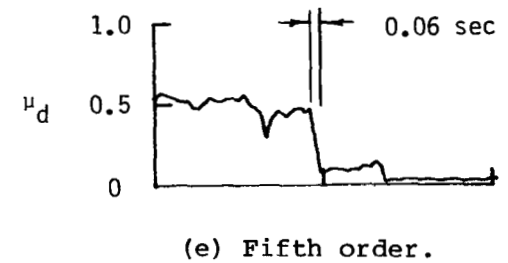
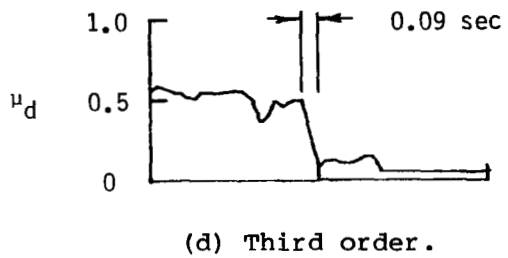
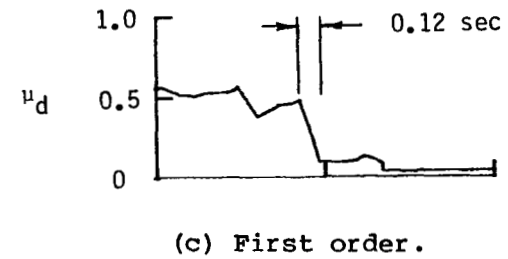
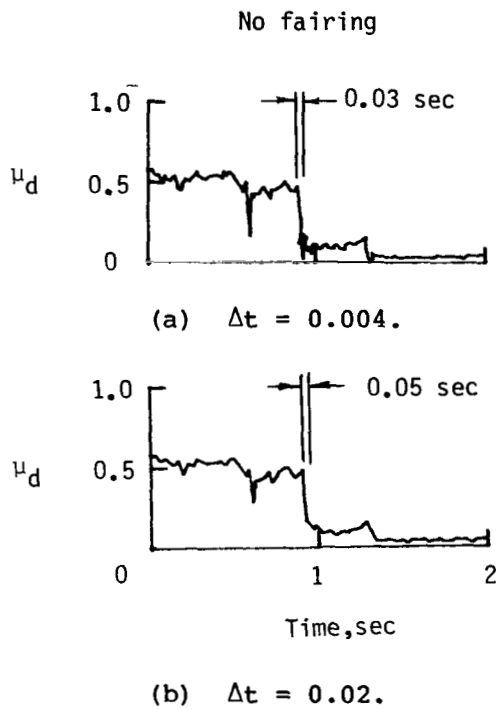
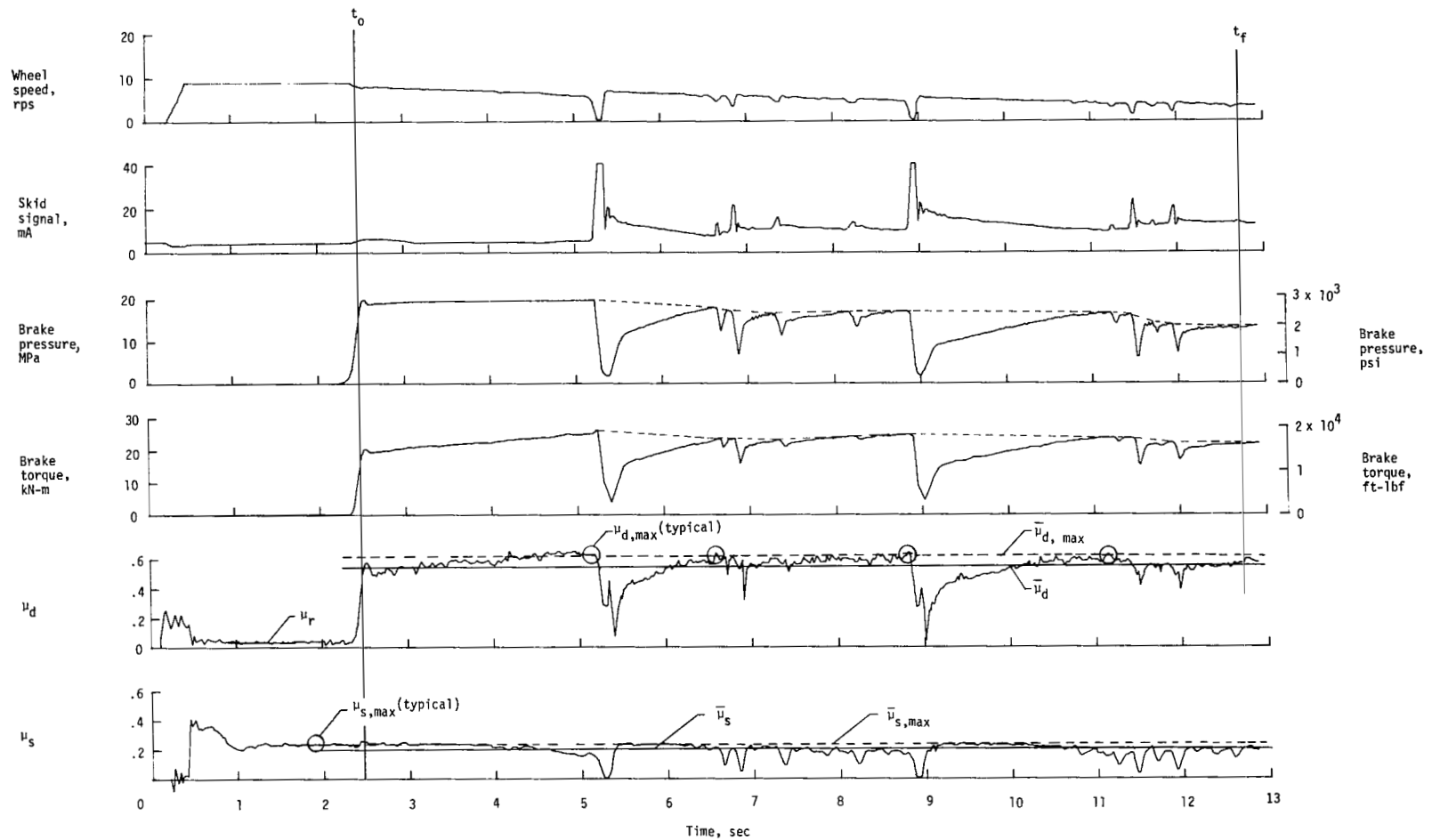
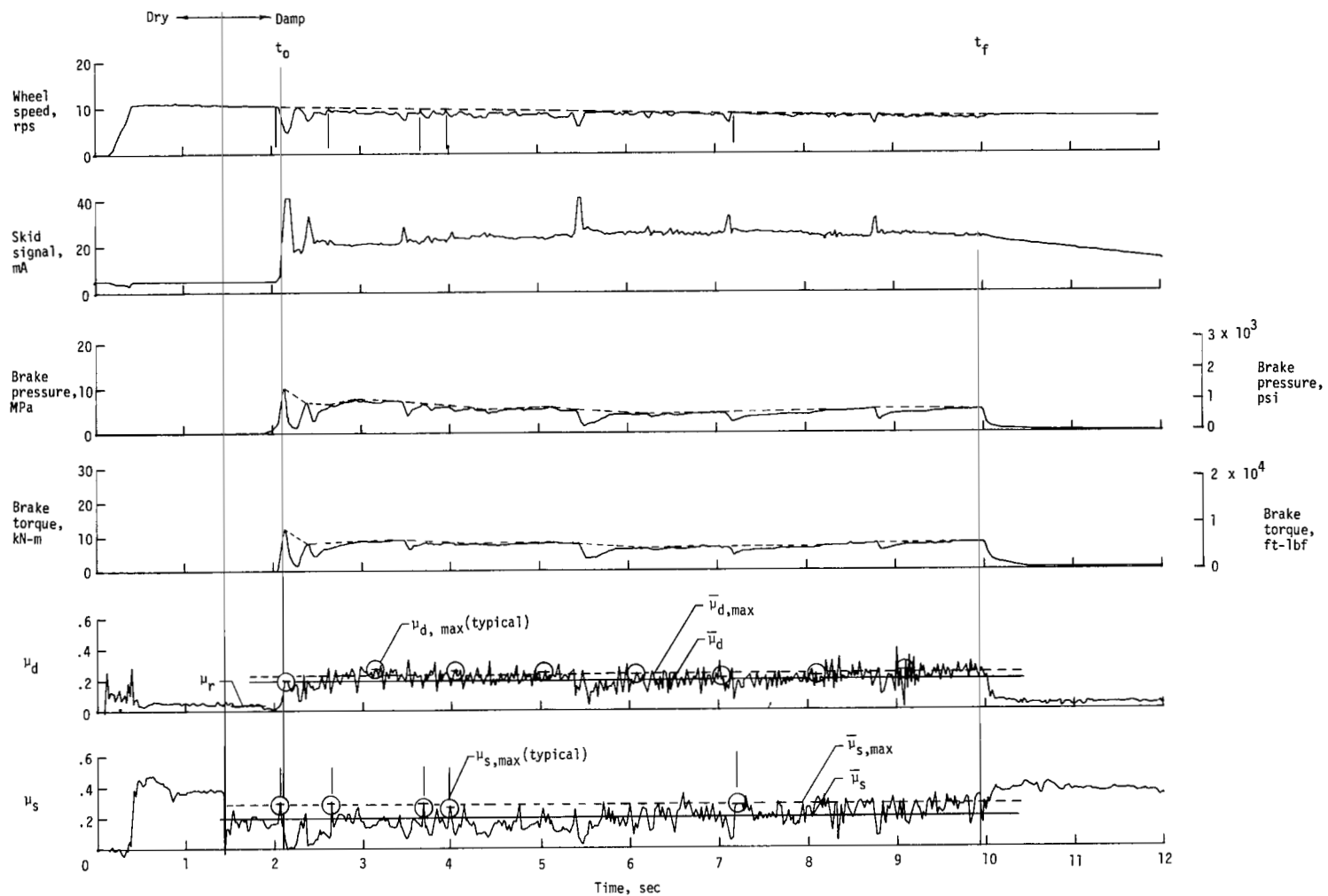


Figure 11.- Least-squares fairing of abrupt friction transition in run 33.



(a) Run 42. Nominal carriage speed, 40 knots; vertical load, 85 kN (19 000 lbf); yaw angle,  $30^\circ$ ; brake supply pressure, 21 MPa (3000 psi); tire condition, new; surface condition, dry.

Figure 12.- Definition of various friction terms.



(b) Run 55. Nominal carriage speed, 57 knots; vertical load, 85 kN (19 300 lbf); yaw angle,  $6^\circ$ ; brake supply pressure, 21 MPa (3000 psi); tire condition, new; surface condition, damp.

Figure 12.- Concluded.

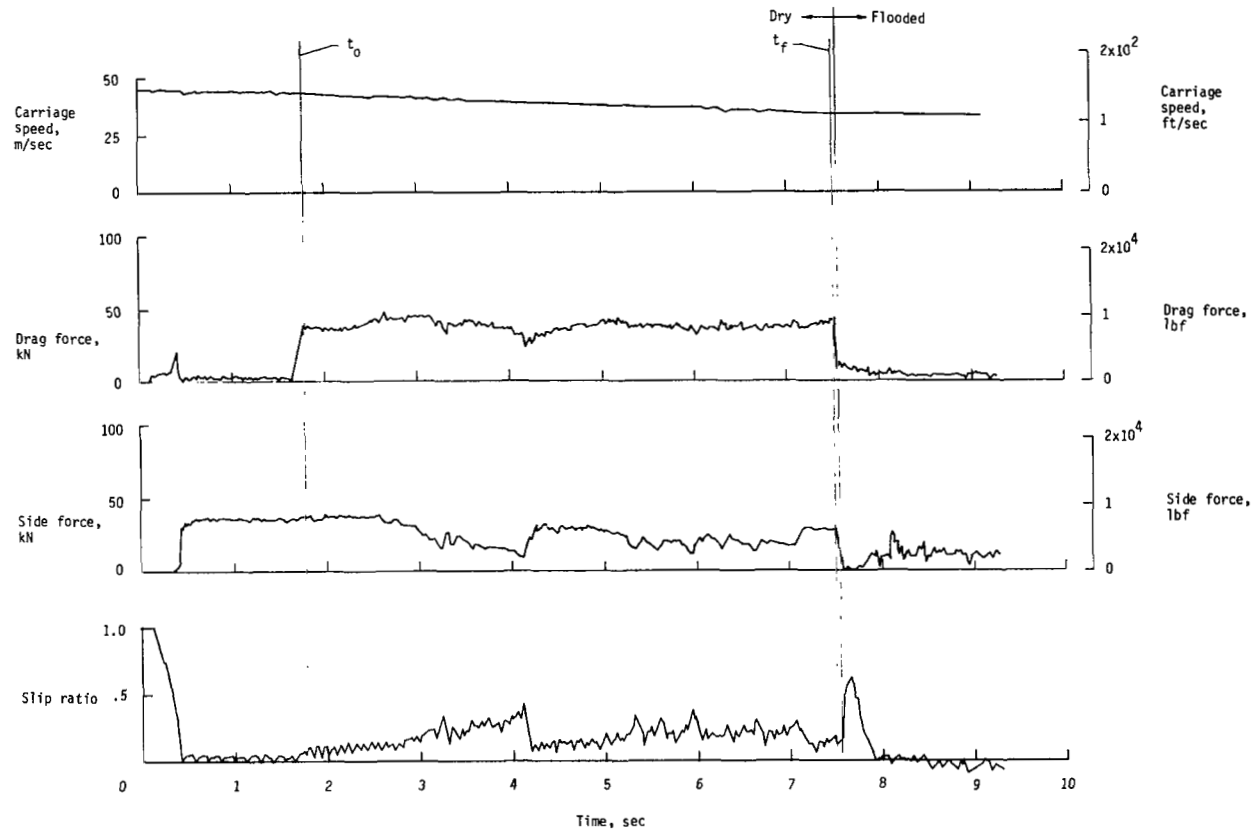
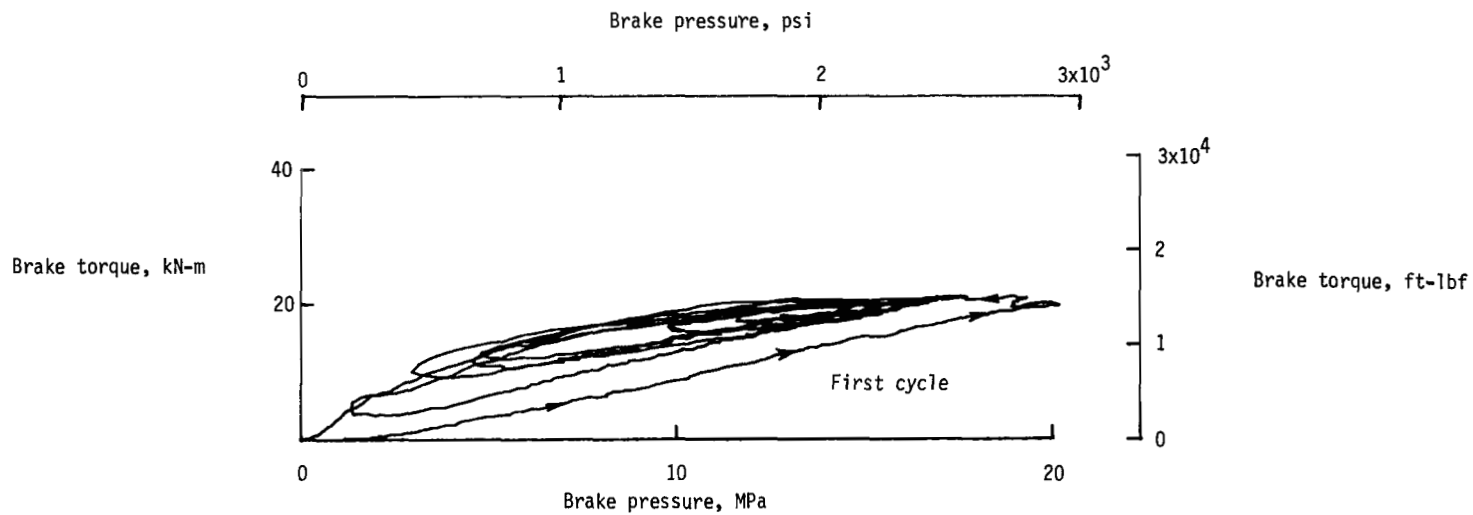
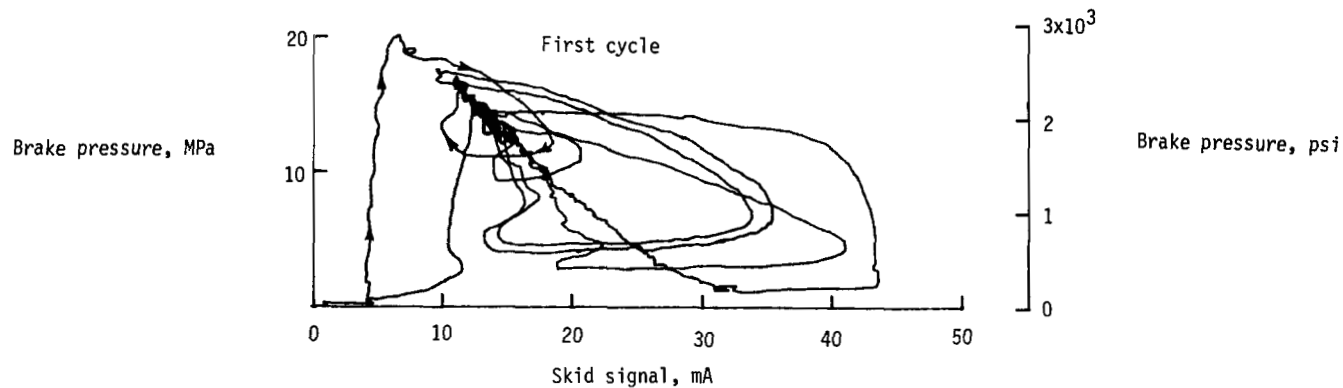


Figure 13.- Typical time histories of variables used to obtain power terms. Run 52. Nominal carriage speed, 75 knots; vertical load, 85 kN (19 100 lbf); yaw angle,  $6^\circ$ ; brake supply pressure, 20 MPa (2900 psi); tire condition, new; surface condition, dry.



(a) Torque-pressure relationship.



(b) Pressure-skid-signal relationship.

Figure 14.- Brake pressure, brake torque, and skid signal relationship. Run 1. Nominal carriage speed, 54 knots; vertical load, 60 kN (13 400 lbf); yaw angle,  $0^\circ$ ; brake supply pressure, 21 MPa (3000 psi); tire condition, new; surface condition, dry, with one damp spot.

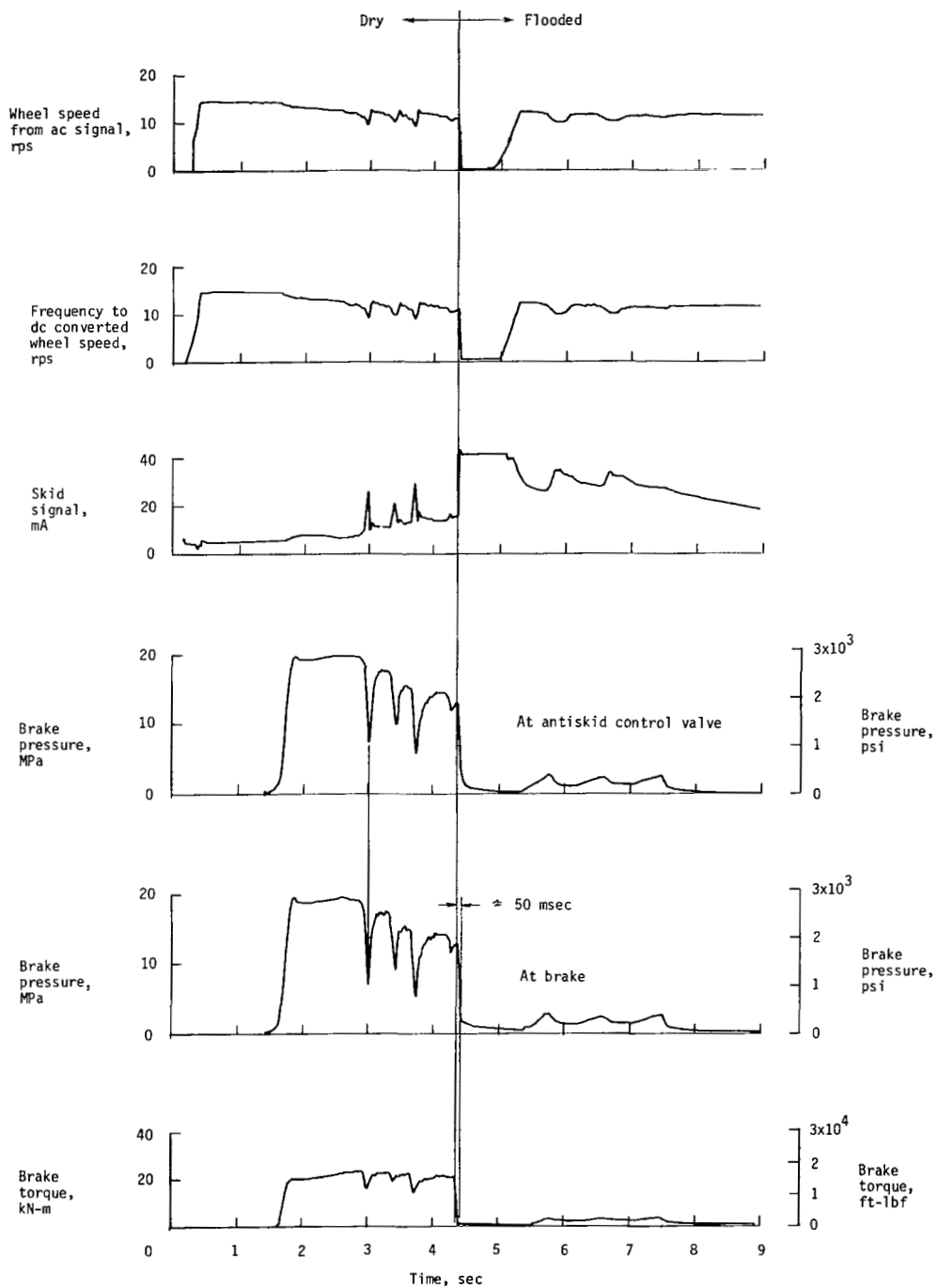
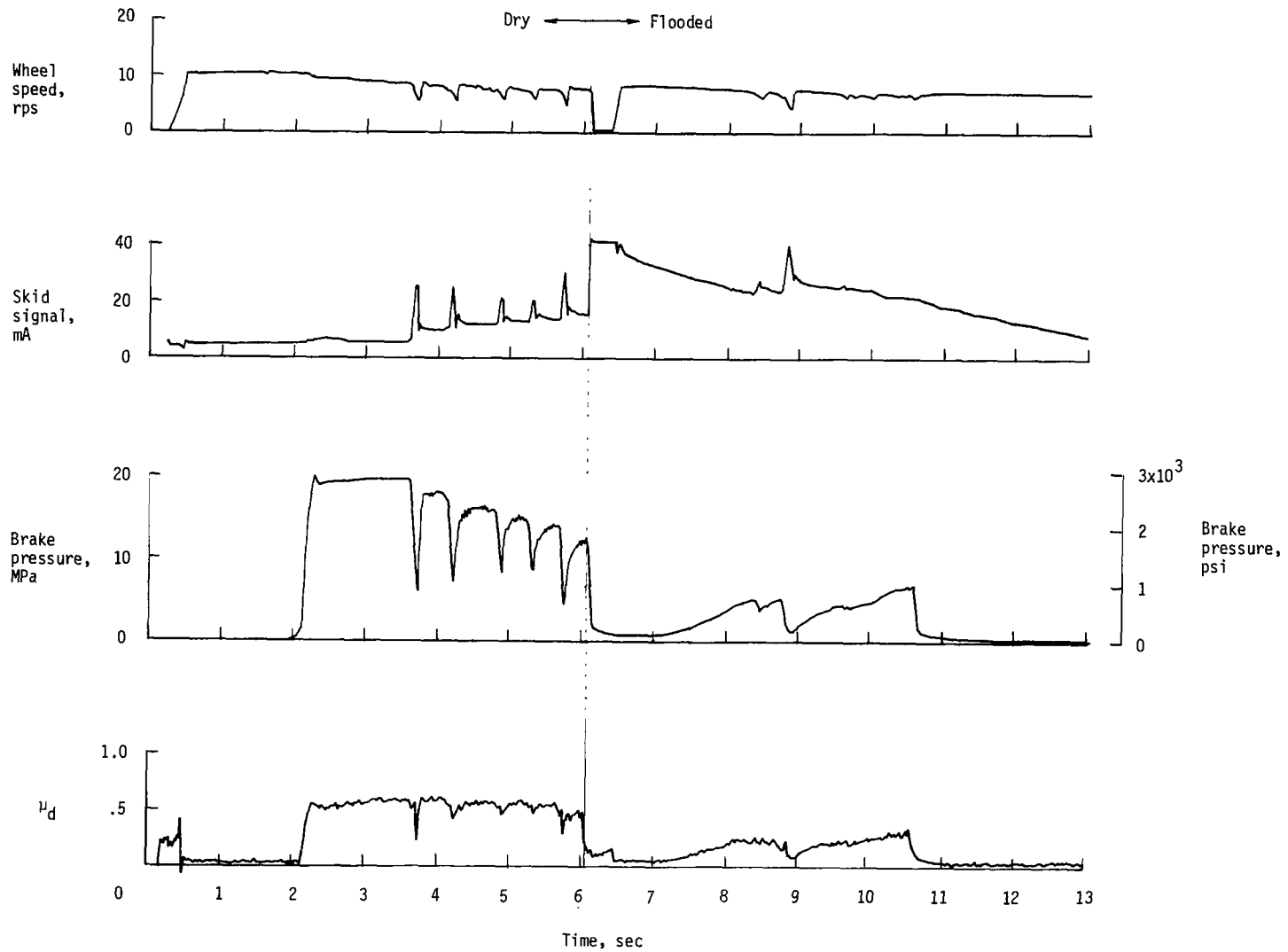
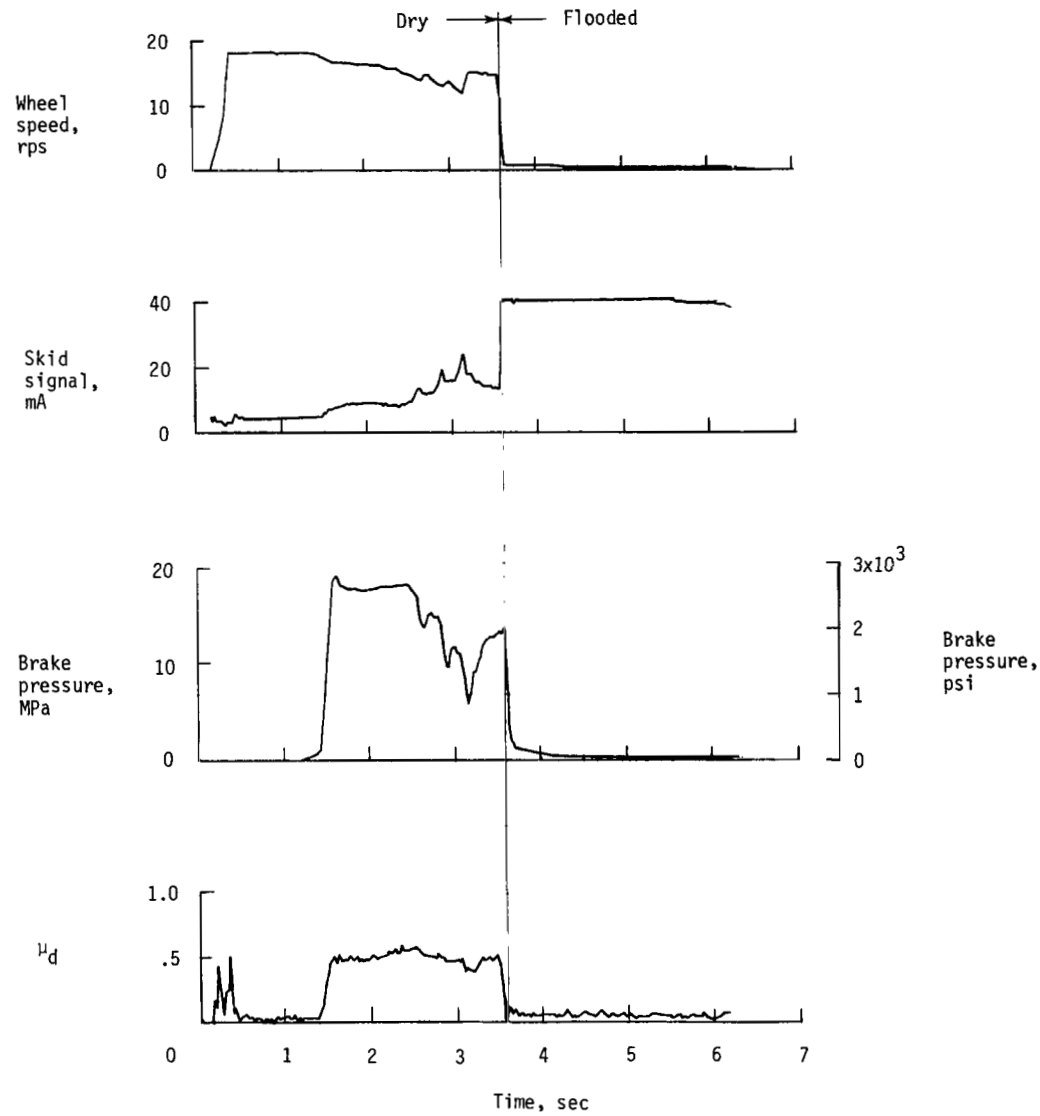


Figure 15.- Typical brake system electronic and hydraulic response. Run 34. Nominal carriage speed, 76 knots; vertical load, 84 kN (18 800 lbf); yaw angle, 0°; brake supply pressure, 21 MPa (3000 psi); tire condition, new; surface condition, dry to flooded.

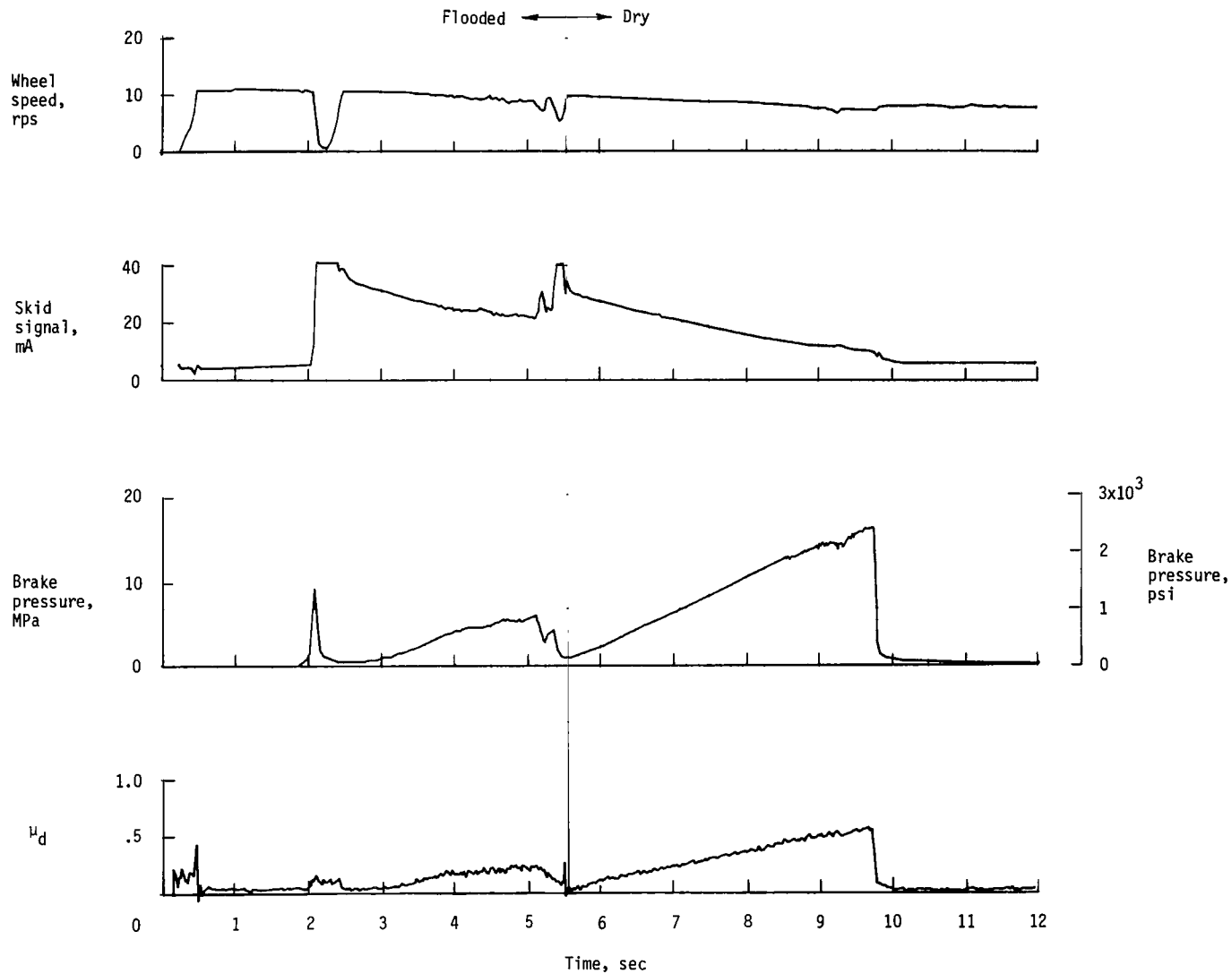


(a) Run 33. Nominal carriage speed, 54 knots; vertical load, 84 kN (18 800 lbf); yaw angle,  $0^\circ$ ; brake supply pressure, 21 MPa (3000 psi); tire condition, new; surface condition, dry to flooded.

Figure 16.- Antiskid-system response to transient runway conditions.

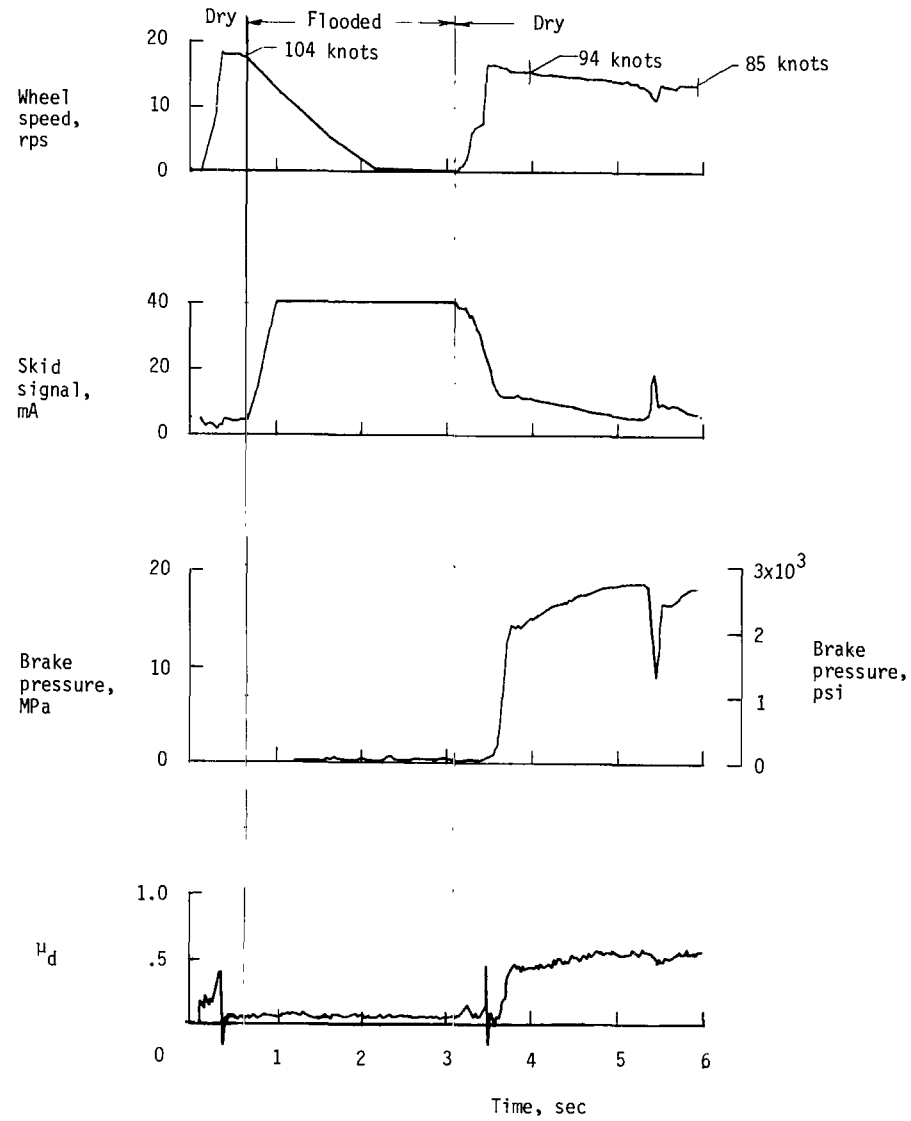


(b) Run 35. Nominal carriage speed, 94 knots; vertical load, 83 kN (18 700 lbf); yaw angle,  $0^\circ$ ; brake supply pressure, 21 MPa (3000 psi); tire condition, new; surface condition, dry to flooded.



(c) Run 36. Nominal carriage speed, 56 knots; vertical load, 84 kN (18 800 lbf); yaw angle,  $0^\circ$ ; brake supply pressure, 21 MPa (3000 psi); tire condition, new; surface condition, flooded to dry.

Figure 16.- Continued.



(d) Run 38. Nominal carriage speed, 94 knots; vertical load, 83 kN (18 700 lbf); yaw angle,  $0^\circ$ ; brake supply pressure, 20 MPa (2900 psi); tire condition, new; surface condition, flooded to dry.

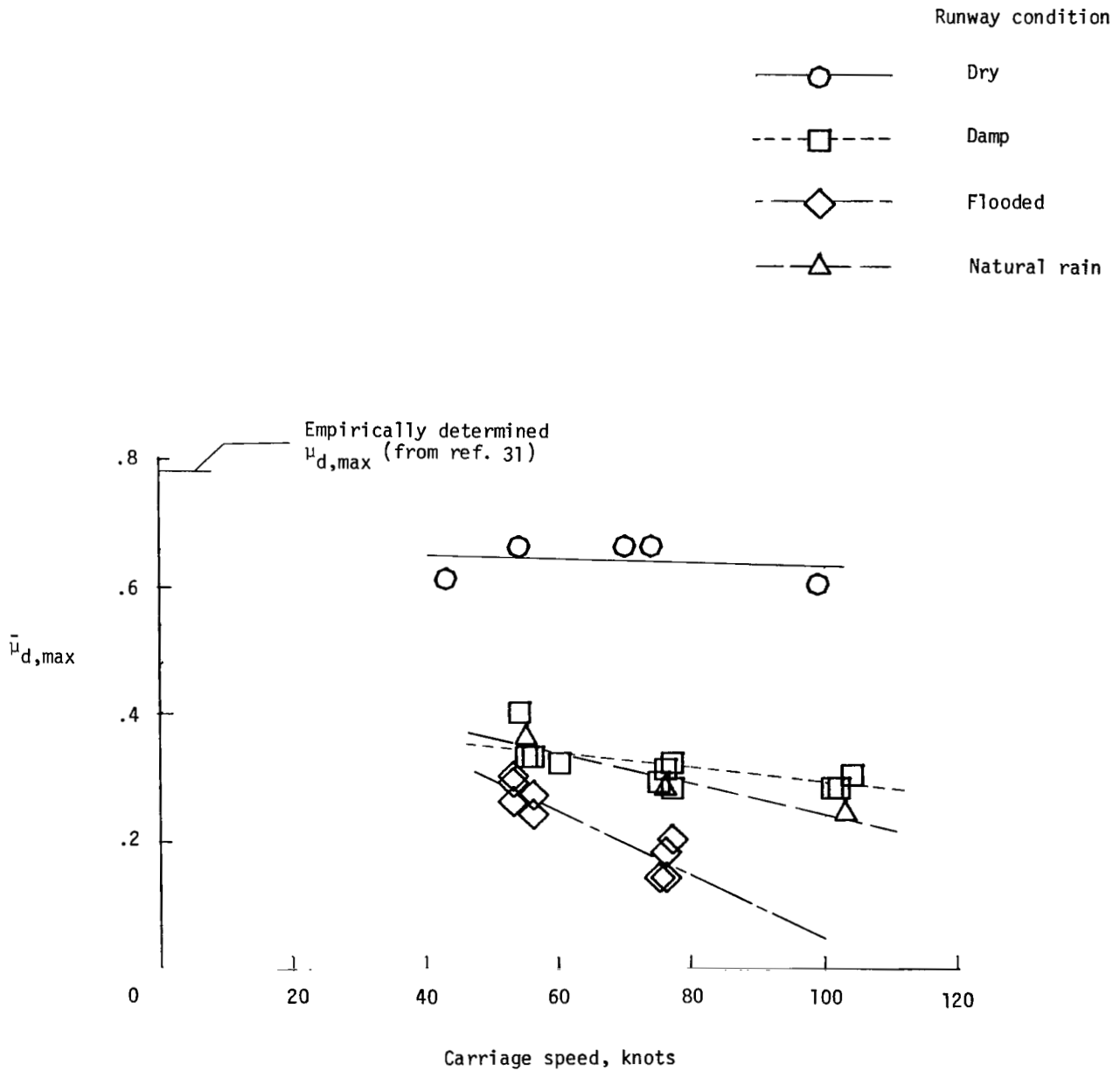


Figure 17.- Effect of carriage speed on maximum achieved drag-force friction coefficient. Vertical load, 80 kN (18 000 lbf); yaw angle, 0°; brake supply pressure, 21 MPa (3000 psi); tire condition, new.

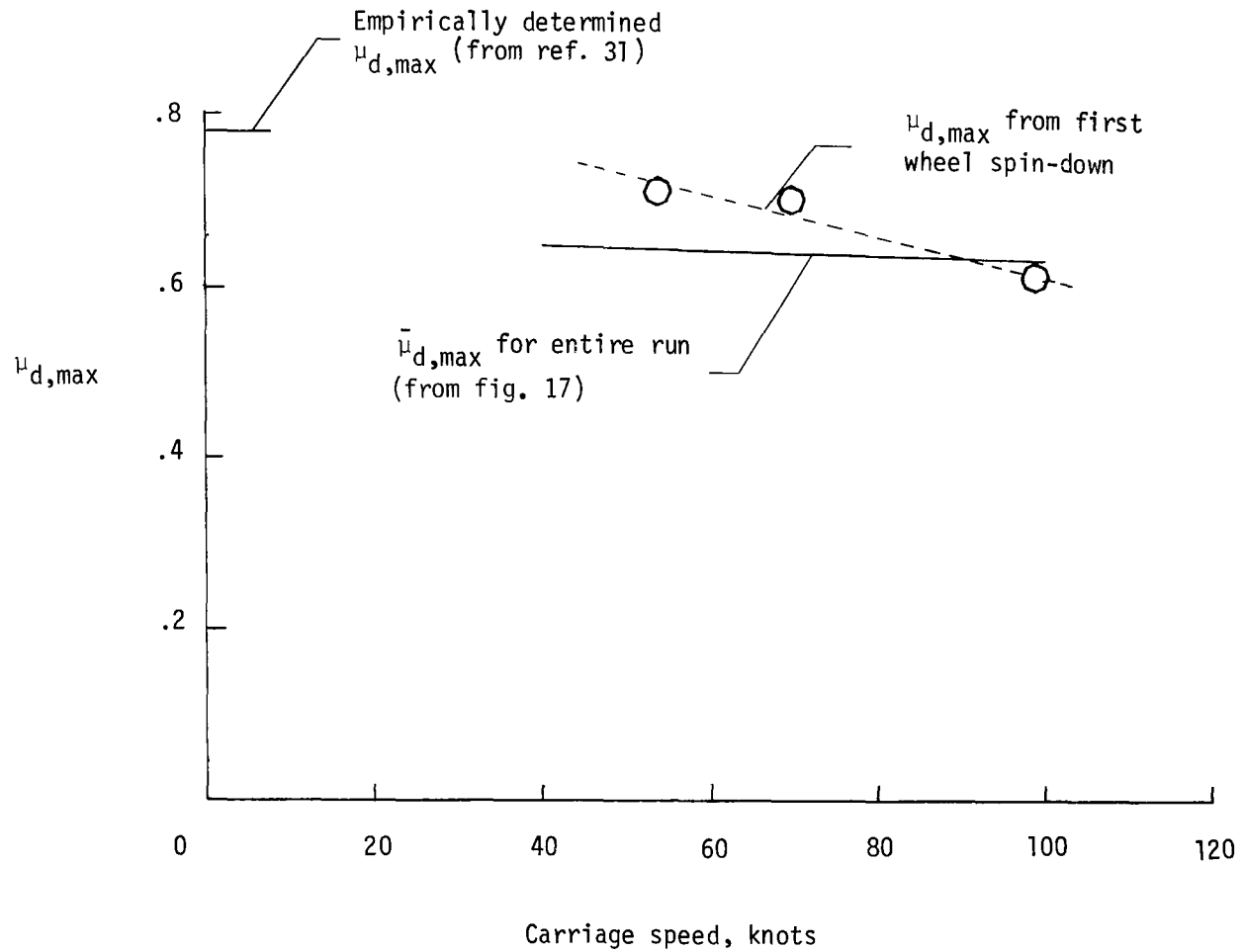


Figure 18.- Dry surface friction coefficients for first wheel spin-down following initial brake application compared with  $\bar{\mu}_{d,max}$  obtained during an entire run.

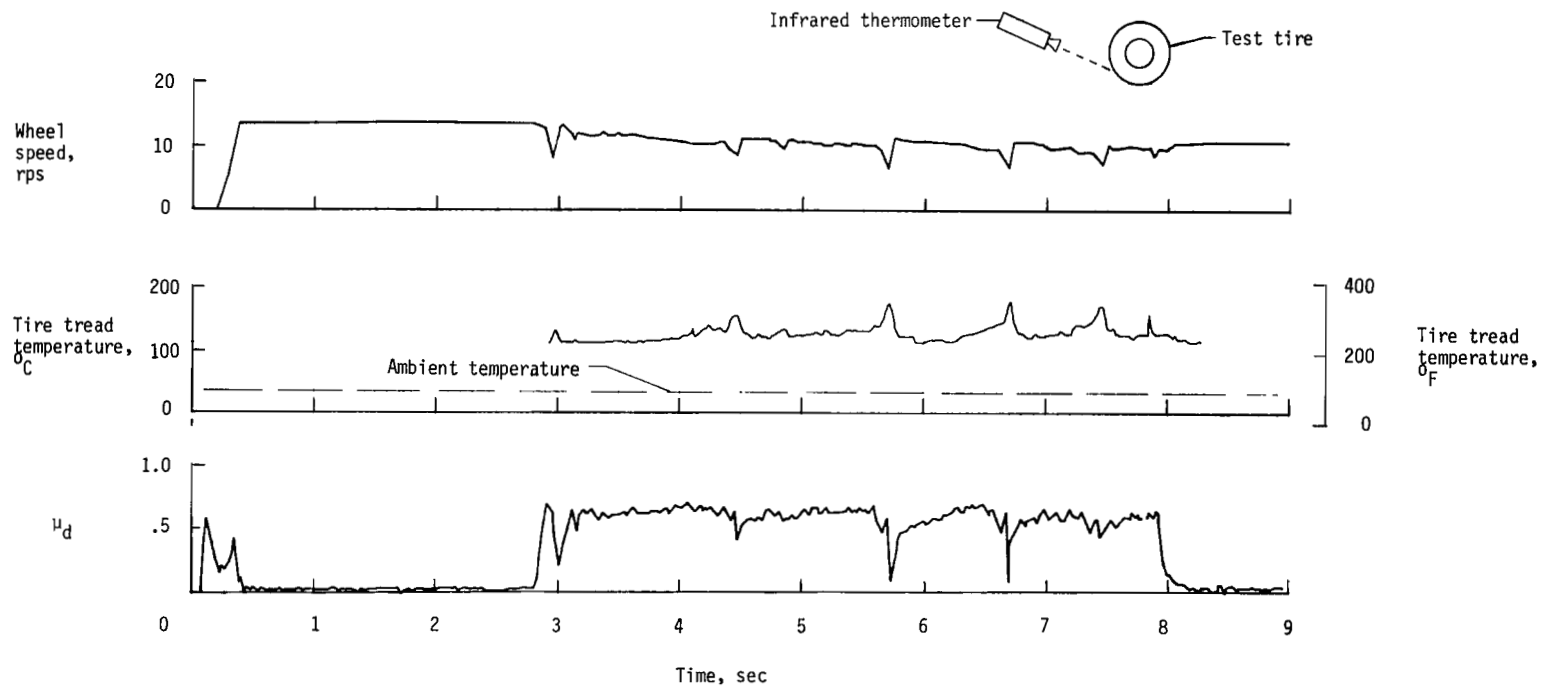


Figure 19.- Time history of tire surface temperature as a function of antiskid cycling. Run 3. Nominal carriage speed, 70 knots; vertical load, 65 kN (14 600 lbf); yaw angle, 0°; brake supply pressure, 21 MPa (3000 psi); tire condition, new; surface condition, dry.

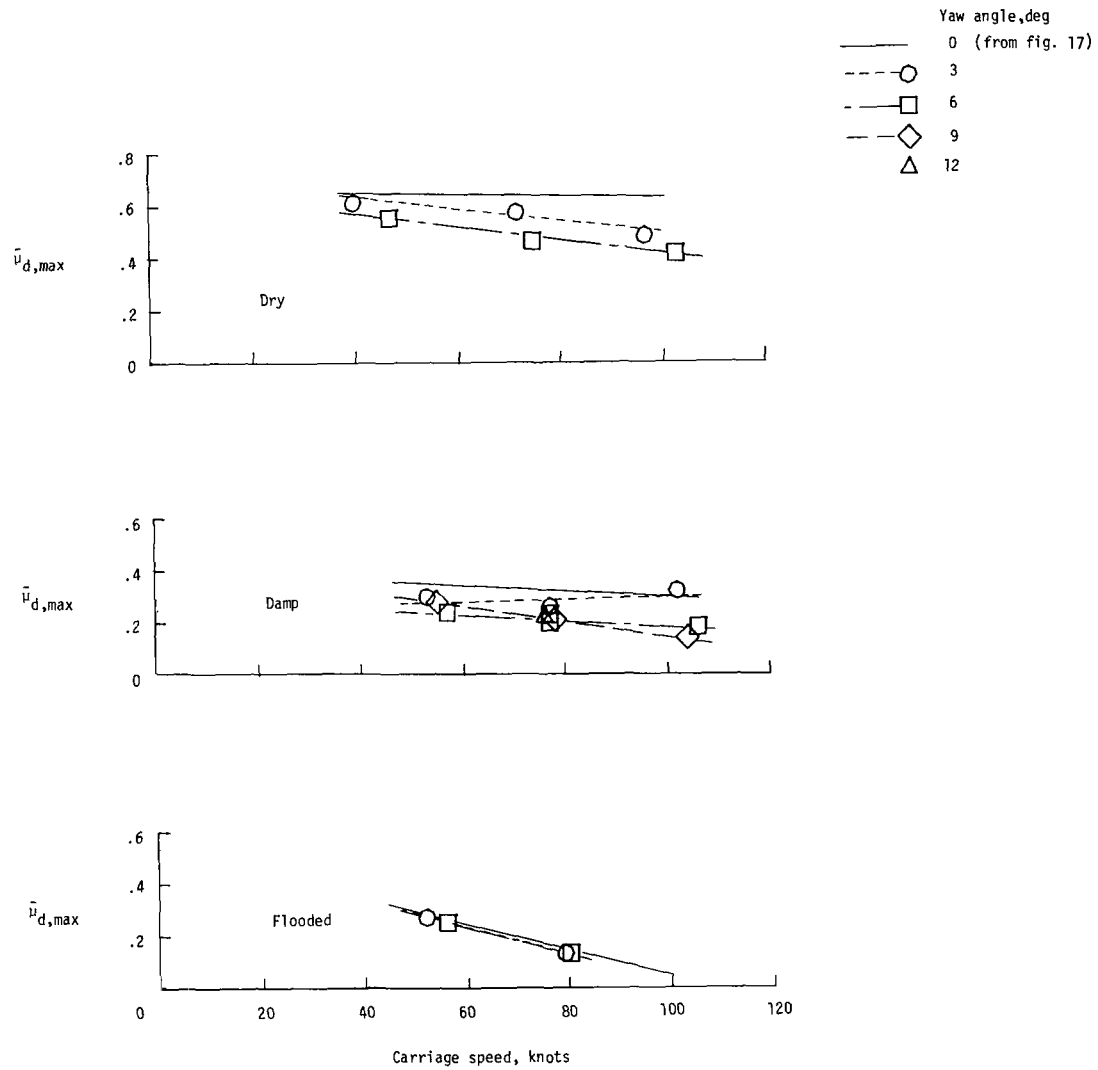


Figure 20.- Effect of yaw angle on maximum drag-force friction coefficient. Vertical load, 80 kN (18 000 lbf); brake supply pressure, 21 MPa (3000 psi); tire condition, new.

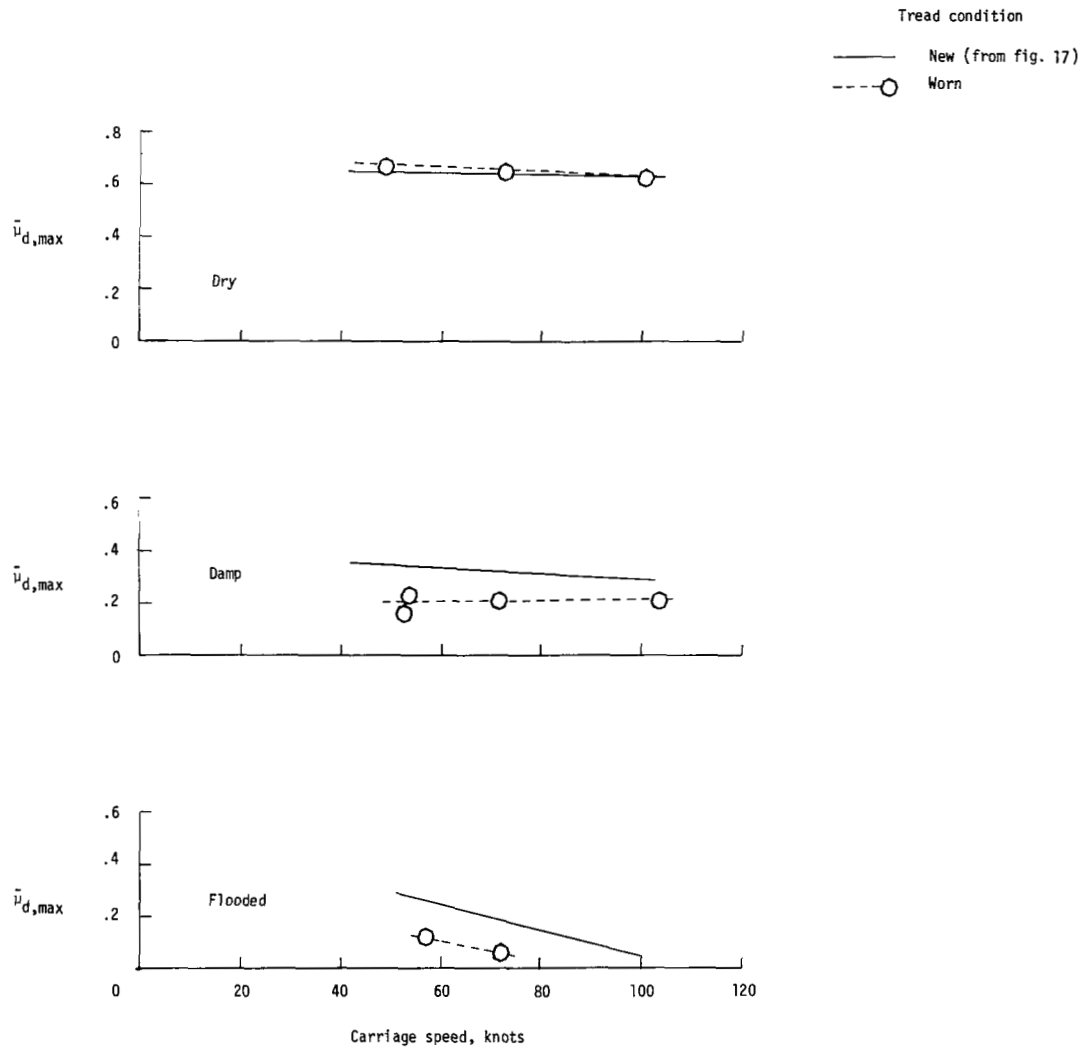


Figure 21.- Effect of tread wear on maximum drag-force friction coefficient. Vertical load, 80 kN (18 000 lbf); yaw angle, 0°; brake supply pressure, 21 MPa (3000 psi).

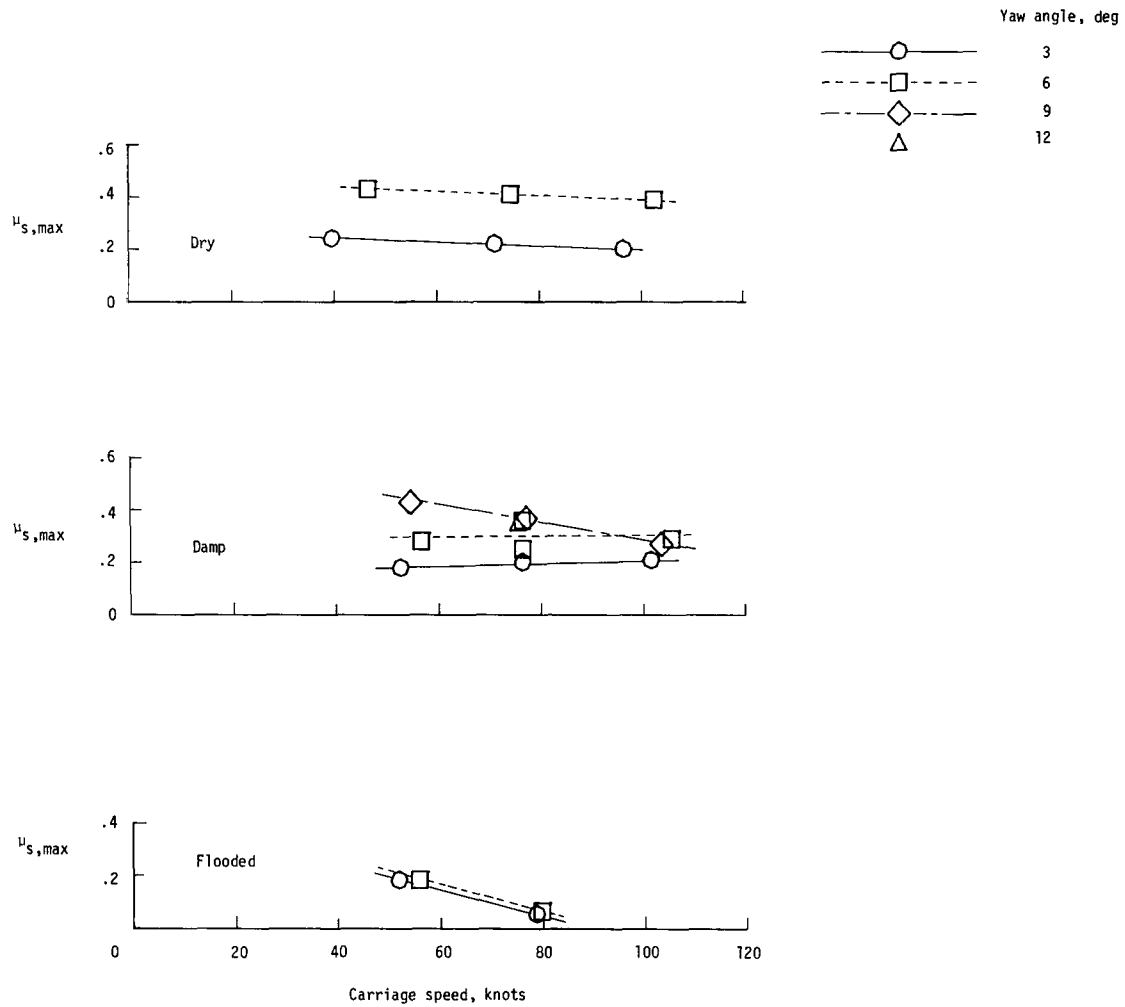


Figure 22.- Effect of carriage speed on maximum achieved side-force friction coefficient. Vertical load, 80 kN (18 000 lbf); free rolling (unbraked); tire condition, new.

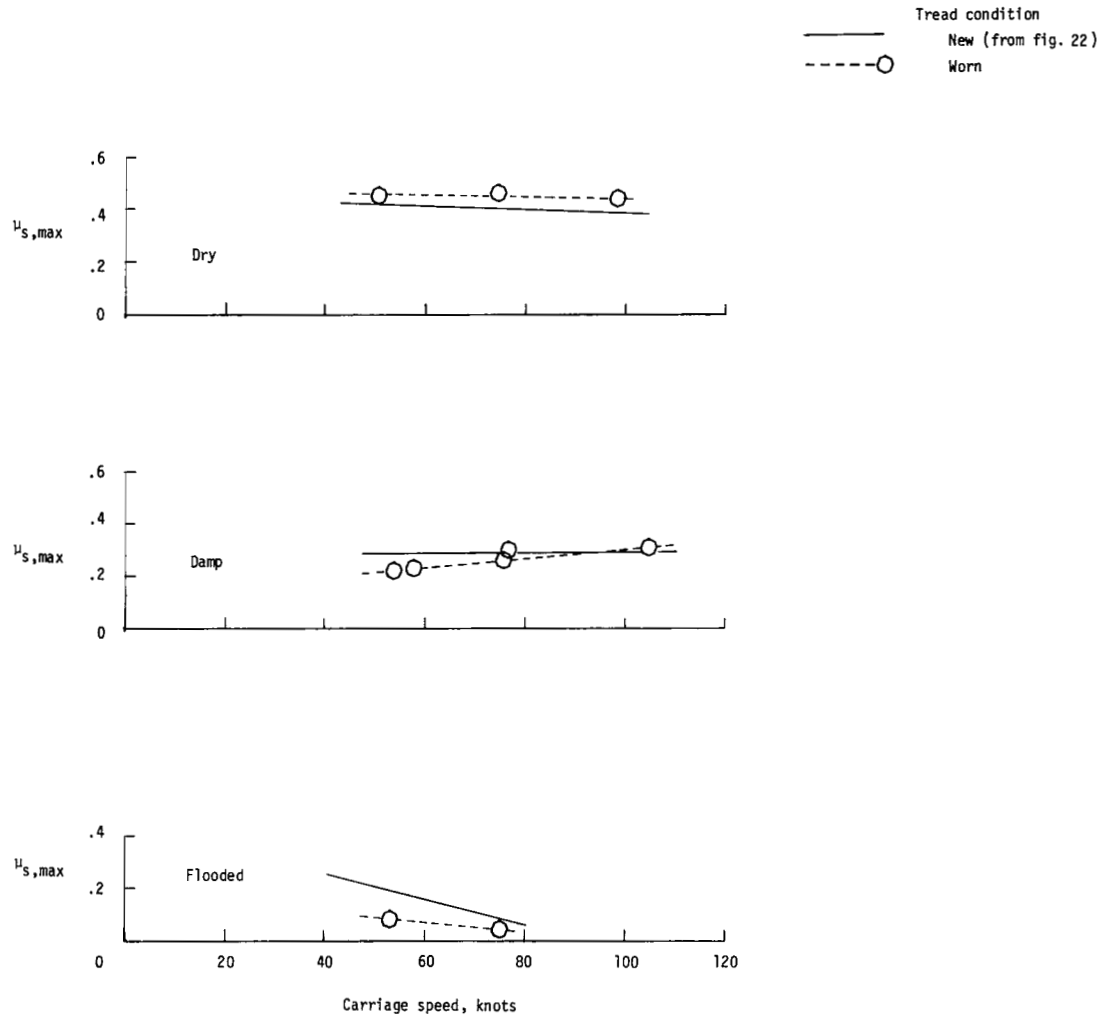
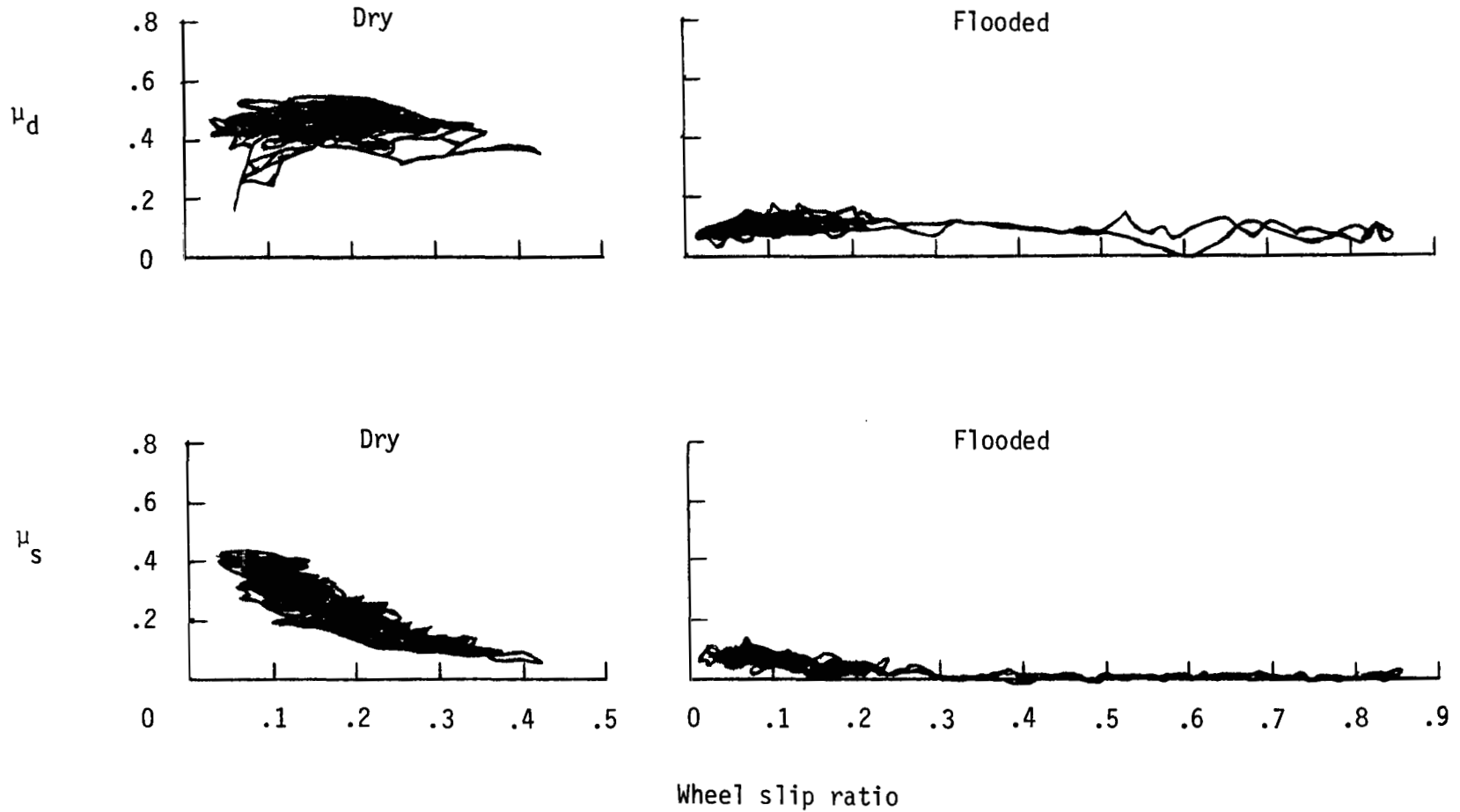


Figure 23.- Effect of tread wear on maximum achieved side-force friction coefficient. Vertical load, 80 kN (18 000 lbf); yaw angle, 6°; free rolling (unbraked).



(a) Run 52. Nominal carriage speed, 75 knots; vertical load, 85 kN (19 000 lbf).

(b) Run 59. Nominal carriage speed, 80 knots; vertical load, 80 kN (17 900 lbf).

Figure 24.- Interaction between braking and cornering. Yaw angle,  $6^\circ$ ; brake supply pressure, 21 MPa (3000 psi); tire condition, new.

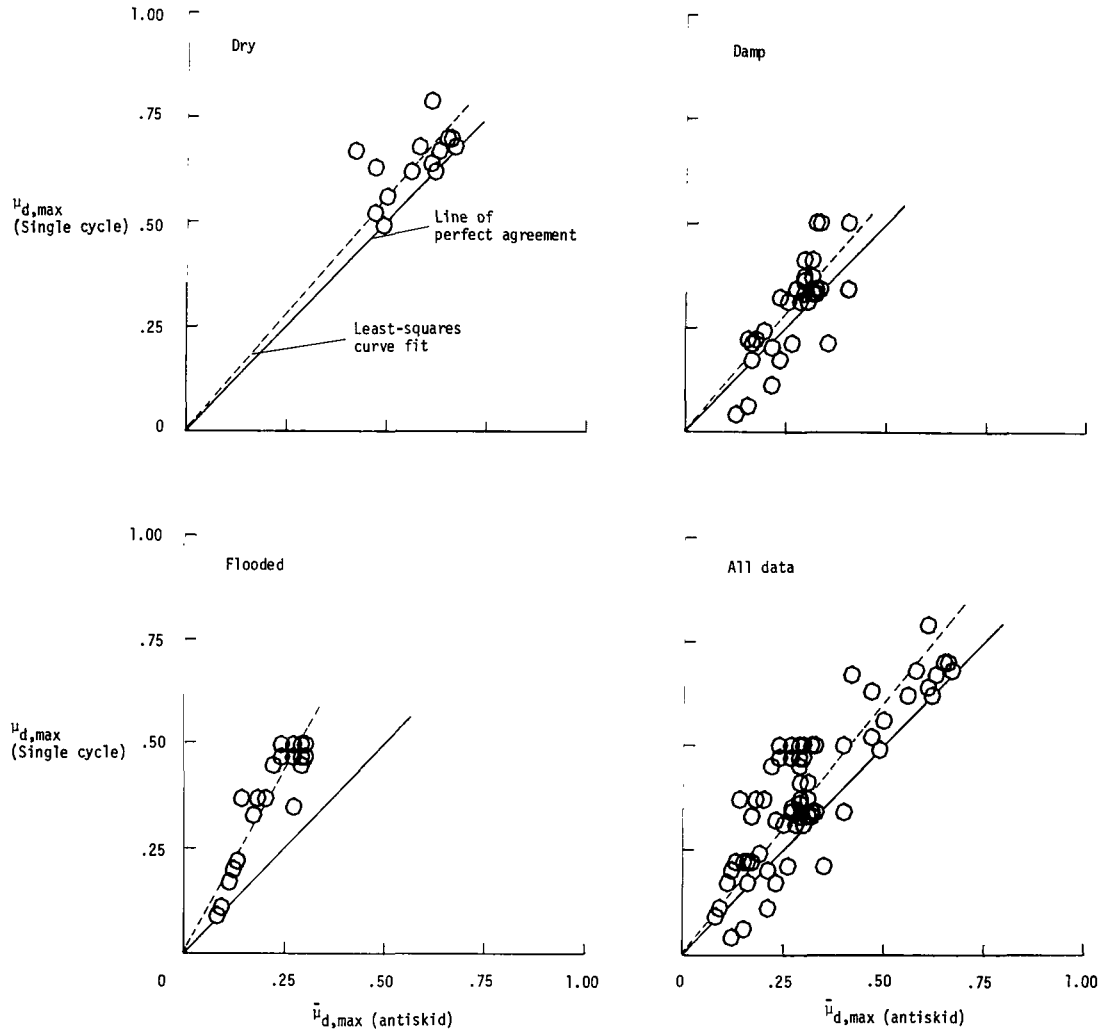


Figure 25.- Effect of cyclic braking on maximum achieved drag-force friction coefficient.

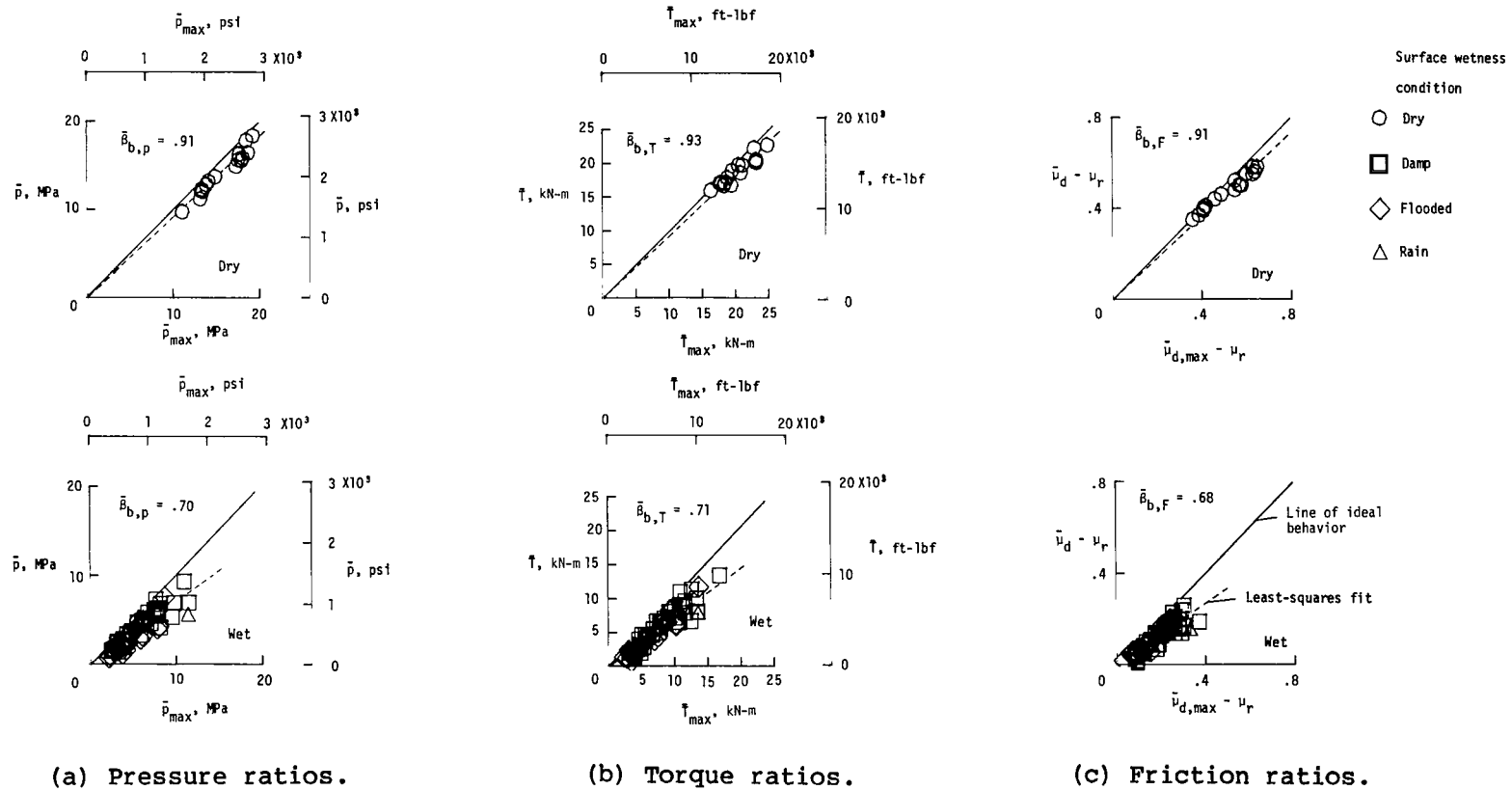
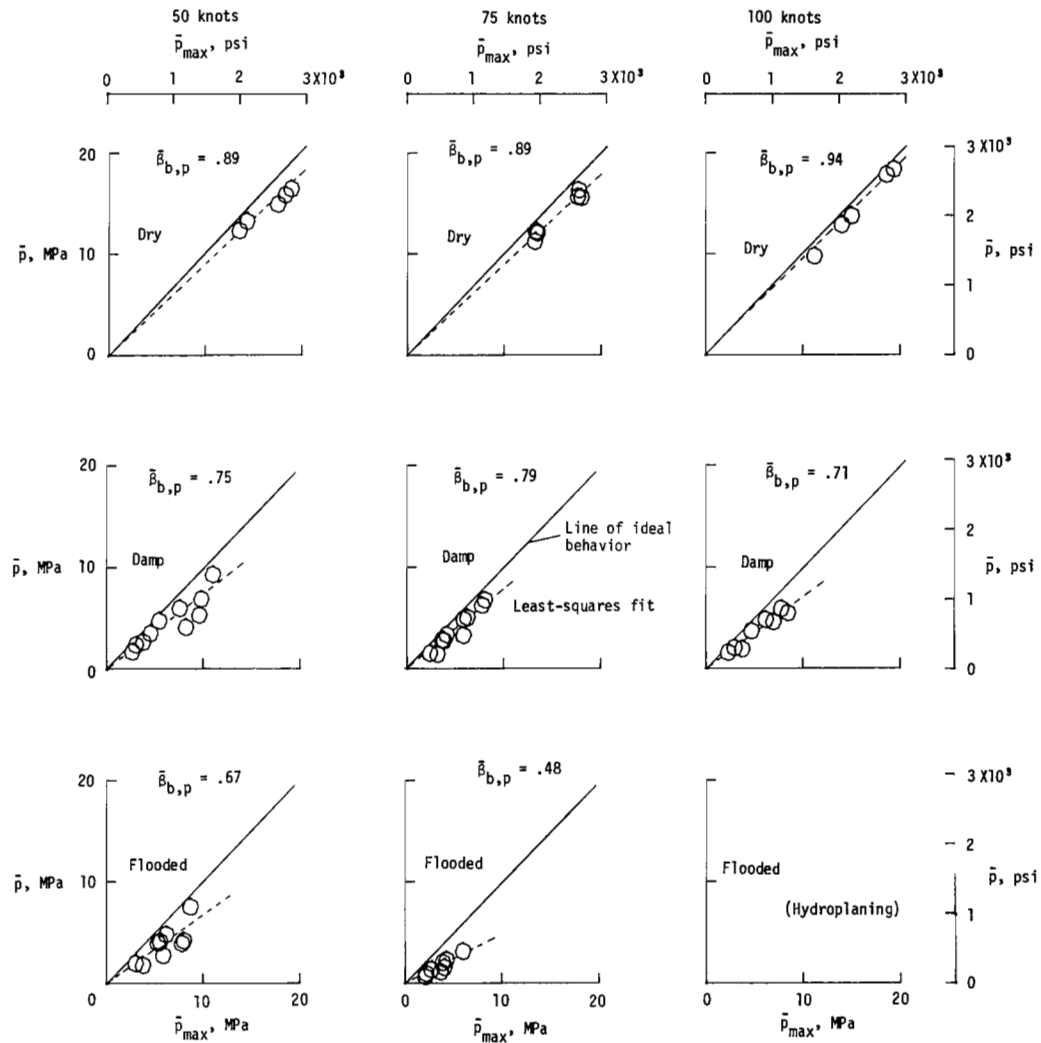
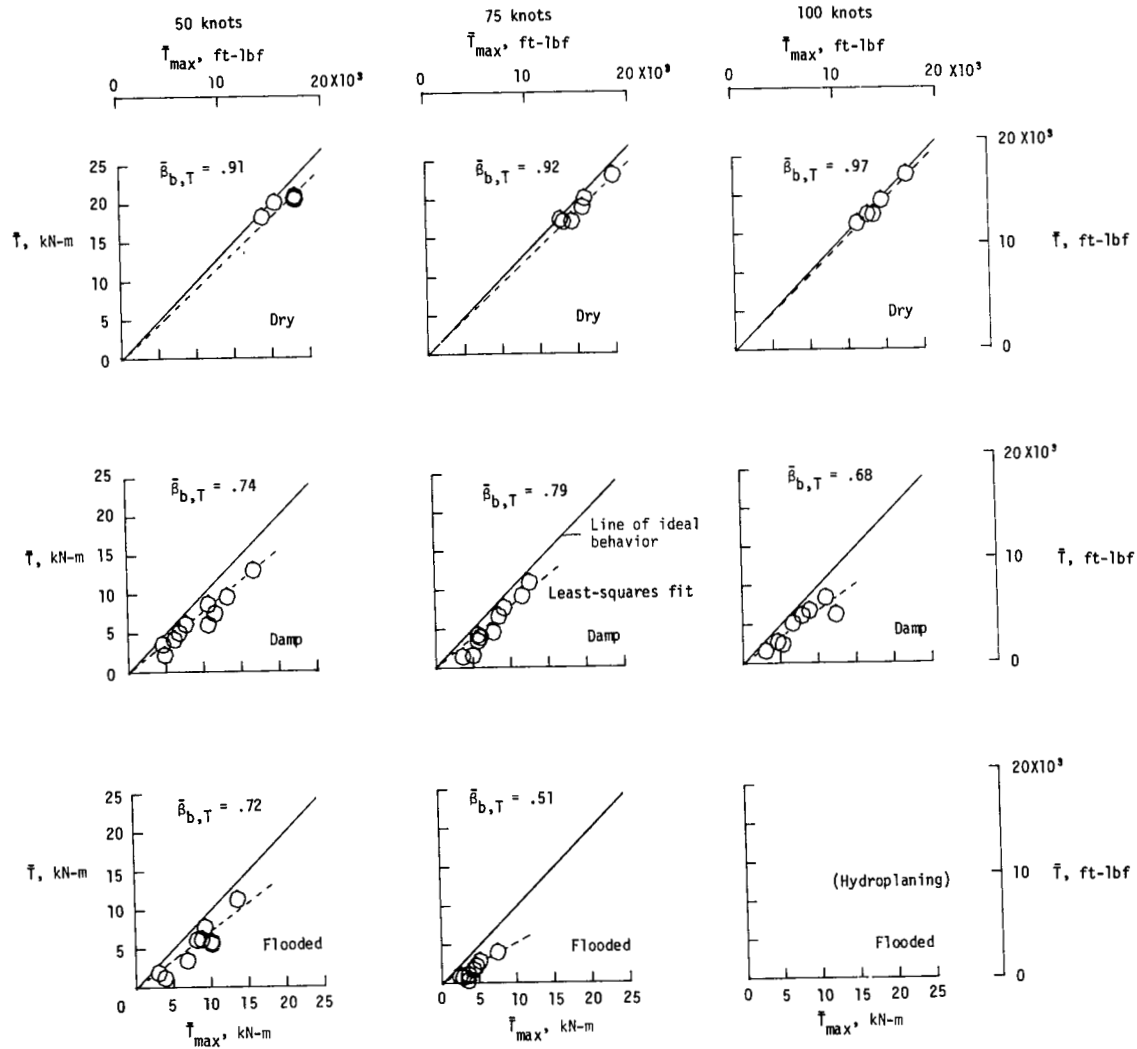


Figure 26.- Ratios of average developed to maximum achieved brake pressure, torque, and drag-force friction coefficient. Data include all runs except those which were torque limited the entire run, those involving tire hydroplaning, and those performed to examine effects of runway friction transition.



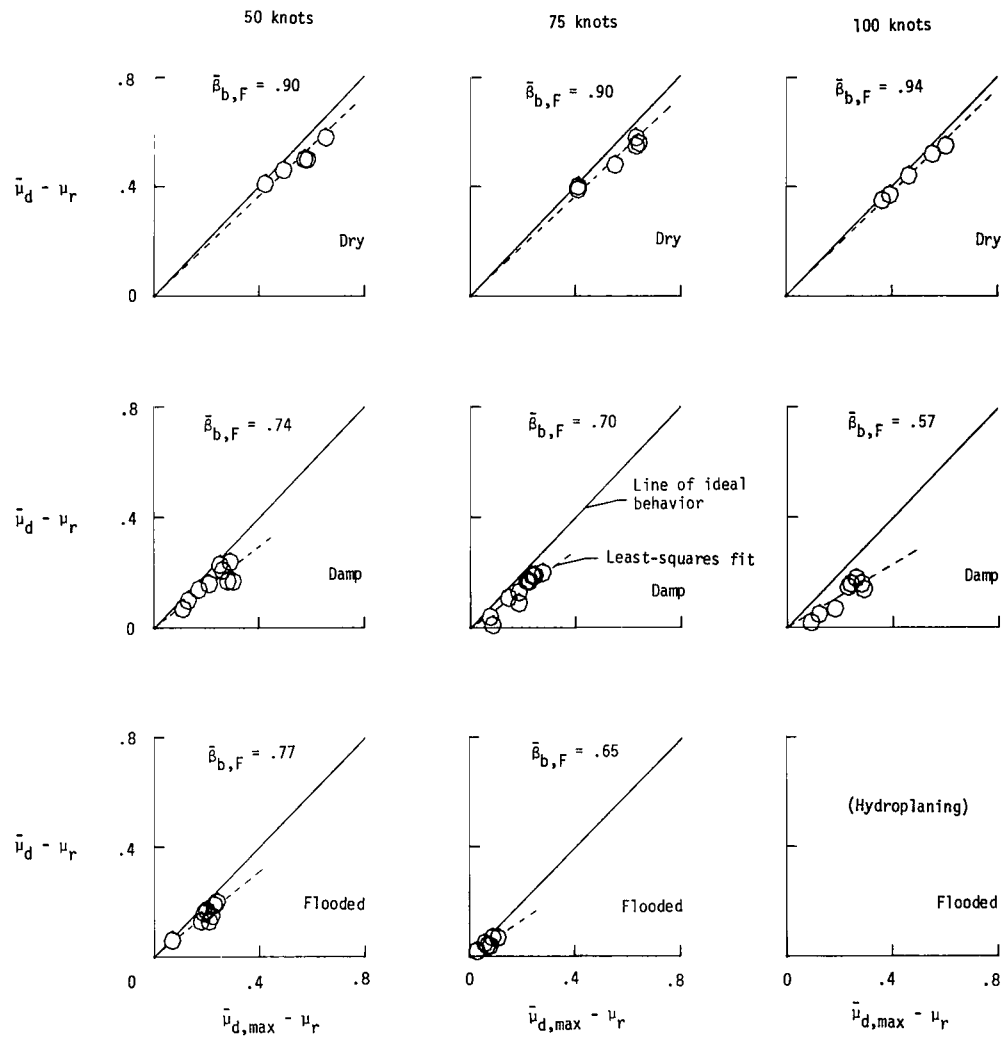
(a) Pressure ratios.

Figure 27.- Effect of carriage speed on brake pressure, torque, and friction ratios. Brake supply pressure, 21 MPa (3000 psi); yaw angles,  $0^\circ$  to  $6^\circ$ .



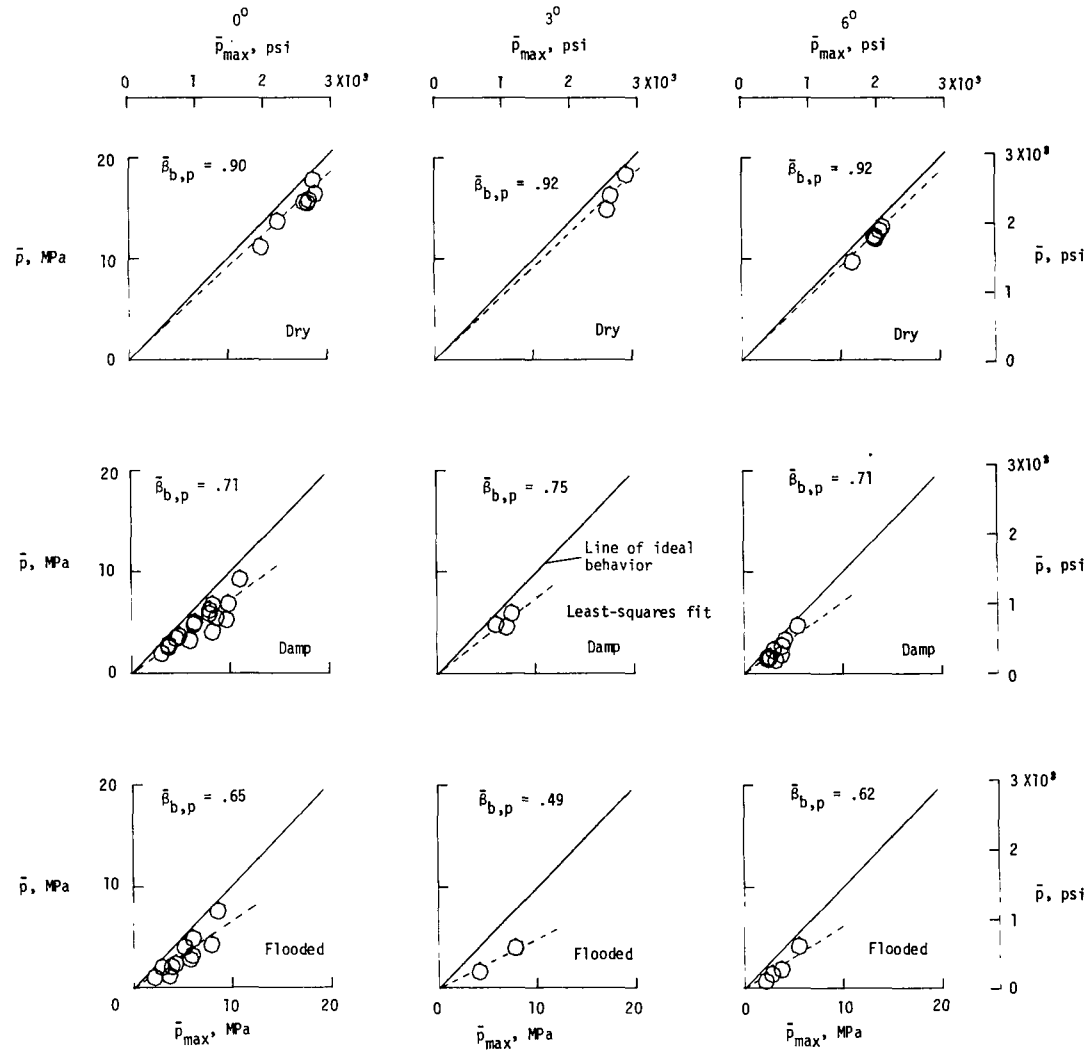
(b) Torque ratios.

Figure 27.- Continued.



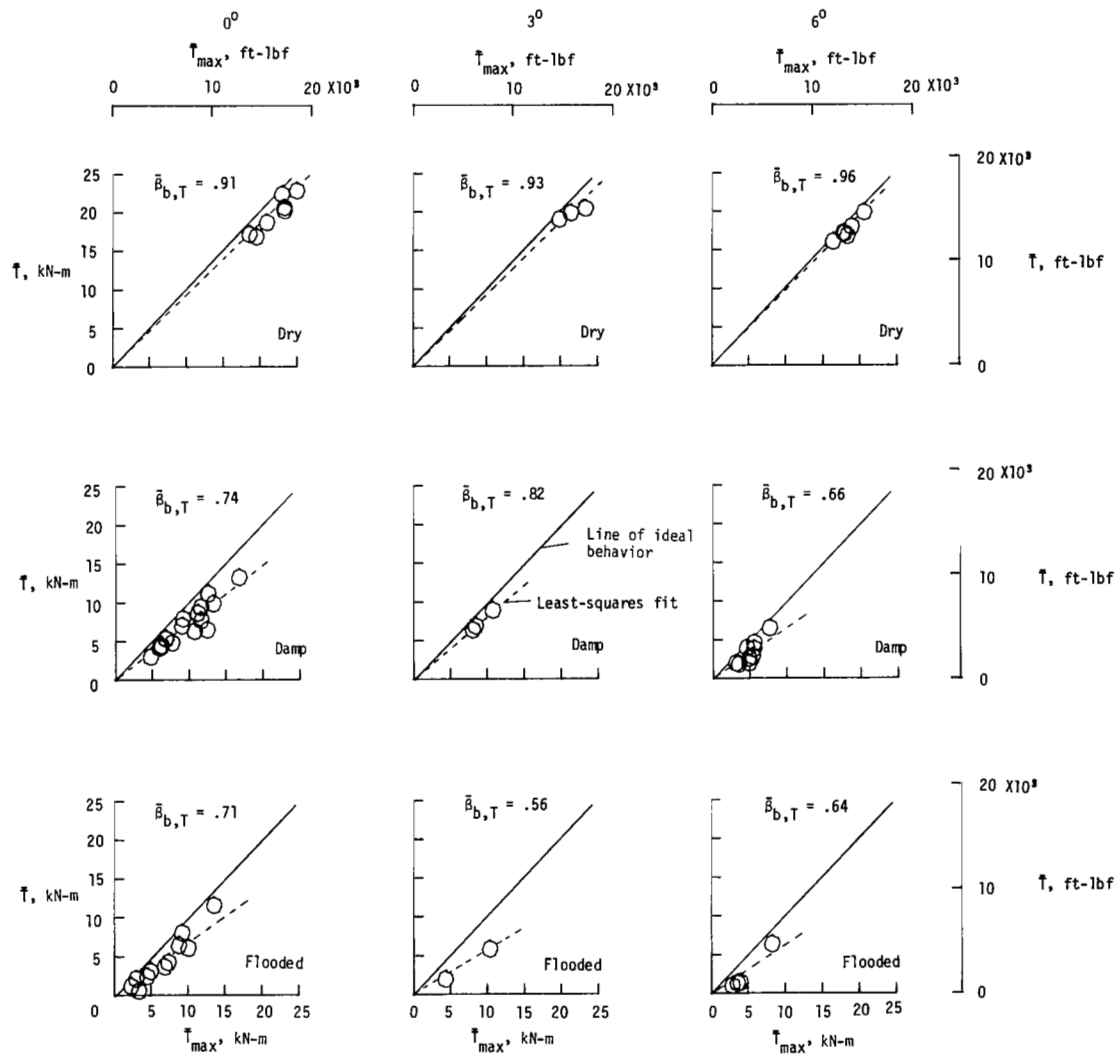
(c) Friction ratios.

Figure 27.- Concluded.



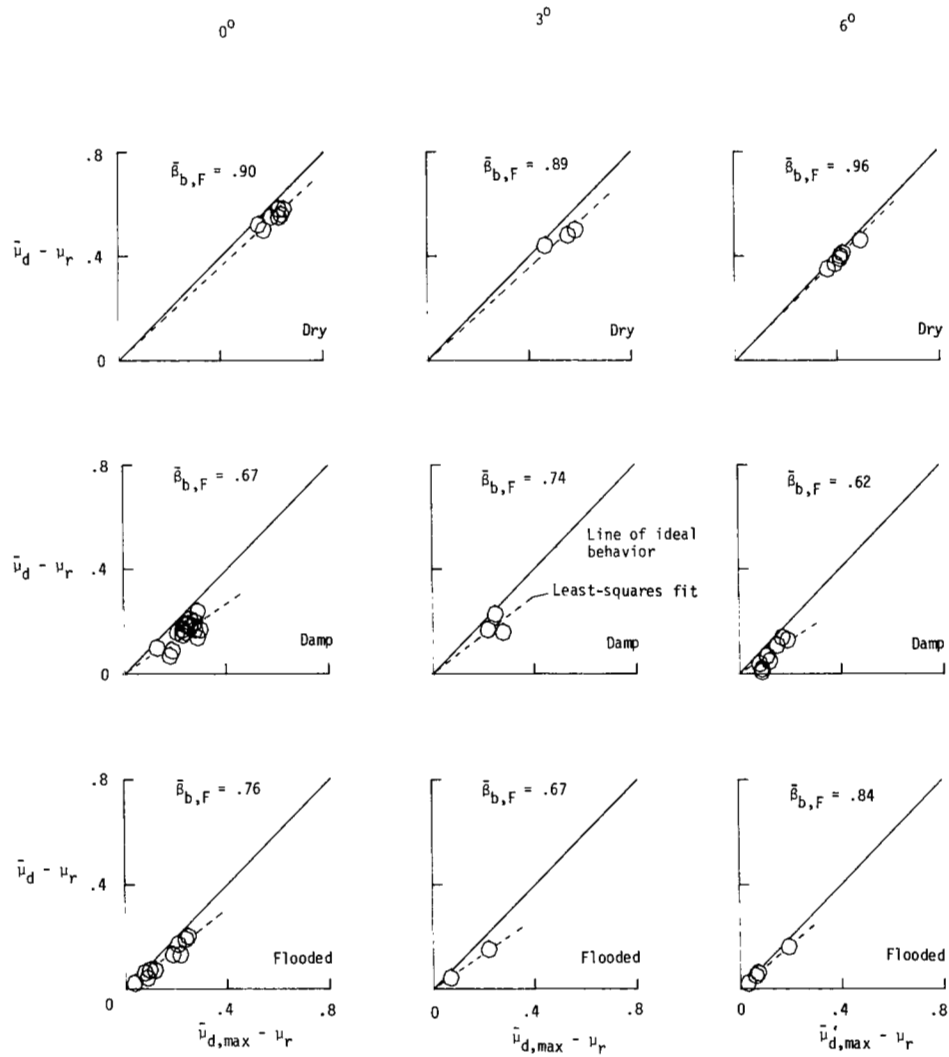
(a) Pressure ratios.

Figure 28.- Effect of yaw angle on brake pressure, torque, and friction ratios.  
 Brake supply pressure, 21 MPa (3000 psi).



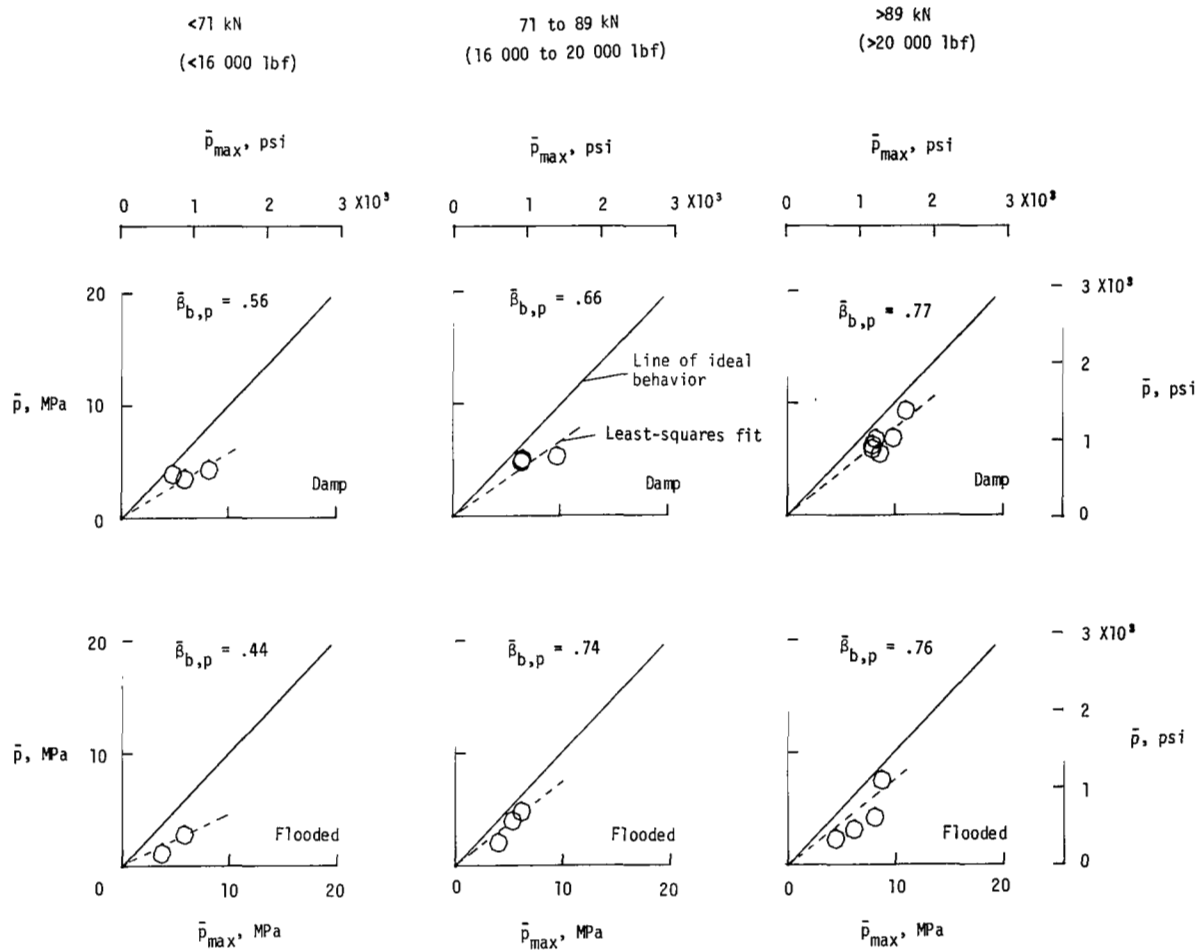
(b) Torque ratios.

Figure 28.- Continued.



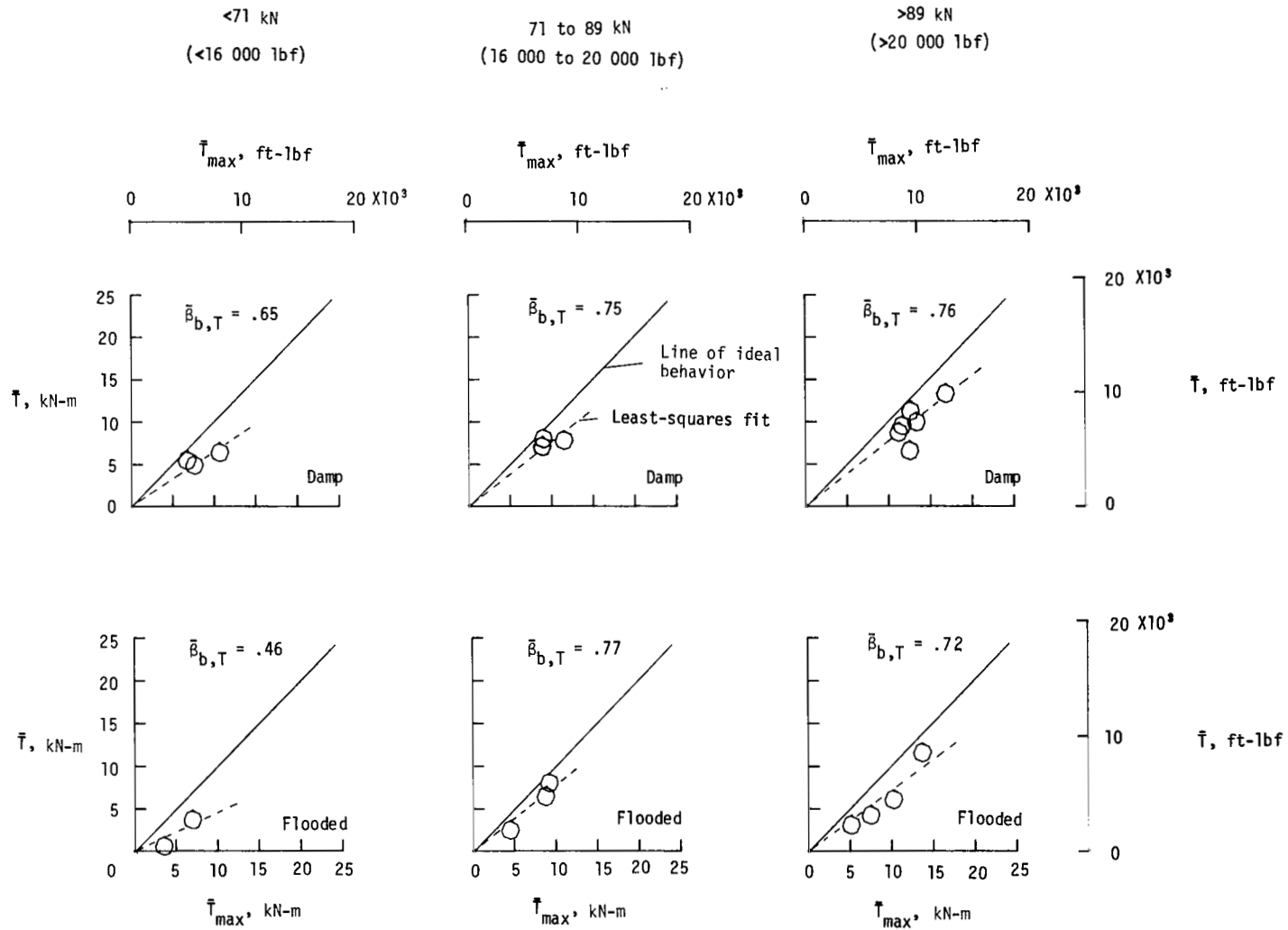
(c) Friction ratios.

Figure 28.- Concluded.



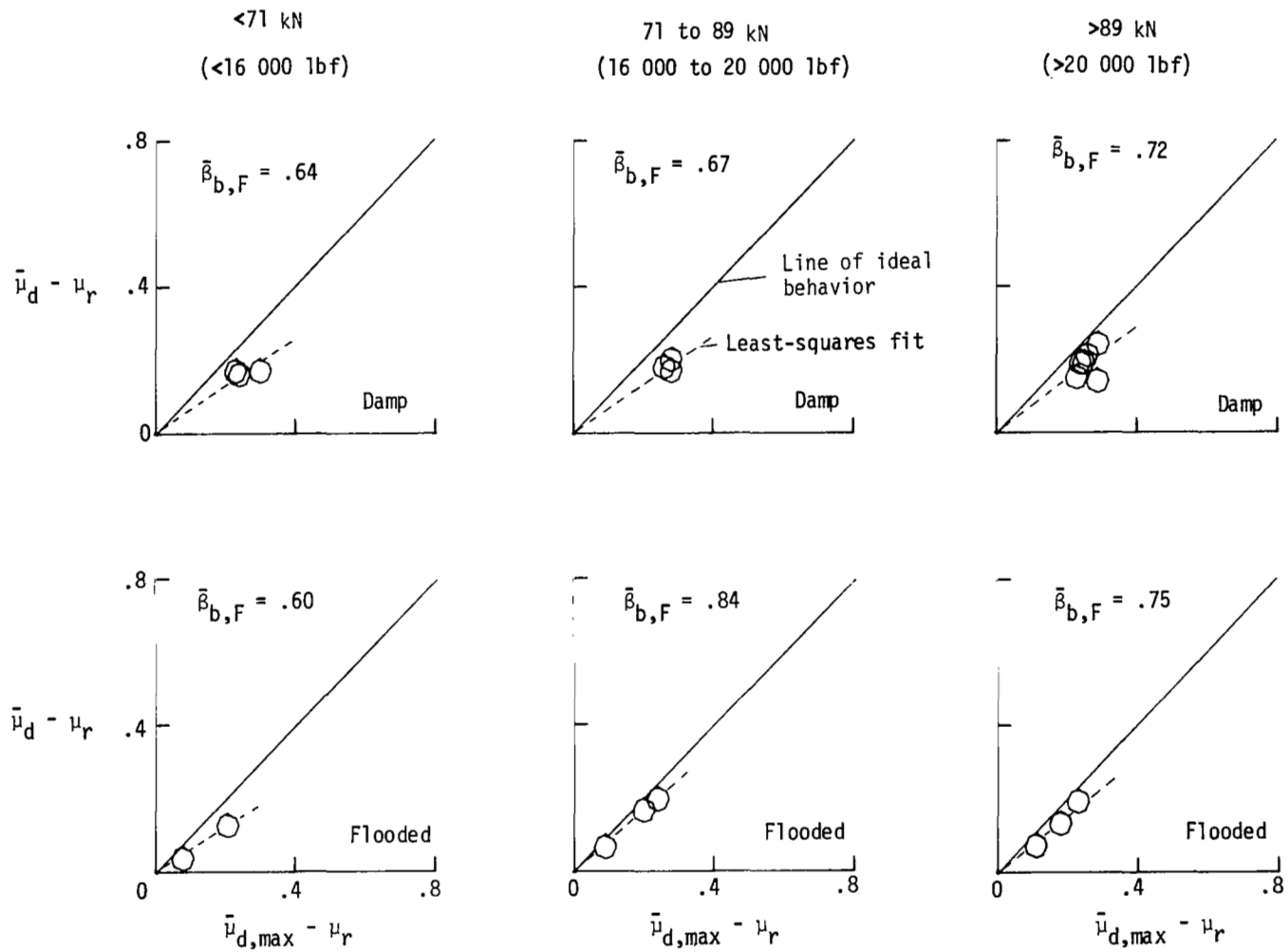
(a) Pressure ratios.

Figure 29.- Effect of vertical-force variations on brake pressure, torque, and friction ratios. Brake supply pressure, 21 MPa (3000 psi); yaw angle,  $0^\circ$ ; tire condition, new.



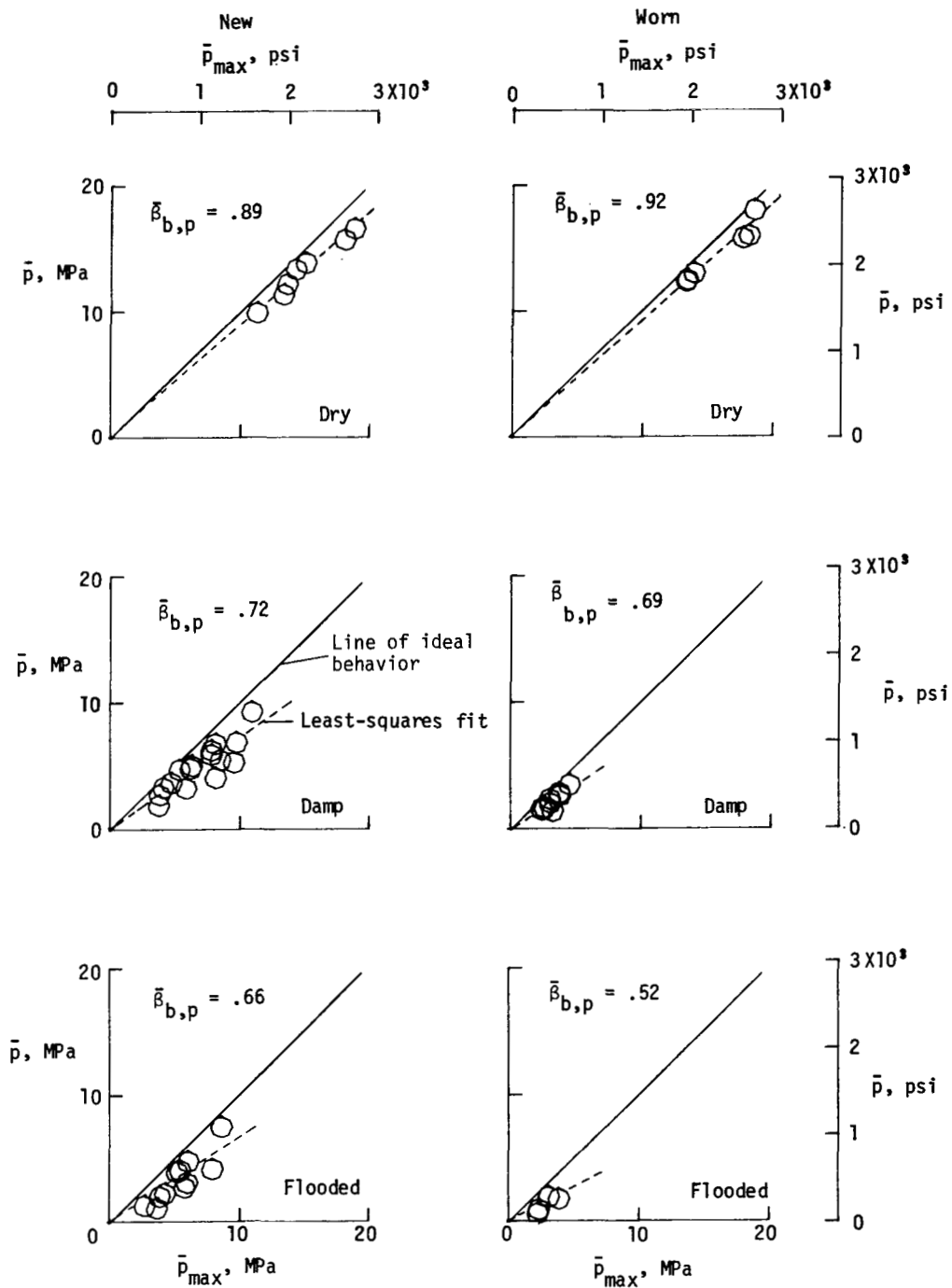
(b) Torque ratios.

Figure 29.- Continued.



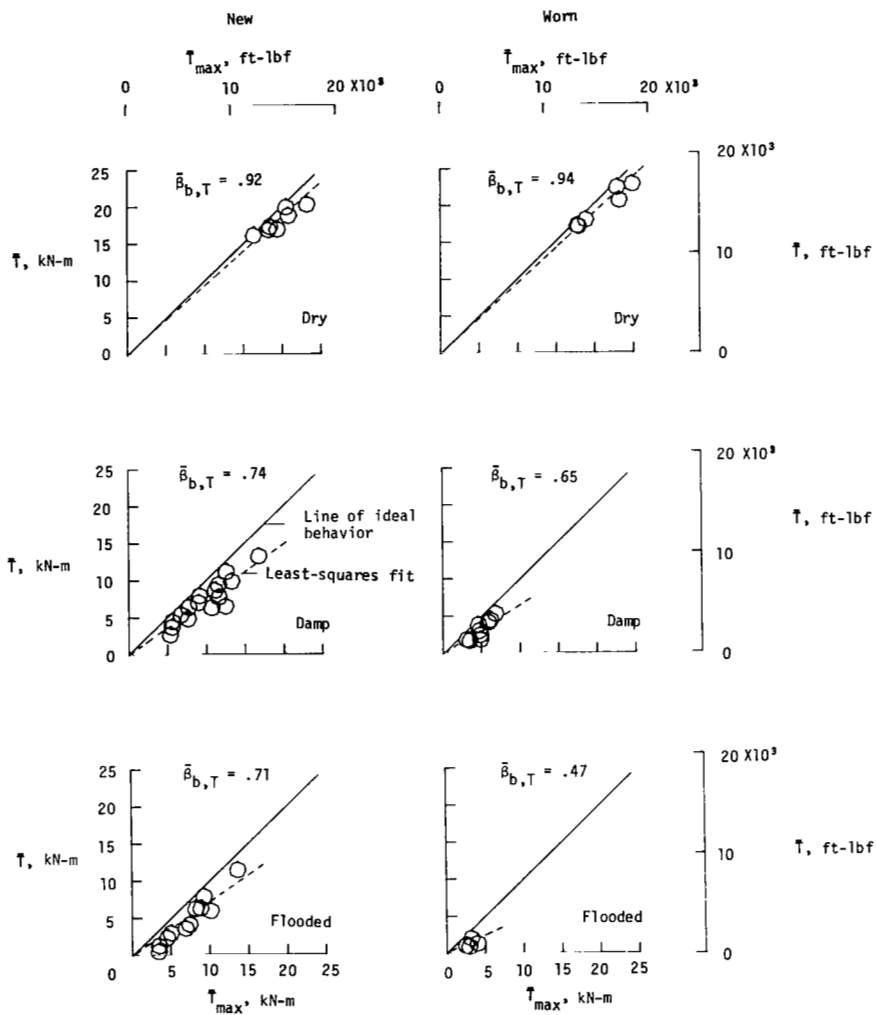
(c) Friction ratios.

Figure 29.- Concluded.



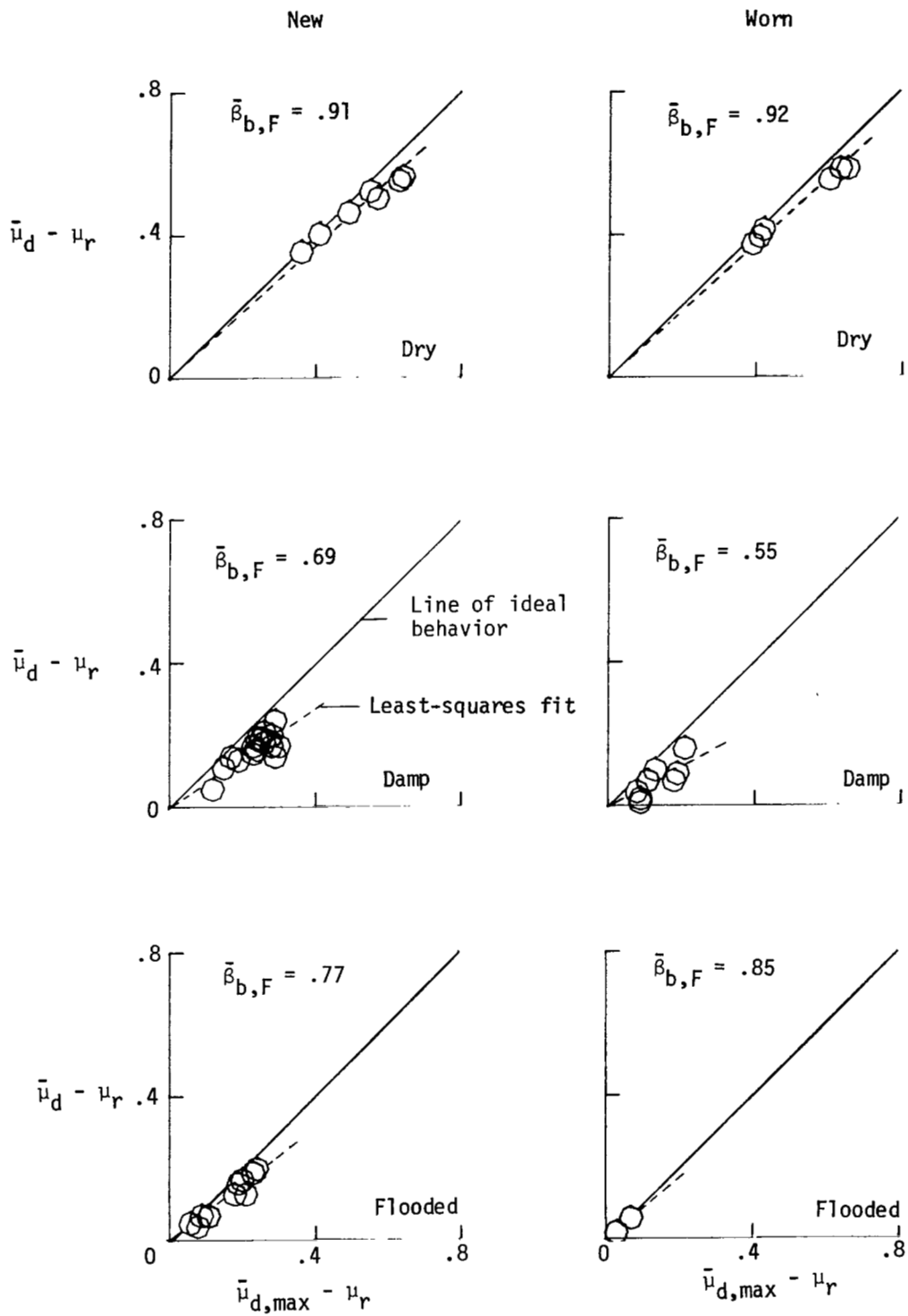
(a) Pressure ratios.

Figure 30.- Effect of tread wear on brake pressure, torque, and friction ratios. Brake supply pressure, 21 MPa (3000 psi); yaw angle,  $0^\circ$  and  $6^\circ$ .



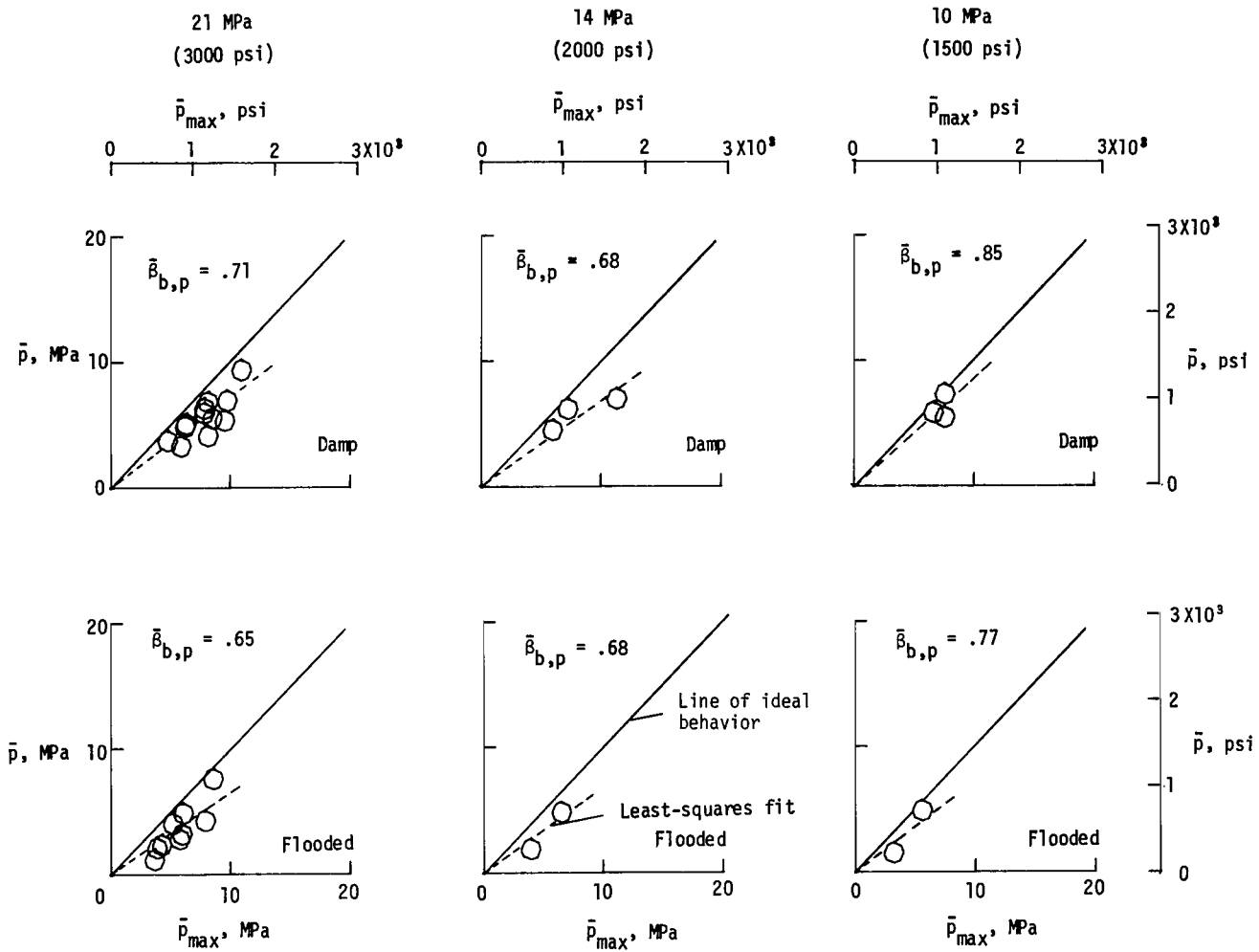
(b) Torque ratios.

Figure 30.- Continued.



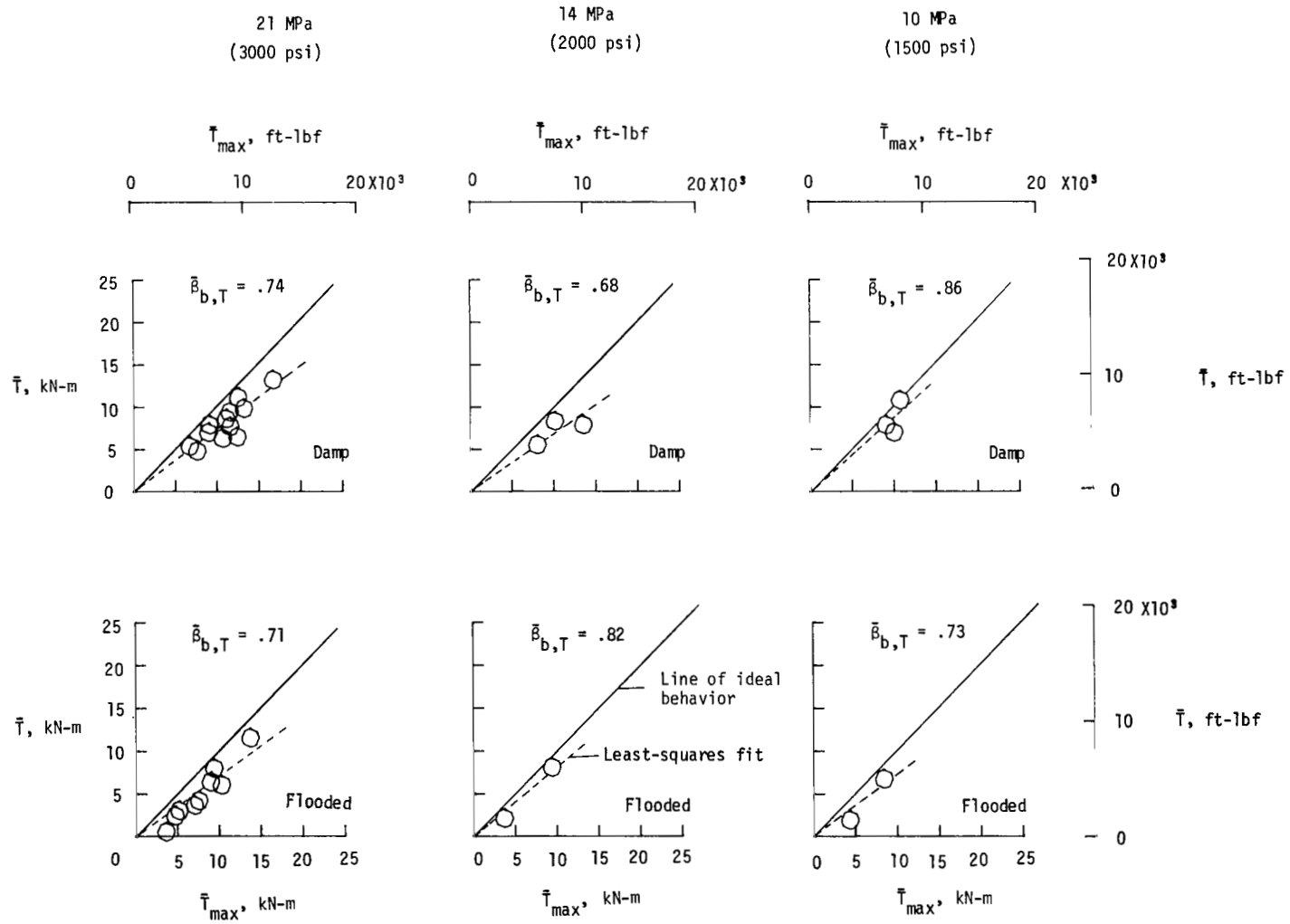
(c) Friction ratios.

Figure 30.- Concluded.



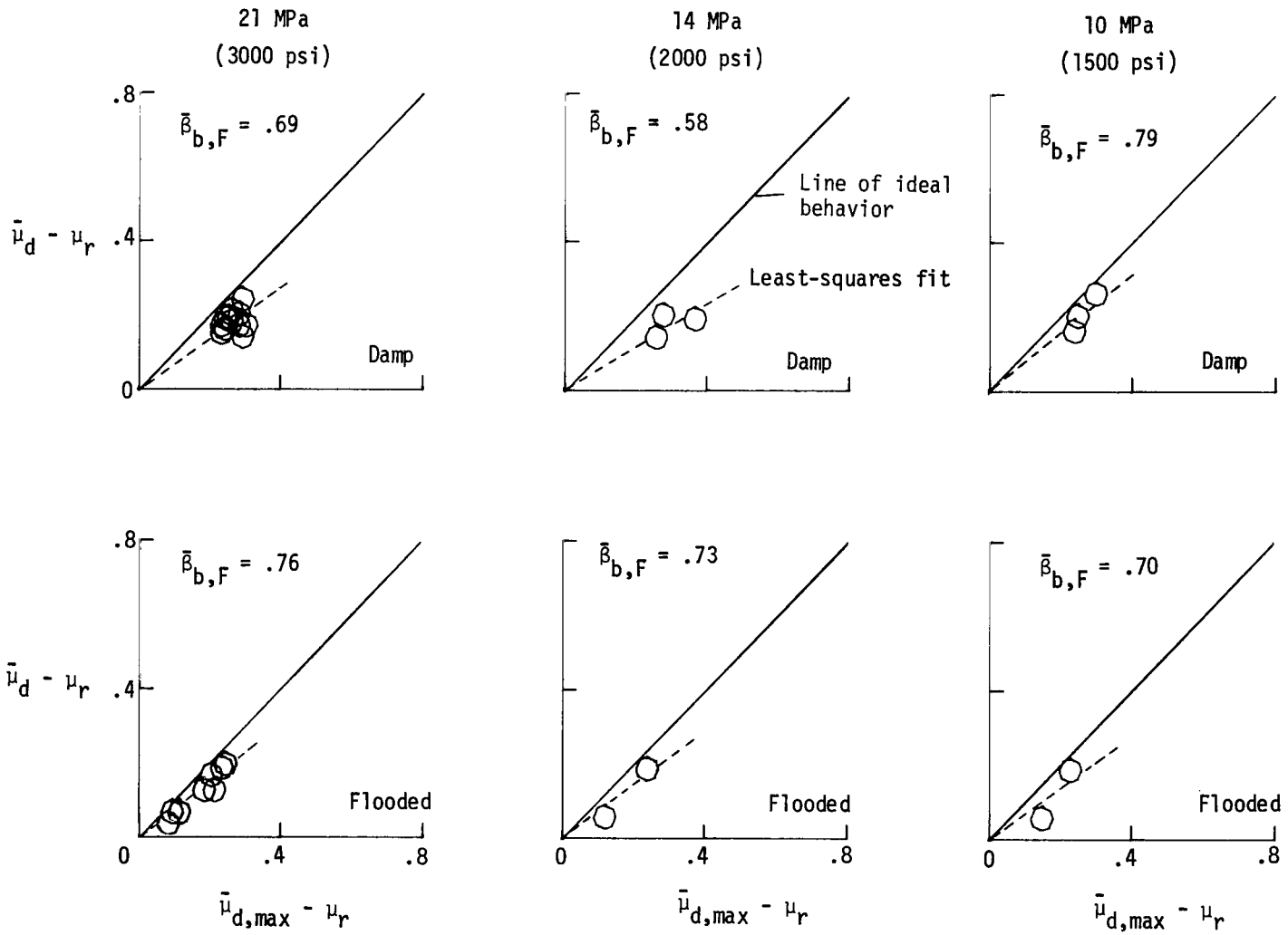
(a) Pressure ratios.

Figure 31.- Effect of brake supply pressure on brake pressure, torque, and friction ratios. Yaw angle,  $0^\circ$ ; tread condition, new.



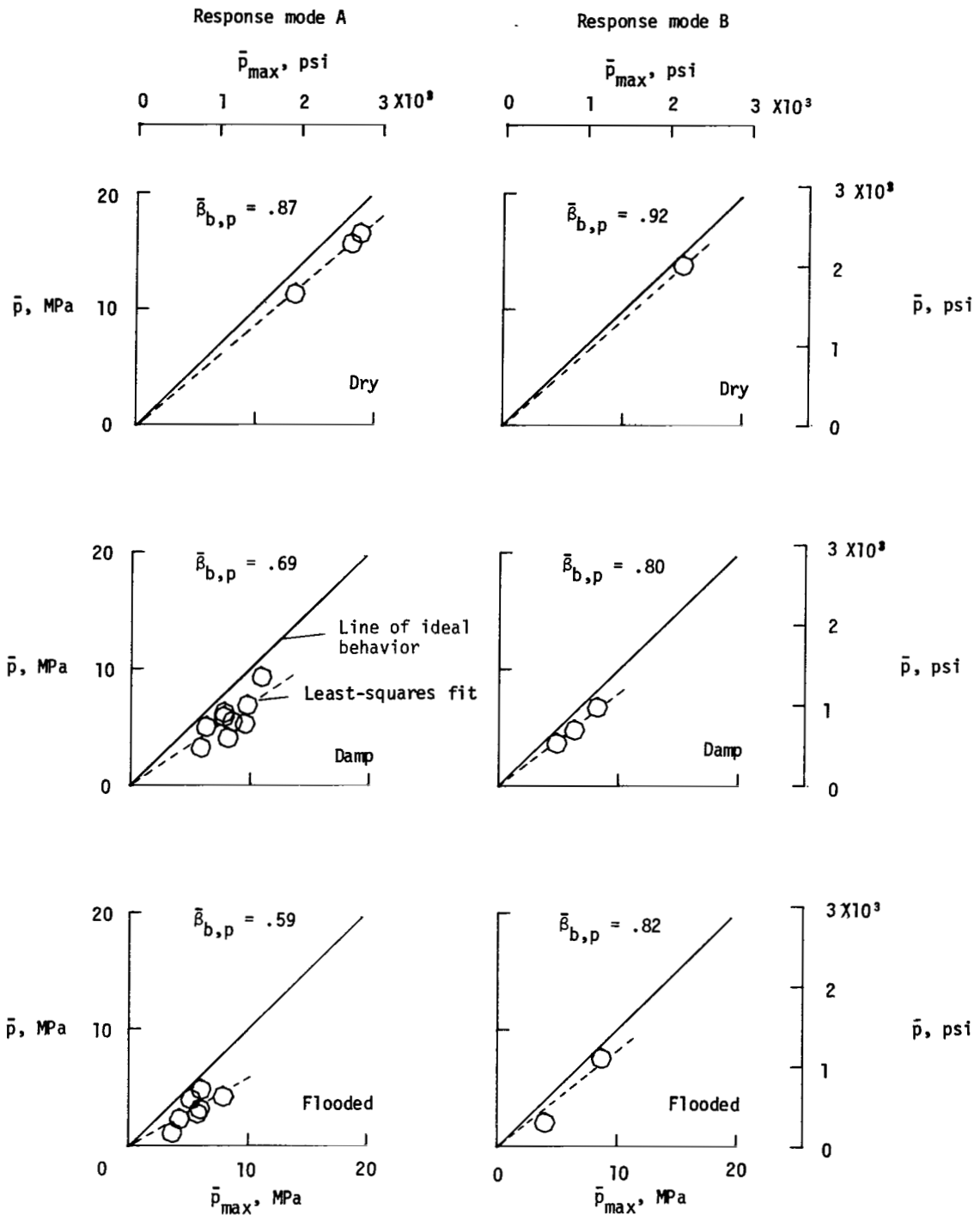
(b) Torque ratios.

Figure 31.- Continued.



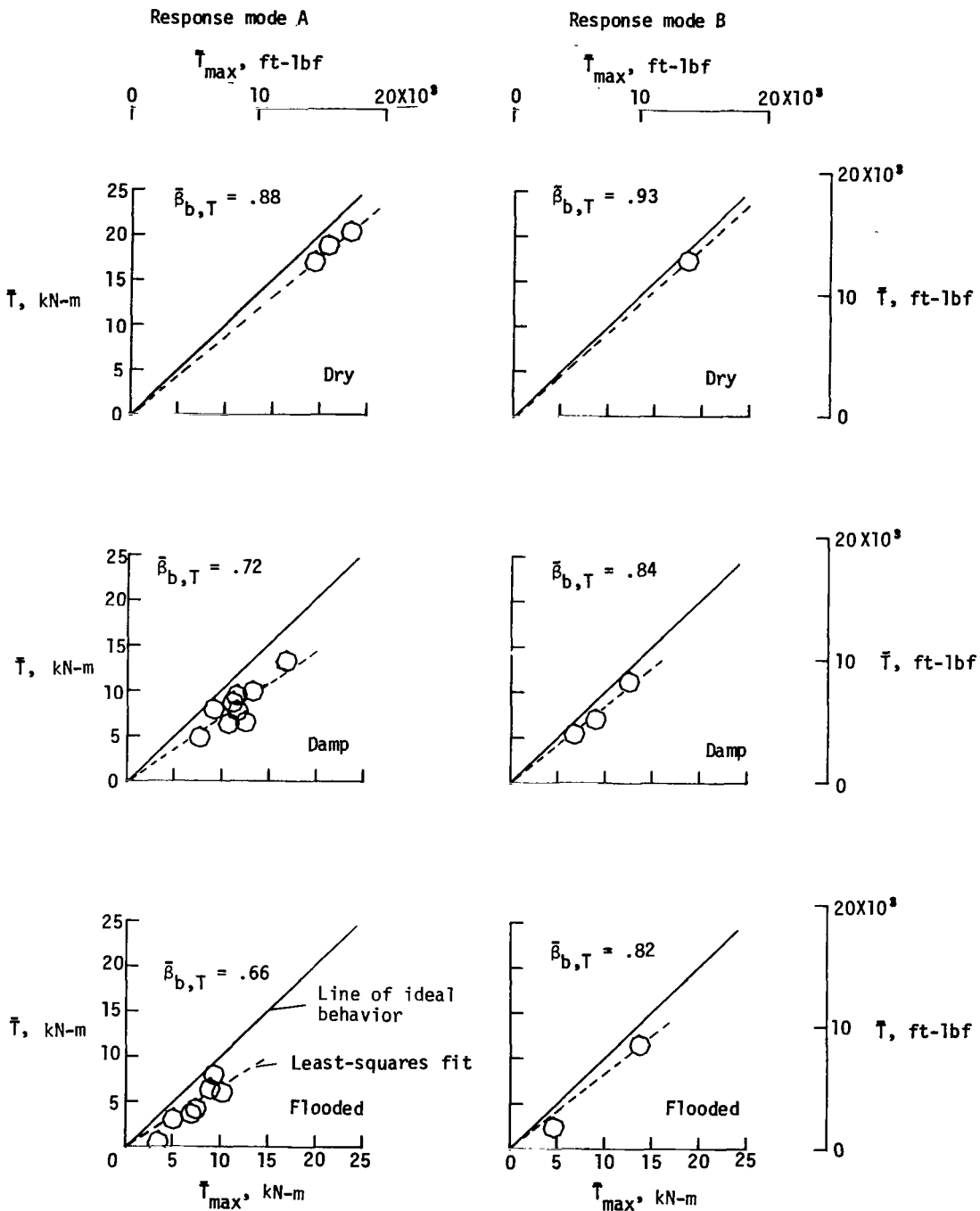
(c) Friction ratios.

Figure 31.- Concluded.



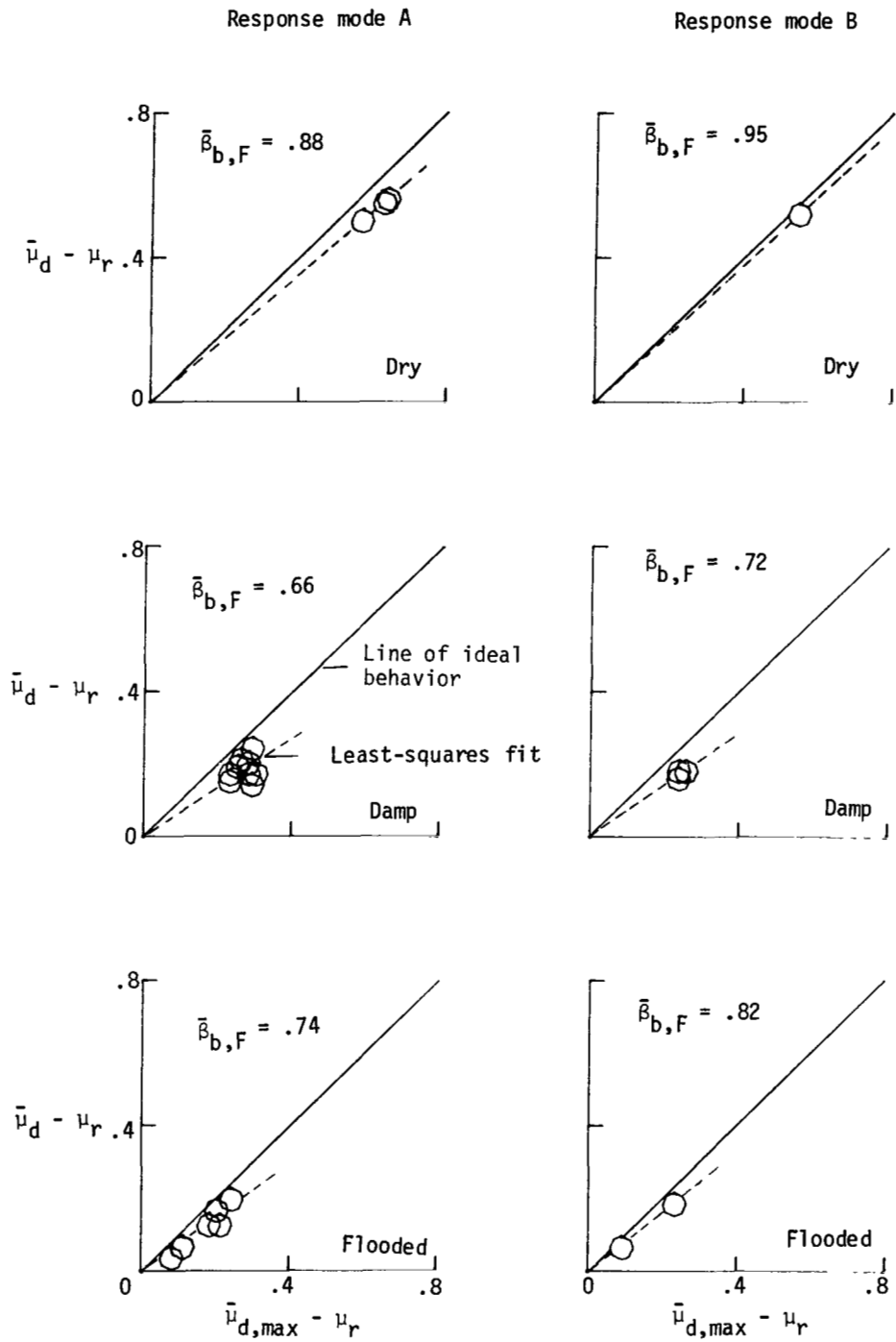
(a) Pressure ratios.

Figure 32.- Effect of system response mode on brake pressure, torque, and friction ratios. Brake supply pressure, 21 MPa (3000 psi); yaw angle,  $0^\circ$ ; tread condition, new.



(b) Torque ratios.

Figure 32.- Continued.



(c) Friction ratios.

Figure 32.- Concluded.

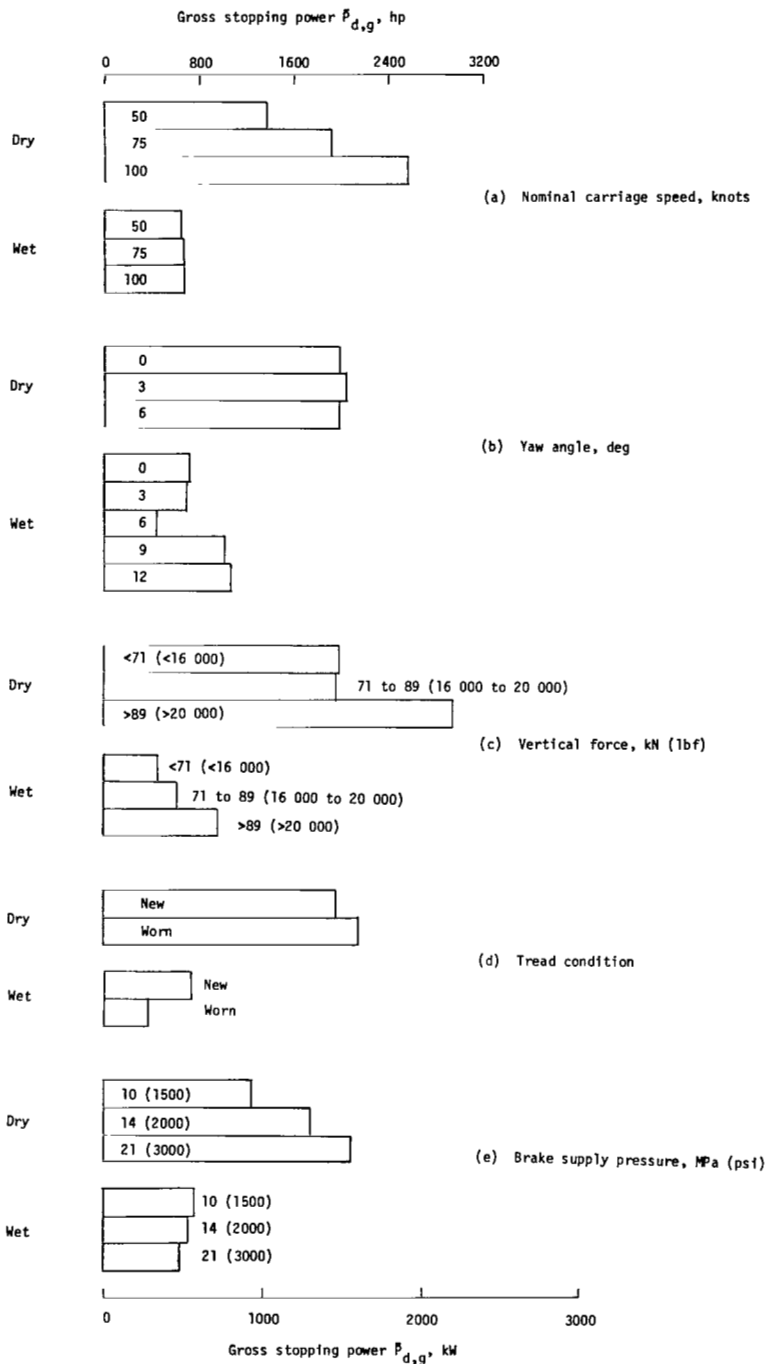


Figure 33.- Effect of test parameter variations on gross stopping power developed by antiskid braking system. Each bar graph represents average of several runs.

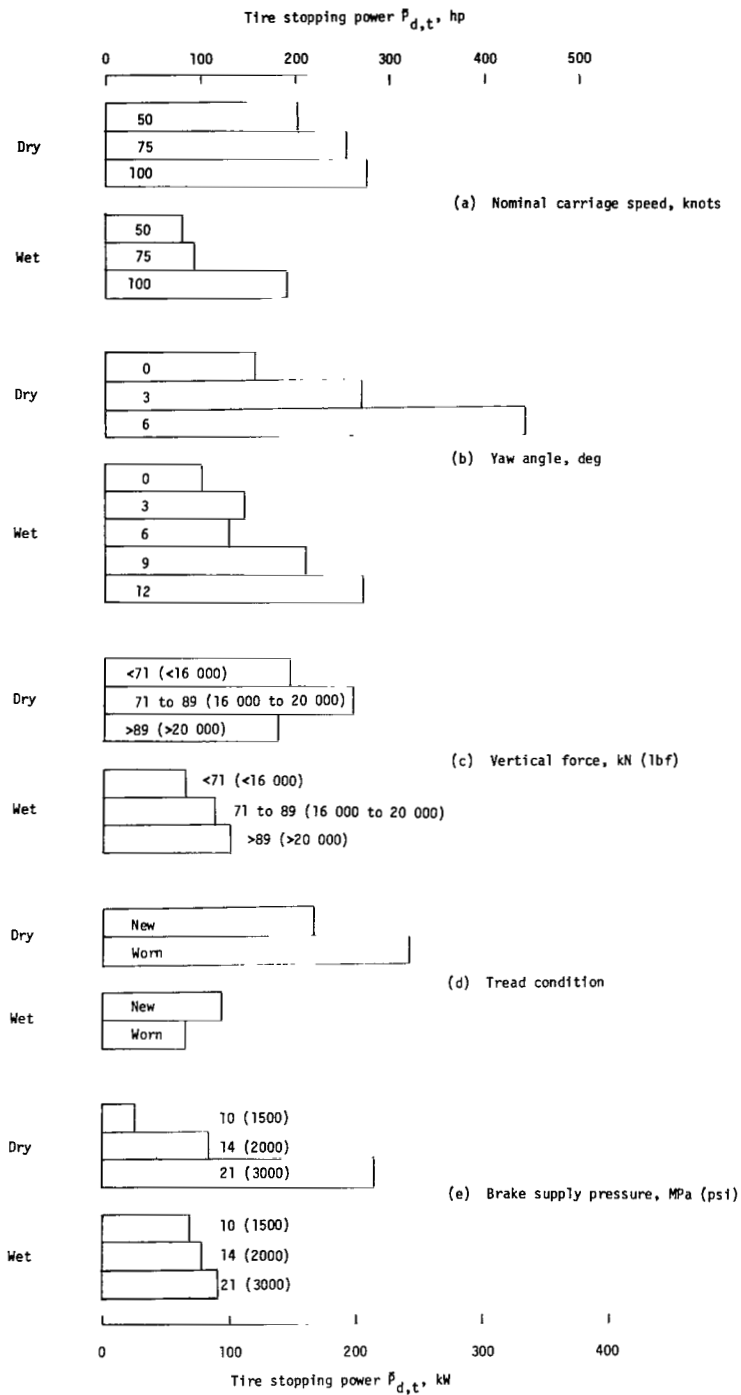


Figure 34.- Effect of test parameter variations on stopping power dissipated by the tire.

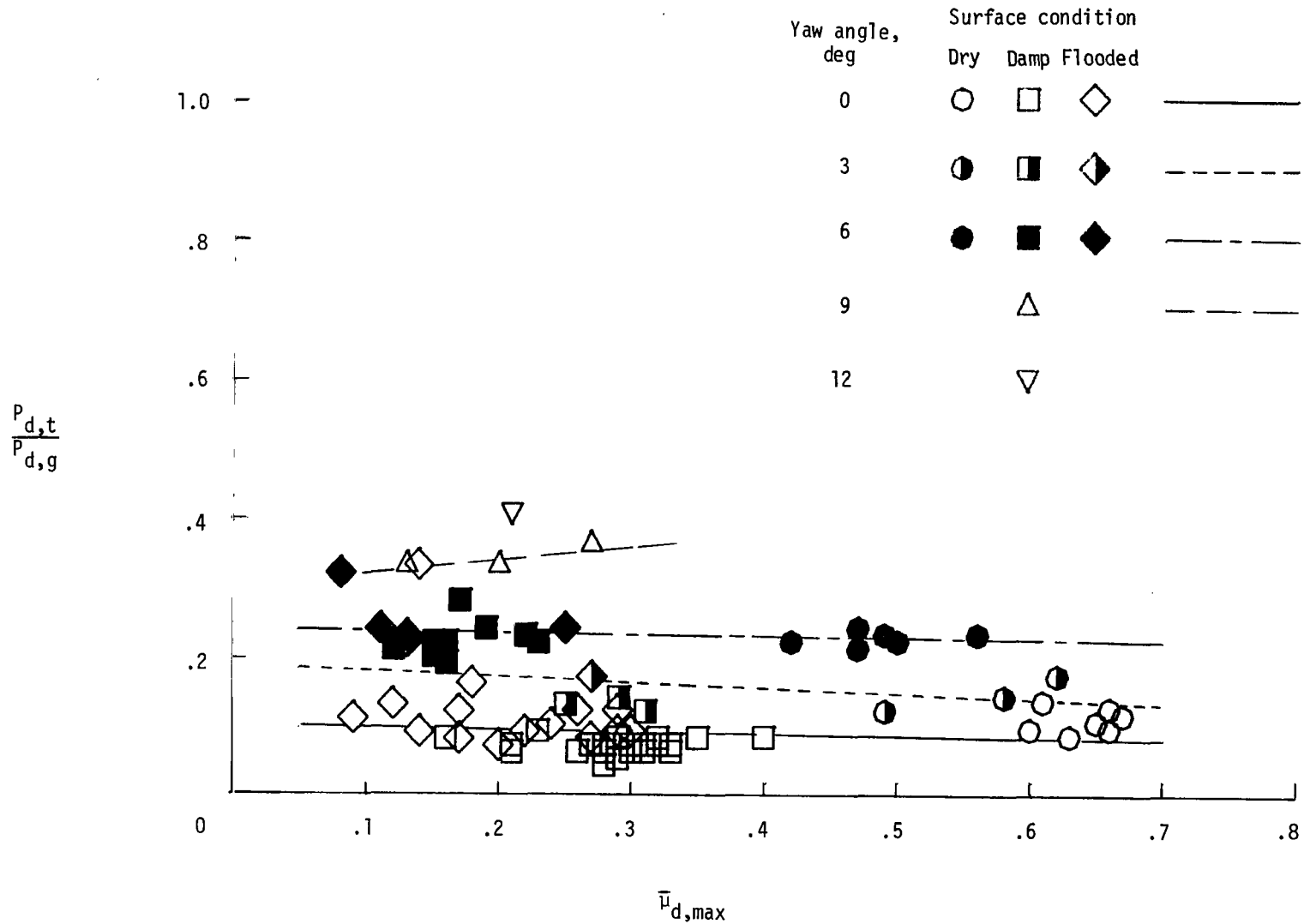


Figure 35.- Effect of maximum drag-force friction coefficient on ratio of tire stopping power to gross stopping power.

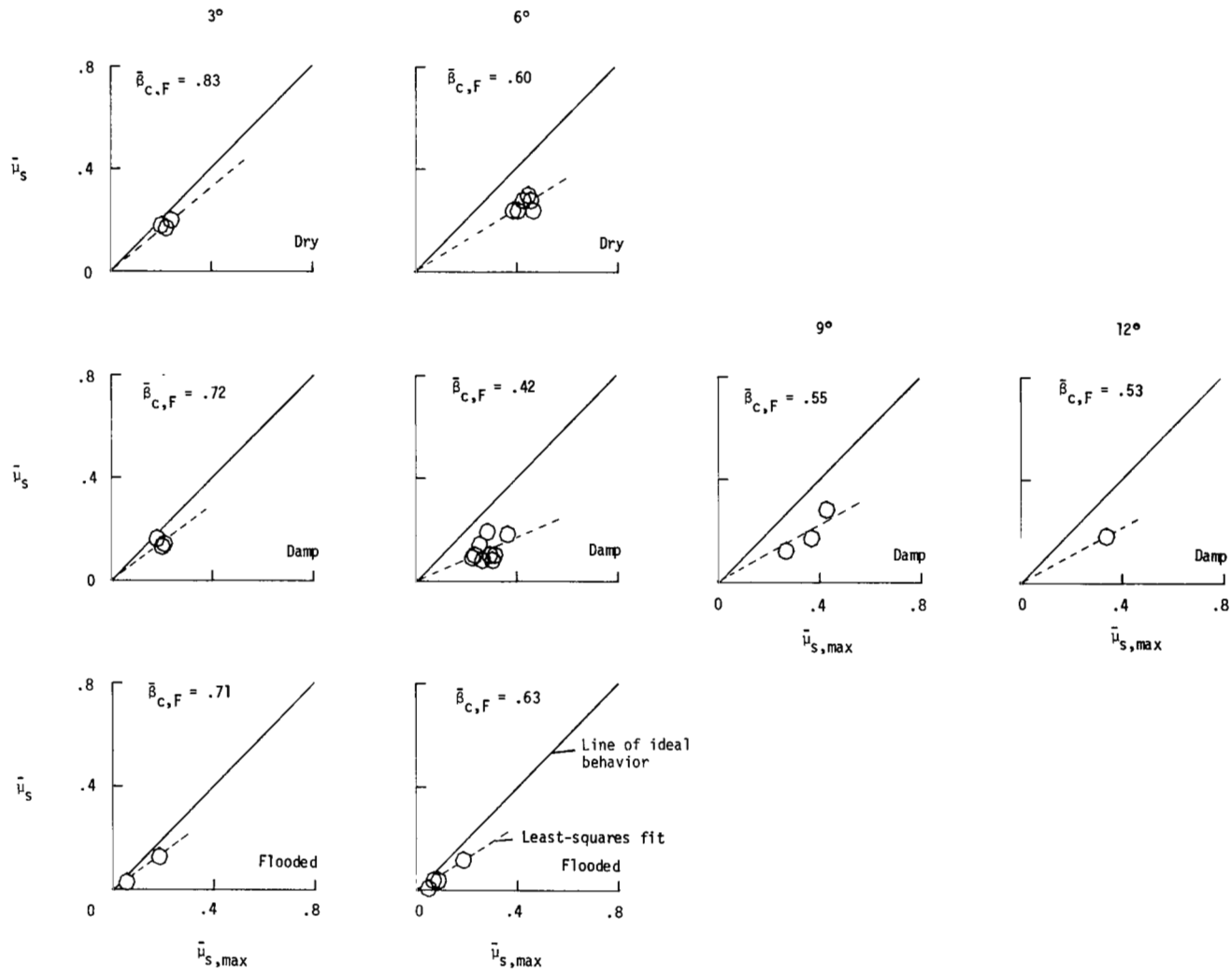


Figure 36.— Effect of yaw angle on cornering-behavior index.

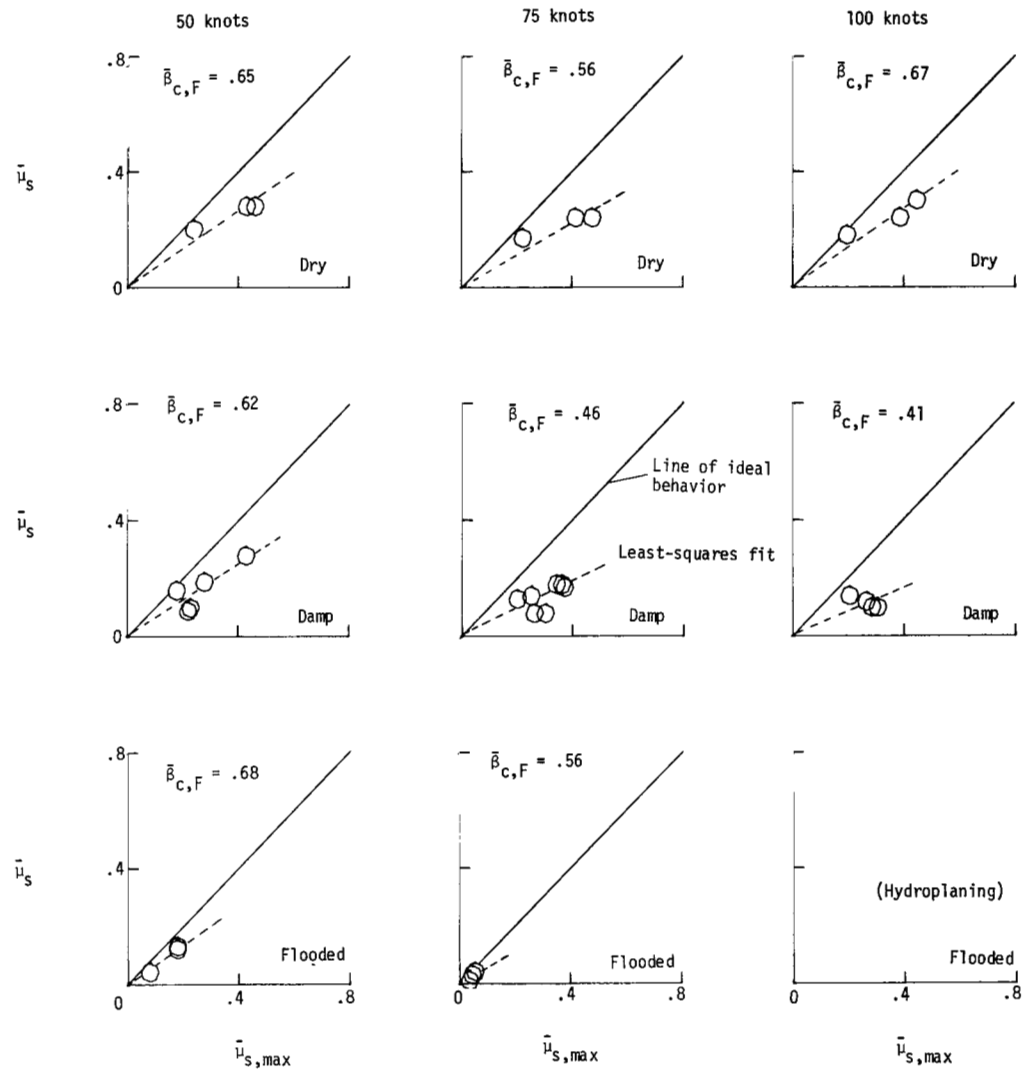


Figure 37.- Effect of carriage speed on cornering-behavior index. Yaw angle,  $6^\circ$ .

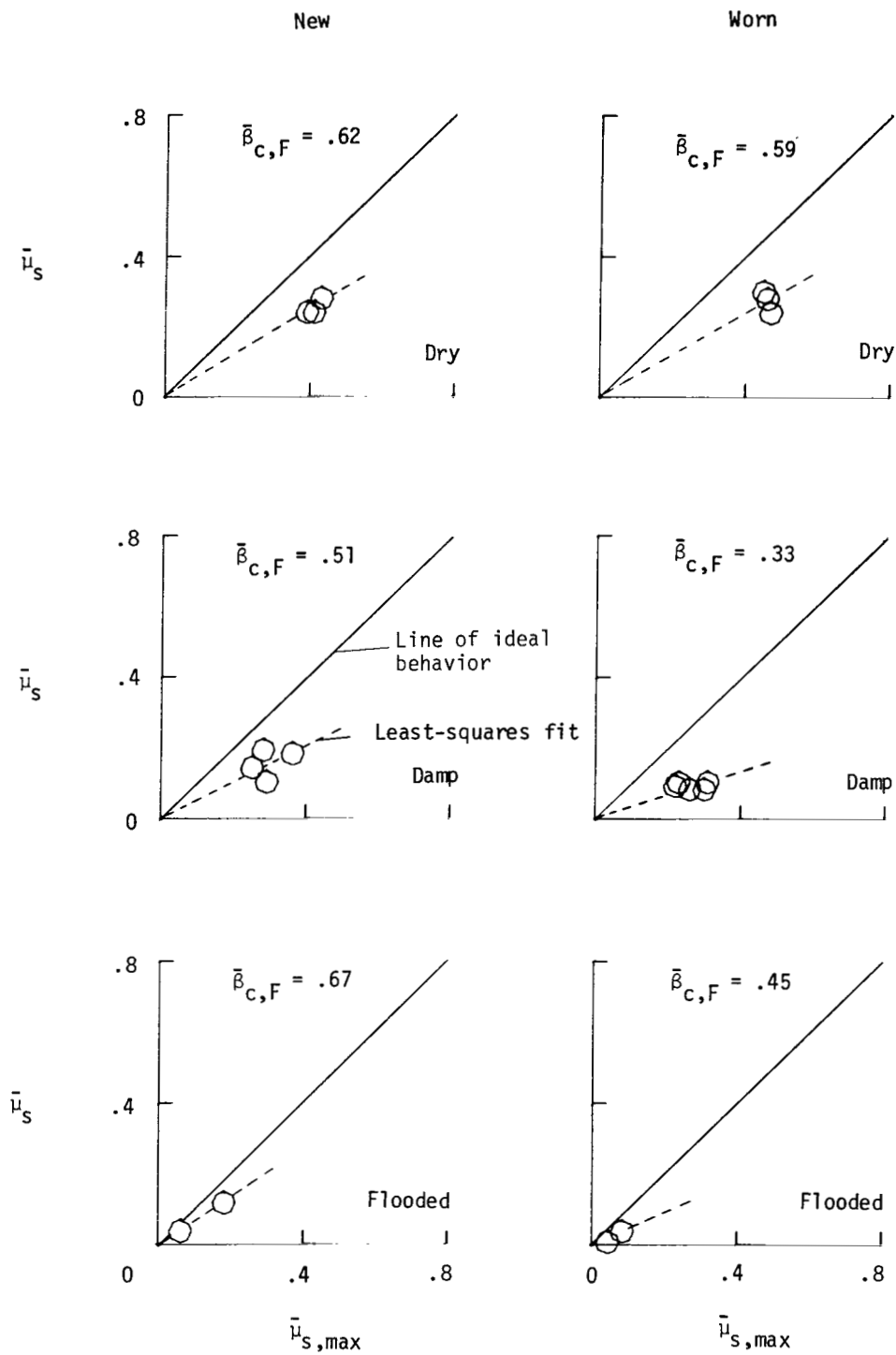


Figure 38.- Effect of tread wear on cornering-behavior index. Yaw angle, 6°.

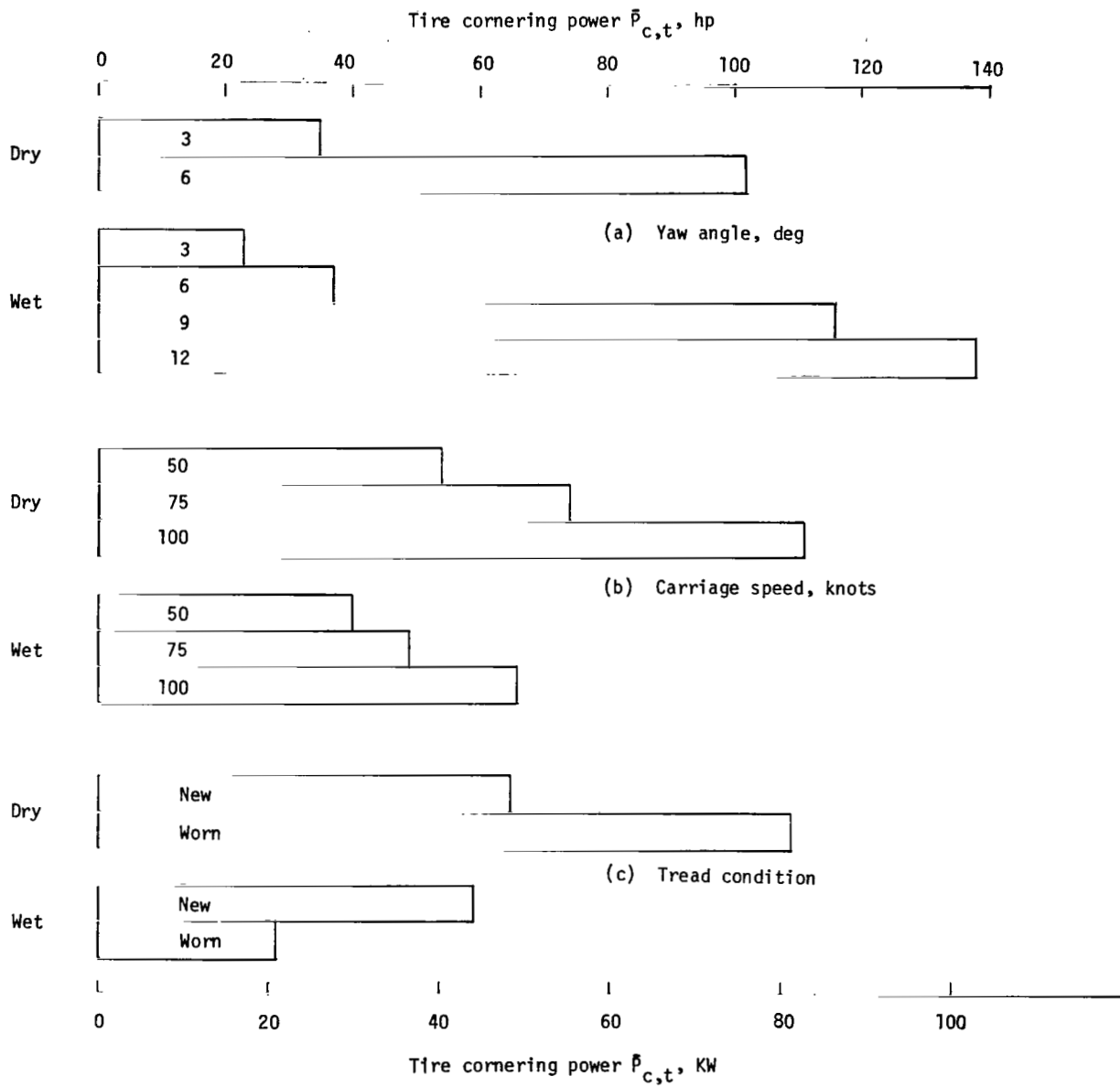


Figure 39.- Effect of test parameter variations on cornering power dissipated by tire.

## APPENDIX

### TIME HISTORIES

This appendix presents time histories in figures A1 to A101 of nine parameters which describe the behavior of the antiskid system during each test condition. These nine parameters, which are wheel speed, slip velocity, skid signal, brake pressure, brake torque, drag-force friction coefficient, side-force friction coefficient, alining torque, and slip ratio, are given for the convenience of the user in studying detail characteristics of the antiskid system.

APPENDIX

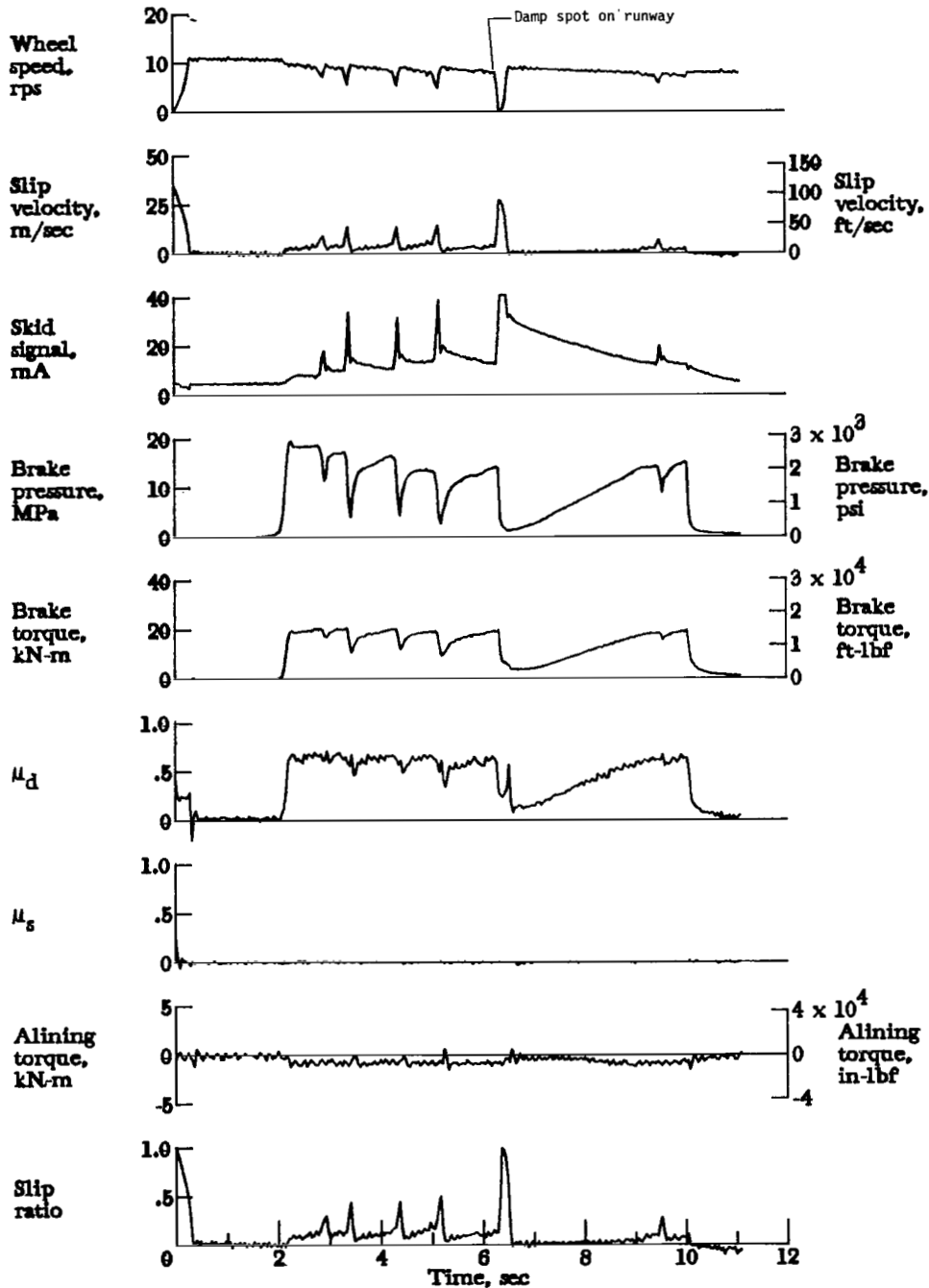


Figure A1.- Time histories for run 1. Nominal carriage speed, 54 knots; vertical load, 59.6 kN (13 400 lbf); yaw angle, 0°; brake supply pressure, 21 MPa (3000 psi); tire condition, new; surface condition, dry.

APPENDIX

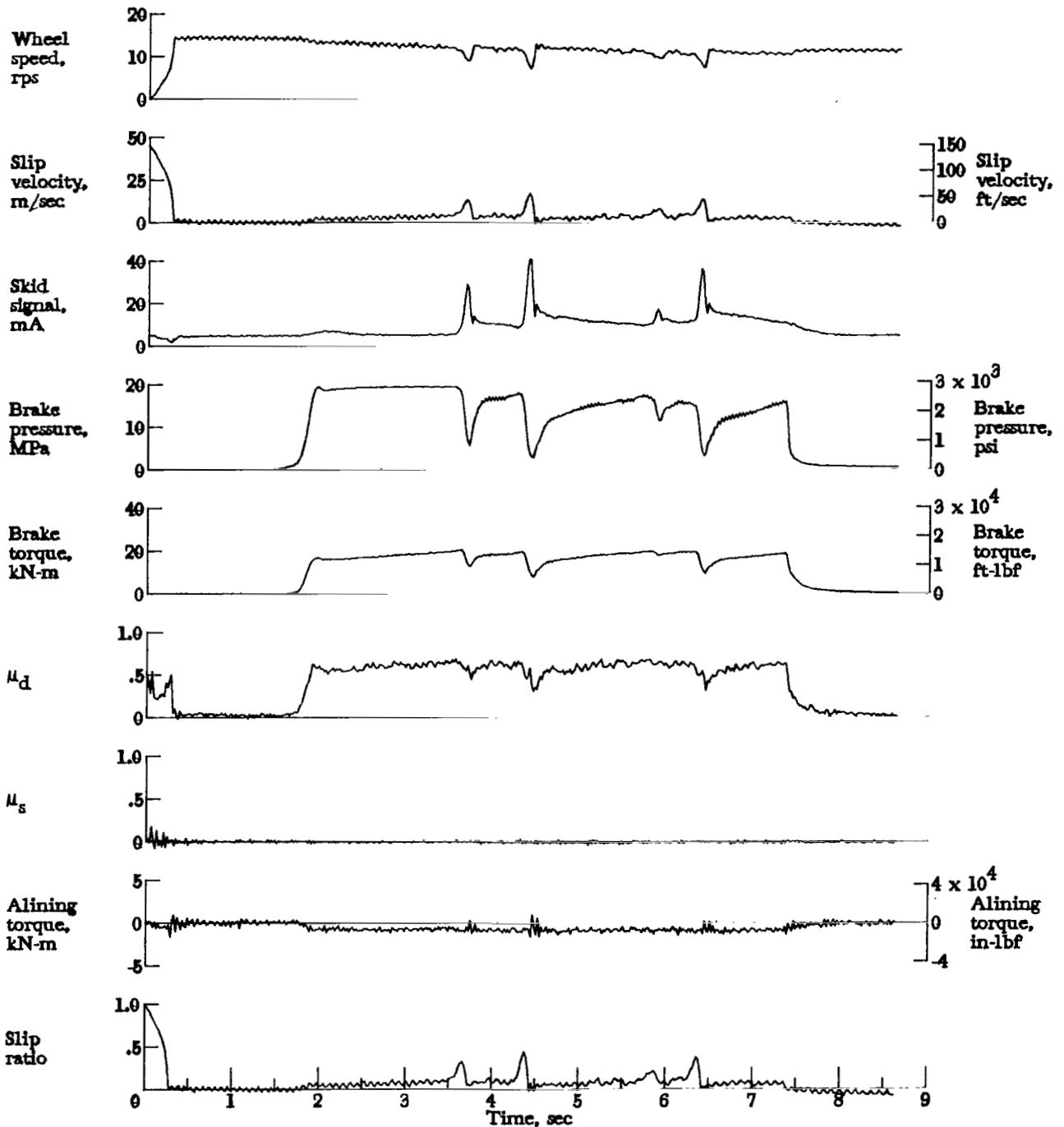


Figure A2.- Time histories for run 2. Nominal carriage speed, 74 knots; vertical load, 60.1 kN (13 500 lbf); yaw angle,  $0^\circ$ ; brake supply pressure, 21 MPa (3000 psi); tire condition, new; surface condition, dry.

APPENDIX

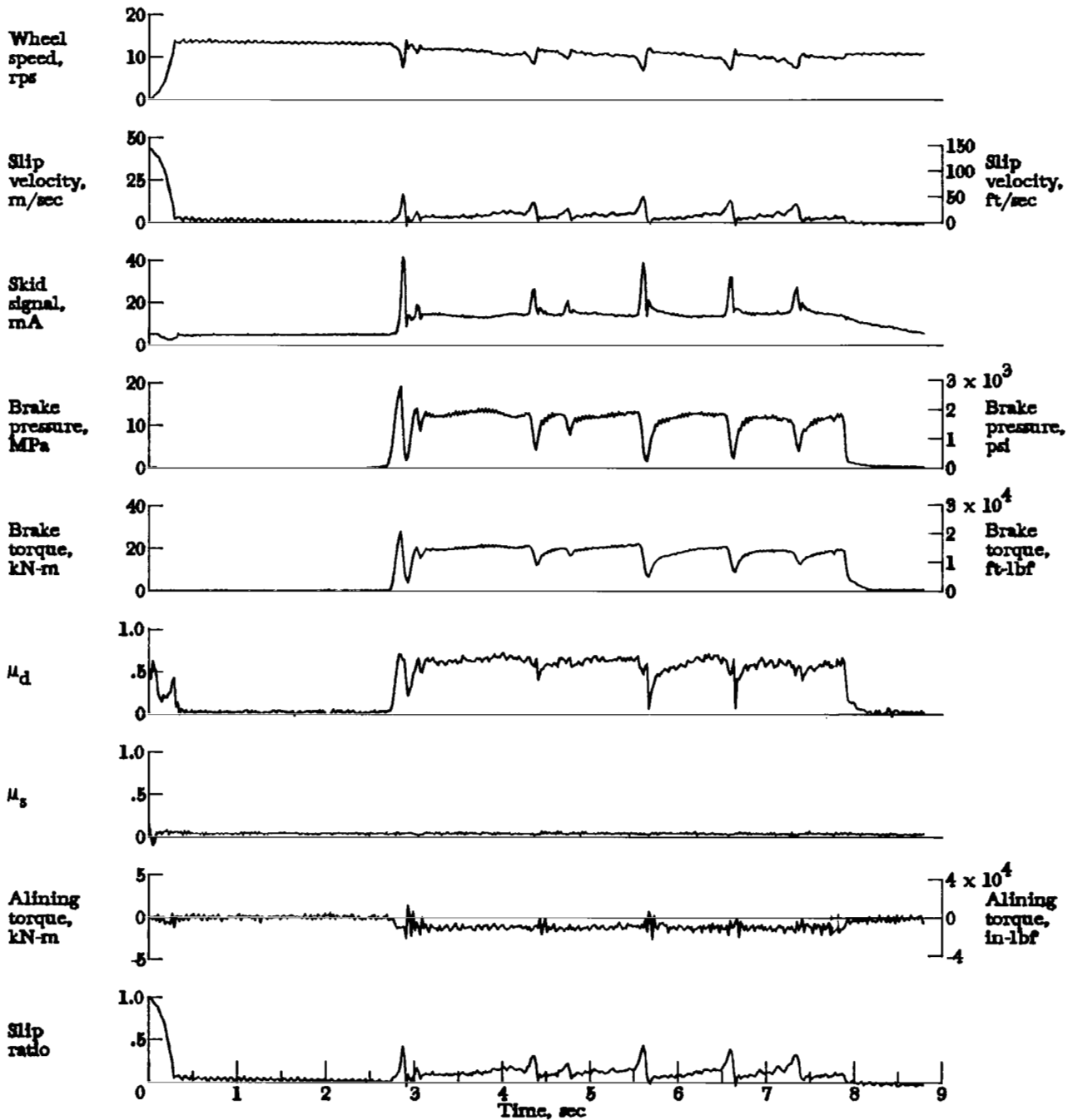


Figure A3.- Time histories for run 3. Nominal carriage speed, 70 knots; vertical load, 64.9 kN (14 600 lbf); yaw angle, 0°; brake supply pressure, 21 MPa (3000 psi); tire condition, new; surface condition, dry.

APPENDIX

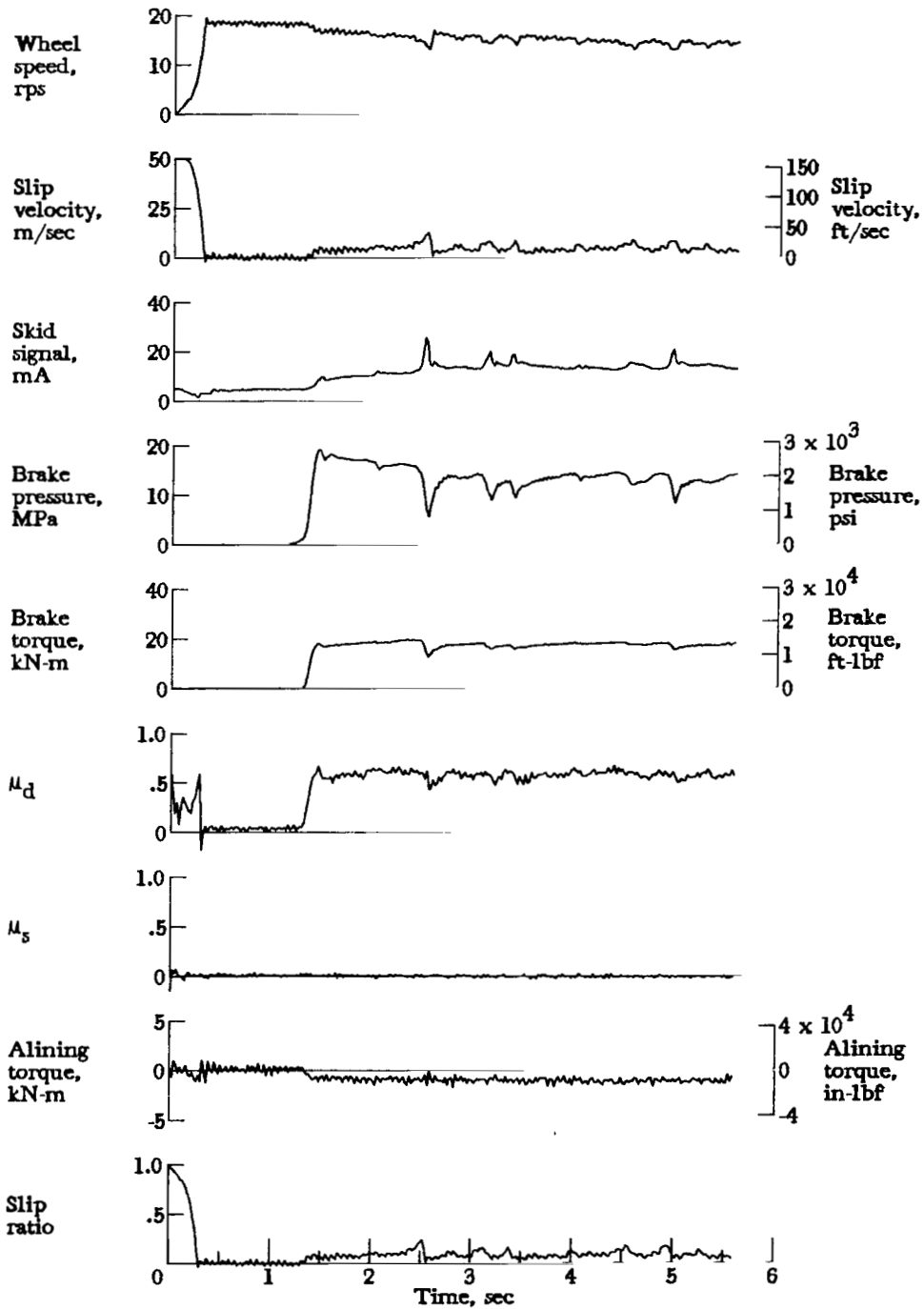


Figure A4.- Time histories for run 4. Nominal carriage speed, 99 knots; vertical load, 61.8 kN (13 900 lbf); yaw angle, 0°; brake supply pressure, 21 MPa (3000 psi); tire condition, new; surface condition, dry.

APPENDIX

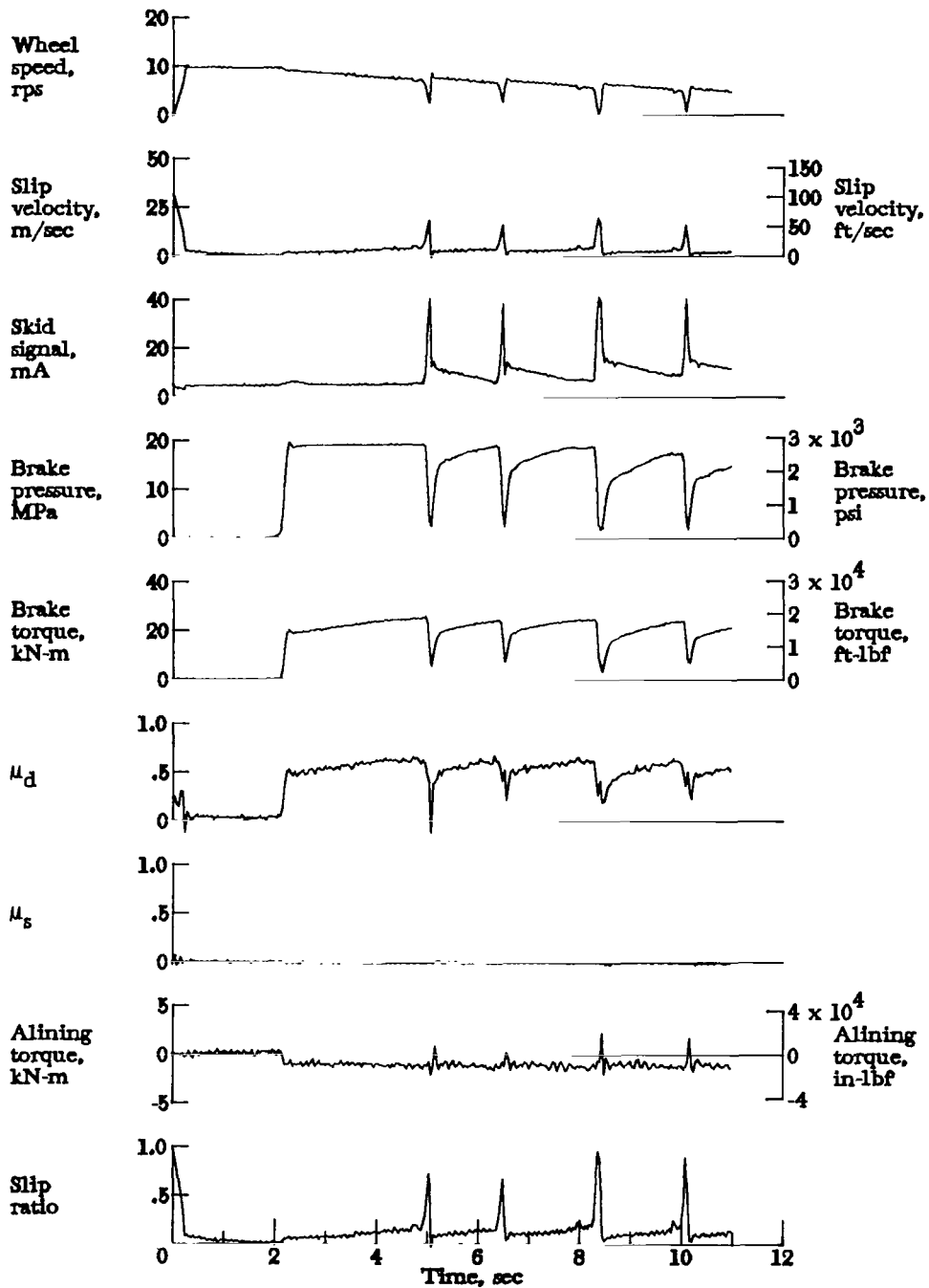


Figure A5.- Time histories for run 5. Nominal carriage speed, 43 knots; vertical load, 83.6 kN (18 800 lbf); yaw angle,  $0^\circ$ ; brake supply pressure, 20 MPa (2900 psi); tire condition, new; surface condition, dry.

APPENDIX

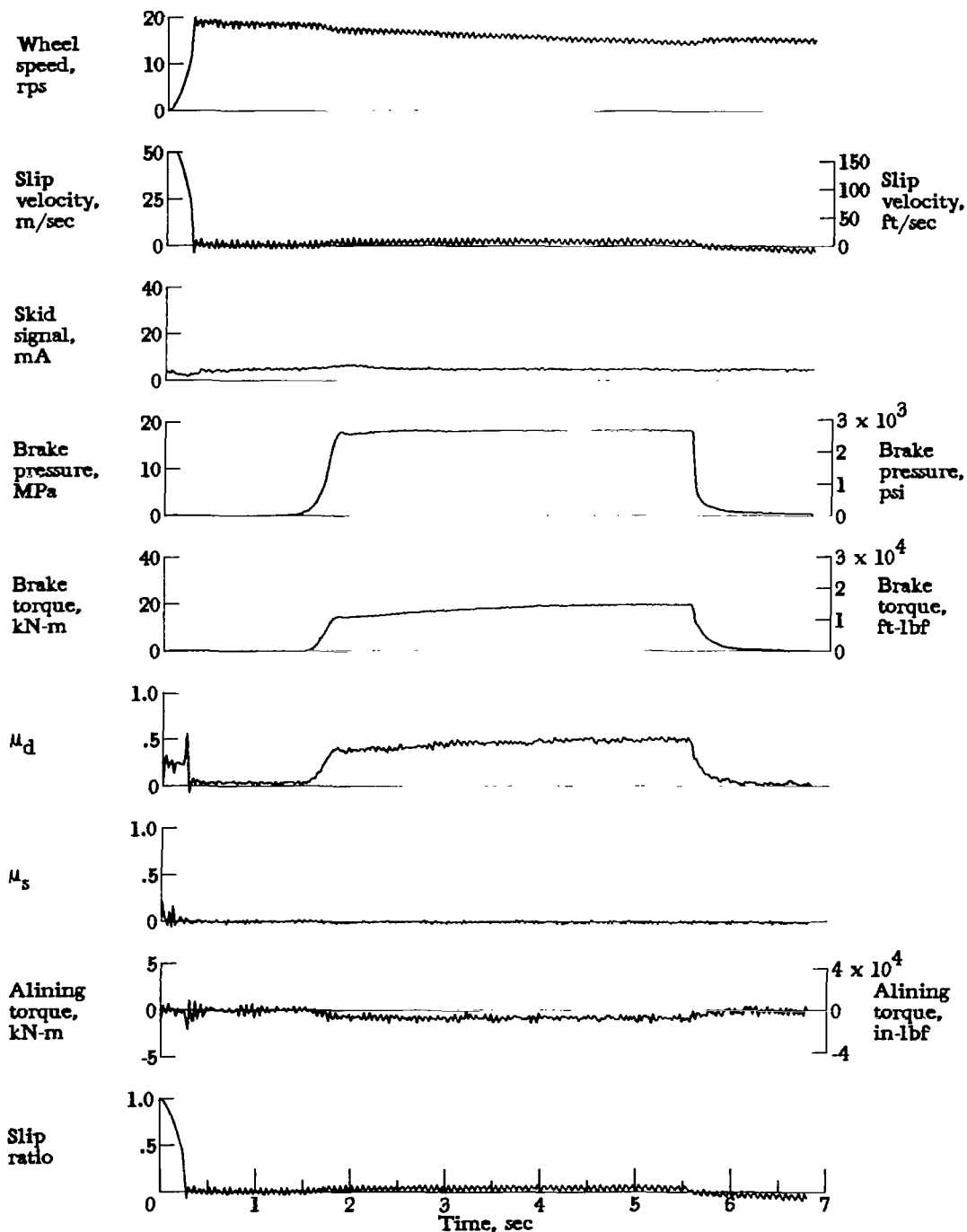


Figure A6.- Time histories for run 6. Nominal carriage speed, 99 knots; vertical load, 82.7 kN (18 600 lbf); yaw angle, 0°; brake supply pressure, 19 MPa (2800 psi); tire condition, new; surface condition, dry.

APPENDIX

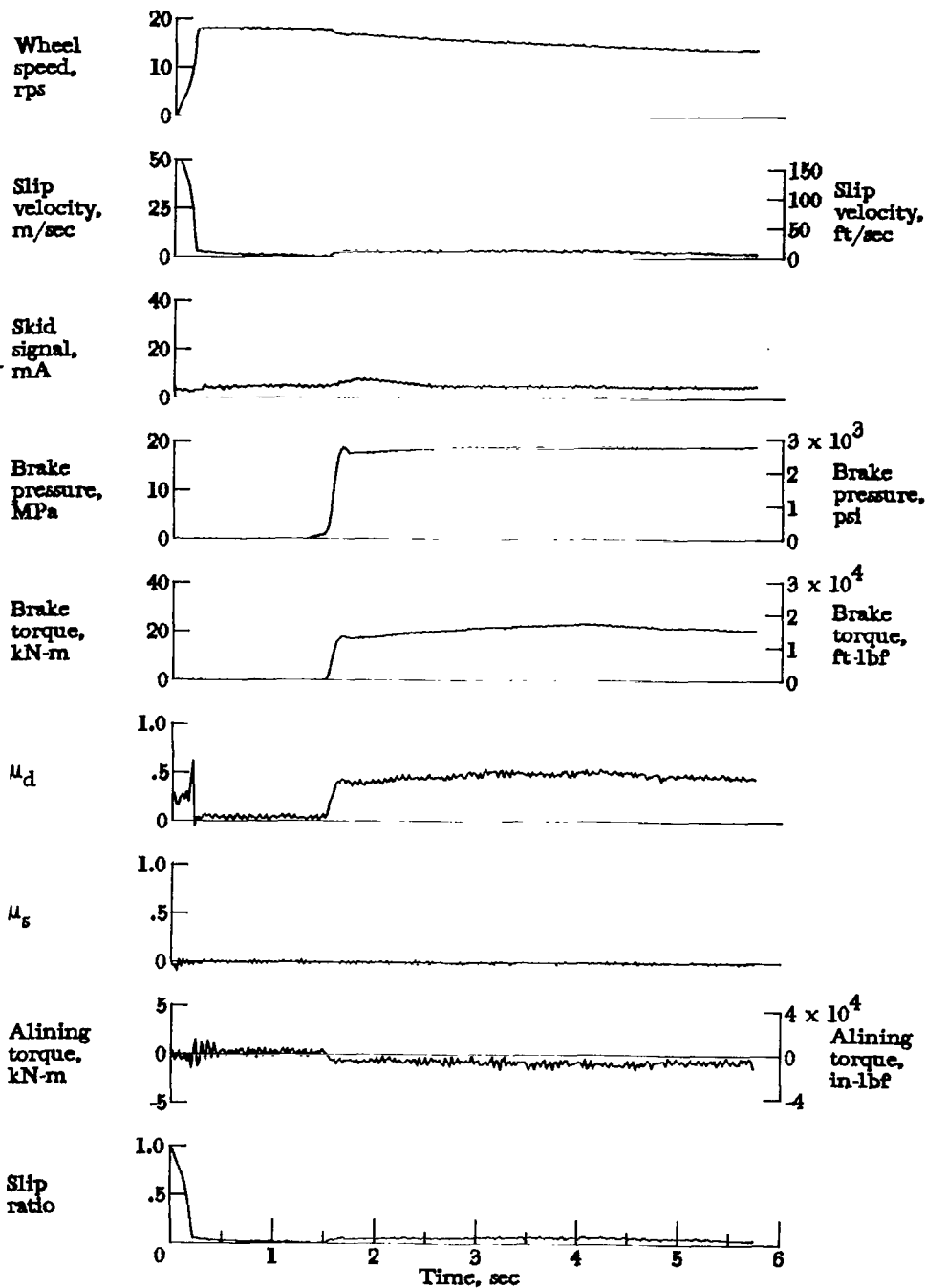


Figure A7.- Time histories for run 7. Nominal carriage speed, 94 knots; vertical load, 97.0 kN (21 800 lbf); yaw angle, 0°; brake supply pressure, 20 MPa (2900 psi); tire condition, new; surface condition, dry.

APPENDIX

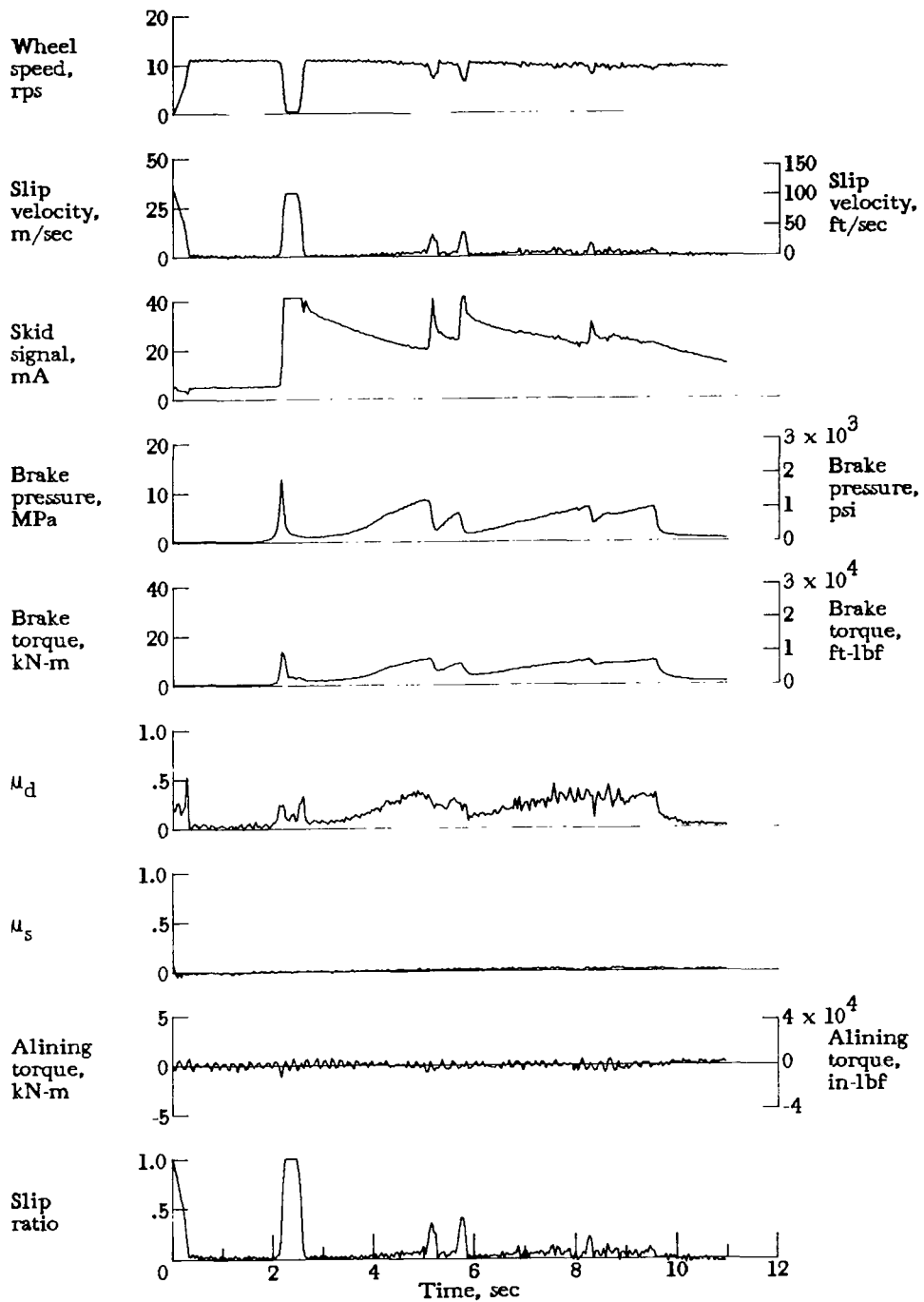


Figure A8.- Time histories for run 8. Nominal carriage speed, 56 knots; vertical load, 59.6 kN (13 400 lbf); yaw angle,  $0^\circ$ ; brake supply pressure, 21 MPa (3000 psi); tire condition, new; surface condition, damp.

APPENDIX

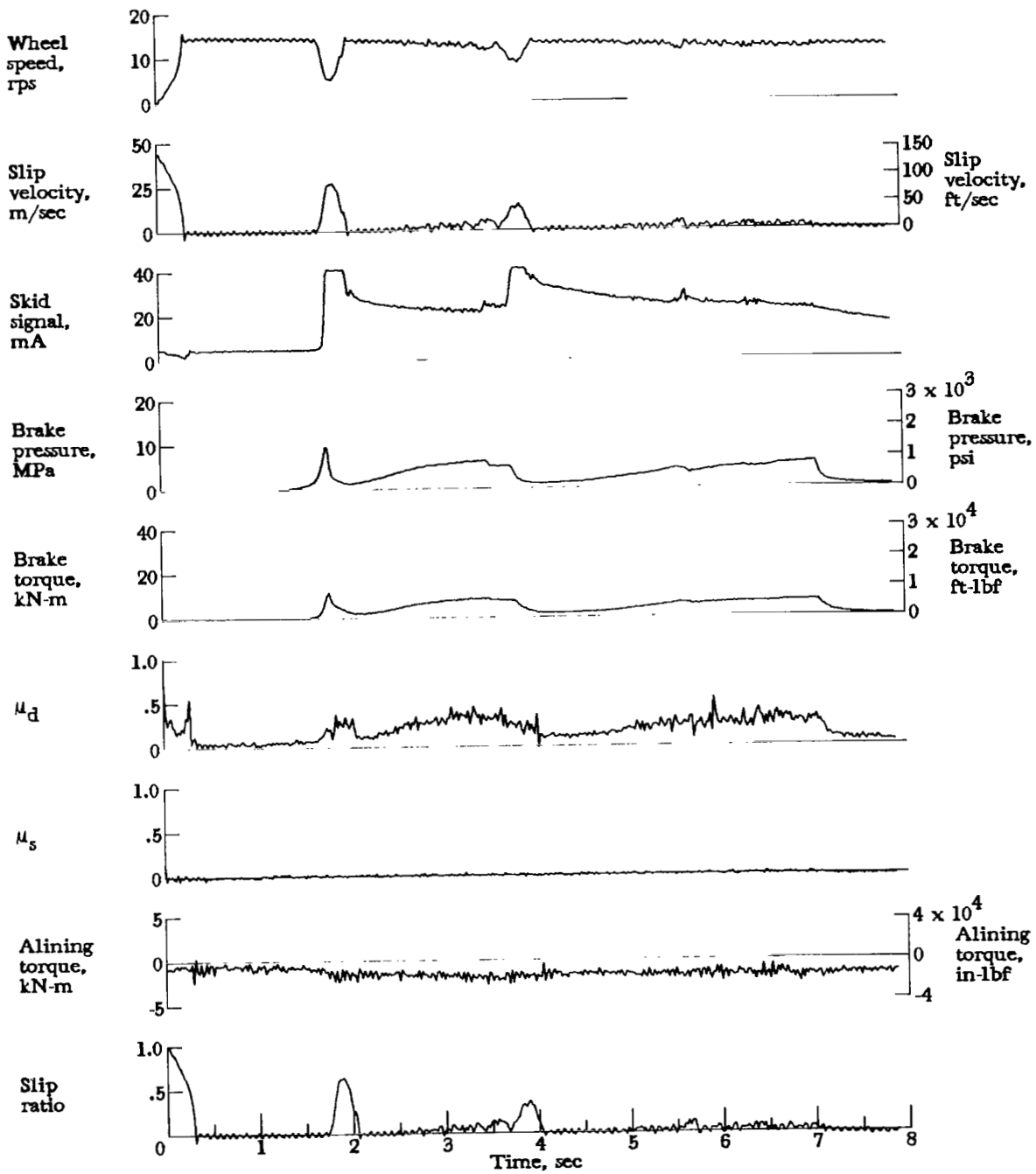


Figure A9.- Time histories for run 9. Nominal carriage speed, 77 knots; vertical load, 59.6 kN (13 400 lbf); yaw angle,  $0^\circ$ ; brake supply pressure, 21 MPa (3000 psi); tire condition, new; surface condition, damp.

APPENDIX

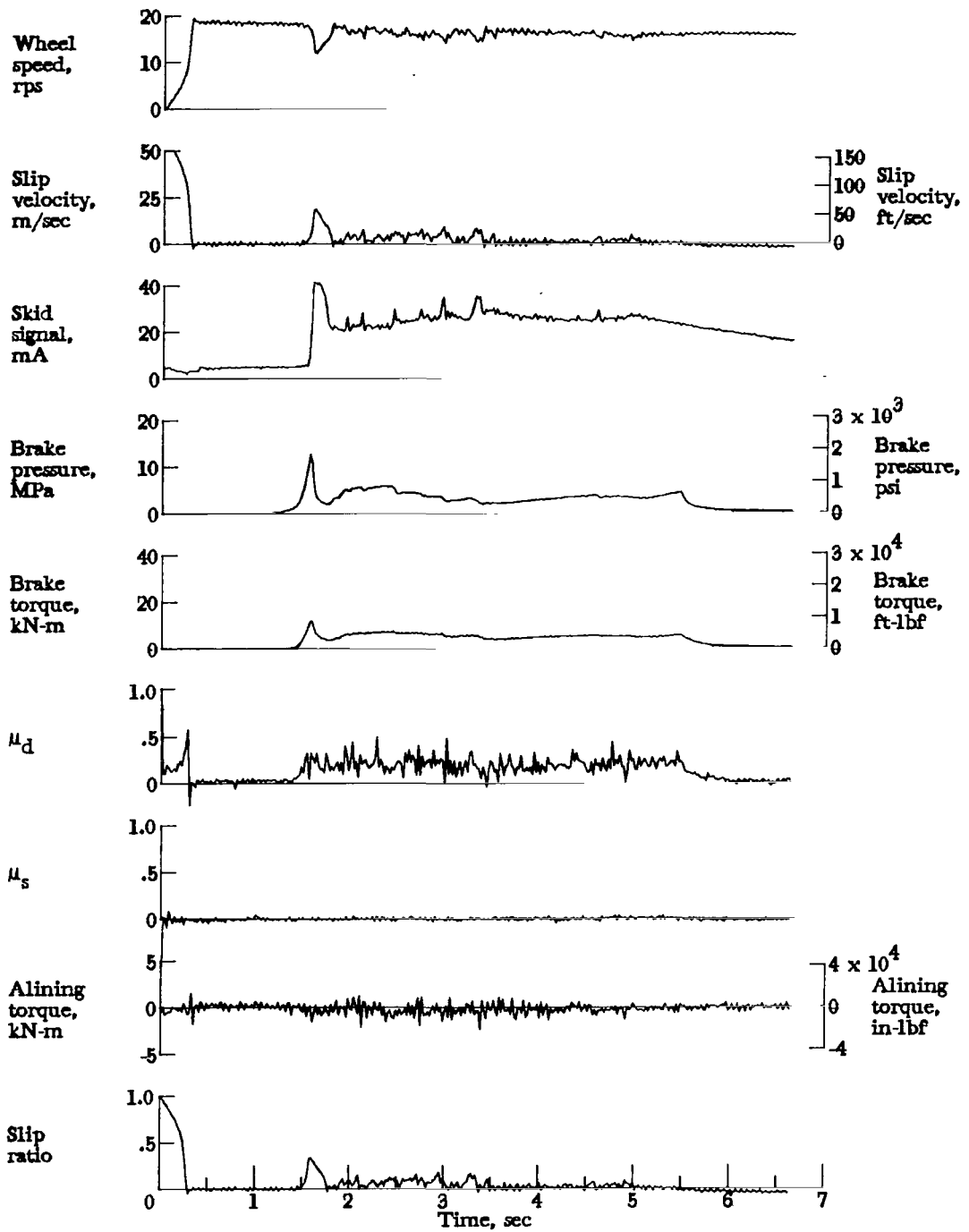


Figure A10.- Time histories for run 10. Nominal carriage speed, 101 knots; vertical load, 59.2 kN (13 300 lbf); yaw angle,  $0^\circ$ ; brake supply pressure, 20 MPa (2900 psi); tire condition, new; surface condition, damp.

APPENDIX

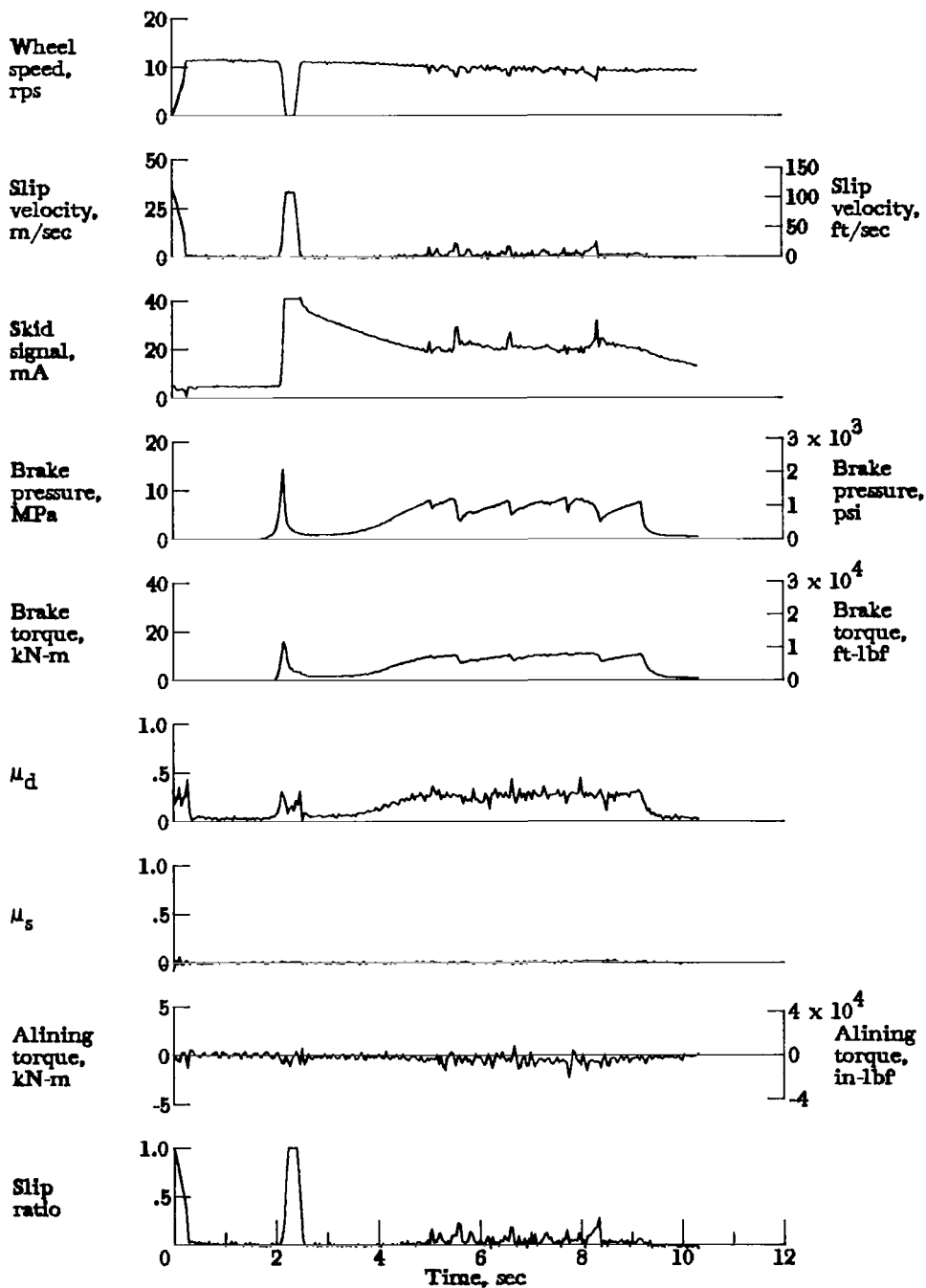


Figure A11.- Time histories for run 11. Nominal carriage speed, 60 knots; vertical load, 82.3 kN (18 500 lbf); yaw angle, 0°; brake supply pressure, 20 MPa (2900 psi); tire condition, new; surface condition, damp.

APPENDIX

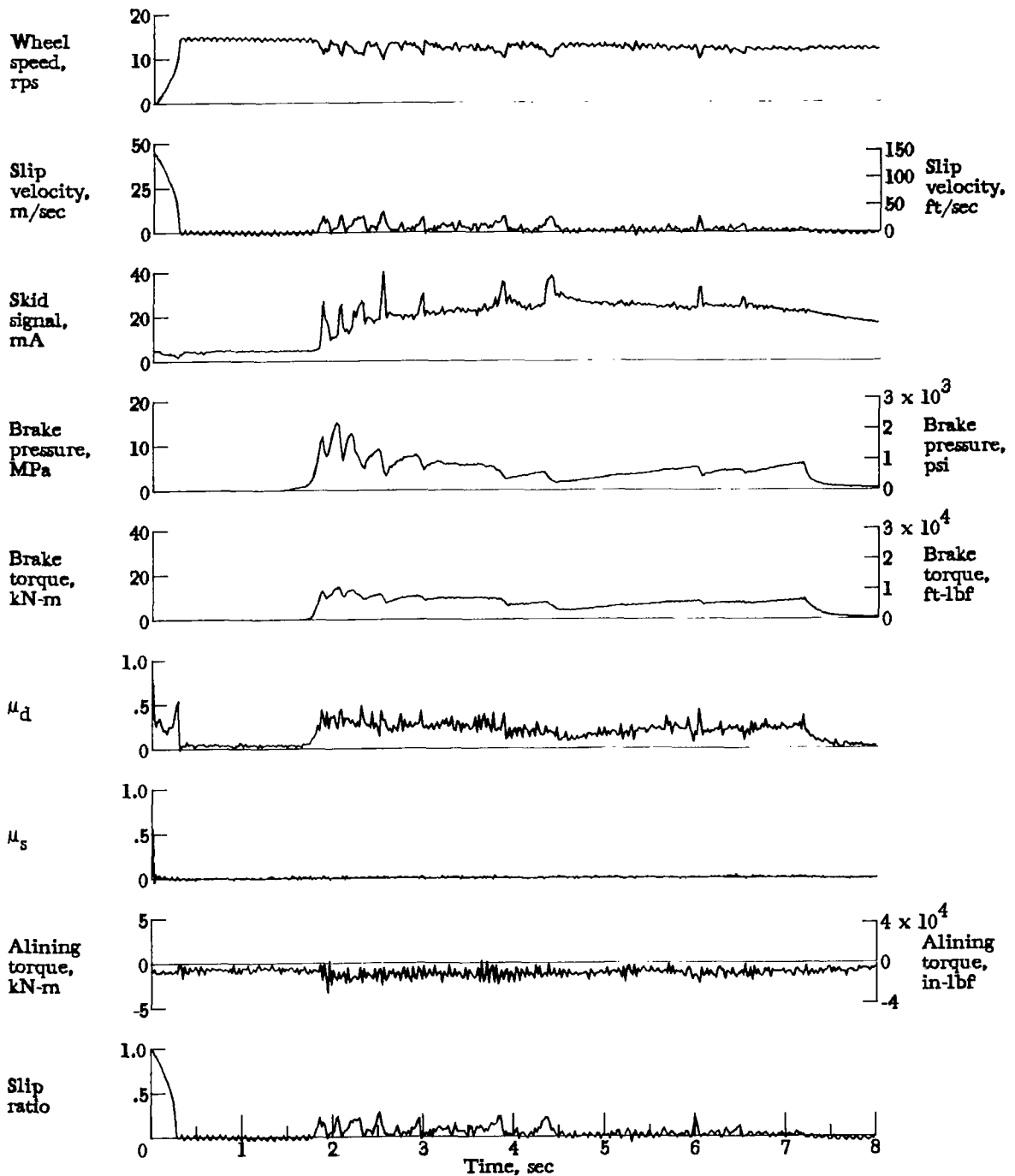


Figure A12.- Time histories for run 12. Nominal carriage speed, 77 knots; vertical load, 82.7 kN (18 600 lbf); yaw angle,  $0^\circ$ ; brake supply pressure, 21 MPa (3000 psi); tire condition, new; surface condition, damp.

APPENDIX

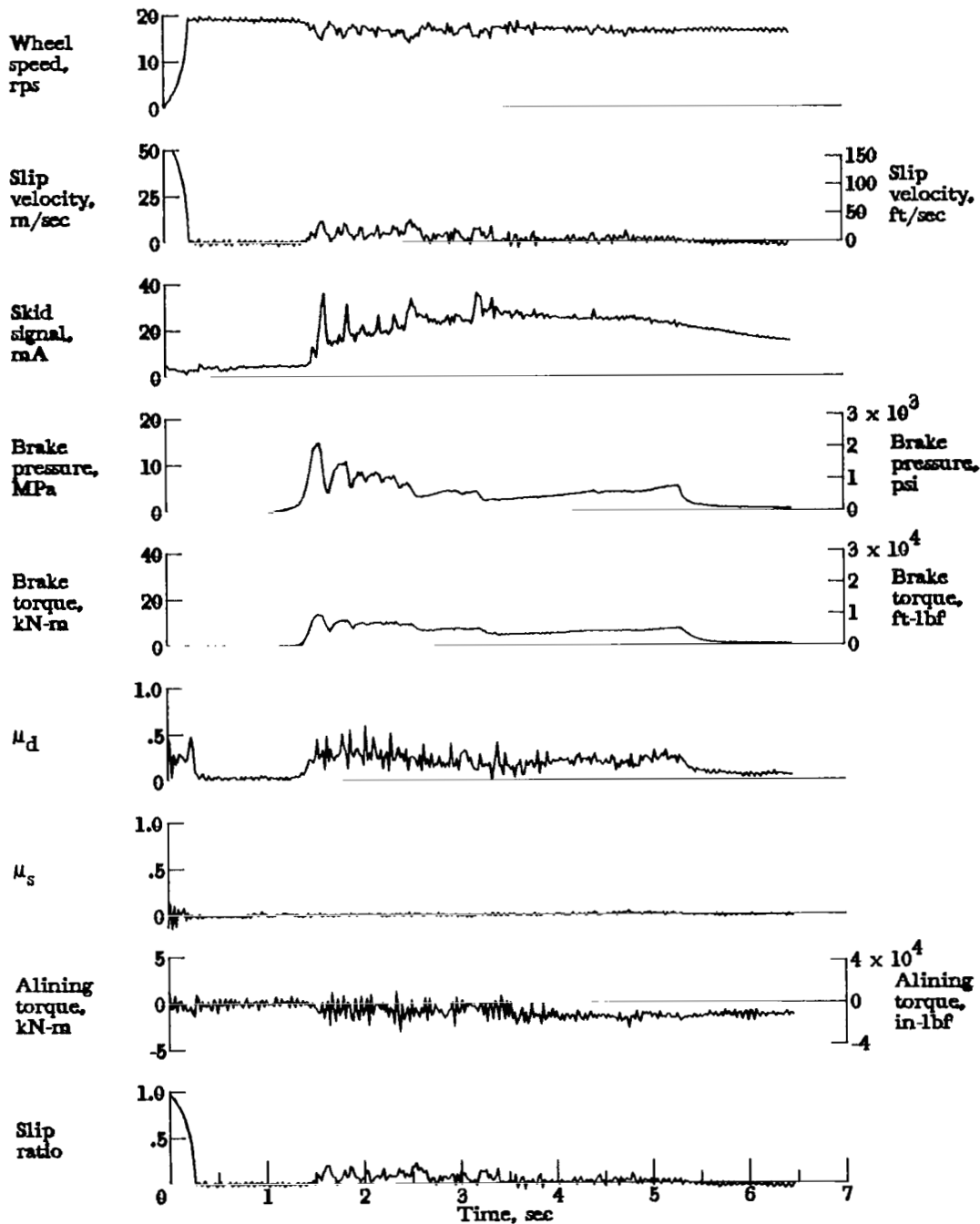


Figure A13.- Time histories for run 13. Nominal carriage speed, 104 knots; vertical load, 82.3 kN (18 500 lbf); yaw angle,  $0^\circ$ ; brake supply pressure, 21 MPa (3000 psi); tire condition, new; surface condition, damp.

APPENDIX

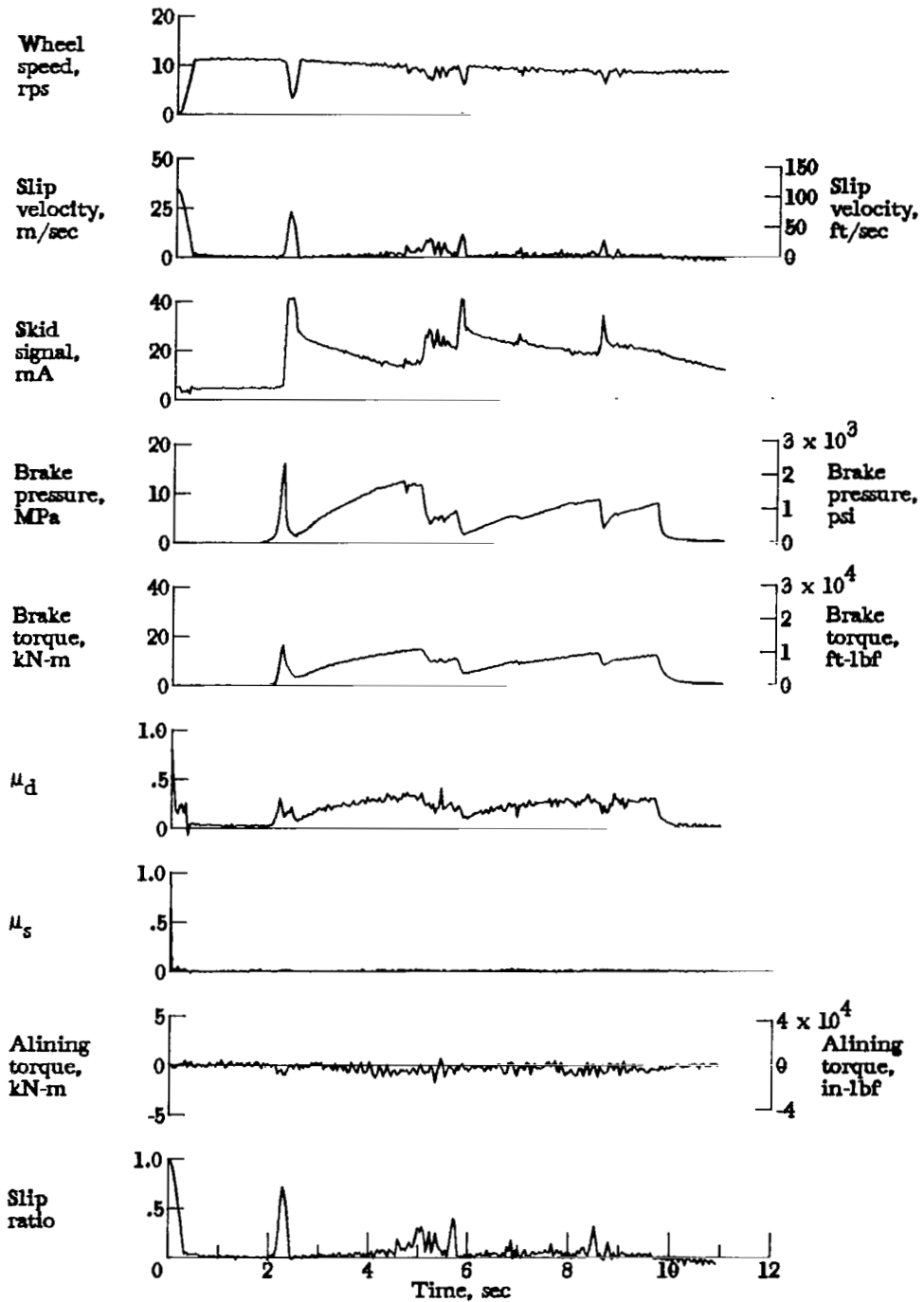


Figure A14.- Time histories for run 14. Nominal carriage speed, 56 knots; vertical load, 97.4 kN (21 900 lbf); yaw angle,  $0^\circ$ ; brake supply pressure, 21 MPa (3000 psi); tire condition, new; surface condition, damp.

APPENDIX

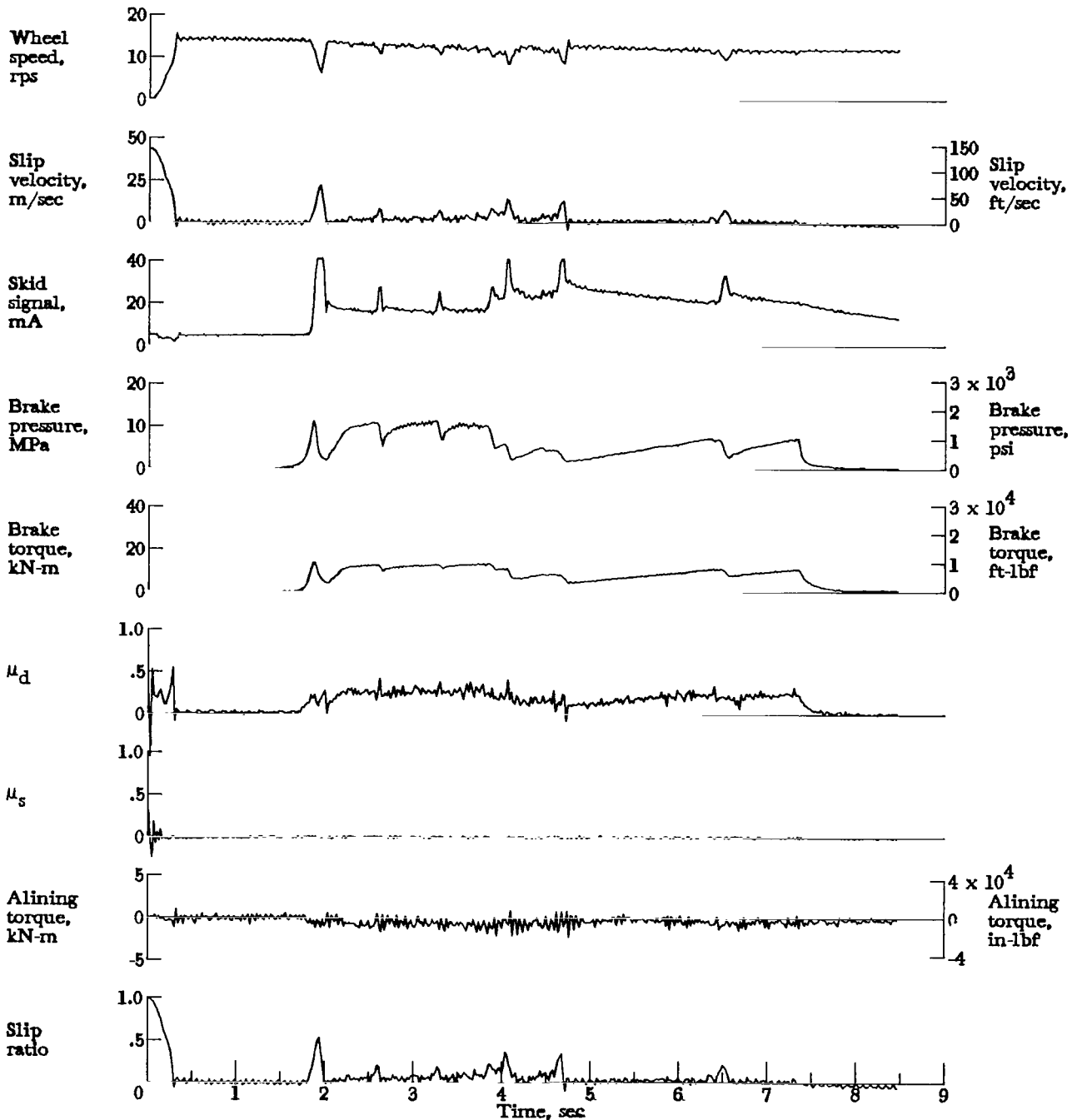


Figure A15.- Time histories for run 15. Nominal carriage speed, 75 knots; vertical load, 97.4 kN (21 900 lbf); yaw angle,  $0^\circ$ ; brake supply pressure, 21 MPa (3000 psi); tire condition, new; surface condition, damp.

APPENDIX

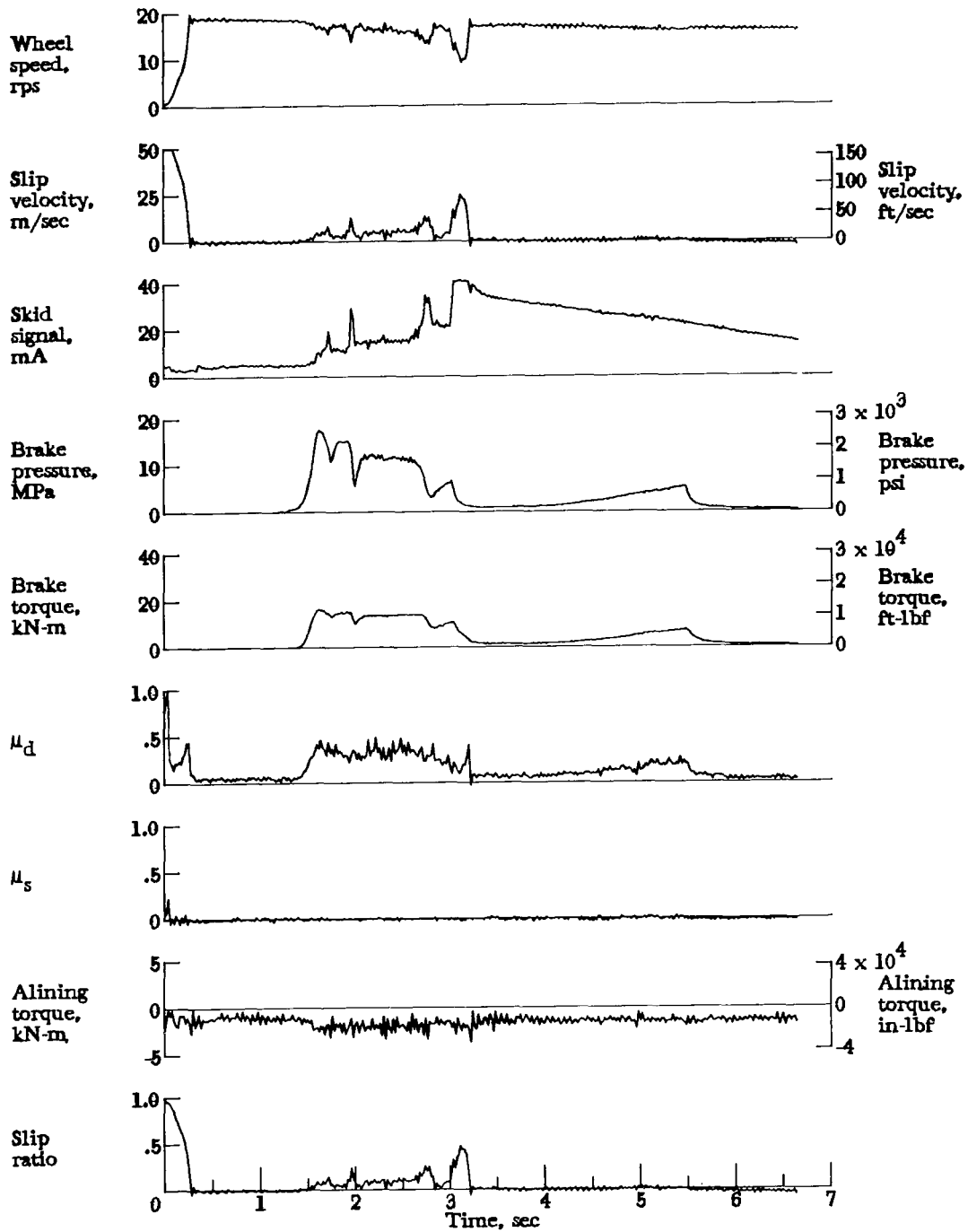


Figure A16.- Time histories for run 16. Nominal carriage speed, 101 knots; vertical load, 97.4 kN (21 900 lbf); yaw angle, 0°; brake supply pressure, 21 MPa (3000 psi); tire condition, new; surface condition, damp.

APPENDIX

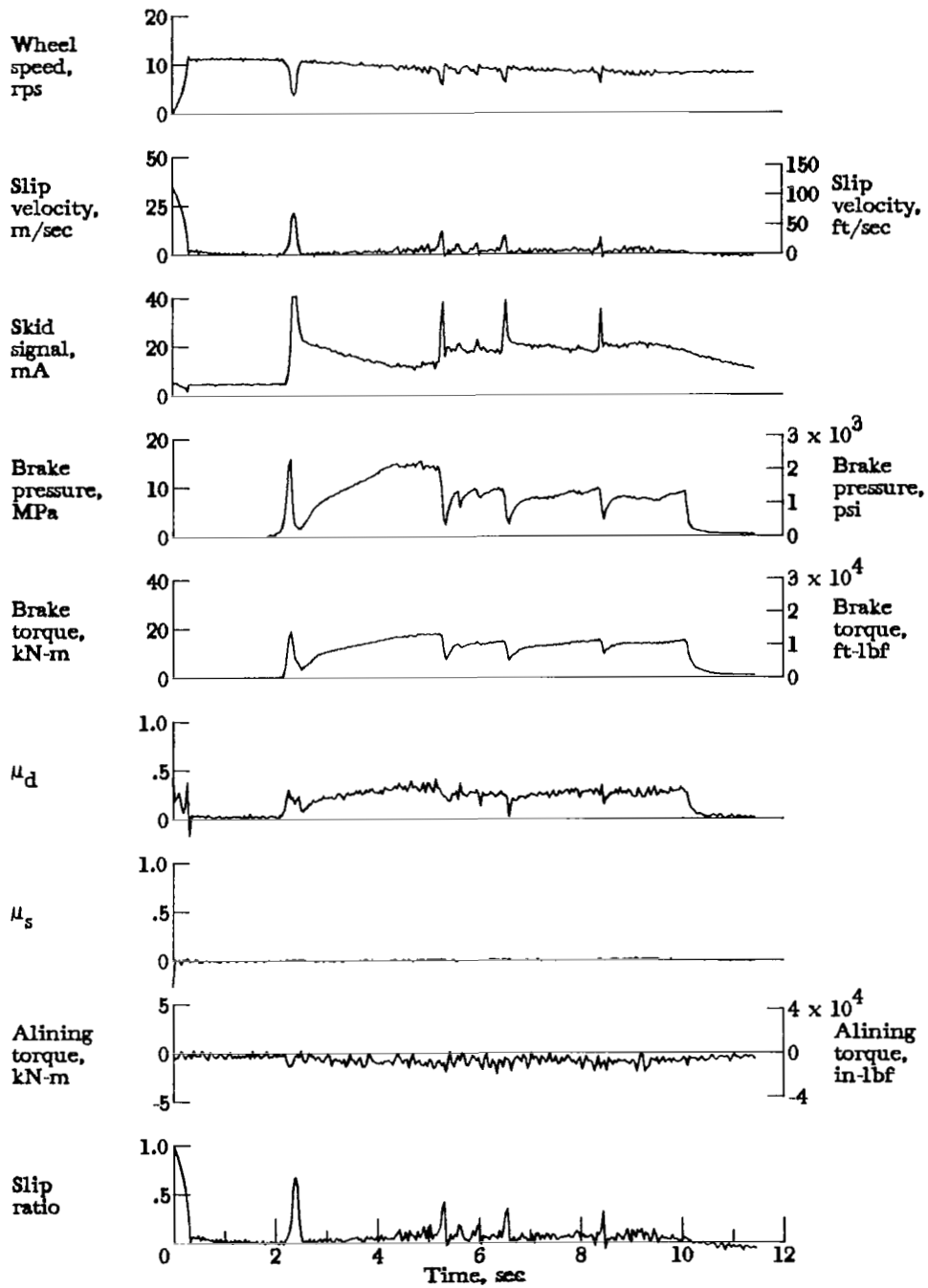


Figure A17.- Time histories for run 17. Nominal carriage speed, 55 knots; vertical load, 120.1 kN (27 000 lbf); yaw angle,  $0^\circ$ ; brake supply pressure, 21 MPa (3000 psi); tire condition, new; surface condition, damp.

APPENDIX

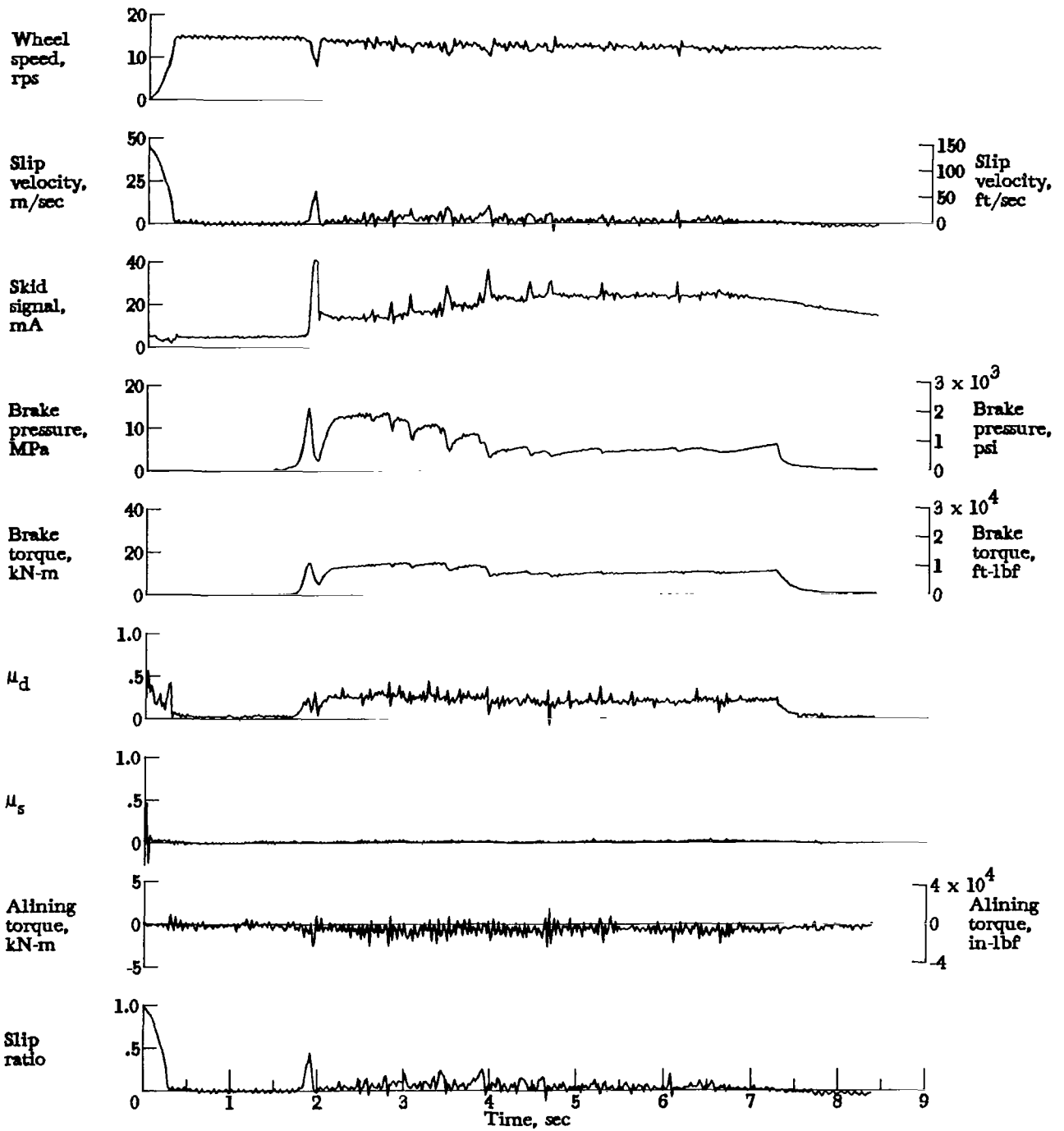


Figure A18.- Time histories for run 18. Nominal carriage speed, 76 knots; vertical load, 120.1 kN (27 000 lbf); yaw angle, 0°; brake supply pressure, 20 MPa (2900 psi); tire condition, new; surface condition, damp.

APPENDIX

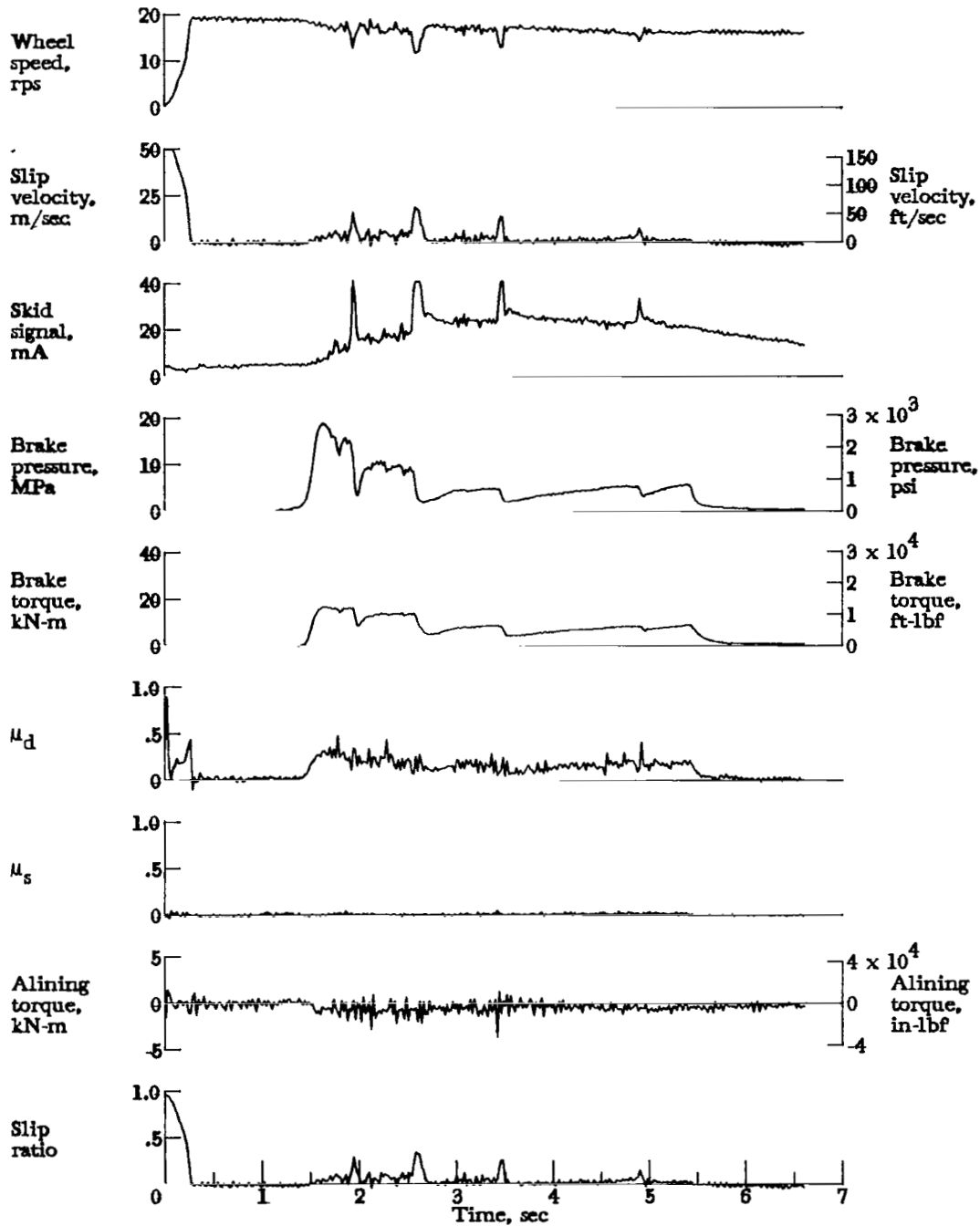


Figure A19.- Time histories for run 19. Nominal carriage speed, 102 knots; vertical load, 120.1 kN (27 000 lbf); yaw angle,  $0^\circ$ ; brake supply pressure, 20 MPa (2900 psi); tire condition, new; surface condition, damp.

APPENDIX

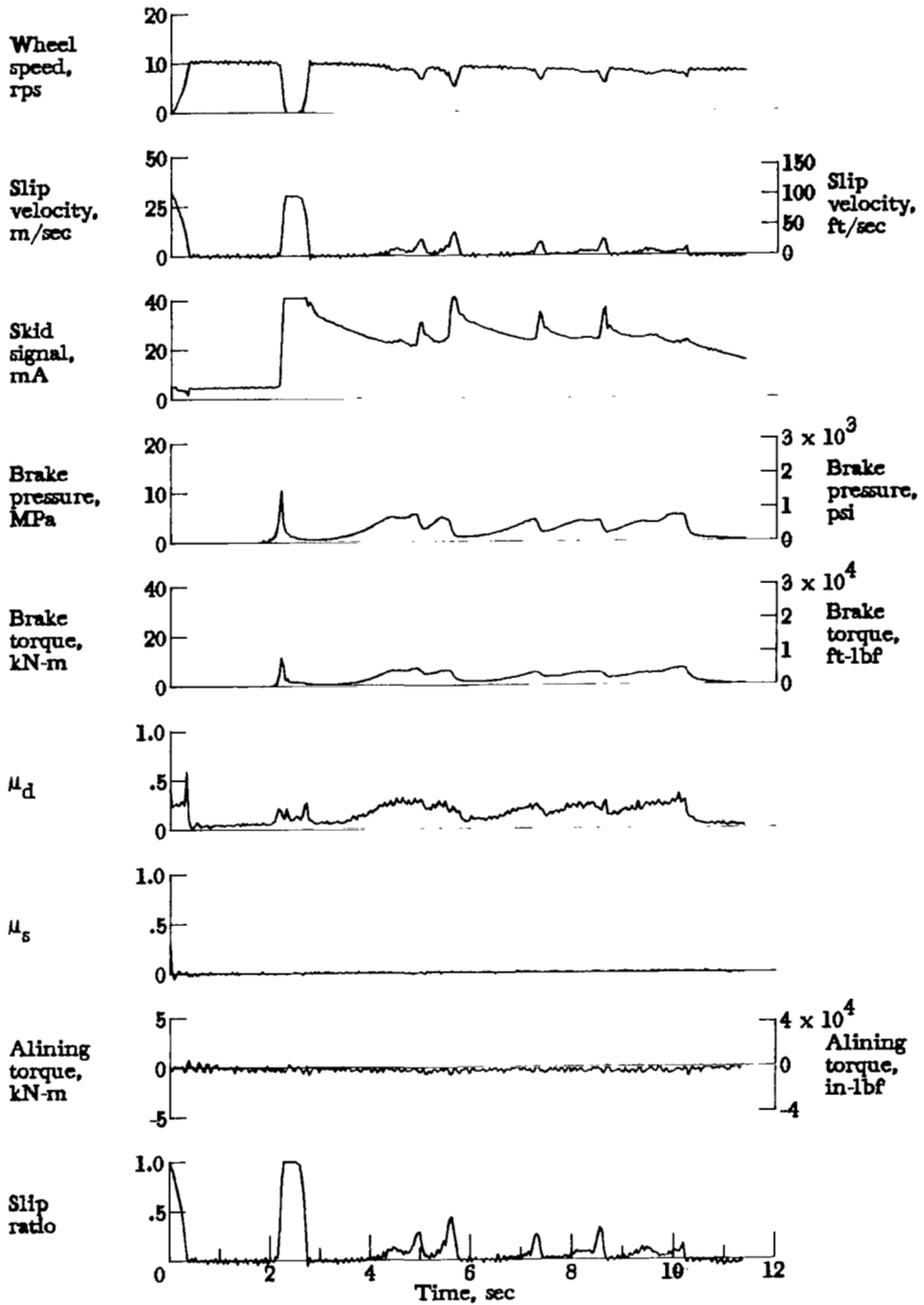


Figure A20.- Time histories for run 20. Nominal carriage speed, 53 knots; vertical load, 58.7 kN (13 200 lbf); yaw angle, 0°; brake supply pressure, 20 MPa (2900 psi); tire condition, new; surface condition, flooded.

APPENDIX

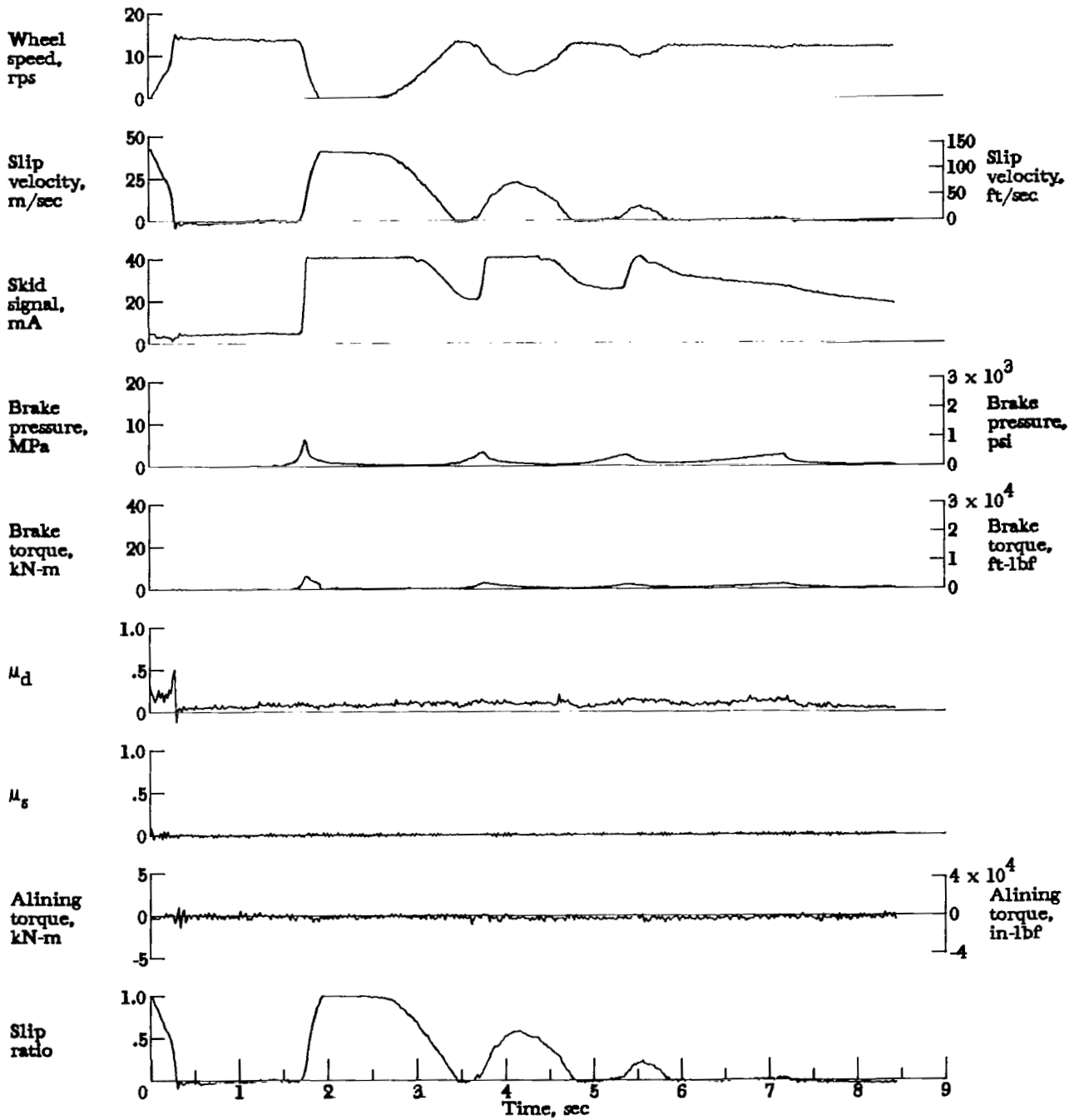


Figure A21.- Time histories for run 21. Nominal carriage speed, 75 knots; vertical load, 59.2 kN (13 300 lbf); yaw angle,  $0^\circ$ ; brake supply pressure, 21 MPa (3000 psi); tire condition, new; surface condition, flooded.

APPENDIX

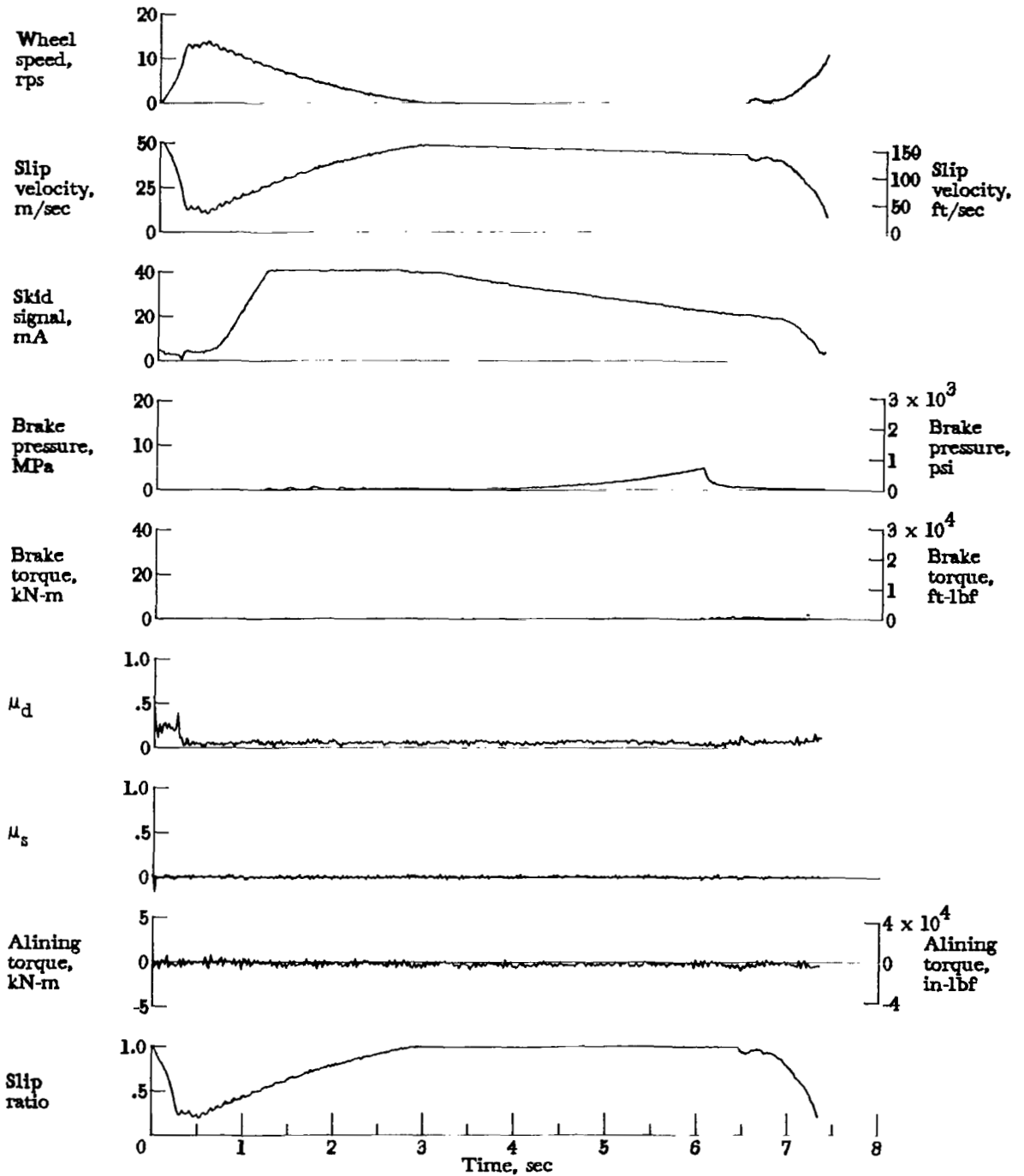


Figure A22.- Time histories for run 22. Nominal carriage speed, 93 knots; vertical load, 58.7 kN (13 200 lbf); yaw angle,  $0^\circ$ ; brake supply pressure, 21 MPa (3000 psi); tire condition, new; surface condition, flooded.

APPENDIX

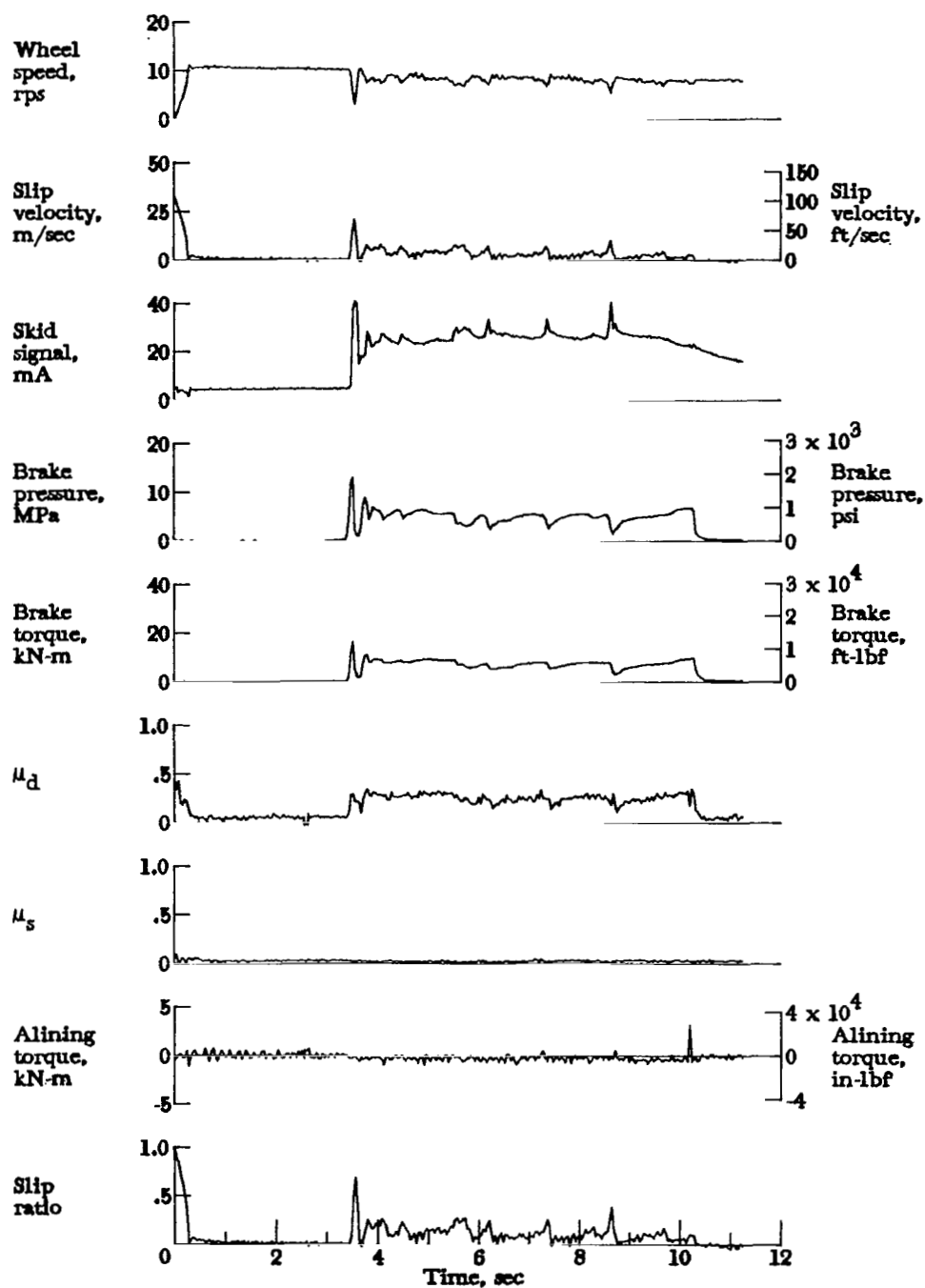


Figure A23.- Time histories for run 23. Nominal carriage speed, 53 knots; vertical load, 77.8 kN (17 500 lbf); yaw angle, 0°; brake supply pressure, 21 MPa (3000 psi); tire condition, new; surface condition, flooded.

APPENDIX

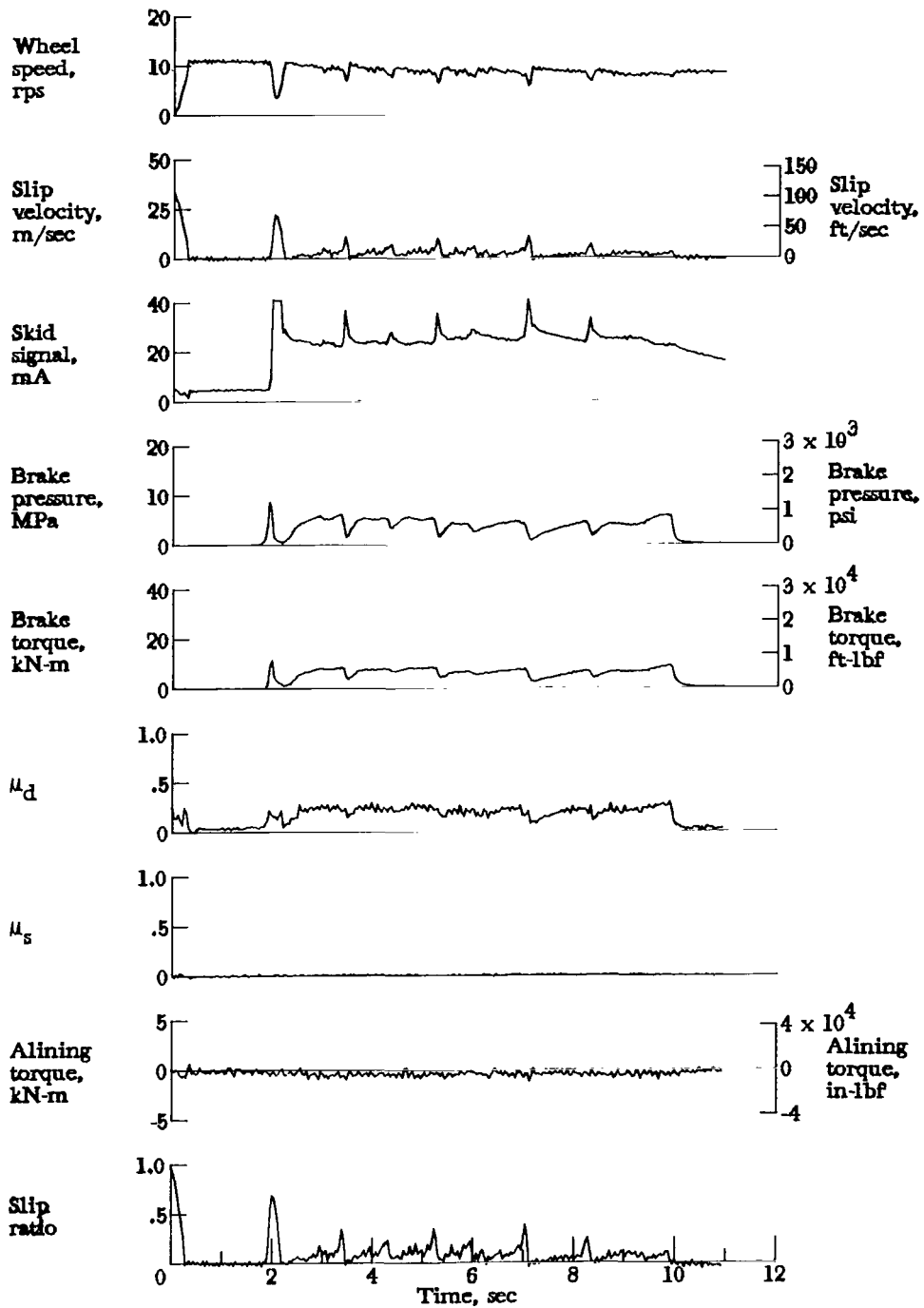


Figure A24.- Time histories for run 24. Nominal carriage speed, 56 knots; vertical load, 81.0 kN (18 200 lbf); yaw angle,  $0^\circ$ ; brake supply pressure, 21 MPa (3000 psi); tire condition, new; surface condition, flooded.

APPENDIX

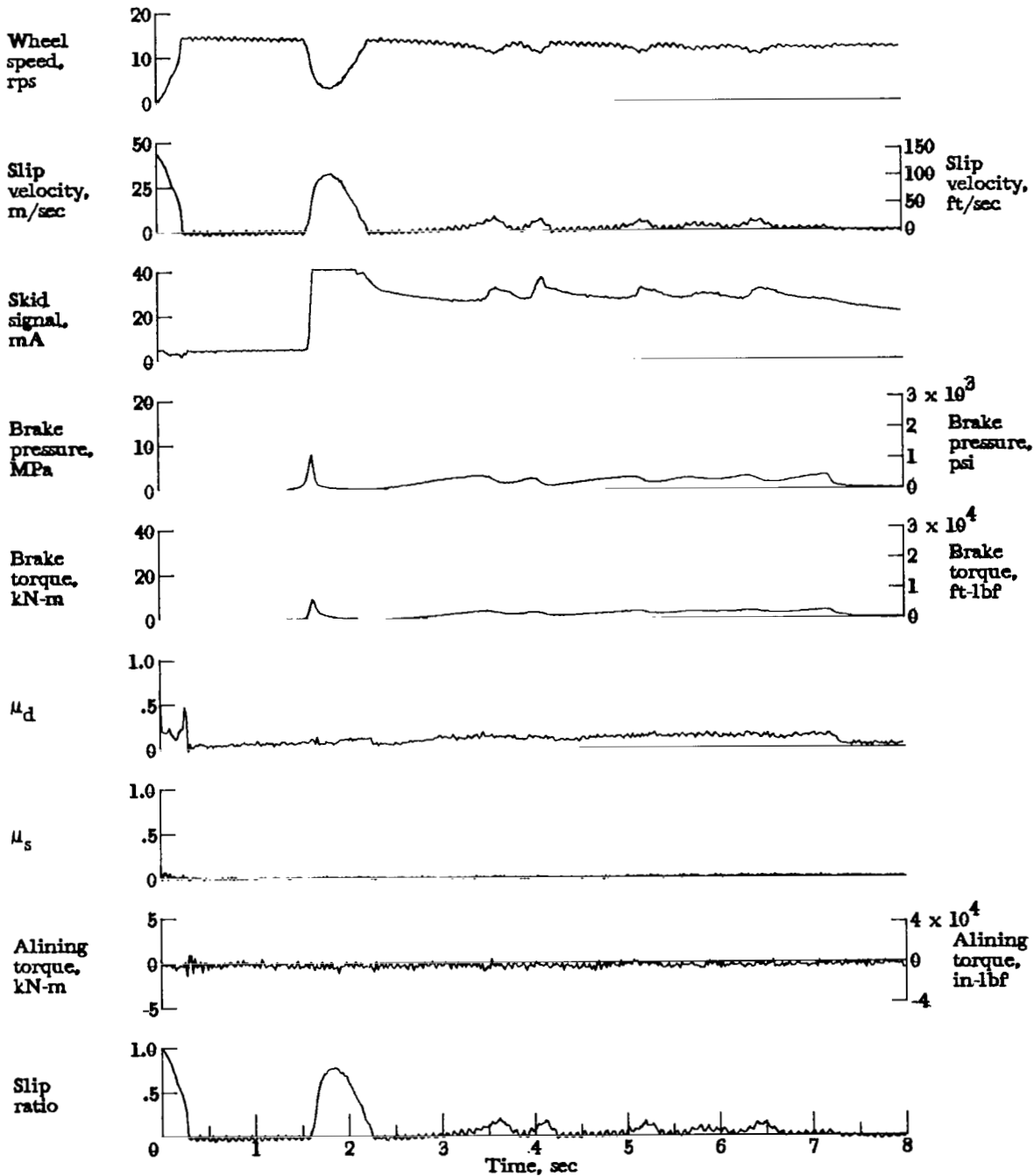


Figure A25.- Time histories for run 25. Nominal carriage speed, 76 knots; vertical load, 81.0 kN (18 200 lbf); yaw angle, 0°; brake supply pressure, 21 MPa (3000 psi); tire condition, new; surface condition, flooded.

APPENDIX

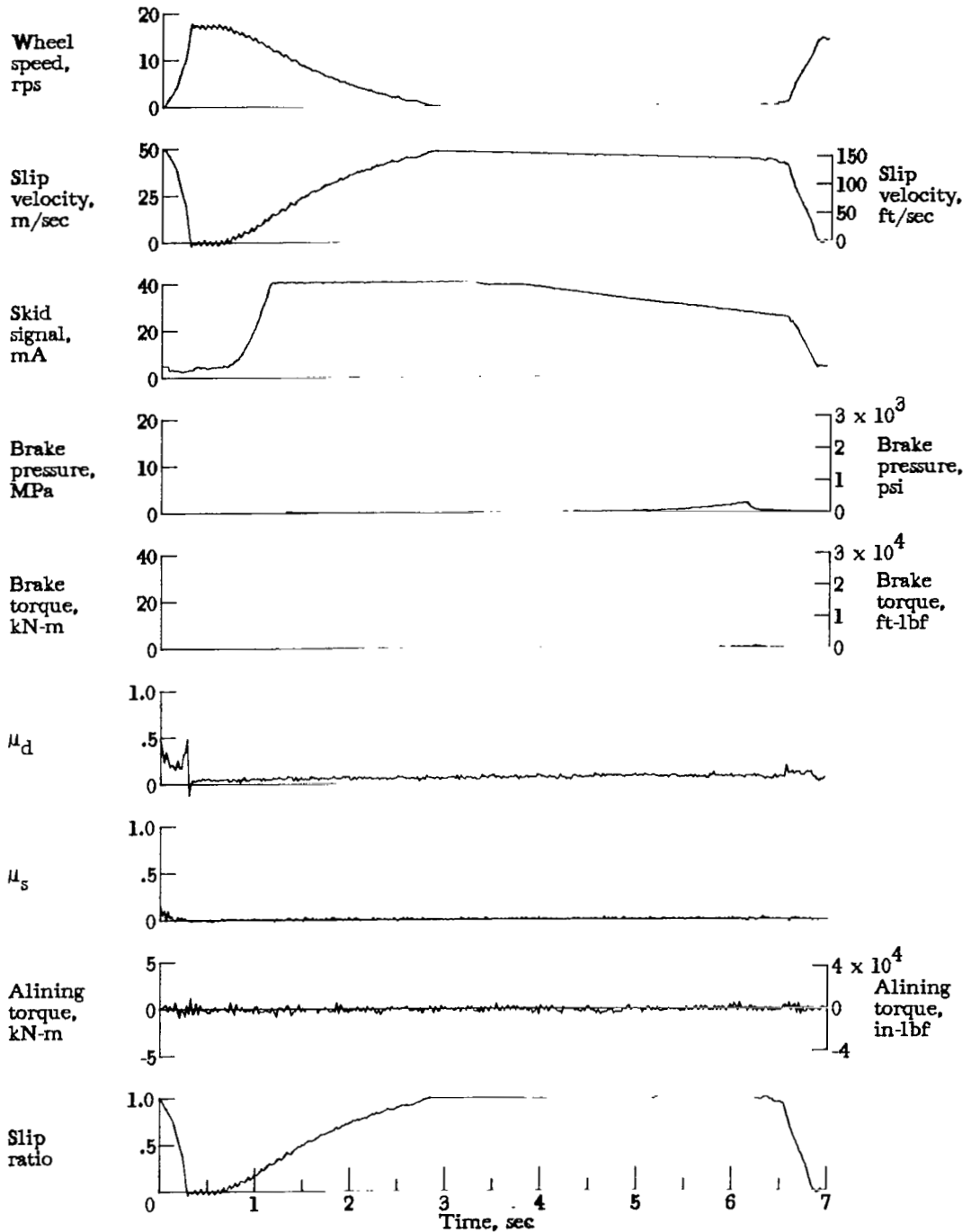


Figure A26.- Time histories for run 26. Nominal carriage speed, 92 knots; vertical load, 80.5 kN (18 100 lbf); yaw angle,  $0^\circ$ ; brake supply pressure, 21 MPa (3000 psi); tire condition, new; surface condition, flooded.

APPENDIX

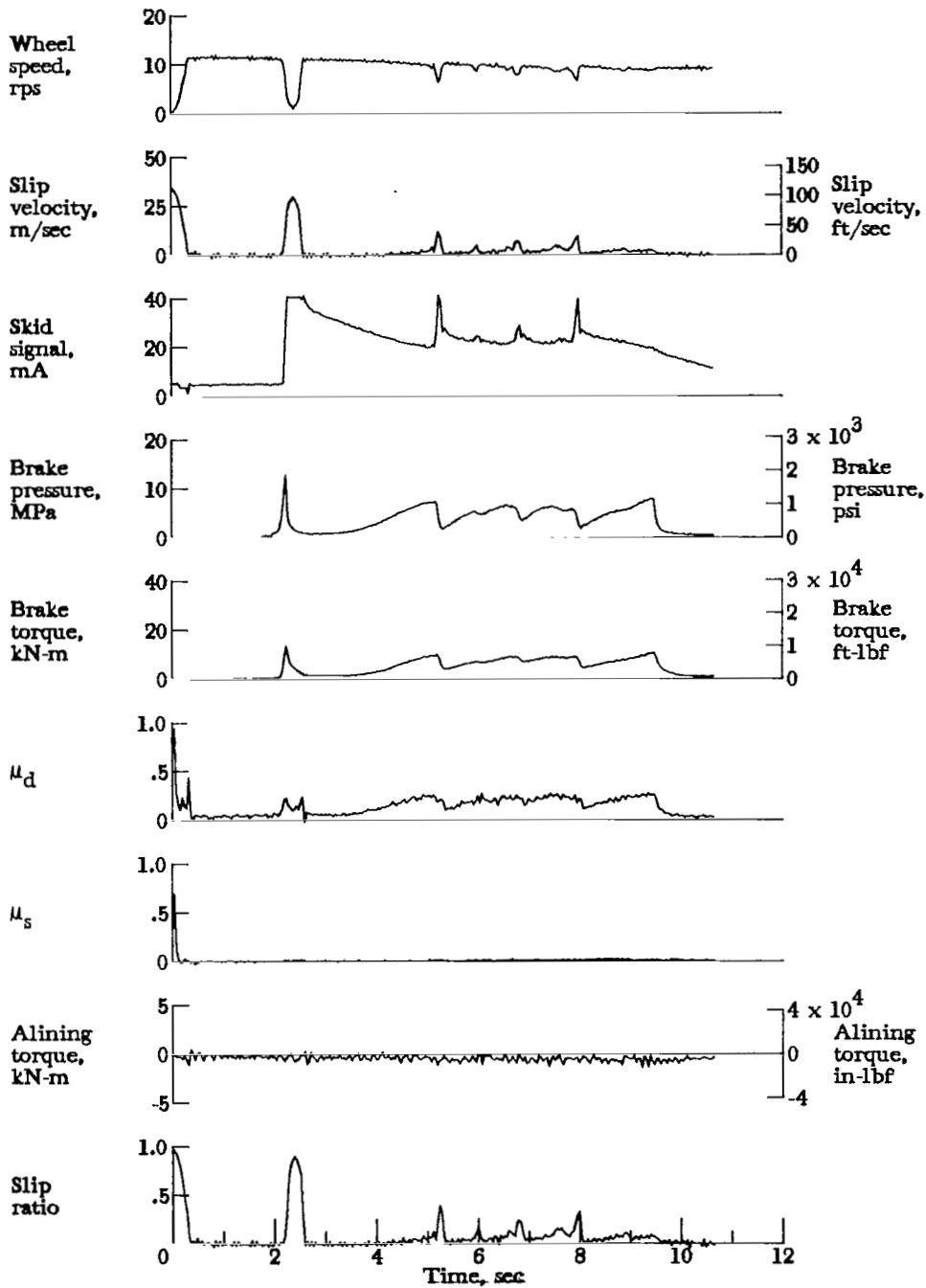


Figure A27.- Time histories for run 27. Nominal carriage speed, 59 knots; vertical load, 101.0 kN (22 700 lbf); yaw angle,  $0^\circ$ ; brake supply pressure, 20 MPa (2900 psi); tire condition, new; surface condition, flooded.

APPENDIX

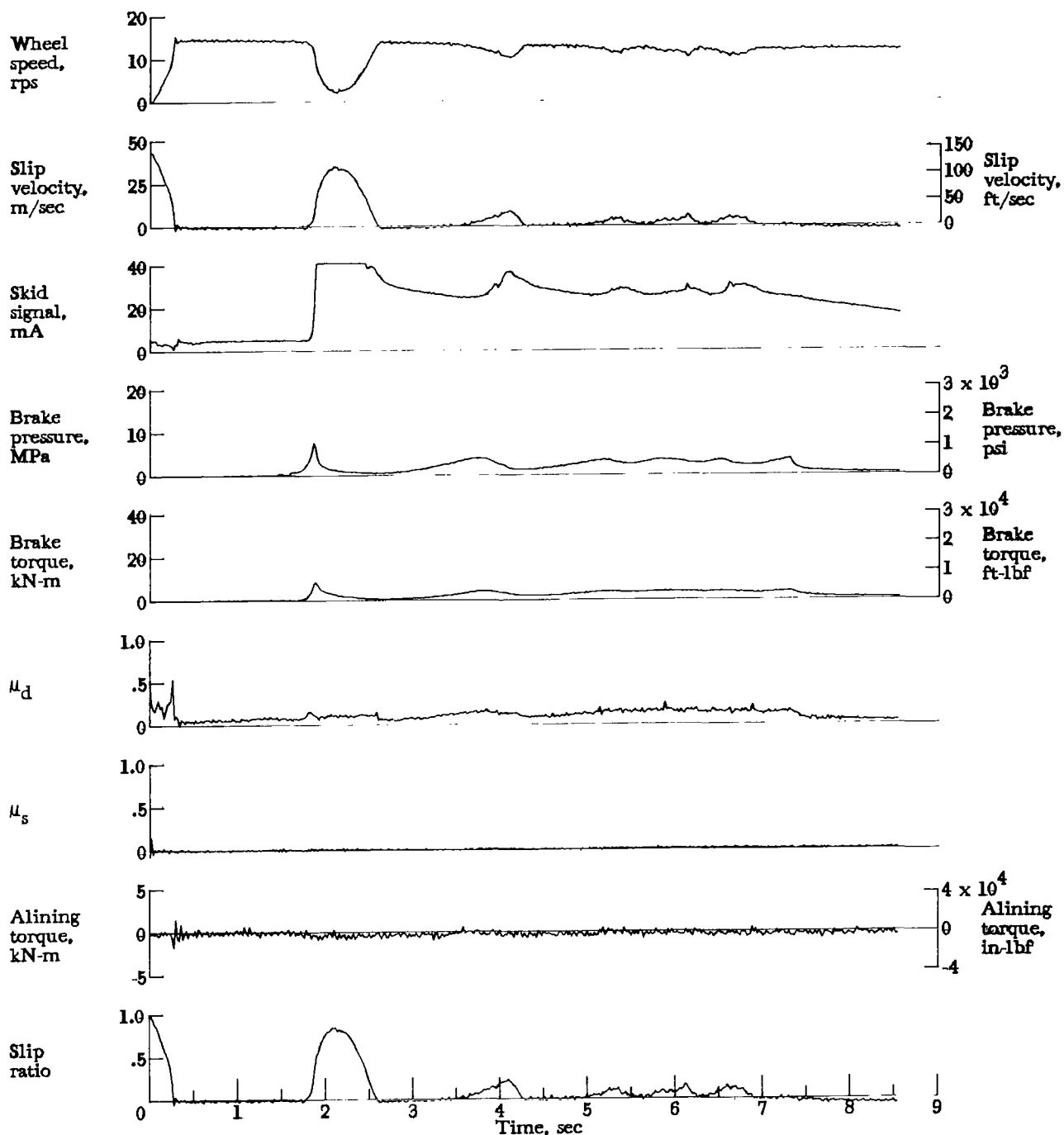


Figure A28.- Time histories for run 28. Nominal carriage speed, 75 knots; vertical load, 94.3 kN (21 200 lbf); yaw angle, 0°; brake supply pressure, 21 MPa (3000 psi); tire condition, new; surface condition, flooded.

APPENDIX

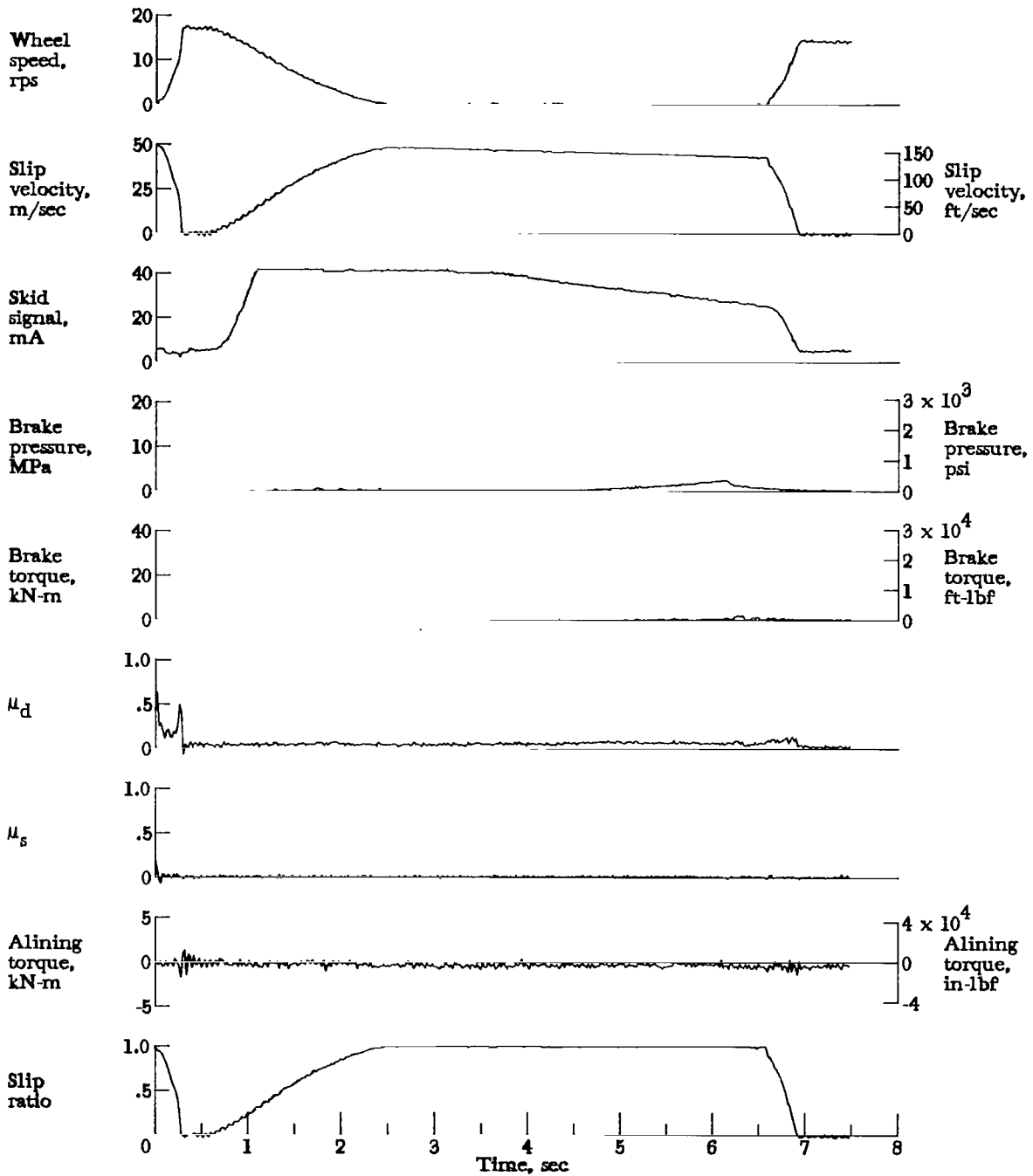


Figure A29.- Time histories for run 29. Nominal carriage speed, 91 knots; vertical load, 93.0 kN (20 900 lbf); yaw angle,  $0^\circ$ ; brake supply pressure, 21 MPa (3000 psi); tire condition, new; surface condition, flooded.

APPENDIX

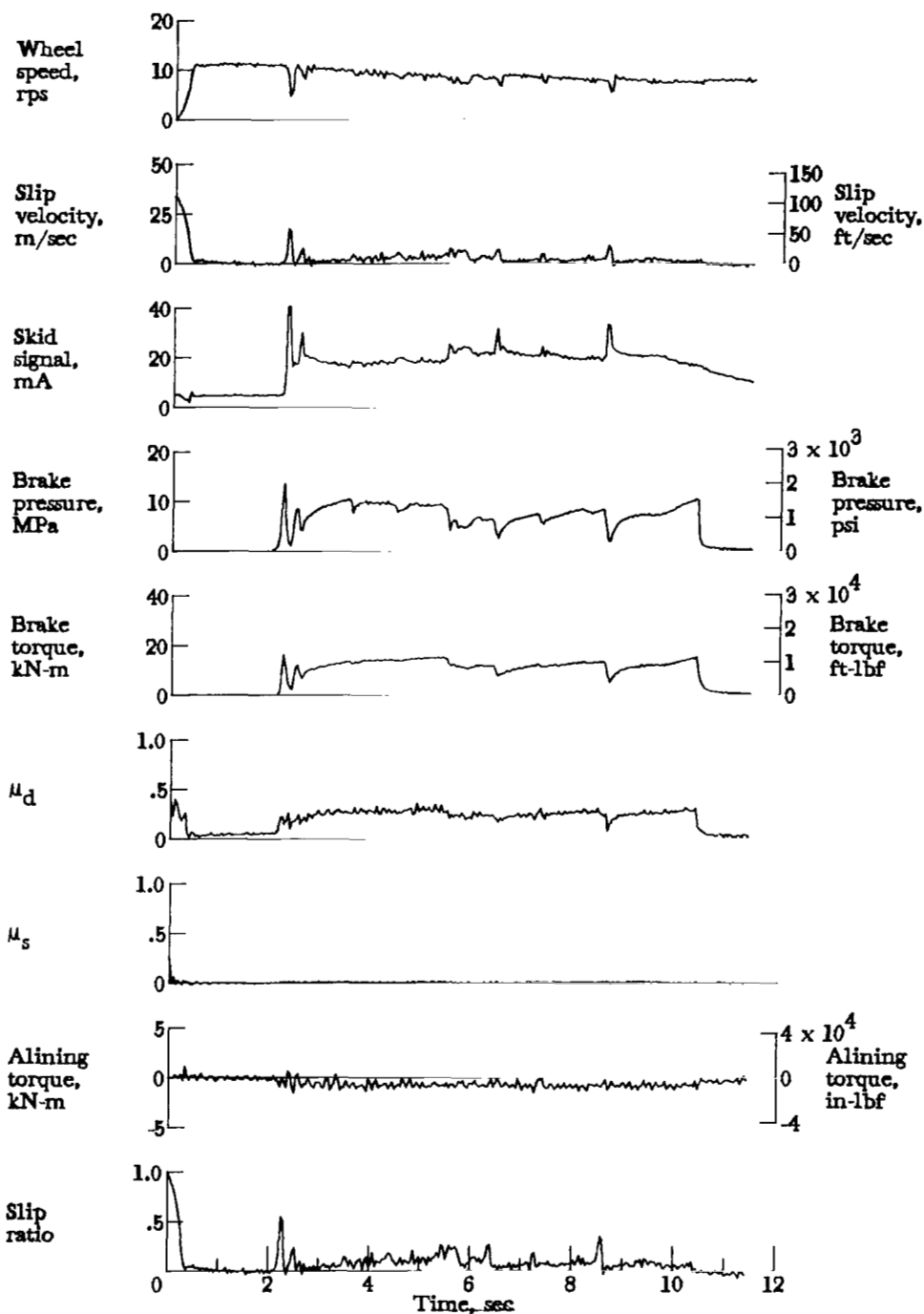


Figure A30.- Time histories for run 30. Nominal carriage speed, 53 knots; vertical load, 127.7 kN (28 700 lbf); yaw angle,  $0^\circ$ ; brake supply pressure, 20 MPa (2900 psi); tire condition, new; surface condition, flooded.

APPENDIX

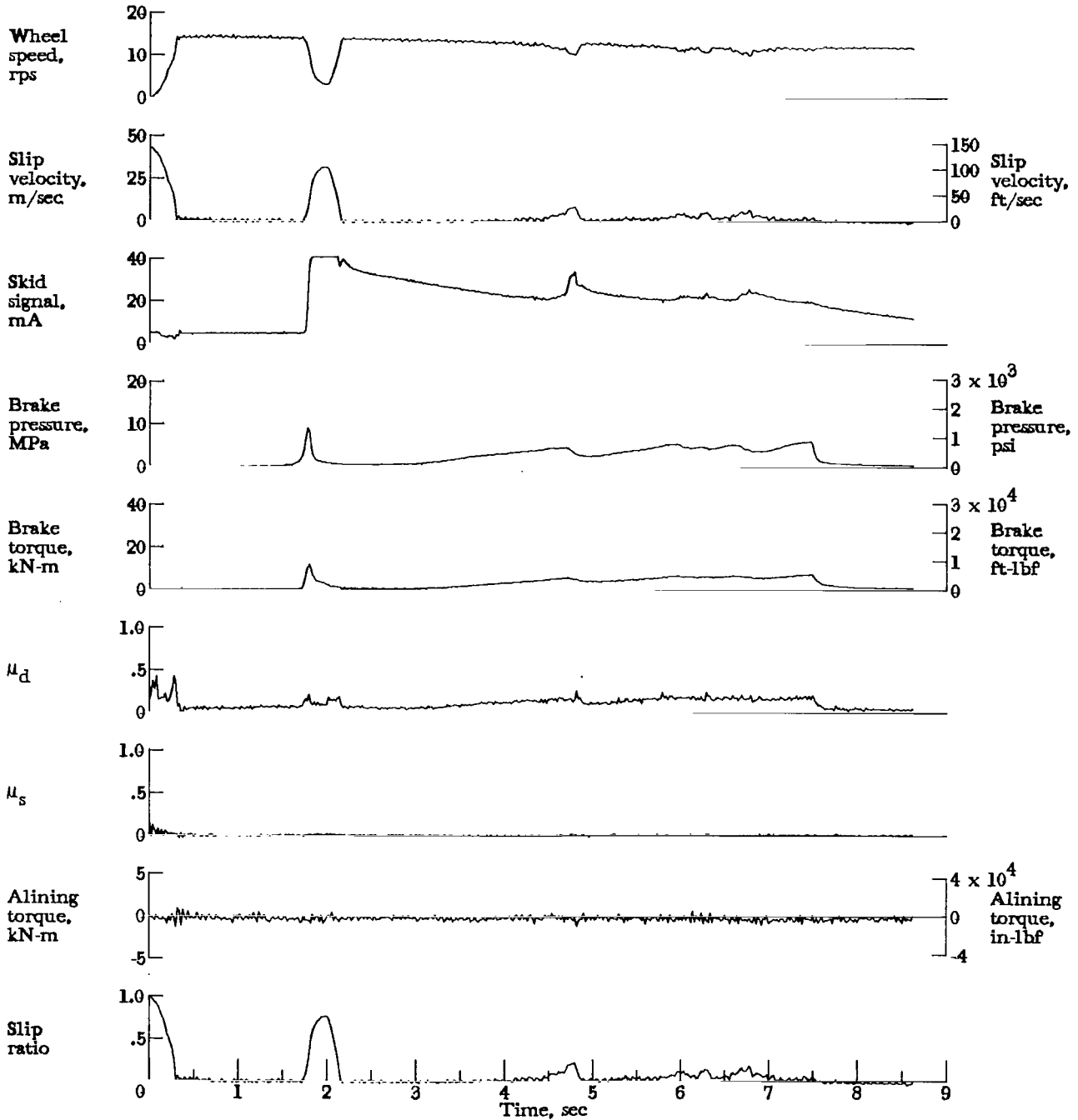


Figure A31.- Time histories for run 31. Nominal carriage speed, 74 knots; vertical load, 125.4 kN (28 200 lbf); yaw angle,  $0^\circ$ ; brake supply pressure, 20 MPa (2900 psi); tire condition, new; surface condition, flooded.

APPENDIX

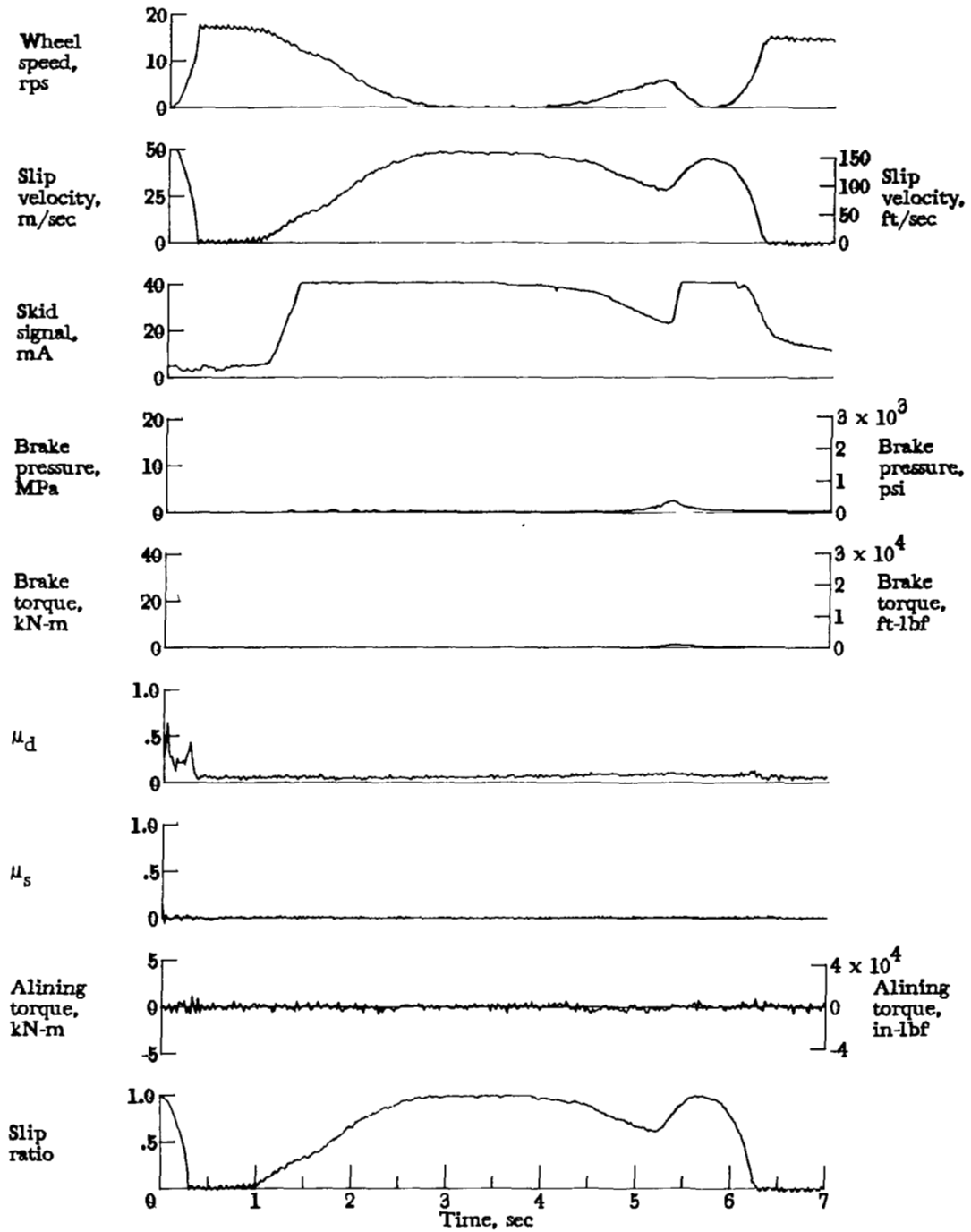


Figure A32.- Time histories for run 32. Nominal carriage speed, 93 knots; vertical load, 116.5 kN (26 200 lbf); yaw angle, 0°; brake supply pressure, 20 MPa (2900 psi); tire condition, new; surface condition, flooded.

APPENDIX

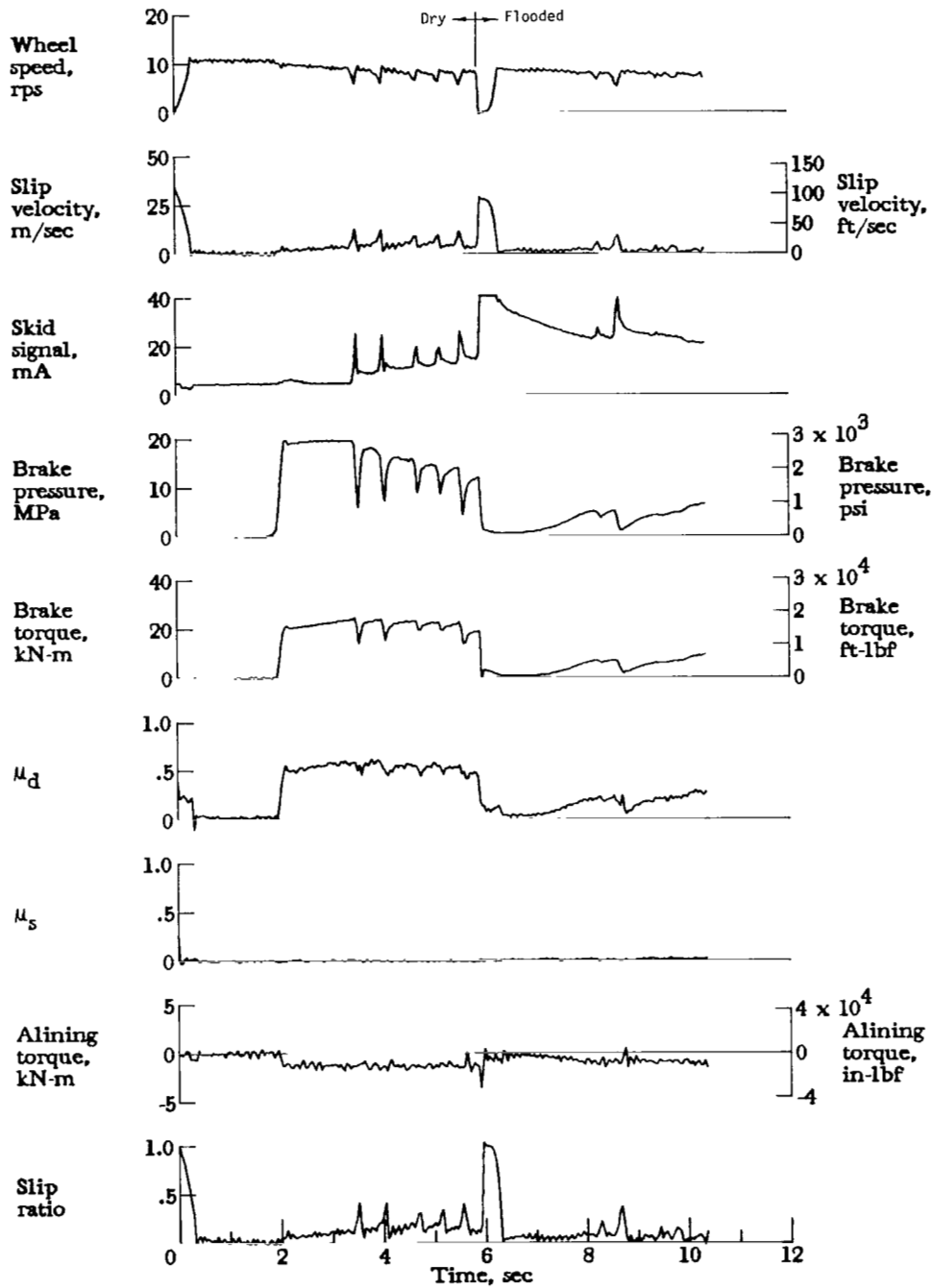


Figure A33.- Time histories for run 33. Nominal carriage speed, 54 knots; vertical load, 83.6 kN (18 800 lbf); yaw angle,  $0^\circ$ ; brake supply pressure, 21 MPa (3000 psi); tire condition, new; surface condition, dry to flooded.

APPENDIX

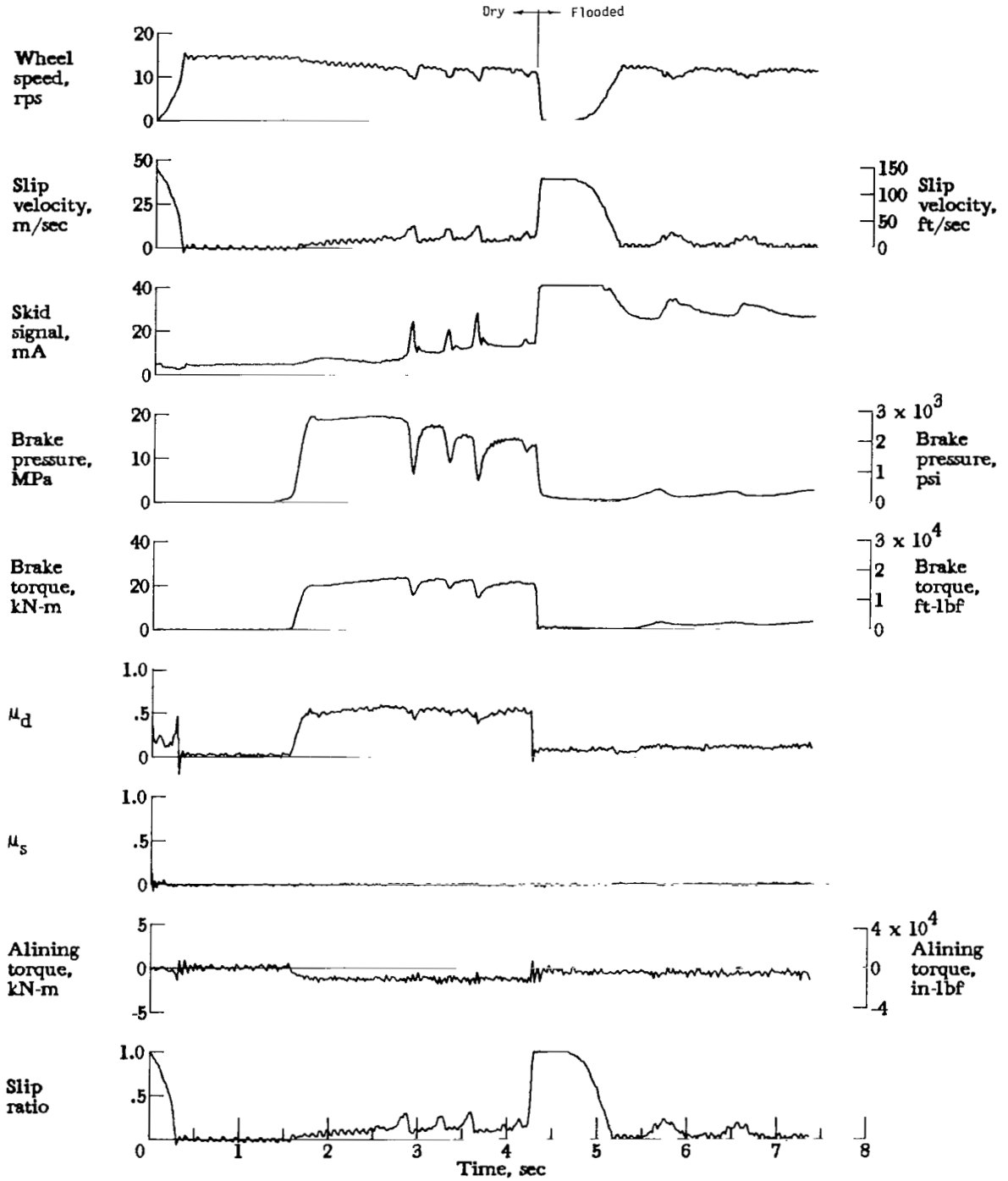


Figure A34.- Time histories for run 34. Nominal carriage speed, 76 knots; vertical load, 83.6 kN (18 800 lbf); yaw angle, 0°; brake supply pressure, 21 MPa (3000 psi); tire condition, new; surface condition, dry to flooded.

APPENDIX

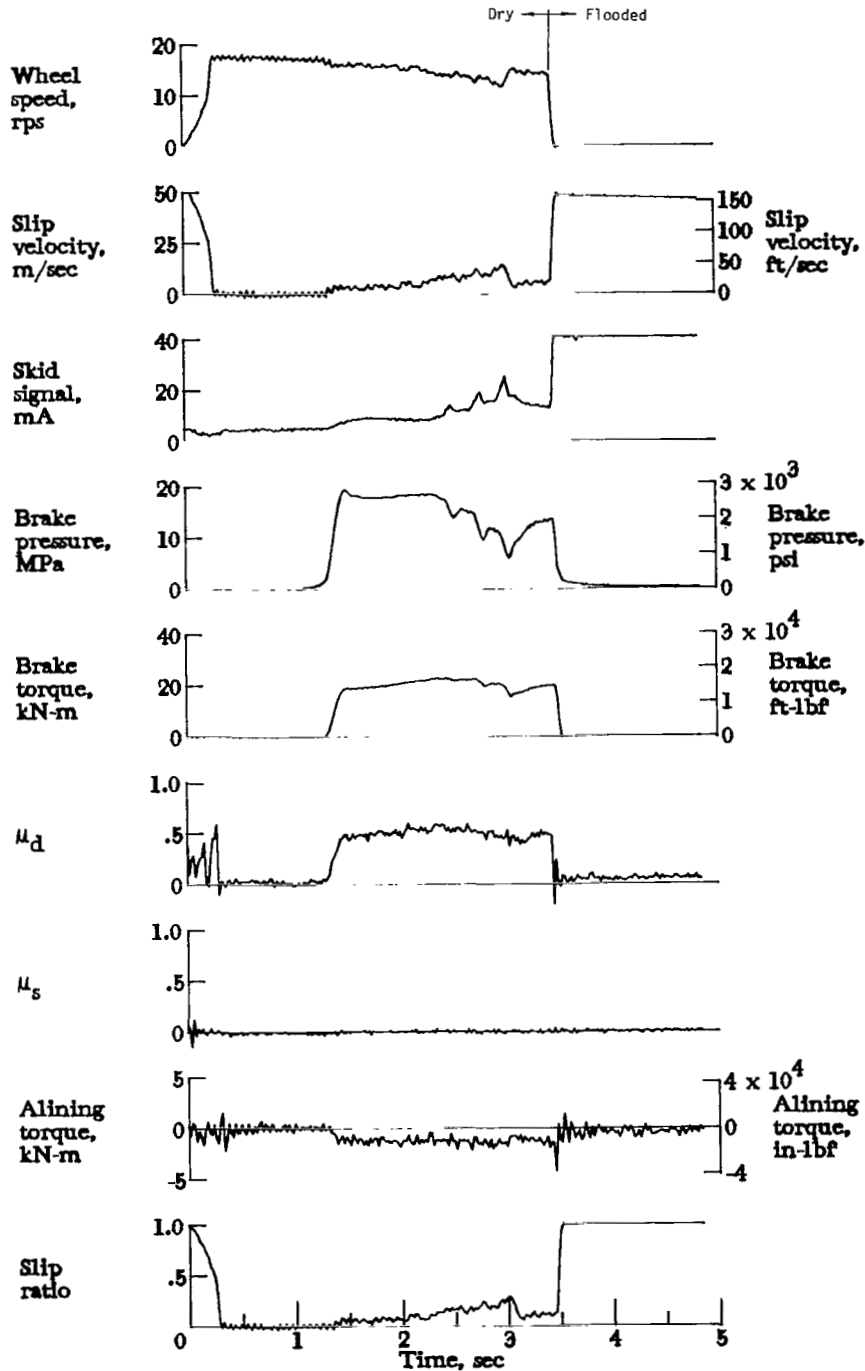


Figure A35.- Time histories for run 35. Nominal carriage speed, 94 knots; vertical load, 83.2 kN (18 700 lbf); yaw angle, 0°; brake supply pressure, 21 MPa (3000 psi); tire condition, new; surface condition, dry to flooded.

APPENDIX

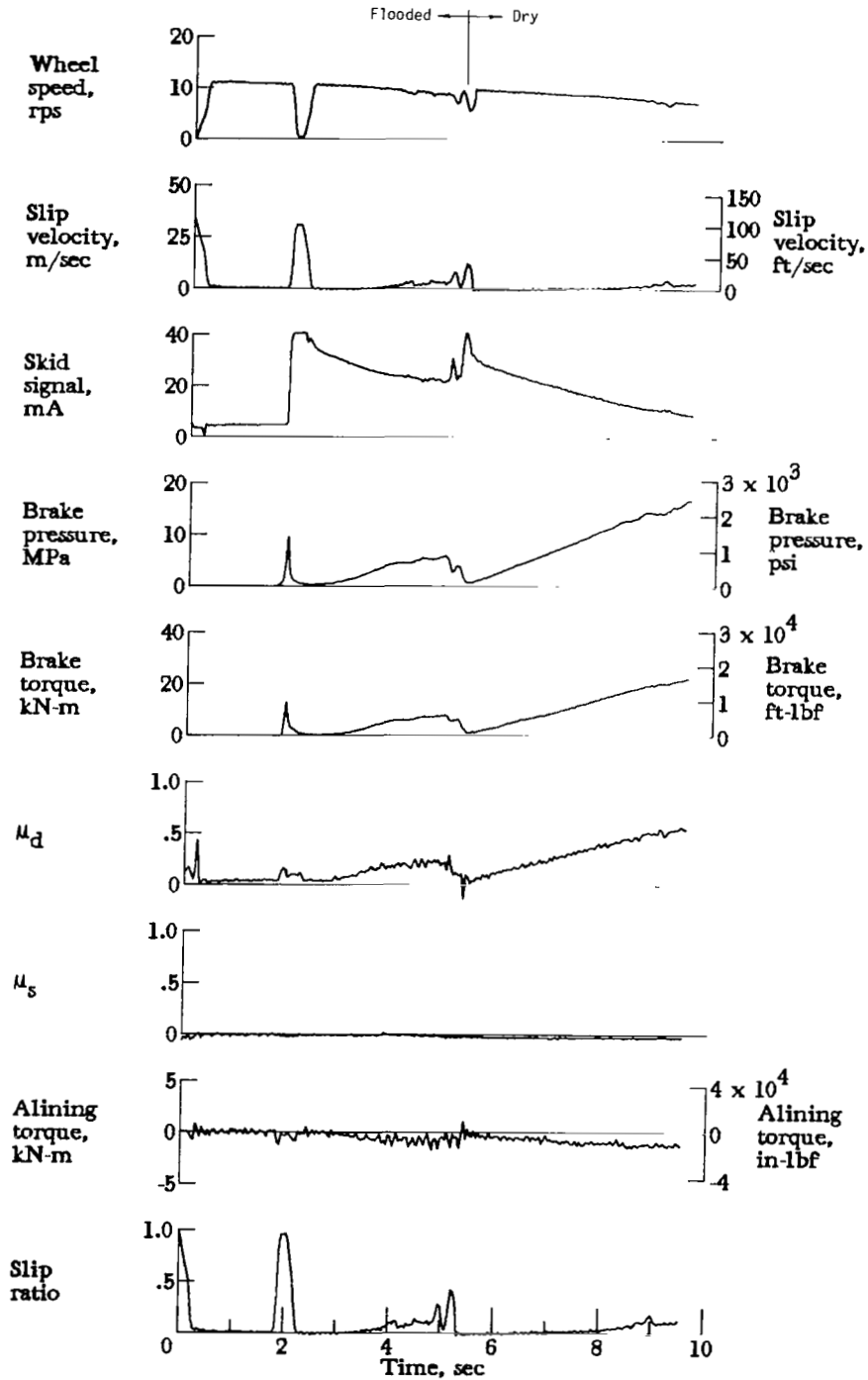


Figure A36.- Time histories for run 36. Nominal carriage speed, 56 knots; vertical load, 83.6 kN (18 800 lbf); yaw angle, 0°; brake supply pressure, 21 MPa (3000 psi); tire condition, new; surface condition, flooded to dry.

APPENDIX

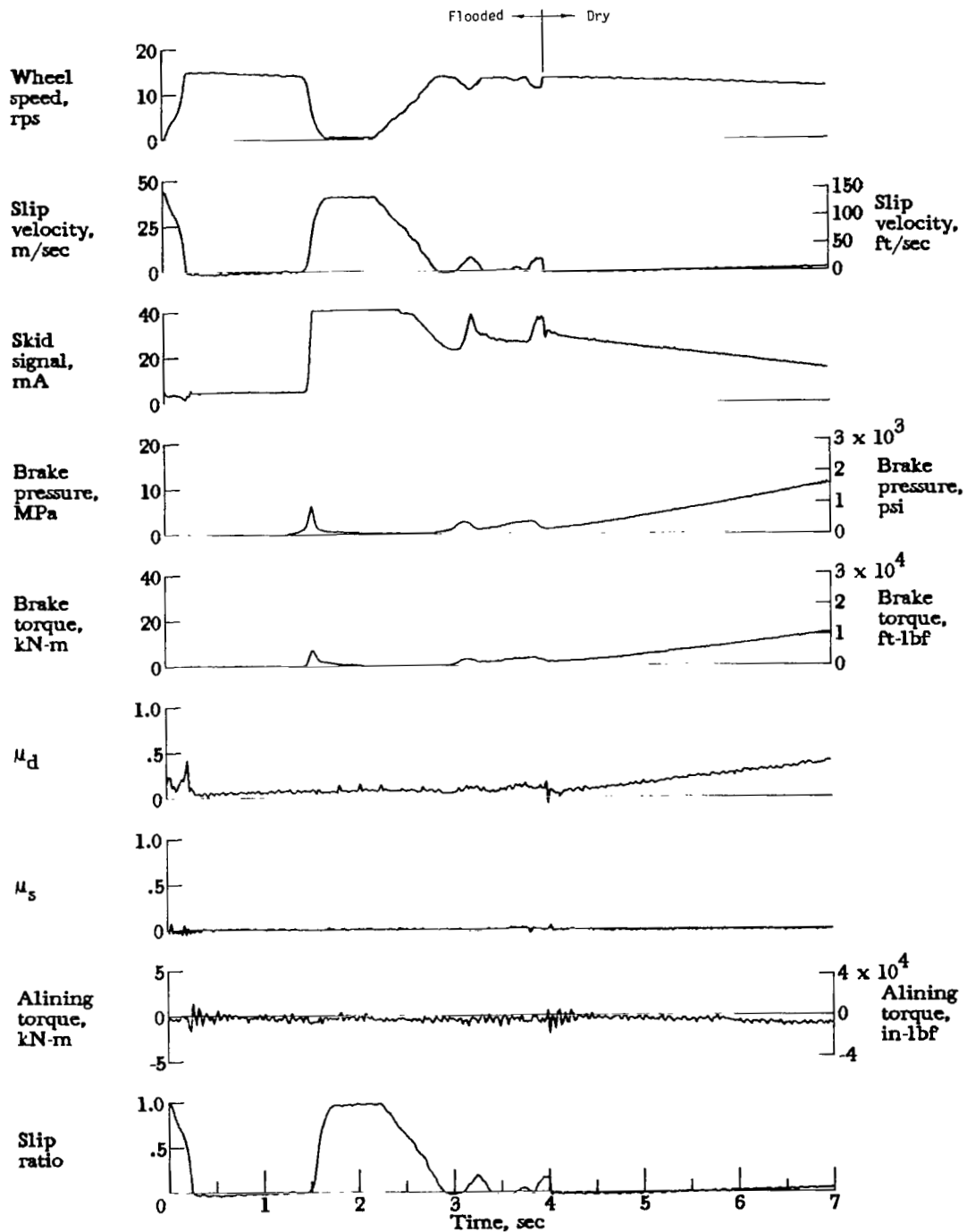


Figure A37.- Time histories for run 37. Nominal carriage speed, 77 knots; vertical load, 83.2 kN (18 700 lbf); yaw angle, 0°; brake supply pressure, 20 MPa (2900 psi); tire condition, new; surface condition, flooded to dry.

APPENDIX

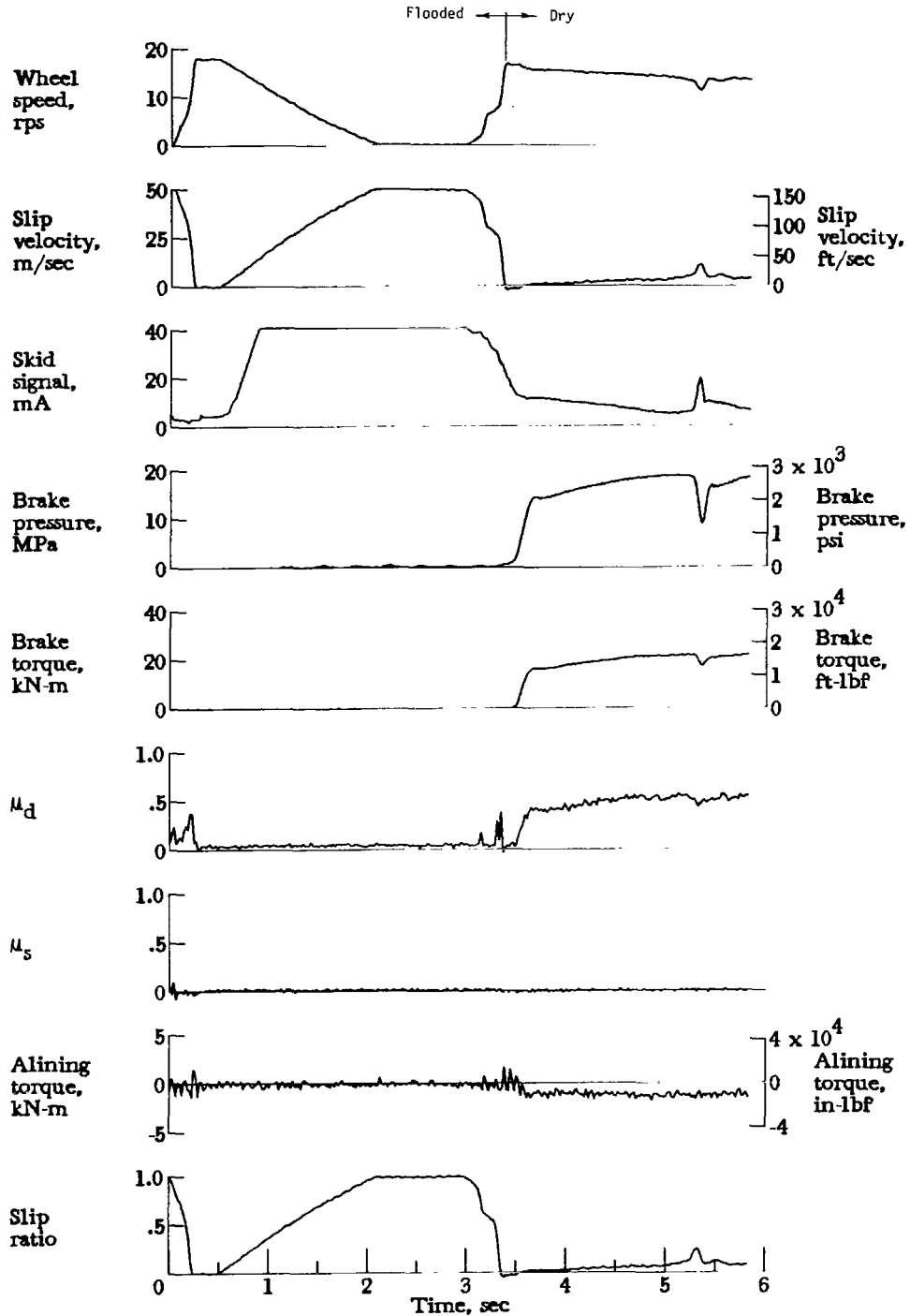


Figure A38.- Time histories for run 38. Nominal carriage speed, 94 knots; vertical load, 83.2 kN (18 700 lbf); yaw angle,  $0^\circ$ ; brake supply pressure, 20 MPa (2900 psi); tire condition, new; surface condition, flooded to dry.

APPENDIX

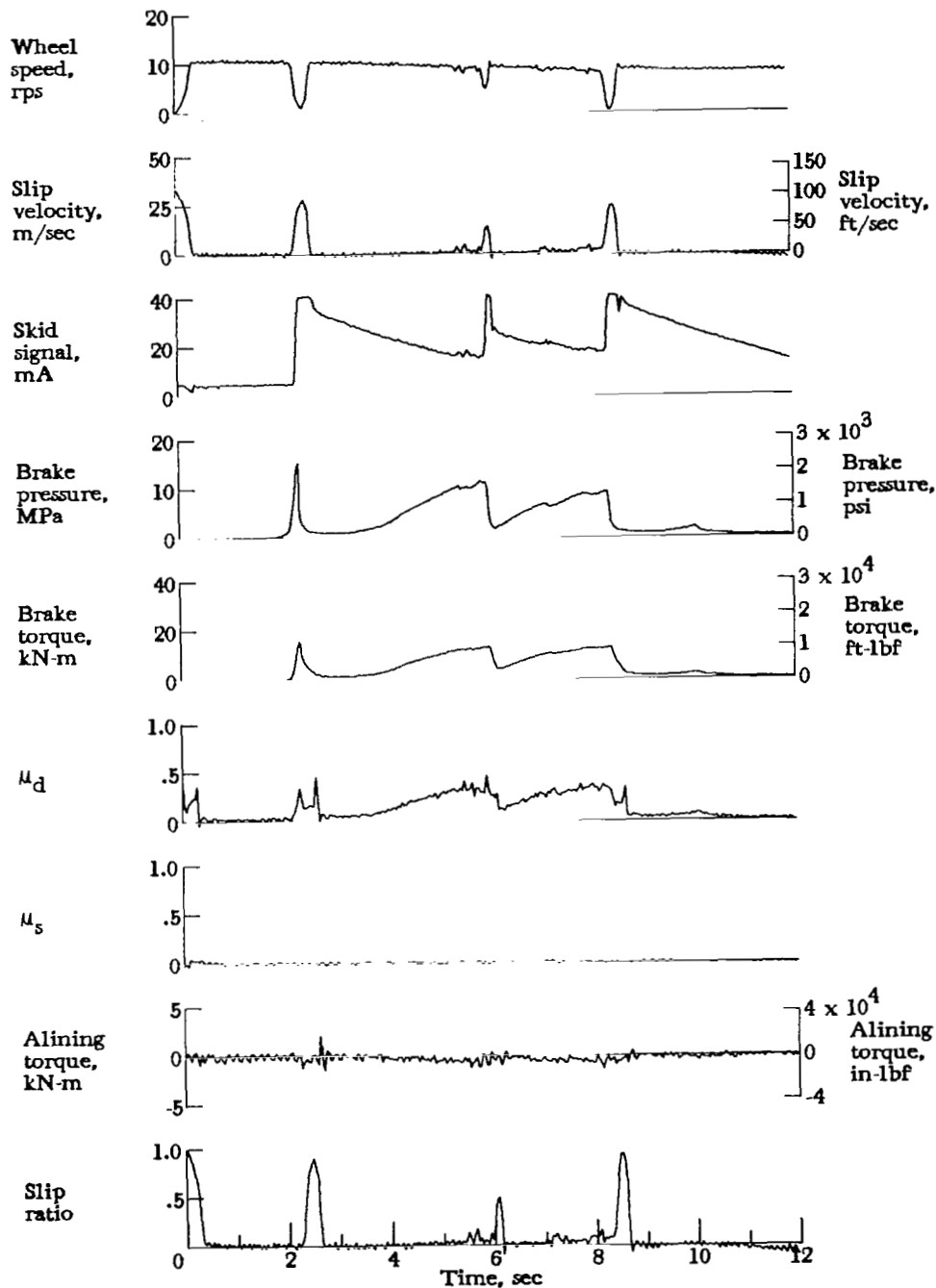


Figure A39.- Time histories for run 39. Nominal carriage speed, 55 knots; vertical load, 82.3 kN (18 500 lbf); yaw angle, 0°; brake supply pressure, 20 MPa (2900 psi); tire condition, new; surface condition, natural rain.

APPENDIX

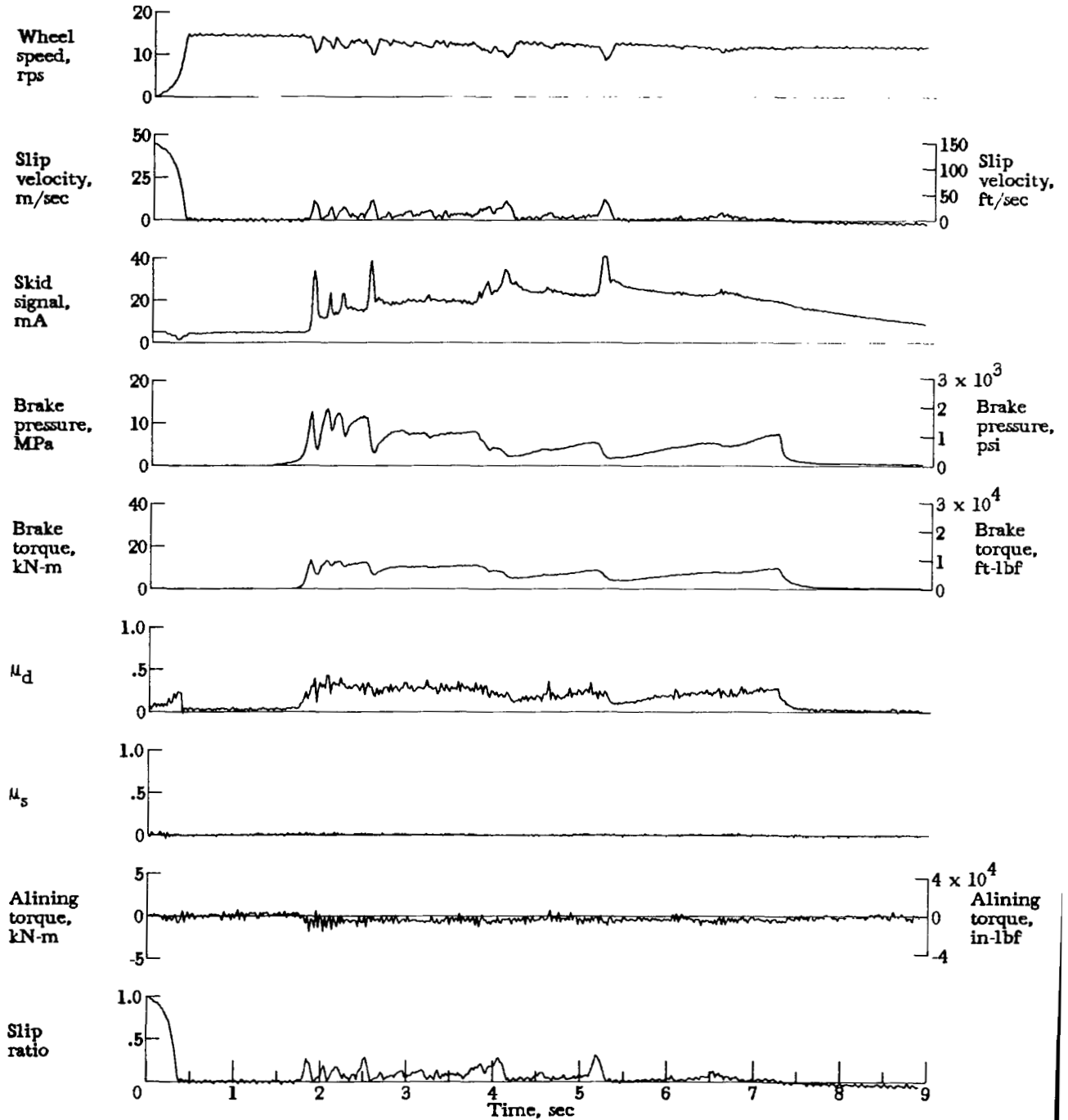


Figure A40.- Time histories for run 40. Nominal carriage speed, 76 knots; vertical load, 82.3 kN (18 500 lbf); yaw angle, 0°; brake supply pressure, 20 MPa (2900 psi); tire condition, new; surface condition, natural rain.

APPENDIX

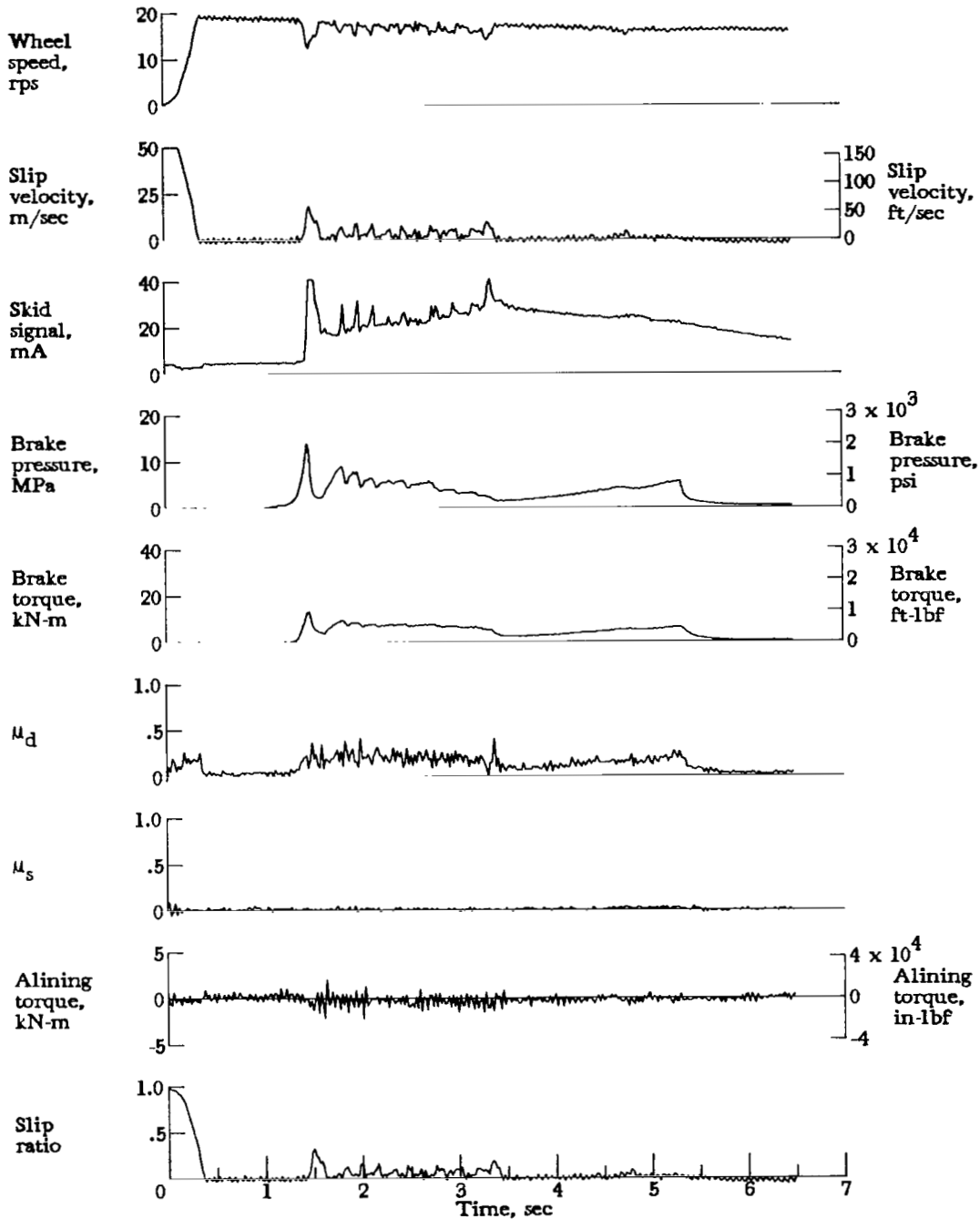


Figure A41.- Time histories for run 41. Nominal carriage speed, 103 knots; vertical load, 82.3 kN (18 500 lbf); yaw angle,  $0^\circ$ ; brake supply pressure, 20 MPa (2900 psi); tire condition, new; surface condition, natural rain.

APPENDIX

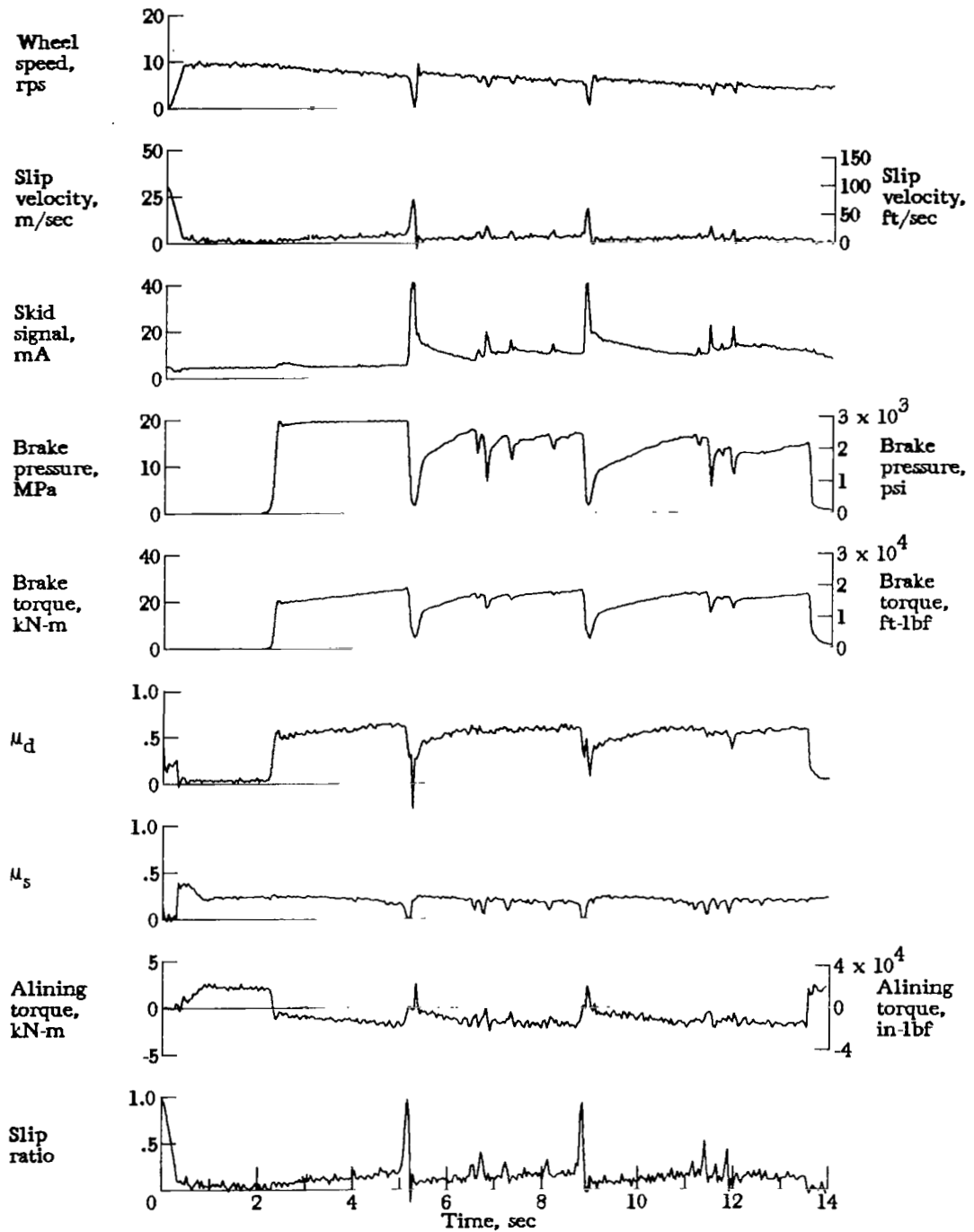


Figure A42.- Time histories for run 42. Nominal carriage speed, 40 knots; vertical load, 84.5 kN (19 000 lbf); yaw angle,  $3^\circ$ ; brake supply pressure, 21 MPa (3000 psi); tire condition, new; surface condition, dry.

APPENDIX

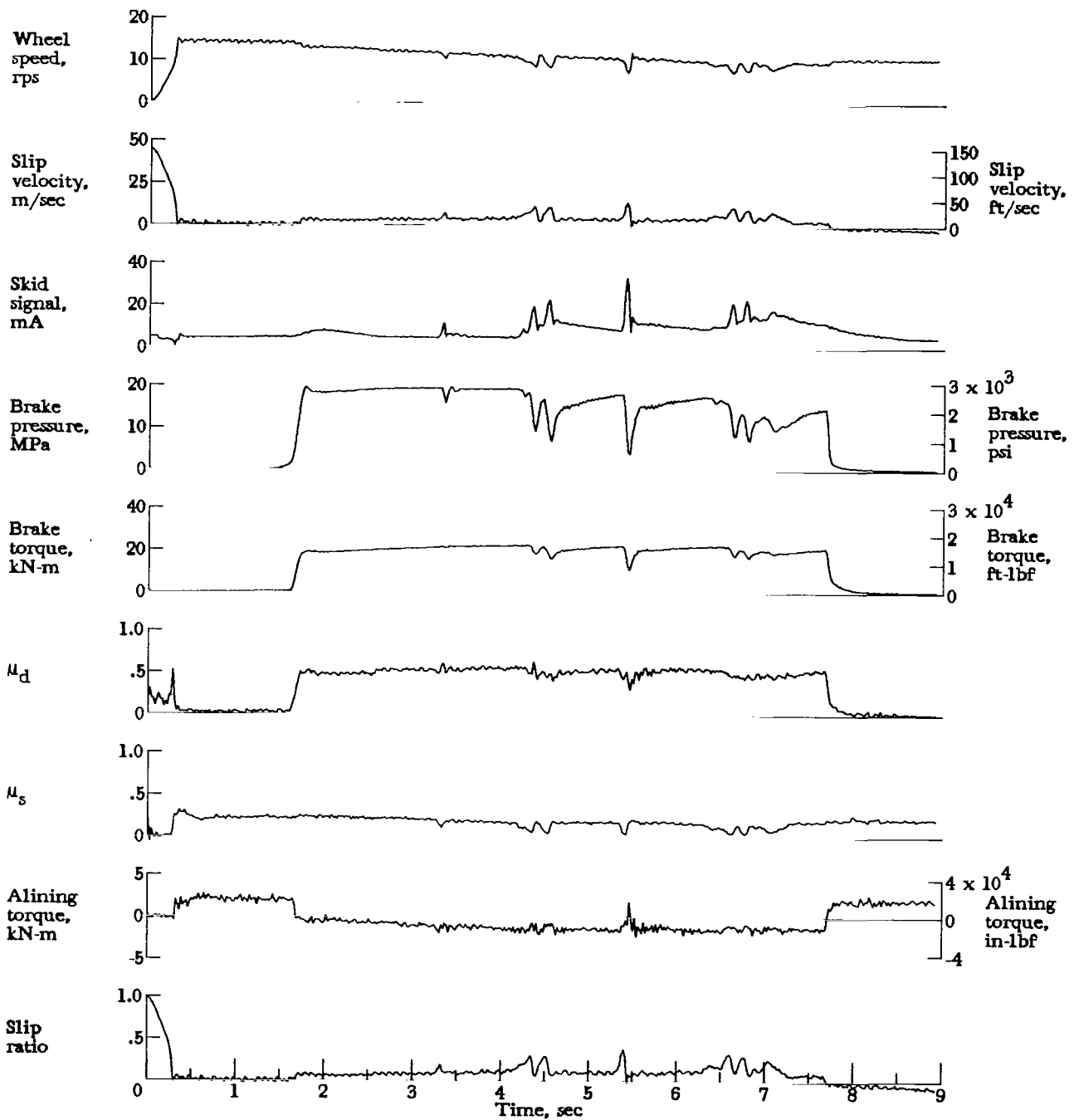


Figure A43.- Time histories for run 43. Nominal carriage speed, 72 knots; vertical load, 85.4 kN (19 200 lbf); yaw angle, 3°; brake supply pressure, 20 MPa (2900 psi); tire condition, new; surface condition, dry.

APPENDIX

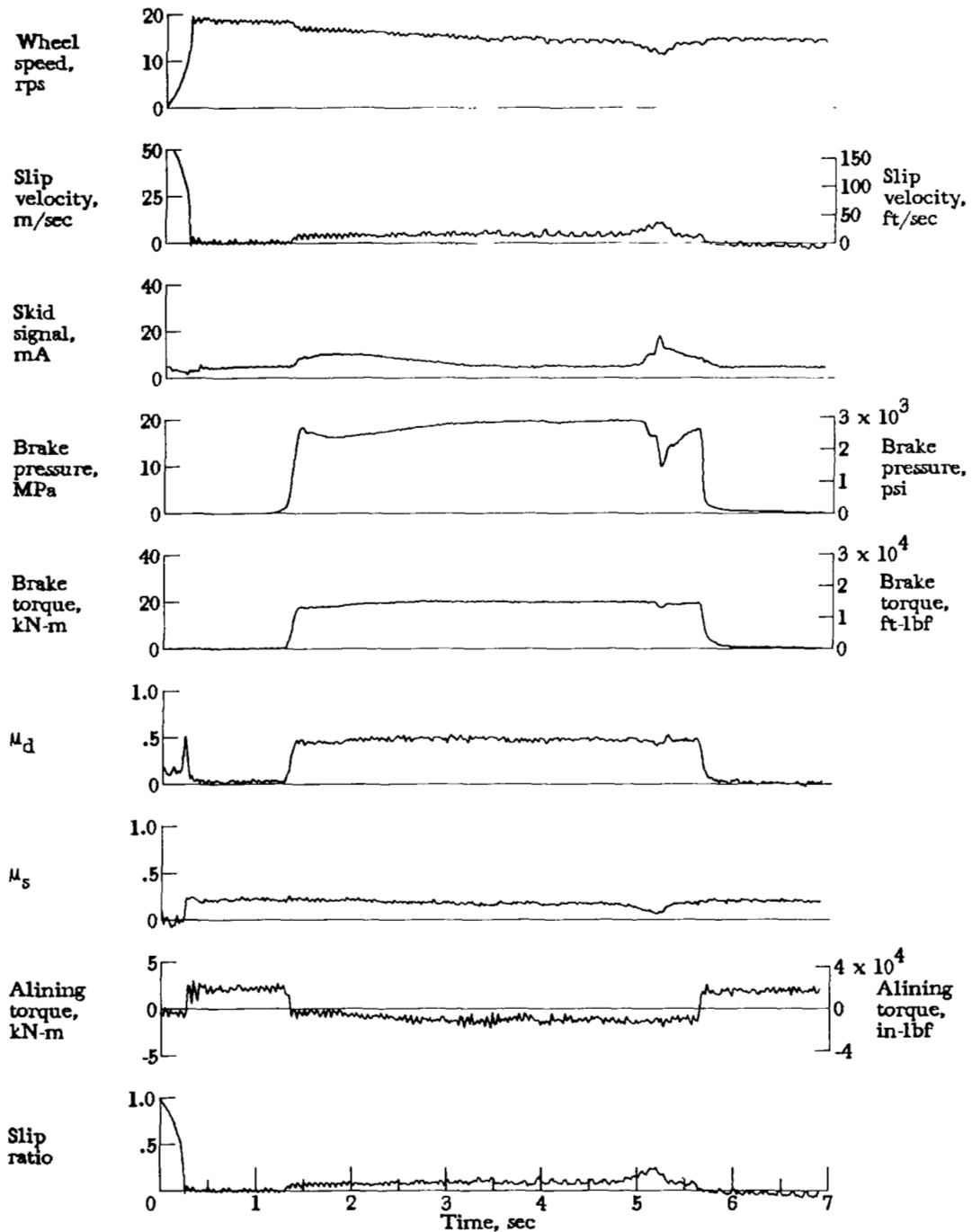


Figure A44.- Time histories for run 44. Nominal carriage speed, 97 knots; vertical load, 86.3 kN (19 400 lbf); yaw angle,  $3^\circ$ ; brake supply pressure, 21 MPa (3000 psi); tire condition, new; surface condition, dry.

APPENDIX

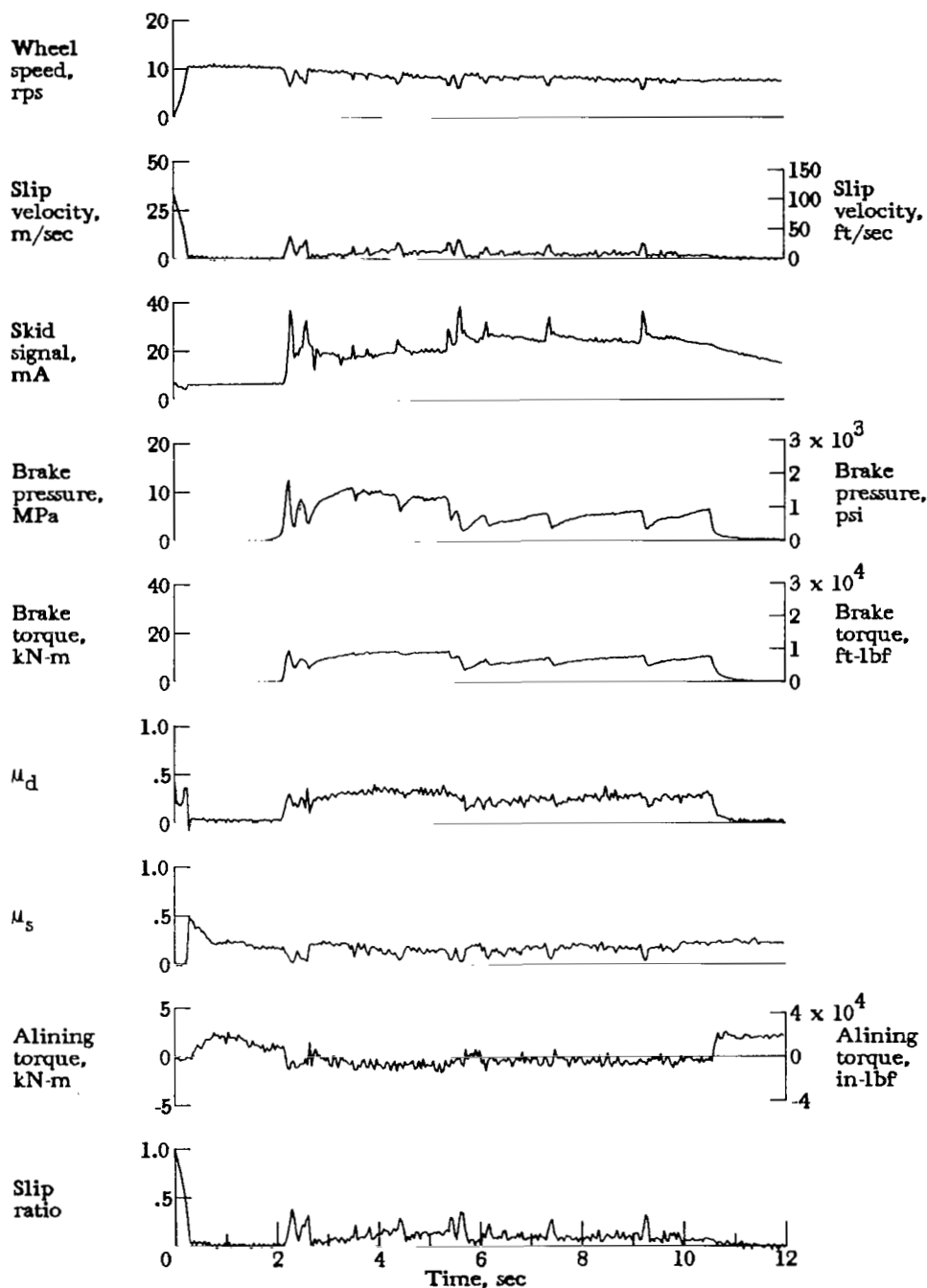


Figure A45.- Time histories for run 45. Nominal carriage speed, 53 knots; vertical load, 84.1 kN (18 900 lbf); yaw angle, 3°; brake supply pressure, 20 MPa (2900 psi); tire condition, new; surface condition, damp.

APPENDIX

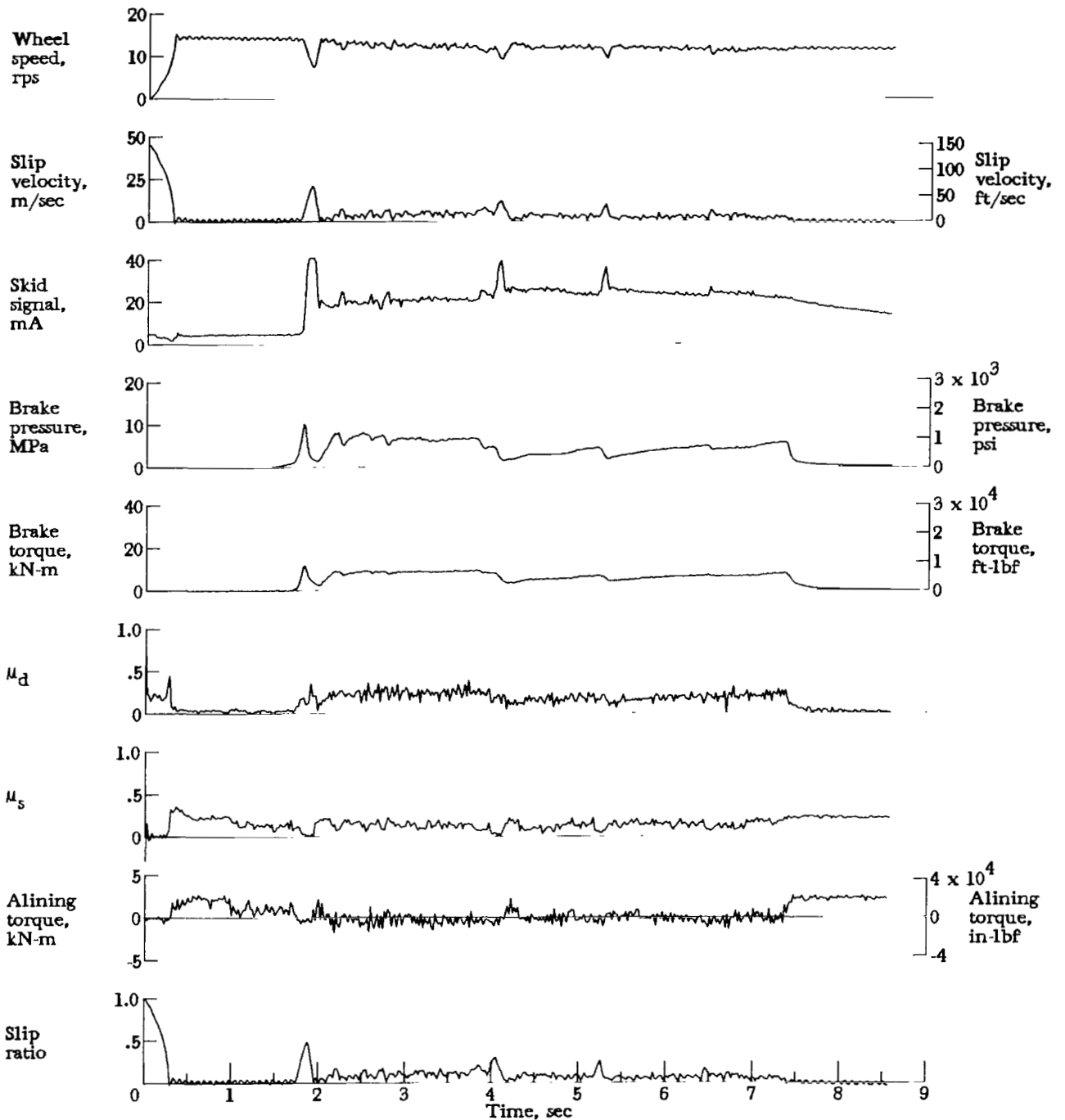


Figure A46.- Time histories for run 46. Nominal carriage speed, 77 knots; vertical load, 83.2 kN (18 700 lbf); yaw angle,  $3^\circ$ ; brake supply pressure, 20 MPa (2900 psi); tire condition, new; surface condition, damp.

APPENDIX

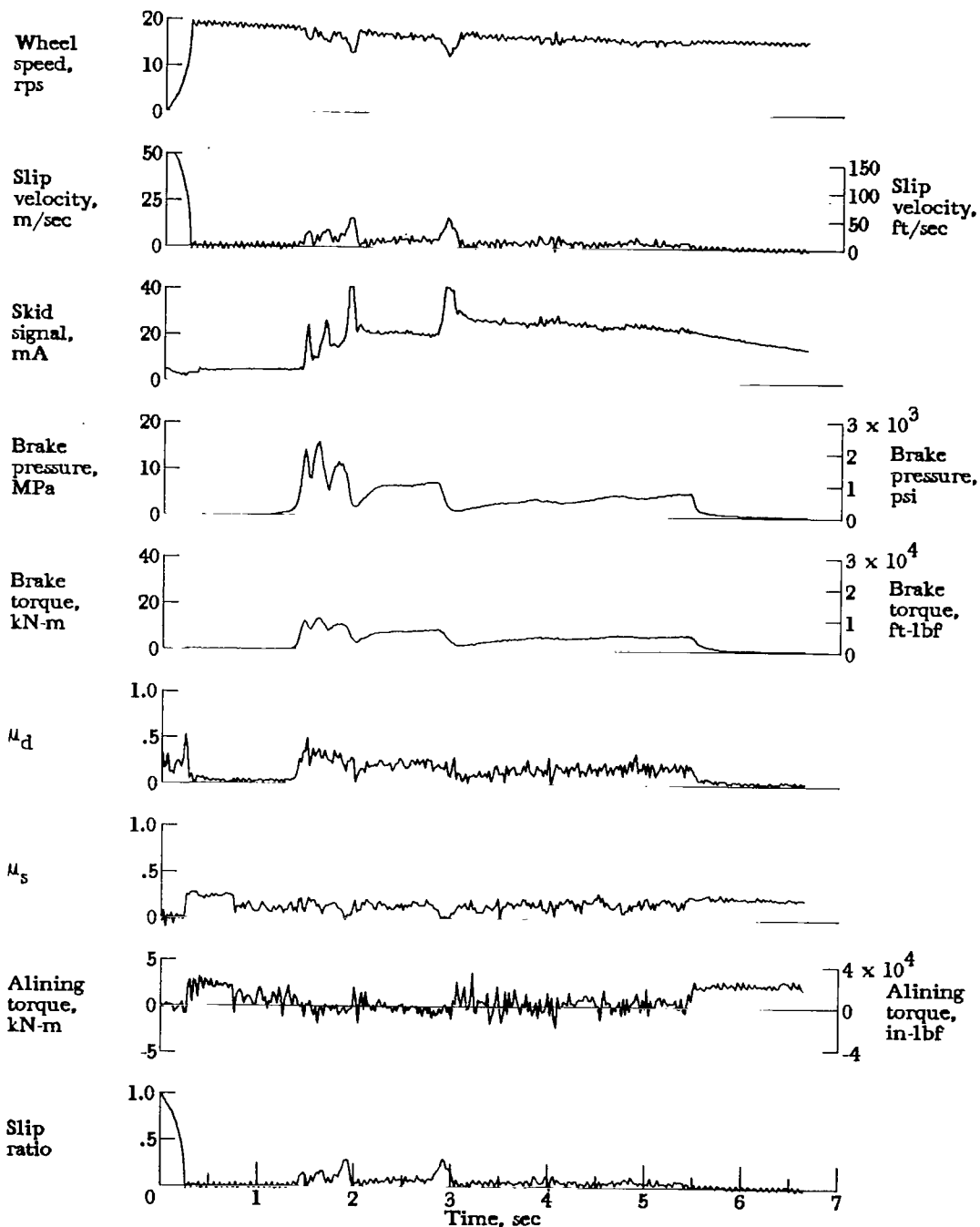


Figure A47.- Time histories for run 47. Nominal carriage speed, 102 knots; vertical load, 84.1 kN (18 900 lbf); yaw angle, 3°; brake supply pressure, 20 MPa (2900 psi); tire condition, new; surface condition, damp.

APPENDIX

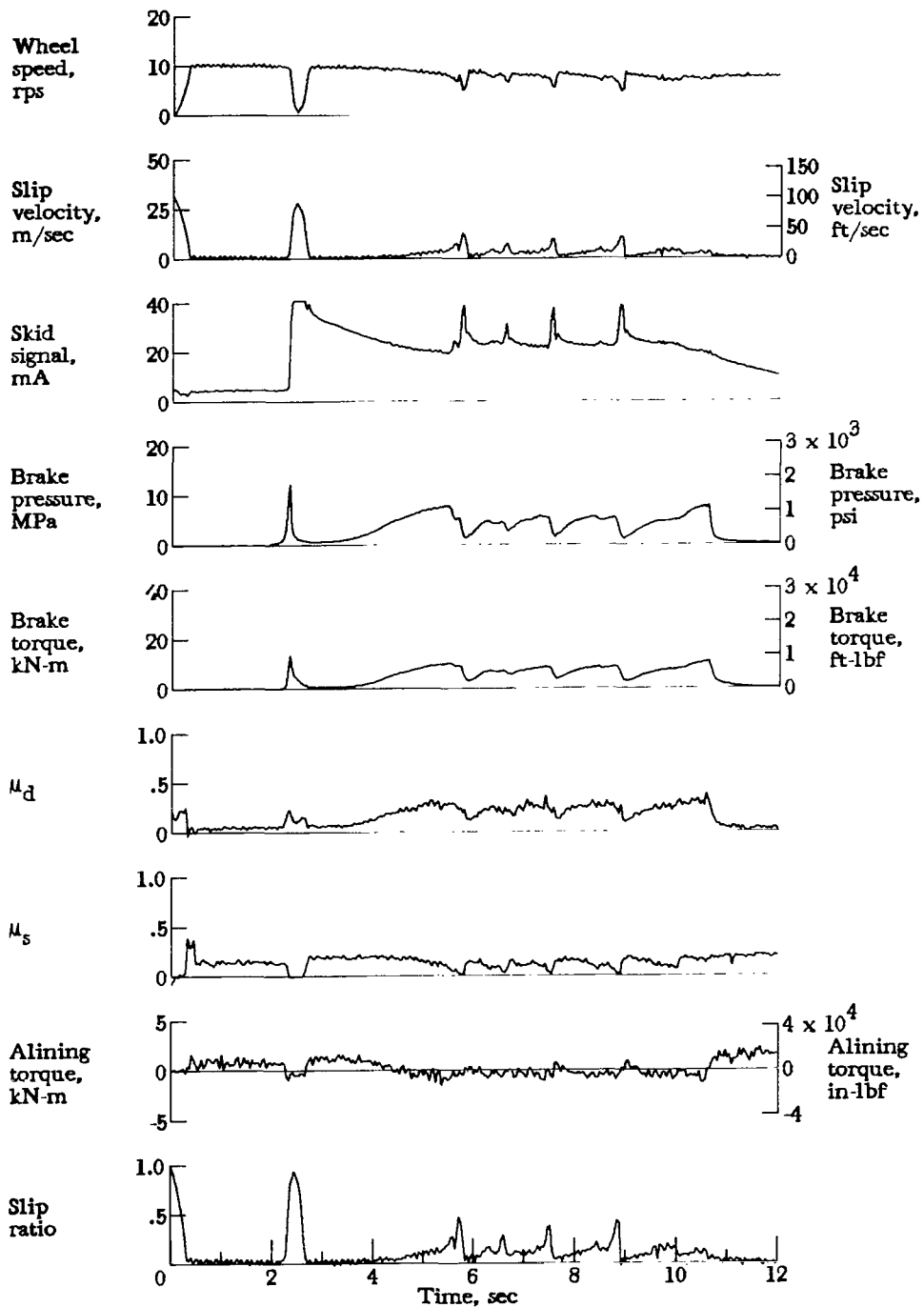


Figure A48.- Time histories for run 48. Nominal carriage speed, 52 knots; vertical load, 83.2 kN (18 700 lbf); yaw angle, 3°; brake supply pressure, 20 MPa (2900 psi); tire condition, new; surface condition, flooded.

APPENDIX

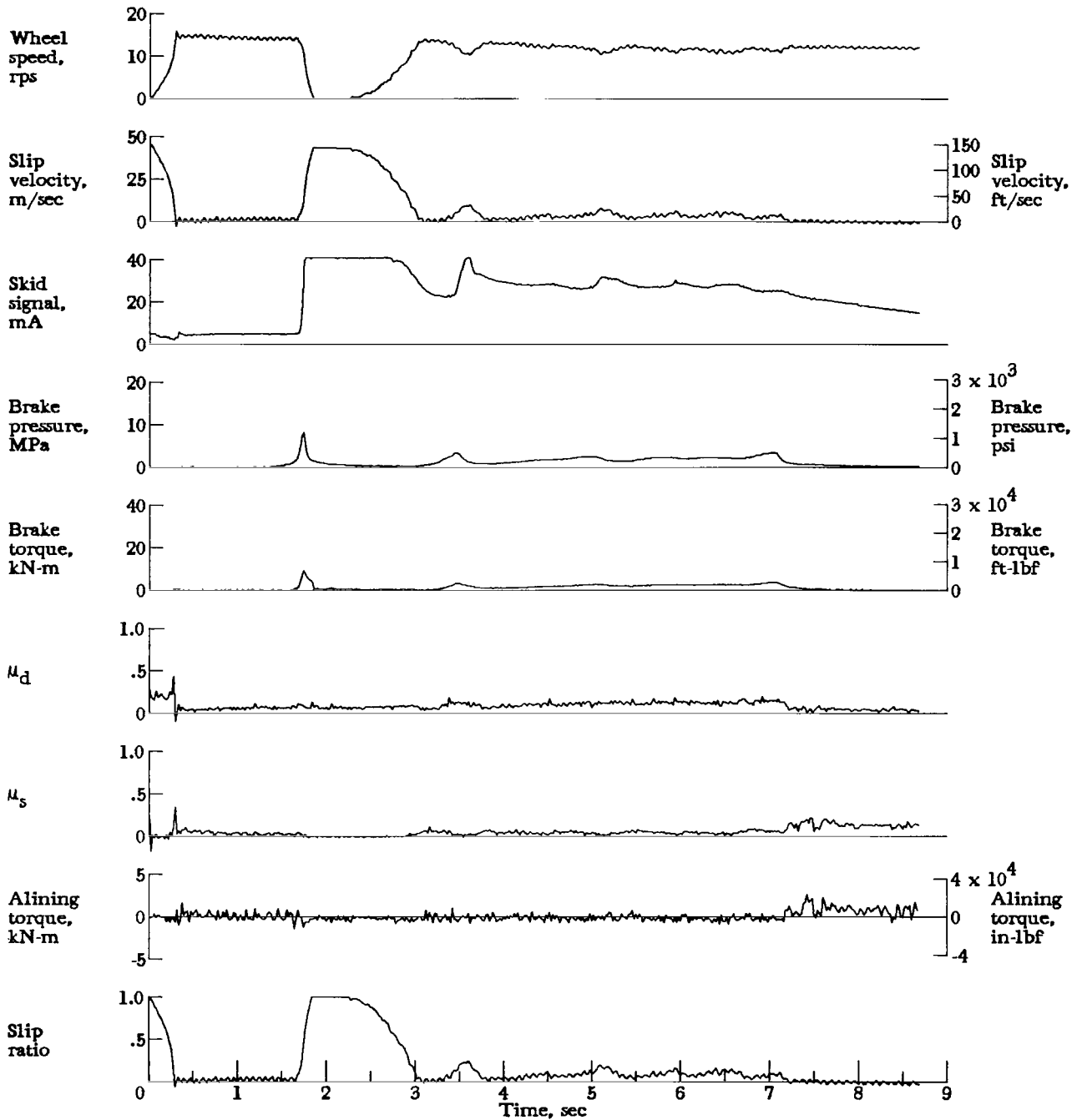


Figure A49.- Time histories for run 49. Nominal carriage speed, 79 knots; vertical load, 82.7 kN (18 600 lbf); yaw angle, 3°; brake supply pressure, 20 MPa (2900 psi); tire condition, new; surface condition, flooded.

APPENDIX

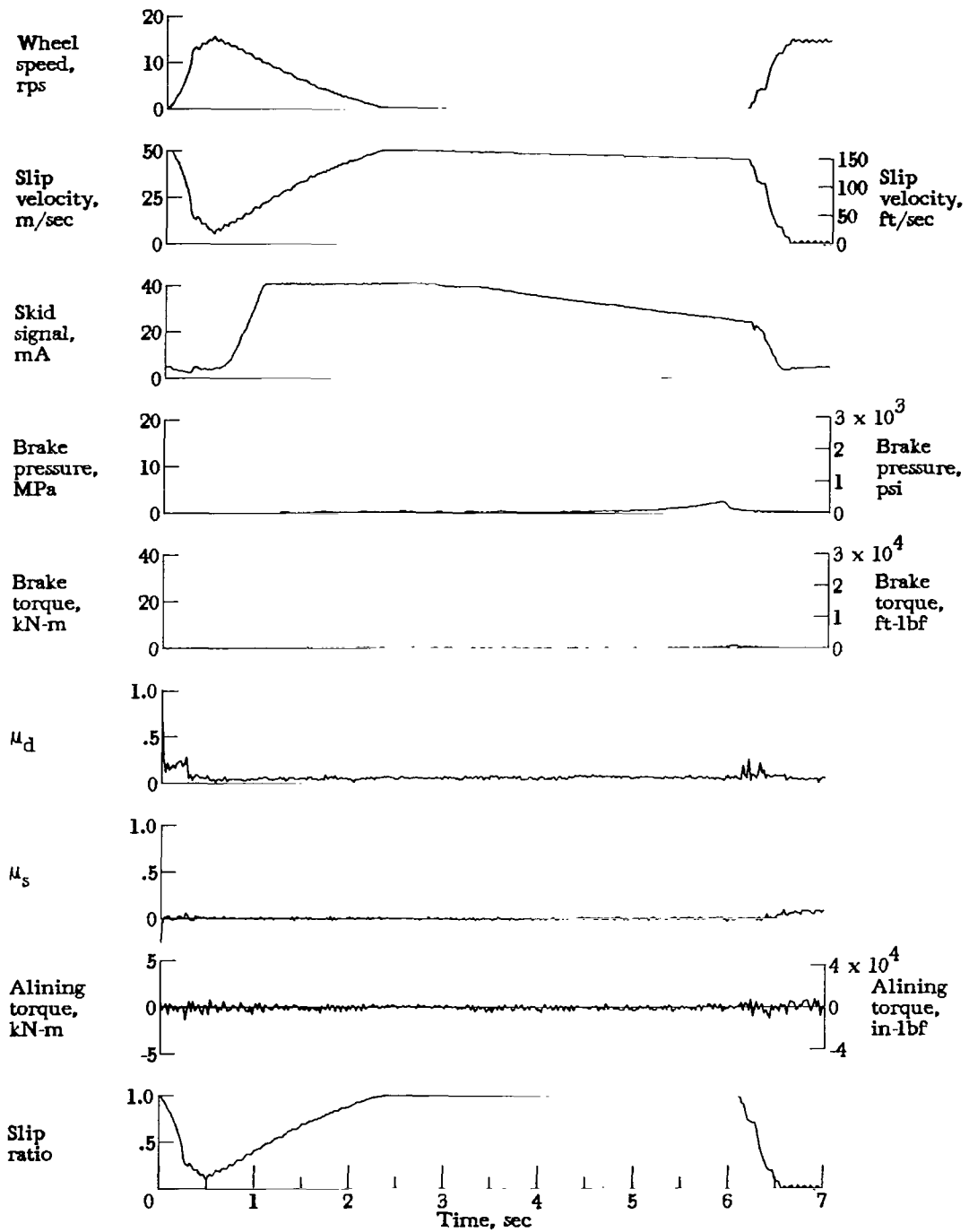


Figure A50.- Time histories for run 50. Nominal carriage speed, 95 knots; vertical load, 81.4 kN (18 300 lbf); yaw angle, 3°; brake supply pressure, 20 MPa (2900 psi); tire condition, new; surface condition, flooded.

APPENDIX

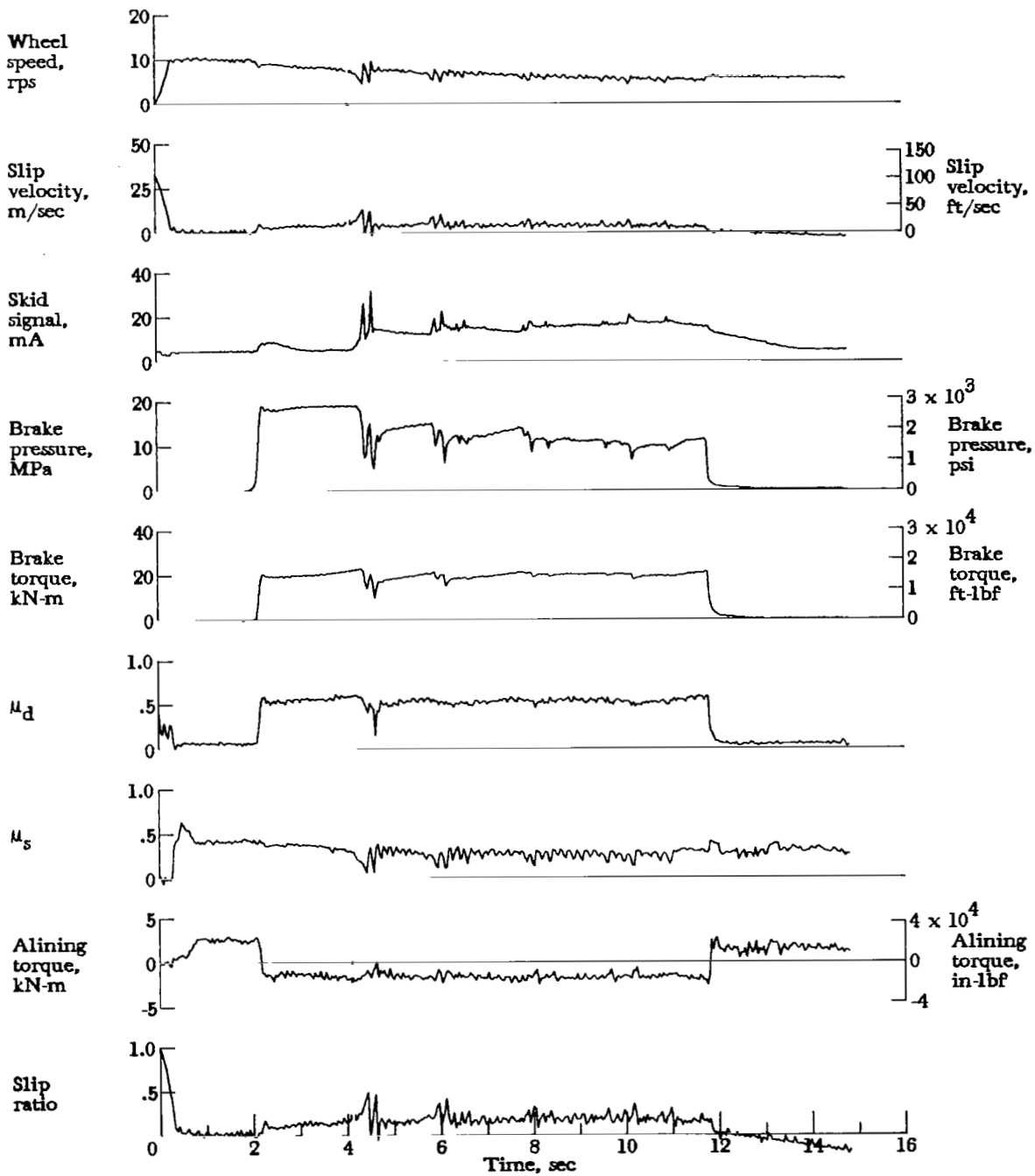


Figure A51.- Time histories for run 51. Nominal carriage speed, 47 knots; vertical load, 85.0 kN (19 100 lbf); yaw angle,  $6^\circ$ ; brake supply pressure, 21 MPa (3000 psi); tire condition, new; surface condition, dry.

APPENDIX

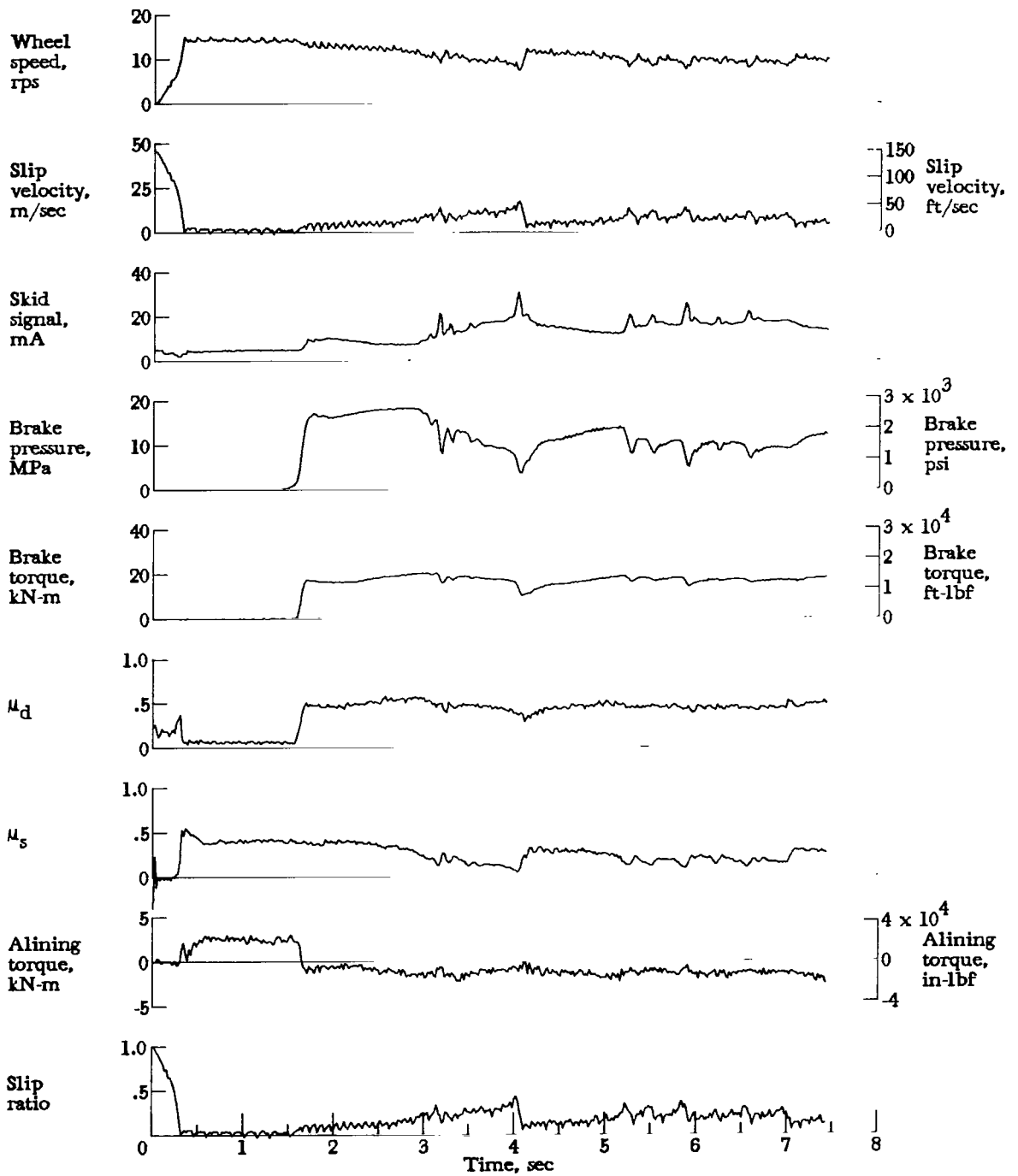


Figure A52.- Time histories for run 52. Nominal carriage speed, 75 knots; vertical load, 85.0 kN (19 100 lbf); yaw angle, 6°; brake supply pressure, 20 MPa (2900 psi); tire condition, new; surface condition, dry.

APPENDIX

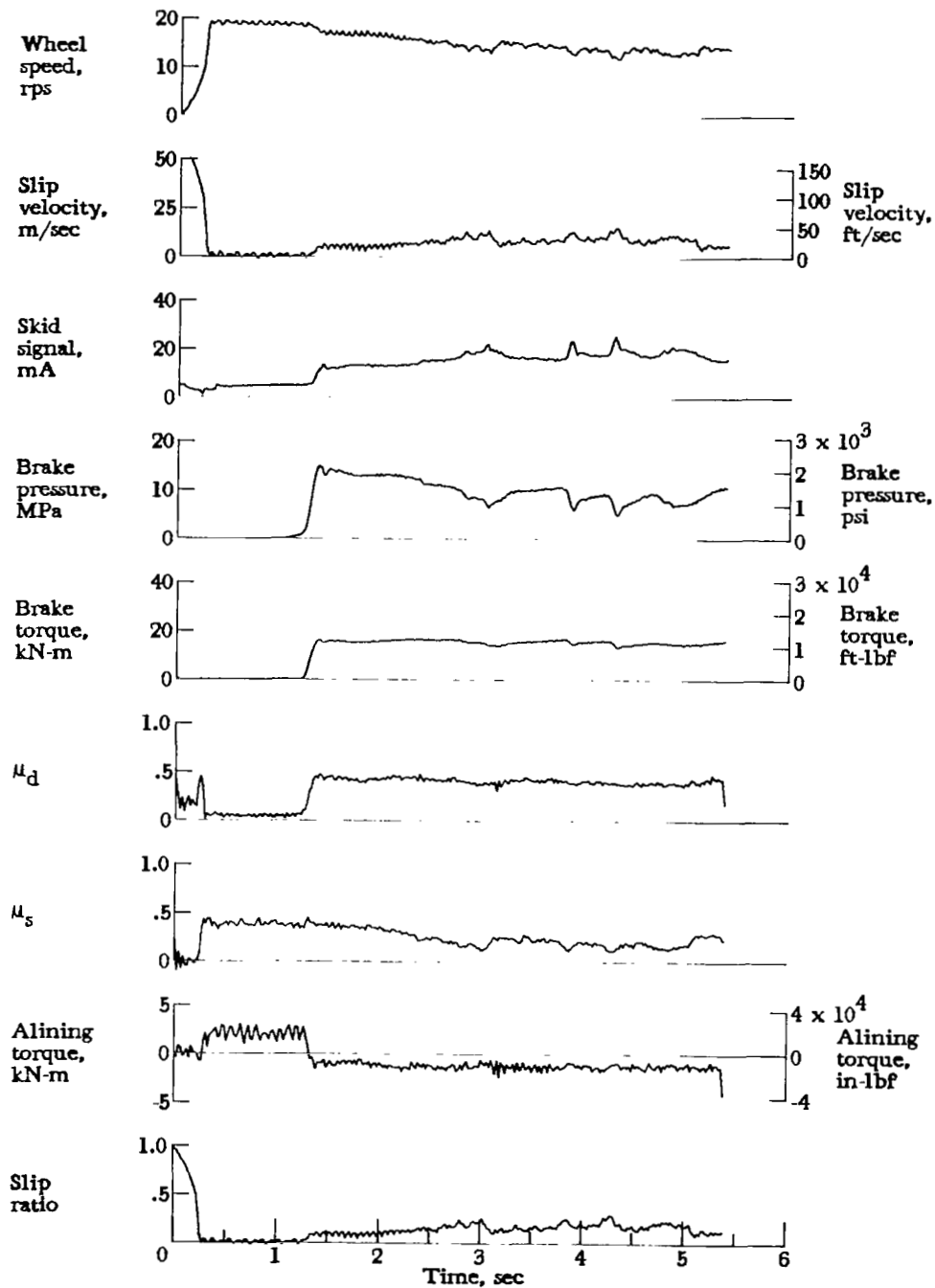


Figure A53.- Time histories for run 53. Nominal carriage speed, 103 knots; vertical load, 85.0 kN (19 100 lbf); yaw angle,  $6^\circ$ ; brake supply pressure, 21 MPa (3000 psi); tire condition, new; surface condition, dry.

APPENDIX

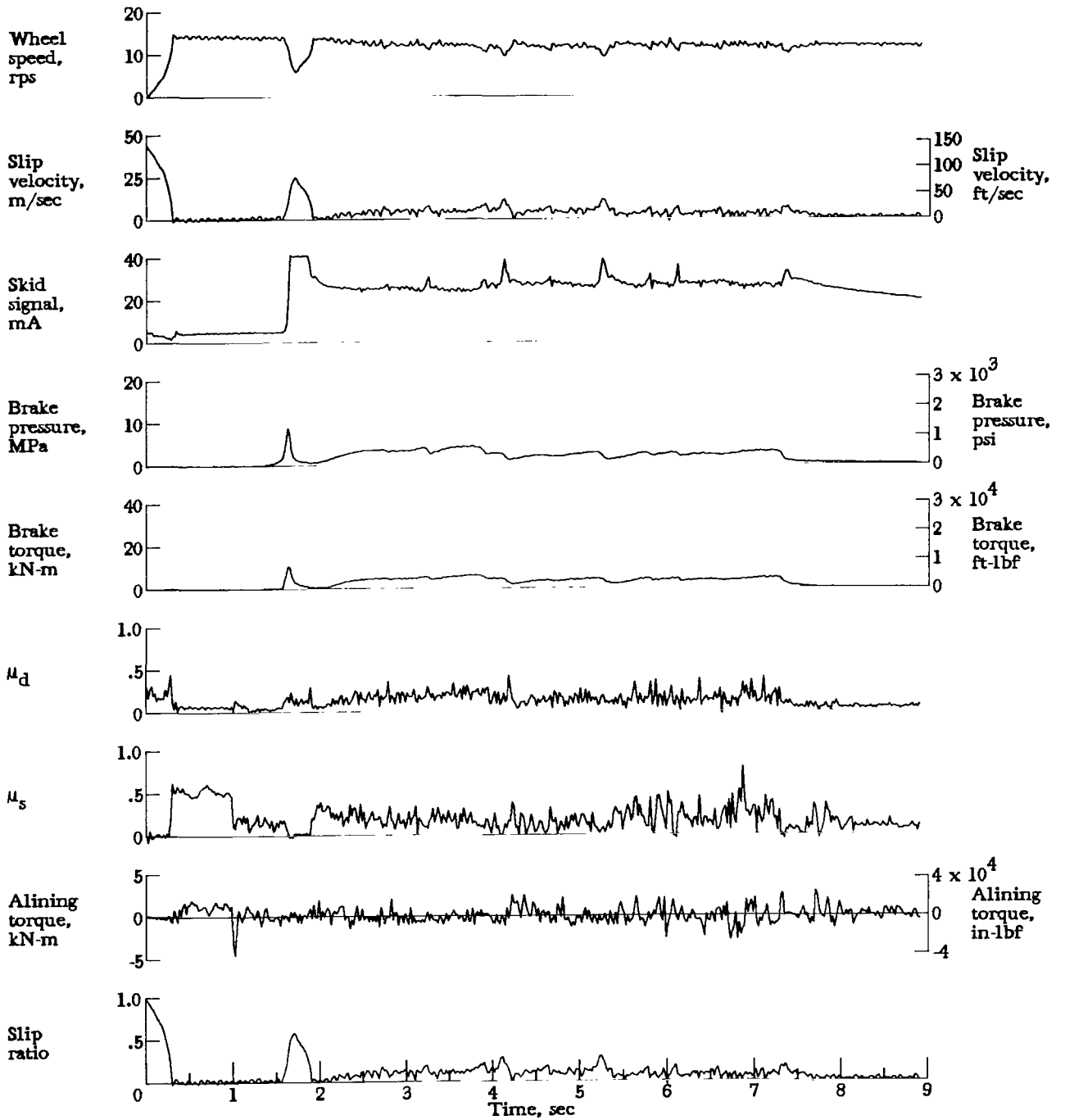


Figure A54.- Time histories for run 54. Nominal carriage speed, 77 knots; vertical load, 61.4 kN (13 800 lbf); yaw angle,  $6^\circ$ ; brake supply pressure, 20 MPa (2900 psi); tire condition, new; surface condition, damp.

APPENDIX

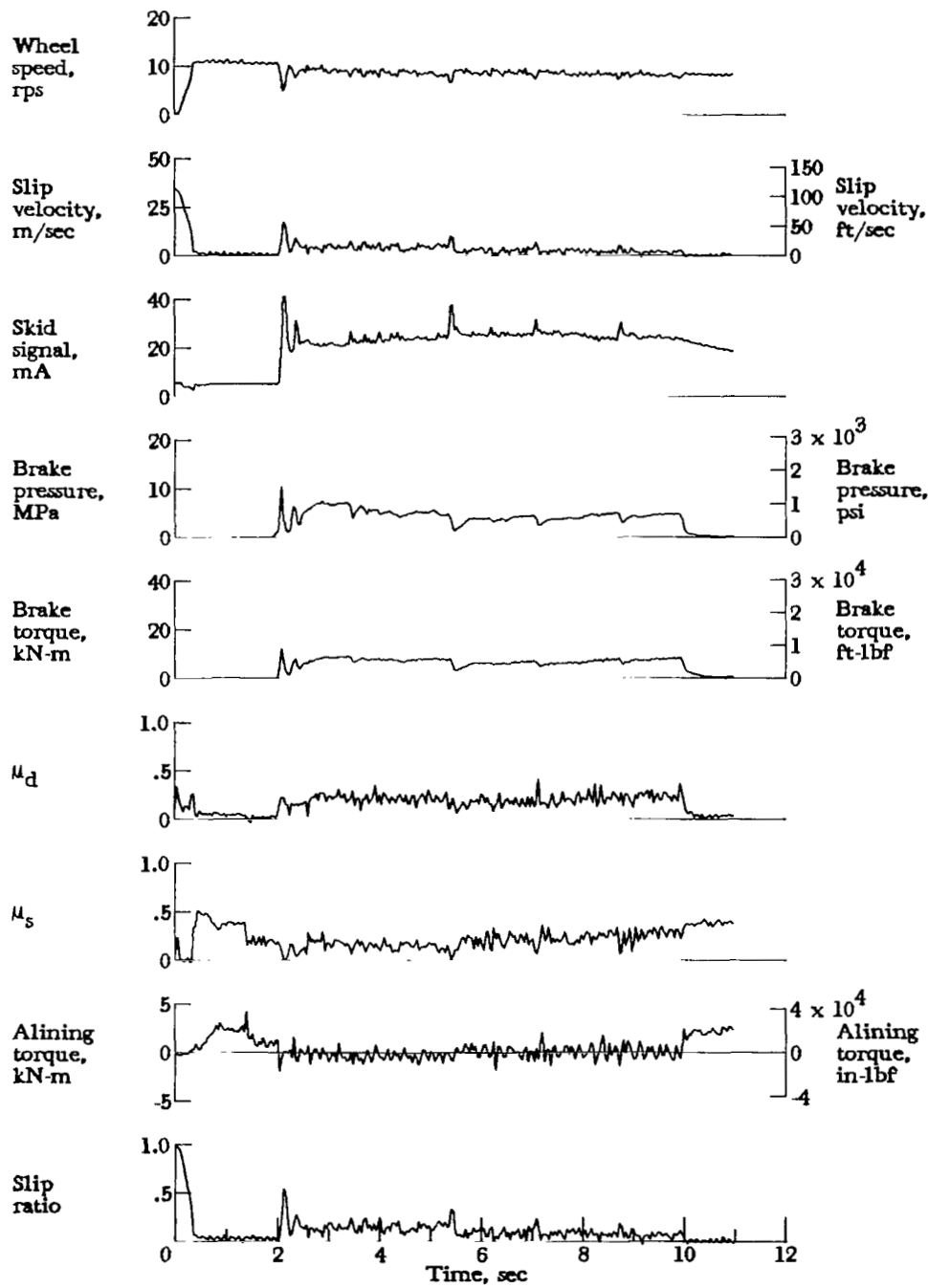


Figure A55.- Time histories for run 55. Nominal carriage speed, 57 knots; vertical load, 85.9 kN (19 300 lbf); yaw angle,  $6^\circ$ ; brake supply pressure, 21 MPa (3000 psi); tire condition, new; surface condition, damp.

APPENDIX

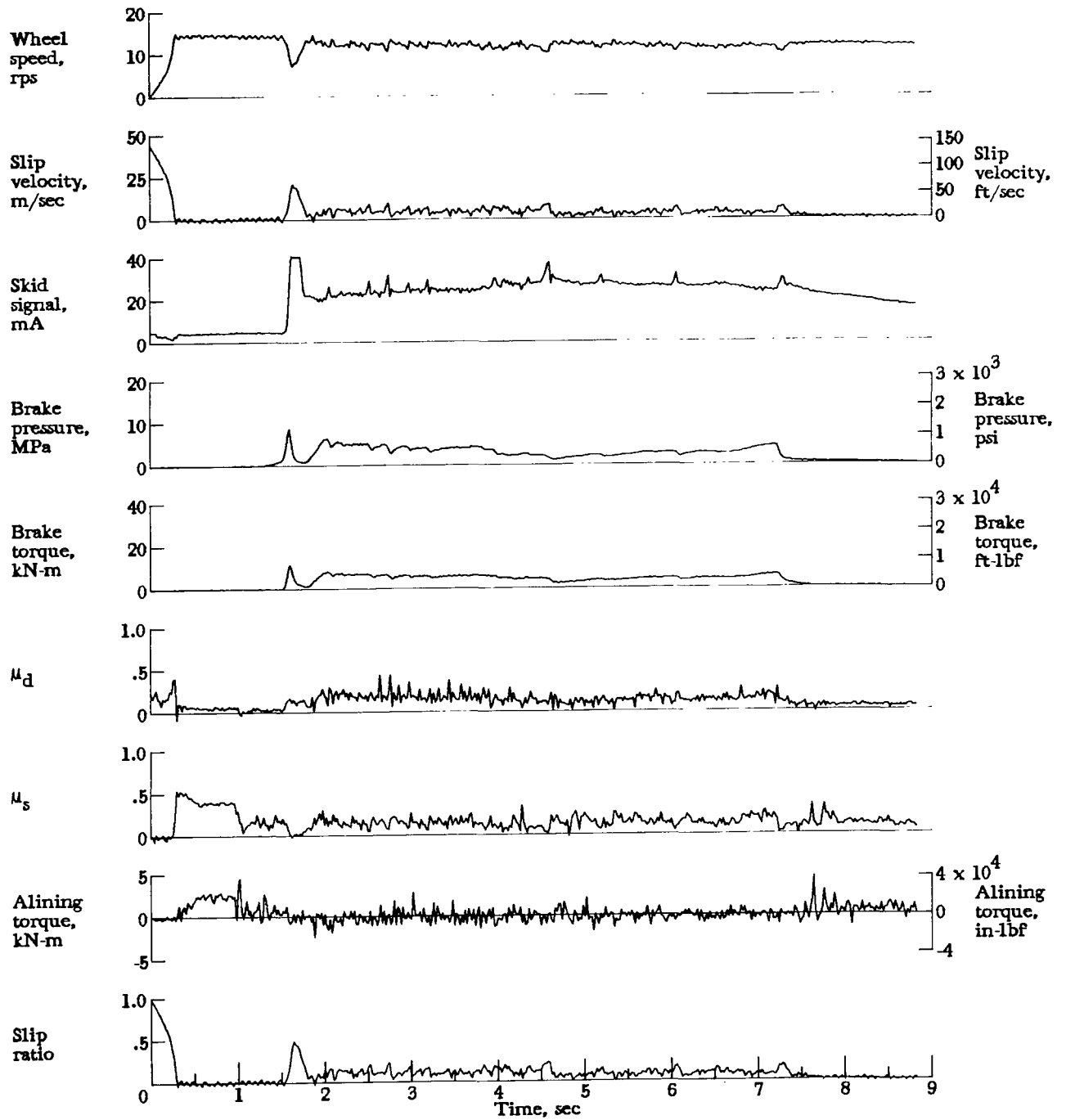


Figure A56.- Time histories for run 56. Nominal carriage speed, 77 knots; vertical load, 84.1 kN (18 900 lbf); yaw angle,  $6^\circ$ ; brake supply pressure, 20 MPa (2900 psi); tire condition, new; surface condition, damp.

APPENDIX

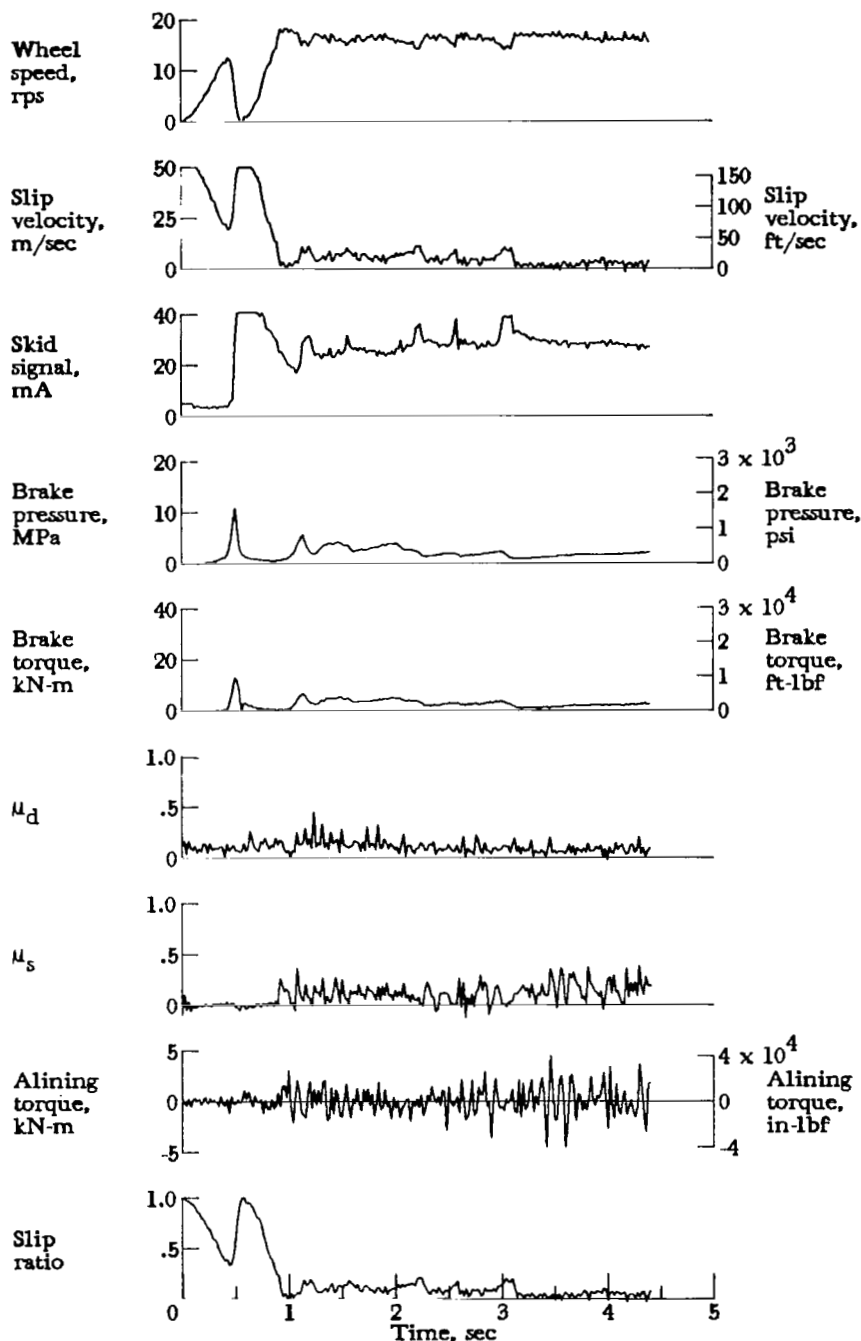


Figure A57.- Time histories for run 57. Nominal carriage speed, 106 knots; vertical load, 77.8 kN (17 500 lbf); yaw angle, 6°; brake supply pressure, 20 MPa (2900 psi); tire condition, new; surface condition, damp.

APPENDIX

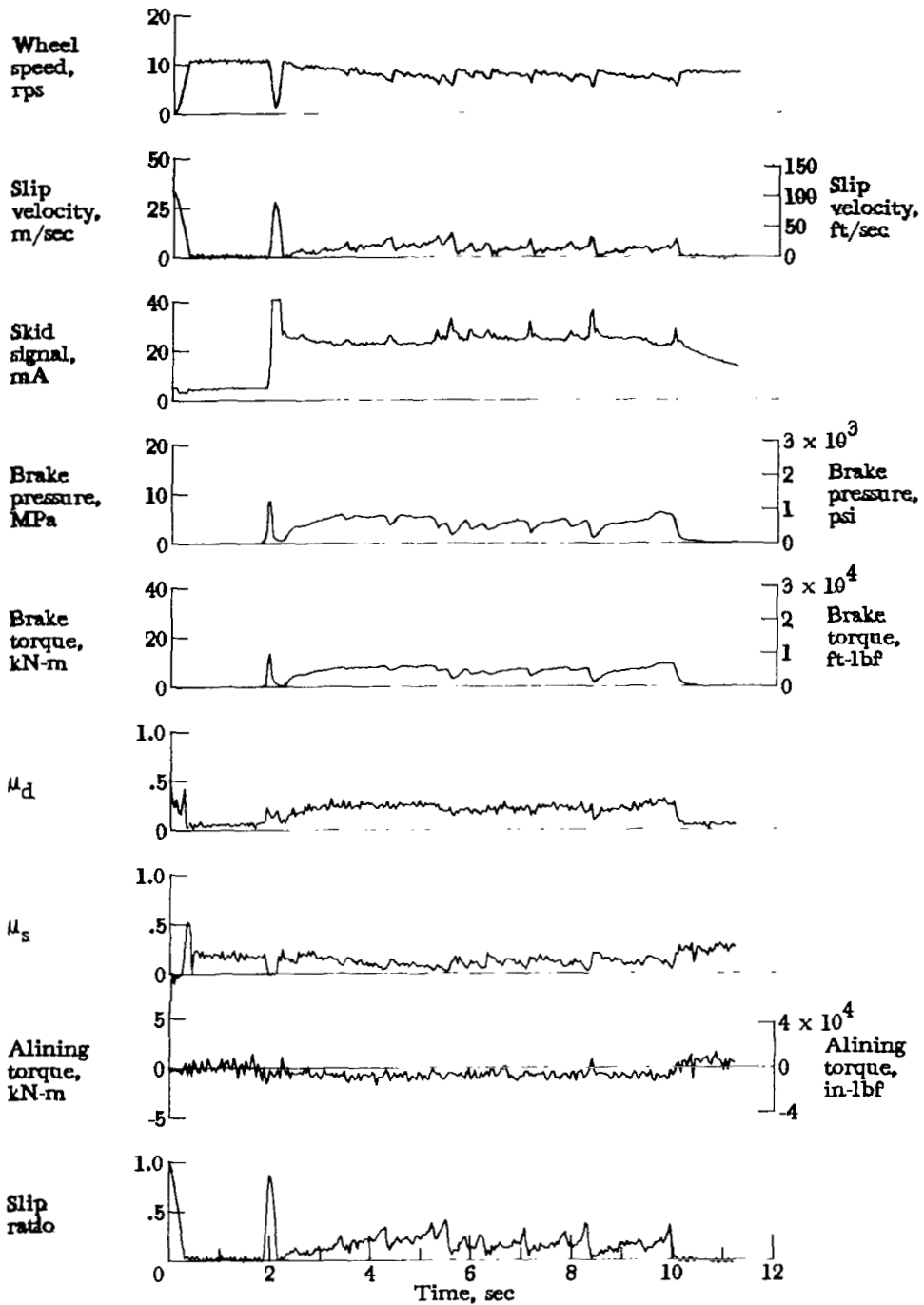


Figure A58.- Time histories for run 58. Nominal carriage speed, 56 knots; vertical load, 83.2 kN (18 700 lbf); yaw angle,  $6^\circ$ ; brake supply pressure, 21 MPa (3000 psi); tire condition, new; surface condition, flooded.

APPENDIX

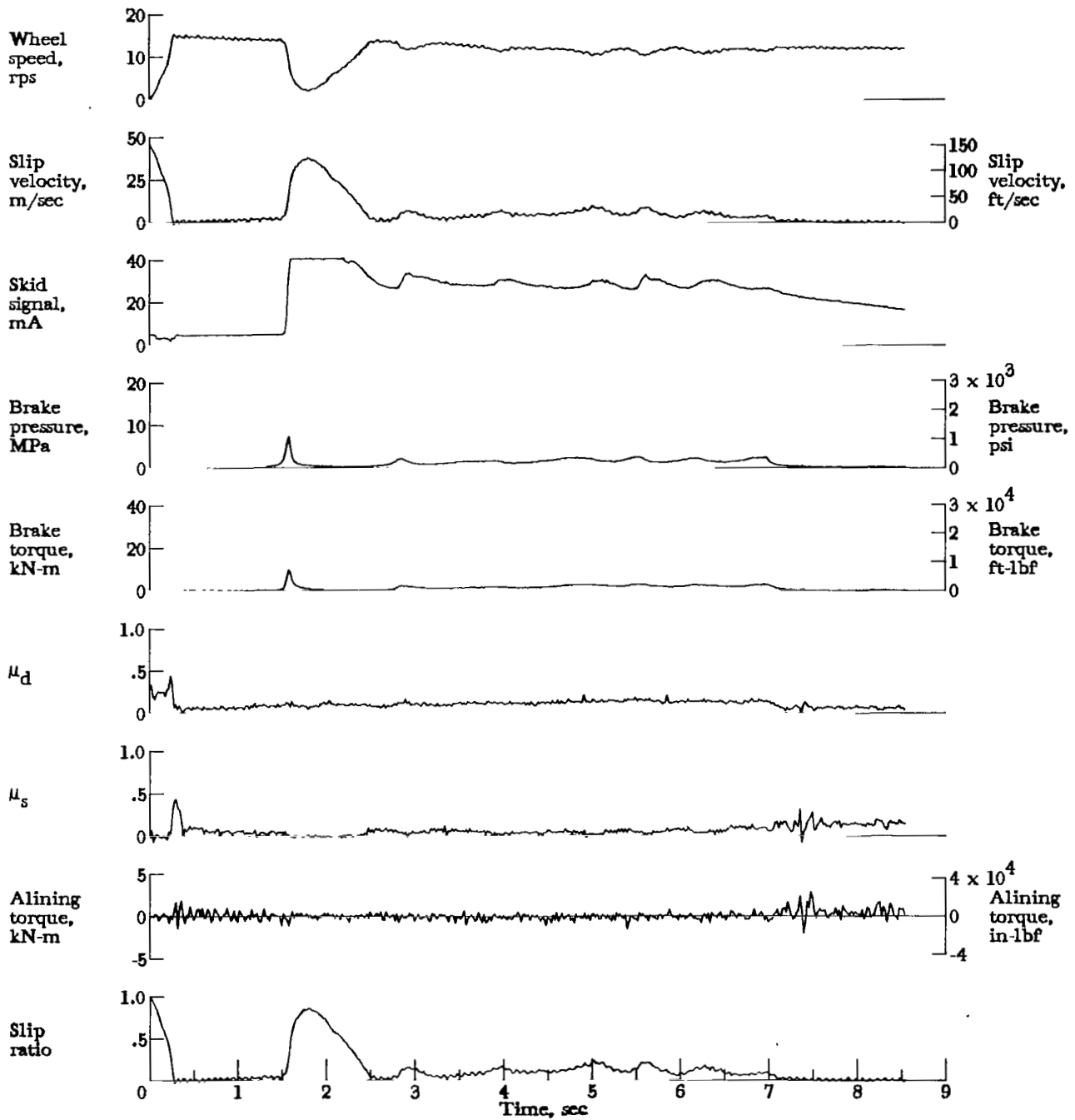


Figure A59.- Time histories for run 59. Nominal carriage speed, 80 knots; vertical load, 79.6 kN (17 900 lbf); yaw angle,  $6^\circ$ ; brake supply pressure, 21 MPa (3000 psi); tire condition, new; surface condition, flooded.

APPENDIX

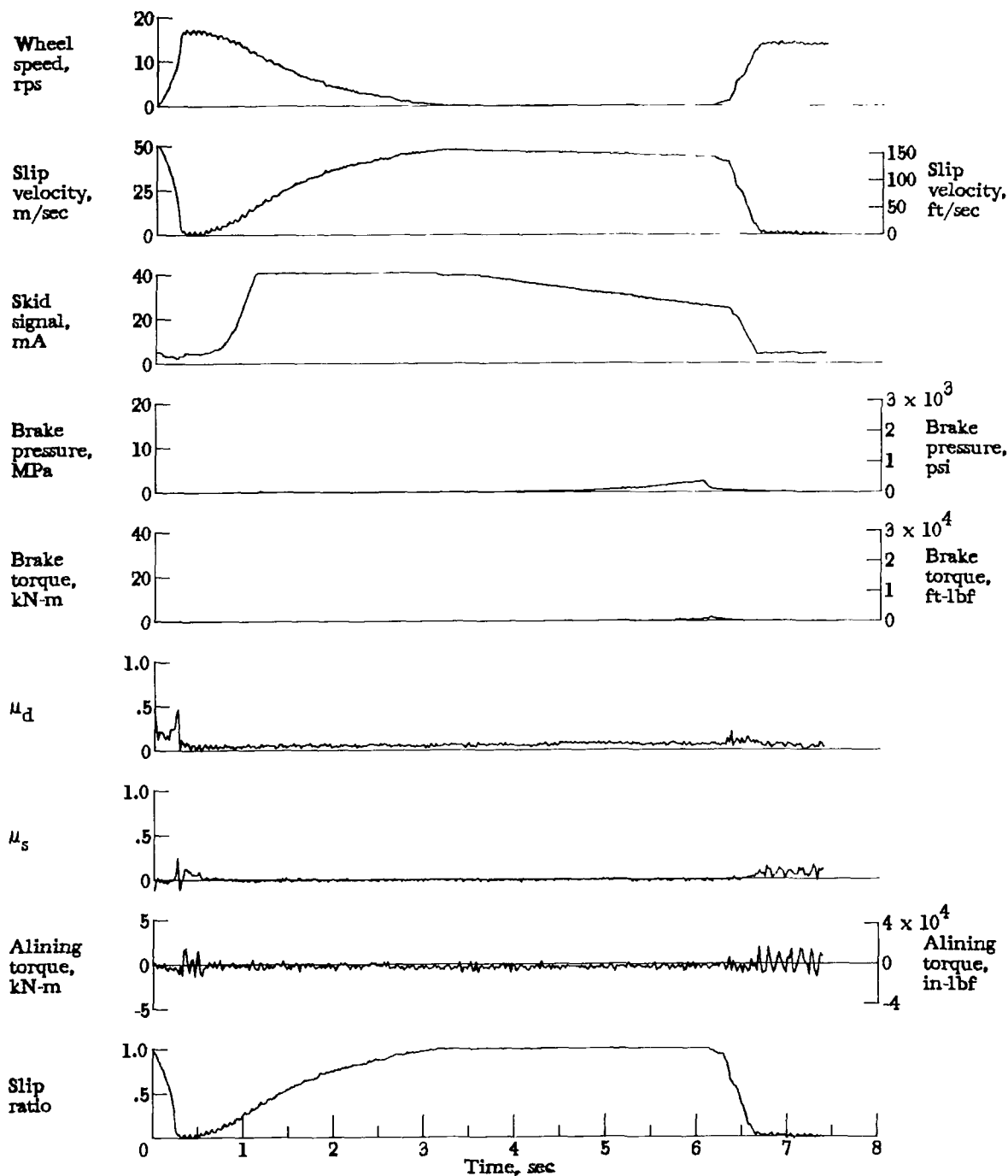


Figure A60.- Time histories for run 60. Nominal carriage speed, 92 knots; vertical load, 78.7 kN (17 700 lbf); yaw angle, 6°; brake supply pressure, 21 MPa (3000 psi); tire condition, new; surface condition, flooded.

APPENDIX

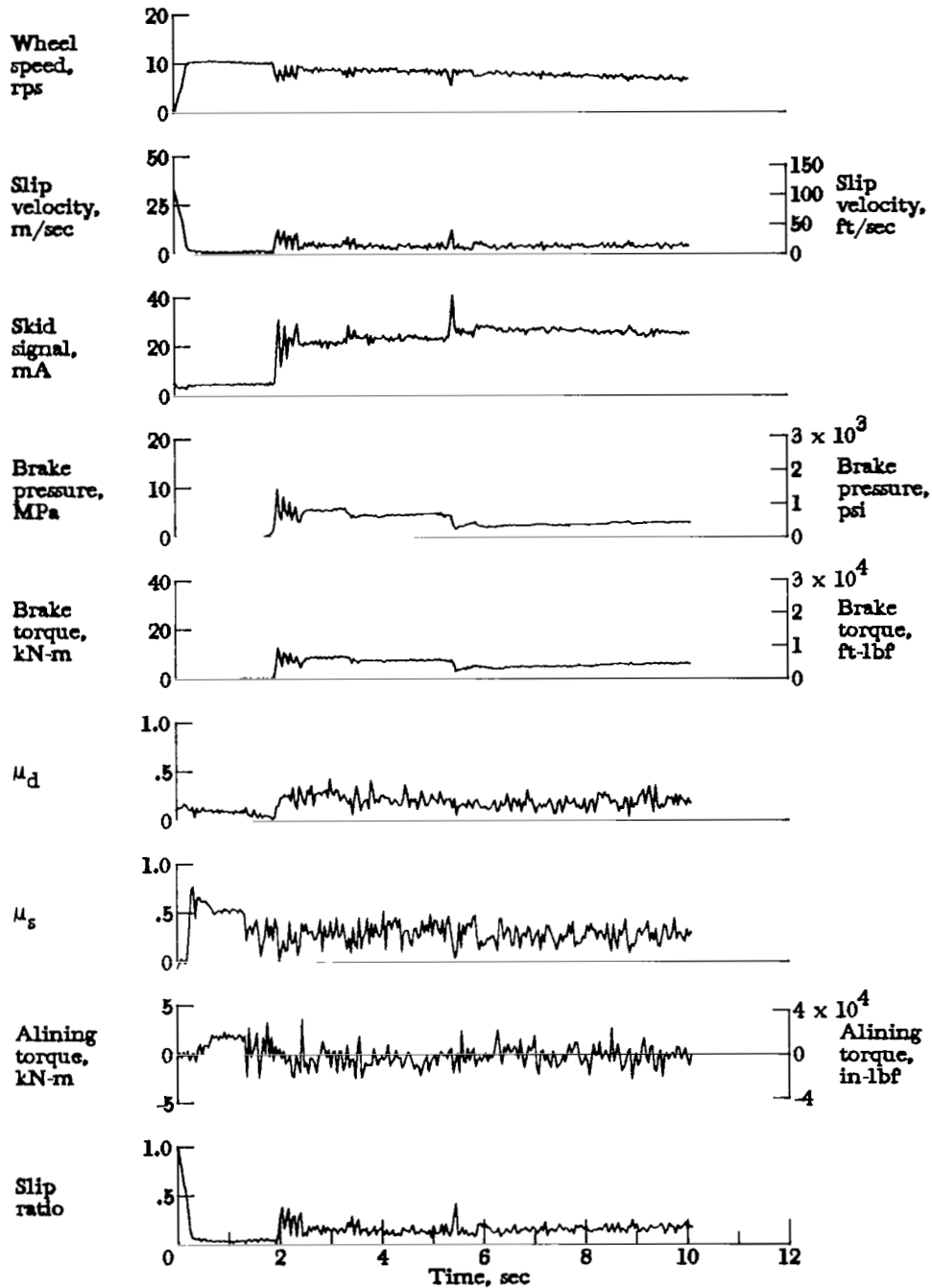


Figure A61.- Time histories for run 61. Nominal carriage speed, 55 knots; vertical load, 85.9 kN (19 300 lbf); yaw angle,  $9^\circ$ ; brake supply pressure, 19 MPa (2800 psi); tire condition, new; surface condition, damp.

APPENDIX

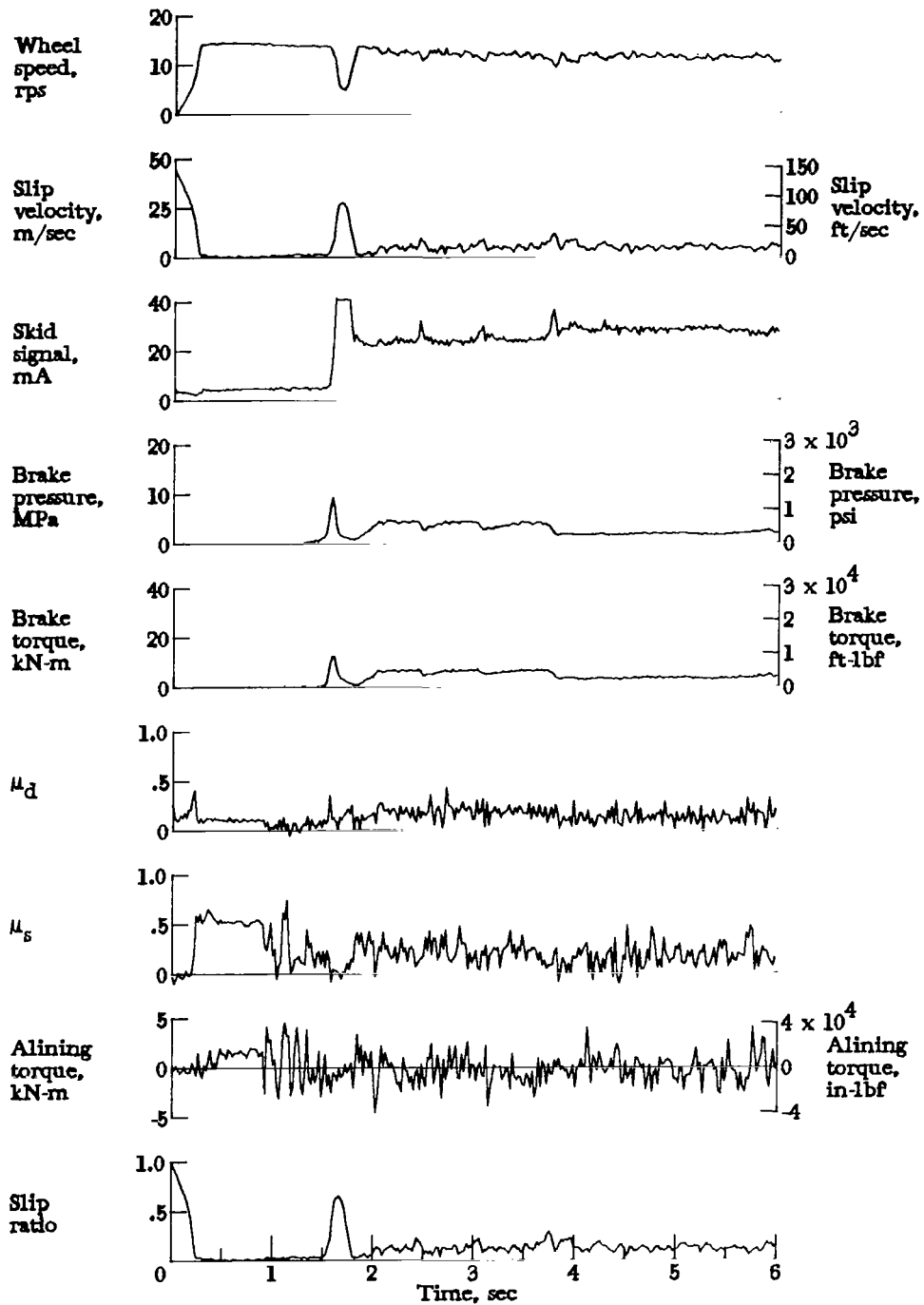


Figure A62.- Time histories for run 62. Nominal carriage speed, 78 knots; vertical load, 85.9 kN (19 300 lbf); yaw angle, 9°; brake supply pressure, 20 MPa (2900 psi); tire condition, new; surface condition, damp.

APPENDIX

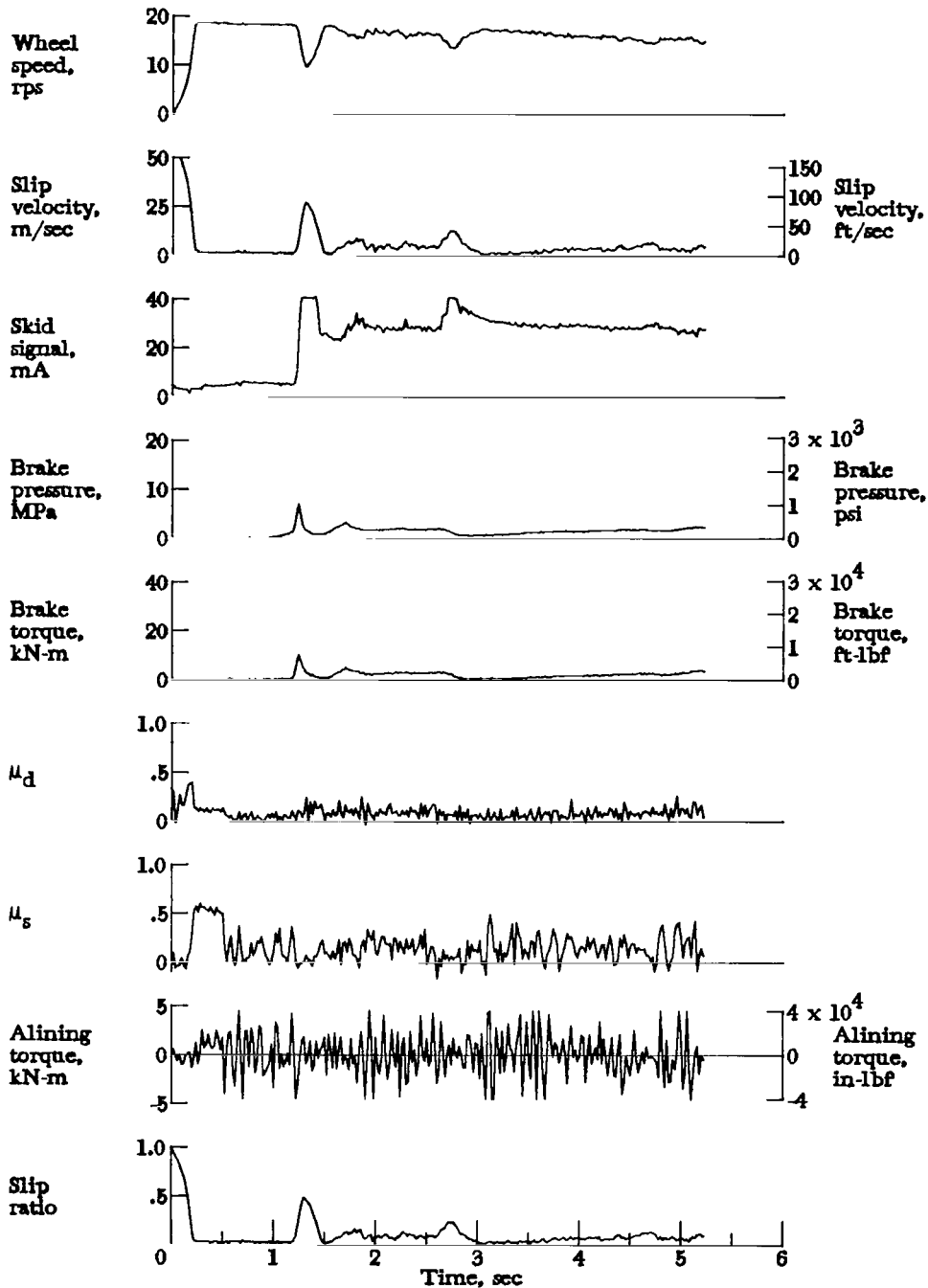


Figure A63.- Time histories for run 63. Nominal carriage speed, 104 knots; vertical load, 84.1 kN (18 900 lbf); yaw angle,  $9^\circ$ ; brake supply pressure, 20 MPa (2900 psi); tire condition, new; surface condition, damp.

APPENDIX

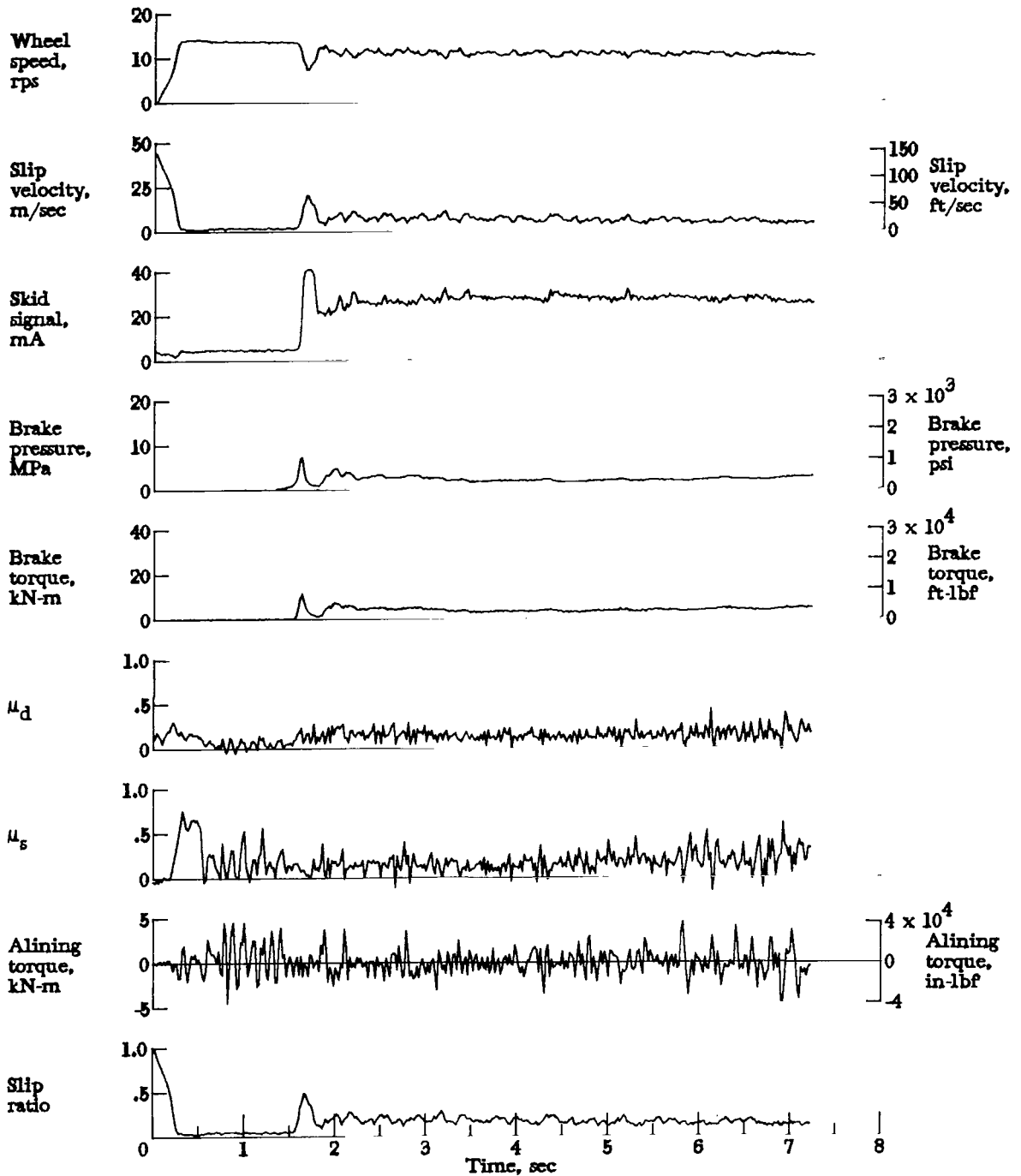


Figure A64.- Time histories for run 64. Nominal carriage speed, 76 knots; vertical load, 85.0 kN (19 100 lbf); yaw angle, 12°; brake supply pressure, 20 MPa (2900 psi); tire condition, new; surface condition, damp.

APPENDIX

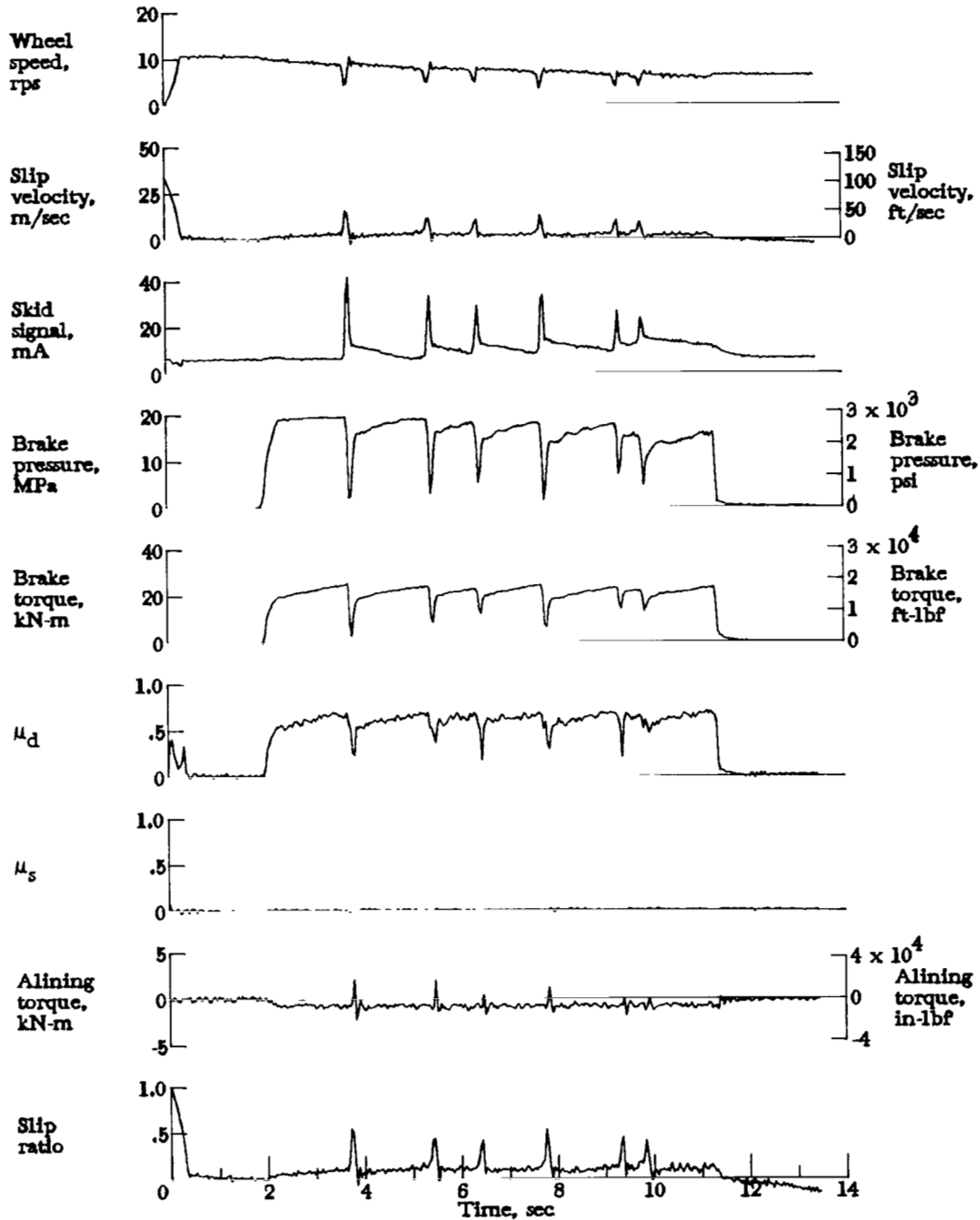


Figure A65.- Time histories for run 65. Nominal carriage speed, 49 knots; vertical load, 72.1 kN (16 200 lbf); yaw angle,  $0^\circ$ ; brake supply pressure, 20 MPa (2900 psi); tire condition, worn; surface condition, dry.

APPENDIX

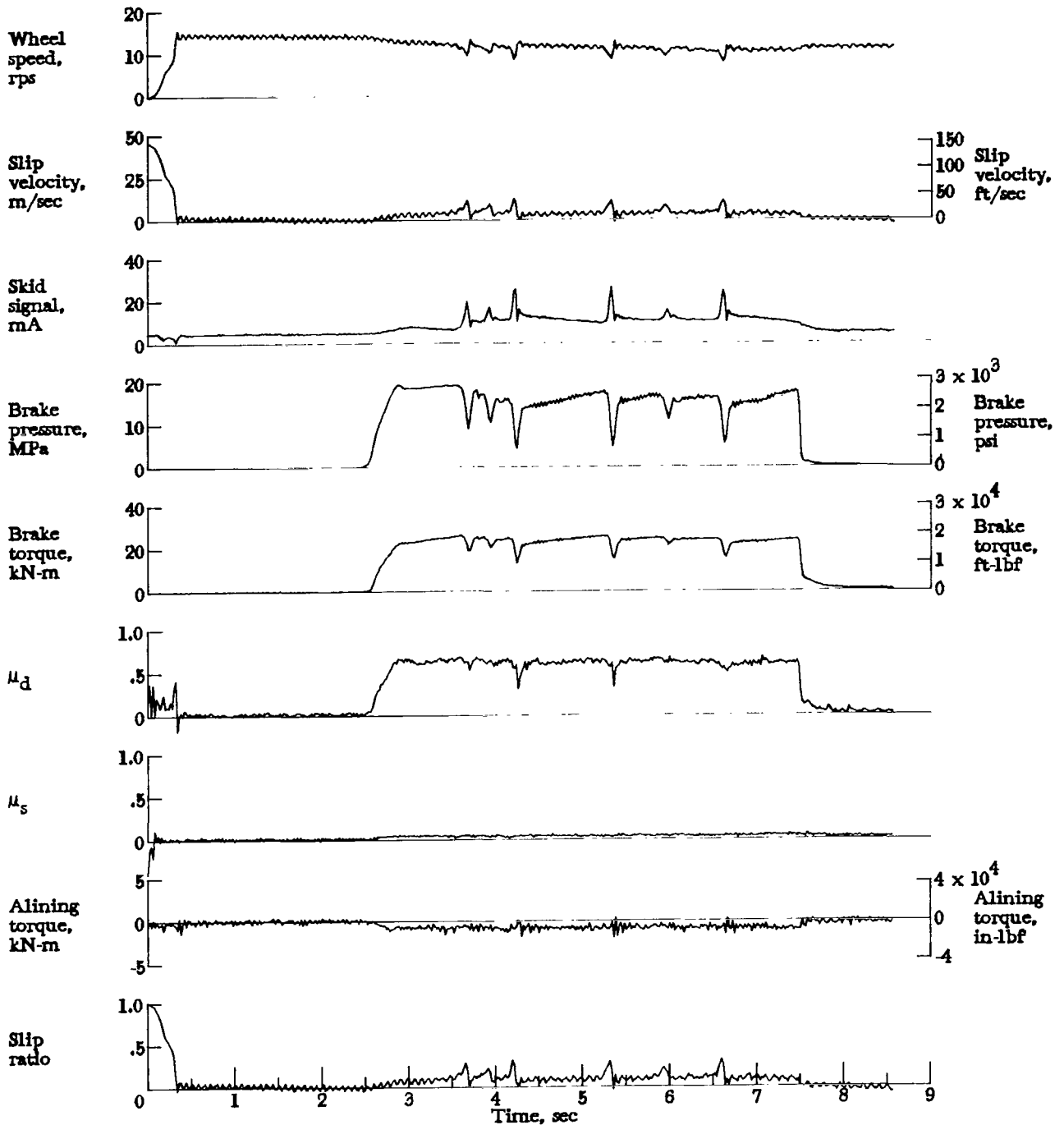


Figure A66.- Time histories for run 66. Nominal carriage speed, 73 knots; vertical load, 76.5 kN (17 200 lbf); yaw angle, 0°; brake supply pressure, 21 MPa (3000 psi); tire condition, worn; surface condition, dry.

APPENDIX

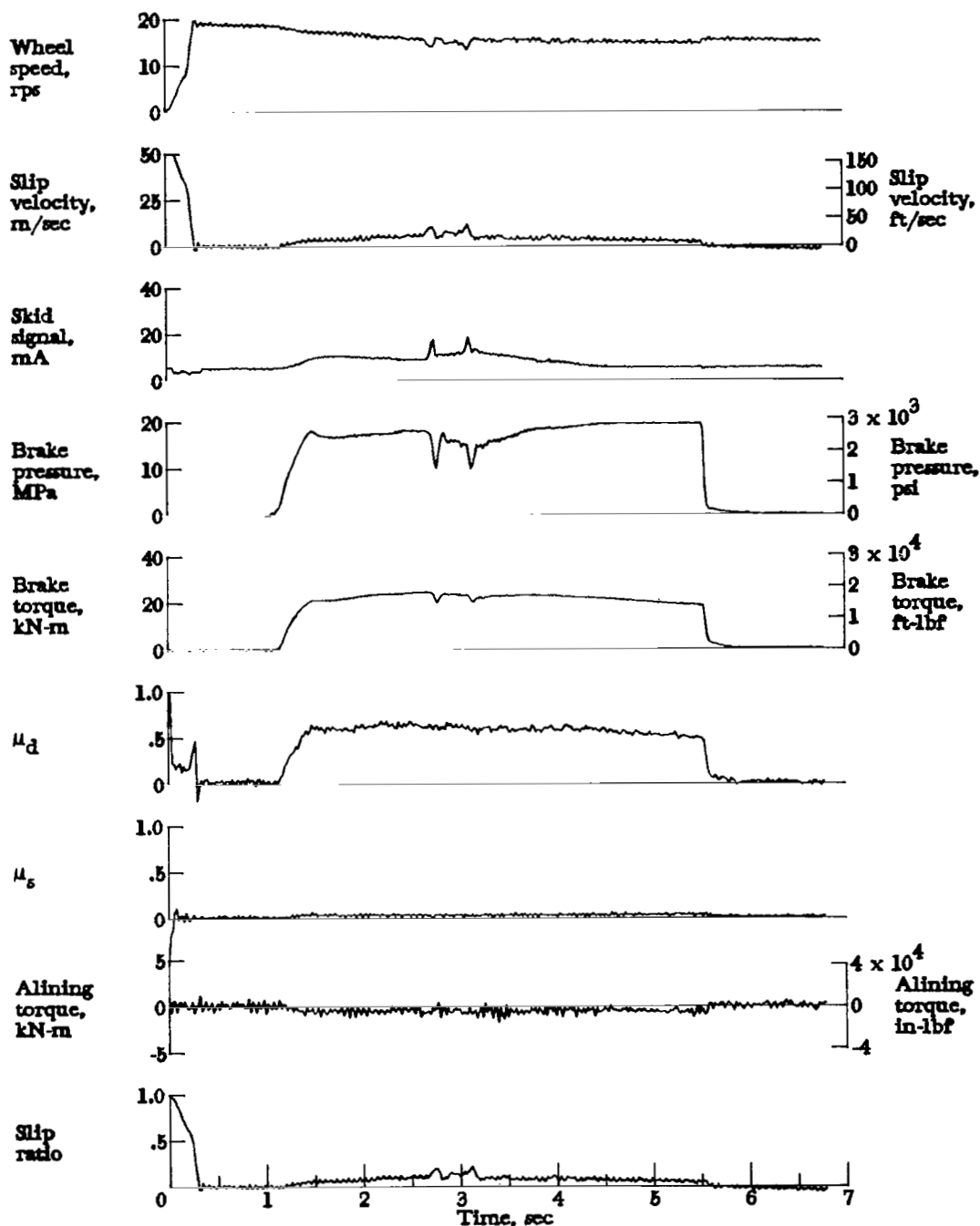


Figure A67.- Time histories for run 67. Nominal carriage speed, 101 knots; vertical load, 76.5 kN (17 200 lbf); yaw angle,  $0^\circ$ ; brake supply pressure, 21 MPa (3000 psi); tire condition, worn; surface condition, dry.

APPENDIX

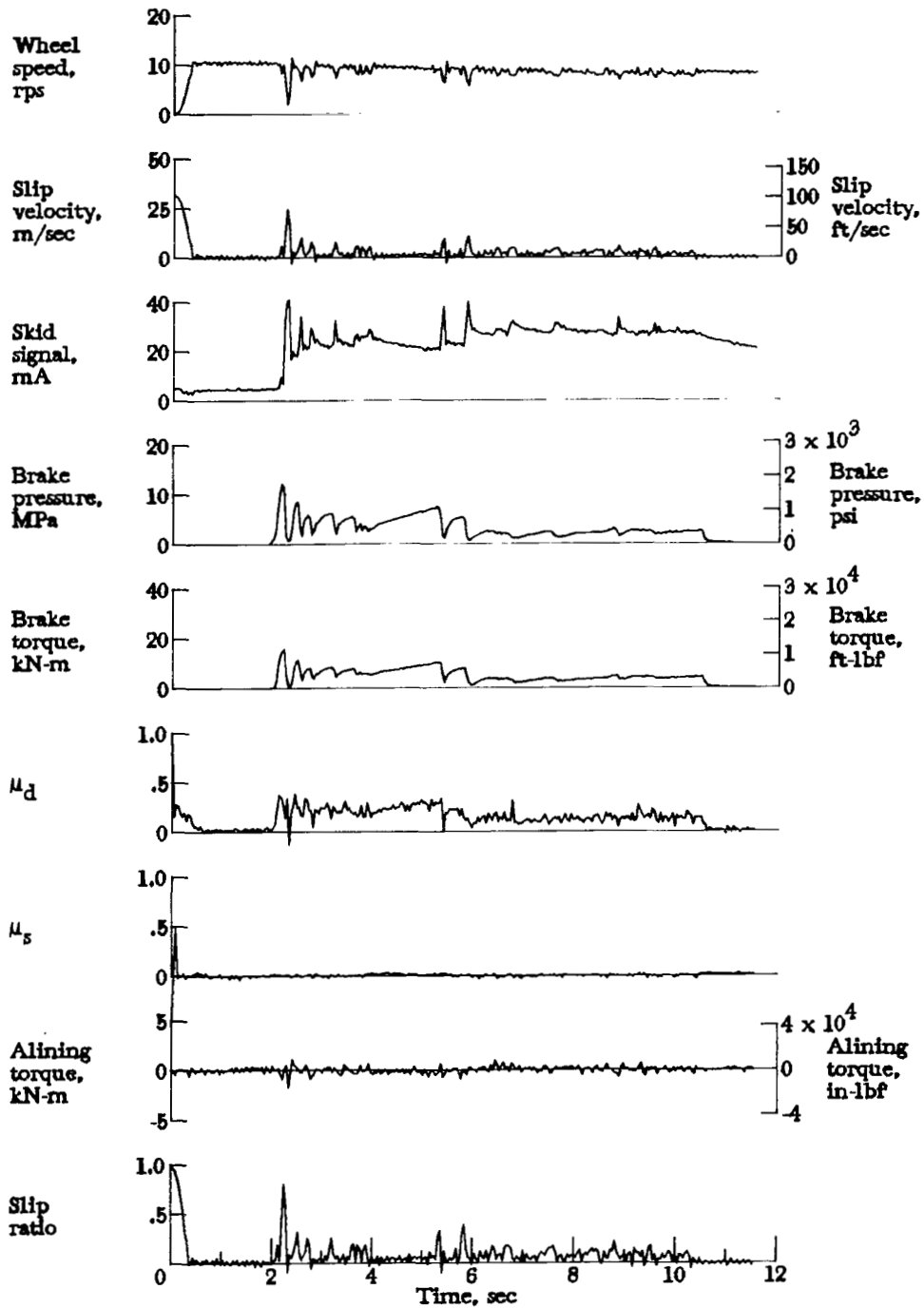


Figure A68.- Time histories for run 68. Nominal carriage speed, 54 knots; vertical load, 71.2 kN (16 000 lbf); yaw angle,  $0^\circ$ ; brake supply pressure, 20 MPa (2900 psi); tire condition, worn; surface condition, damp.

APPENDIX

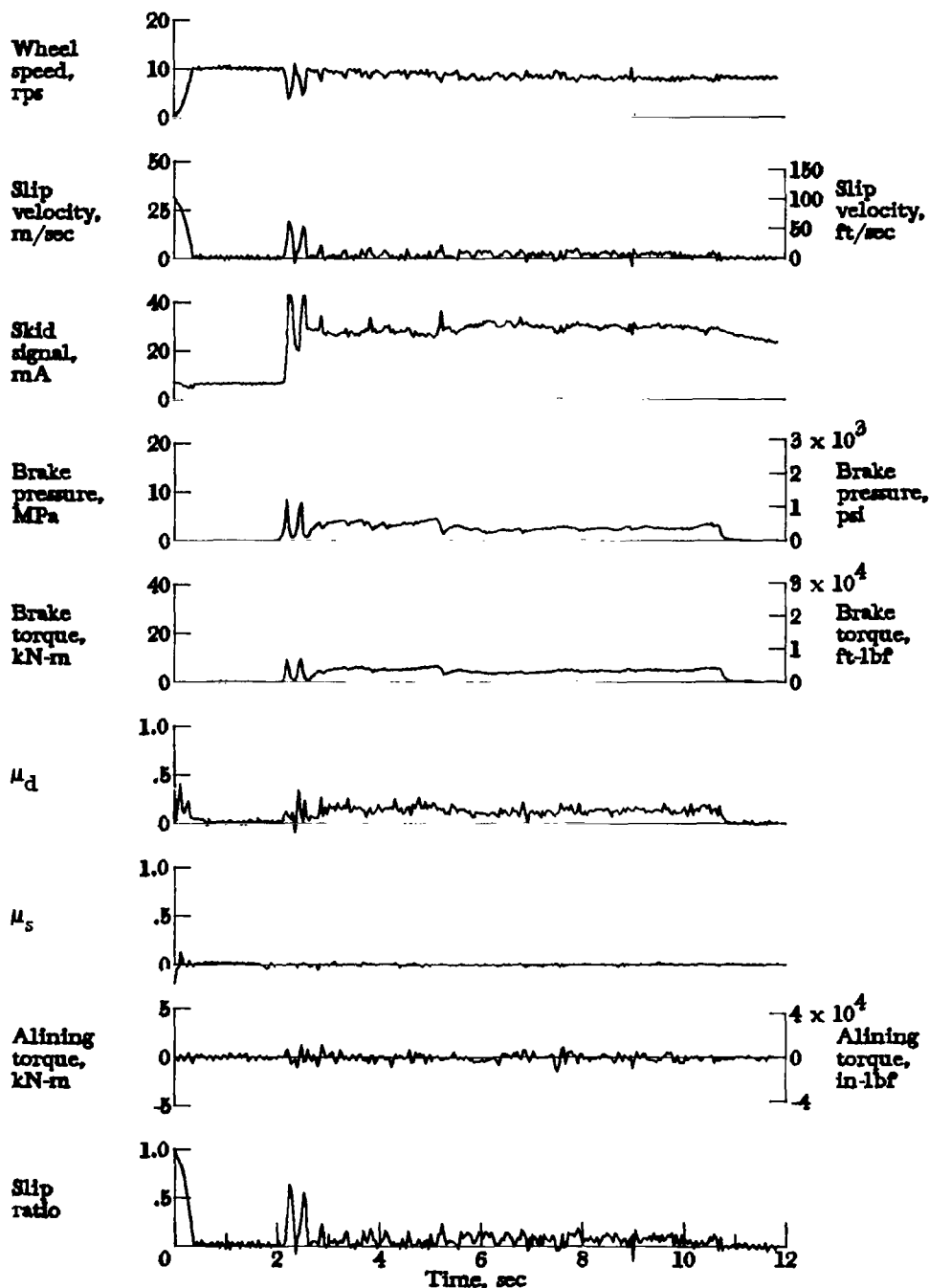


Figure A69.- Time histories for run 69. Nominal carriage speed, 53 knots; vertical load, 89.0 kN (20 000 lbf); yaw angle, 0°; brake supply pressure, 21 MPa (3000 psi); tire condition, worn; surface condition, damp.

APPENDIX

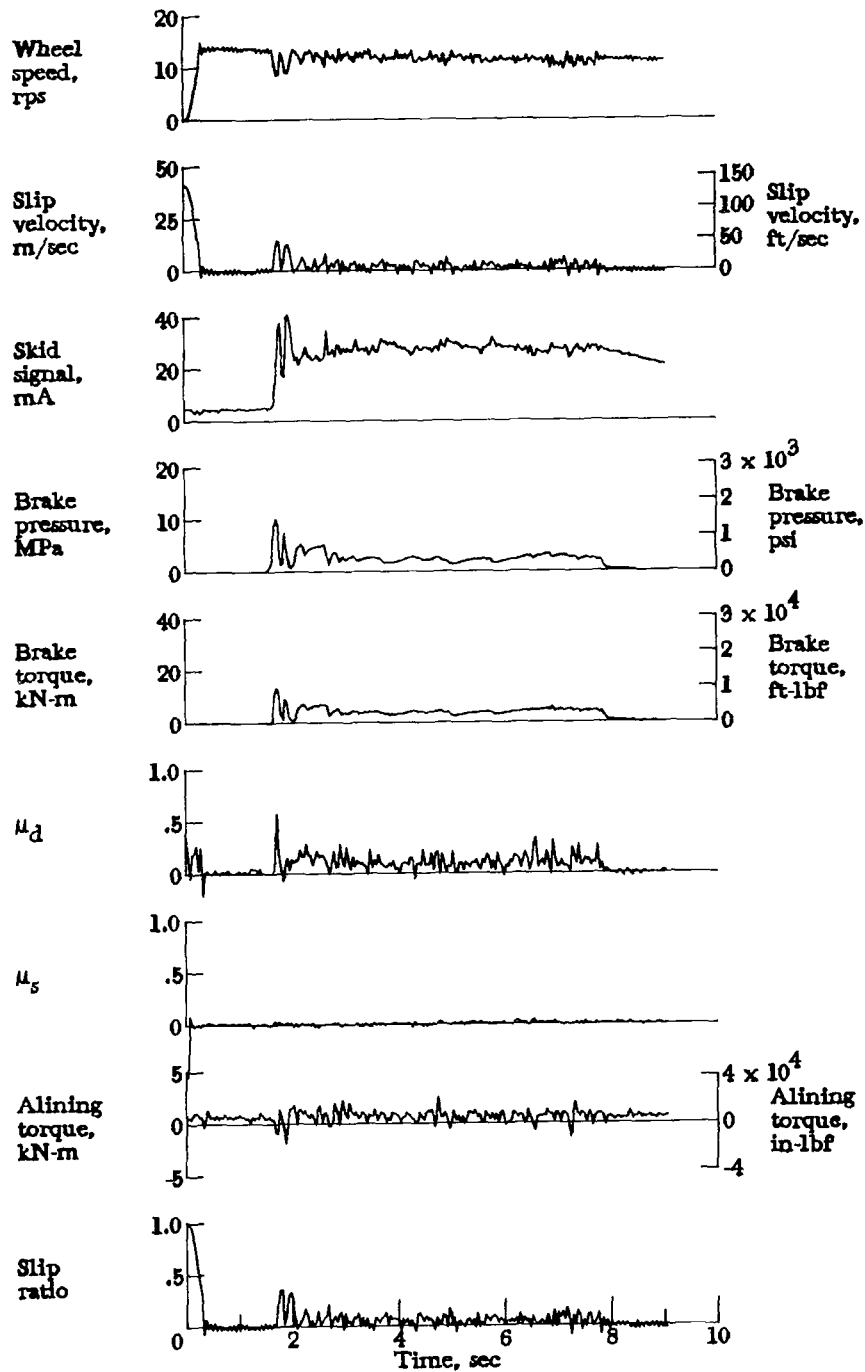


Figure A70.- Time histories for run 70. Nominal carriage speed, 72 knots; vertical load, 87.6 kN (19 700 lbf); yaw angle,  $0^\circ$ ; brake supply pressure, 21 MPa (3000 psi); tire condition, worn; surface condition, damp.

APPENDIX

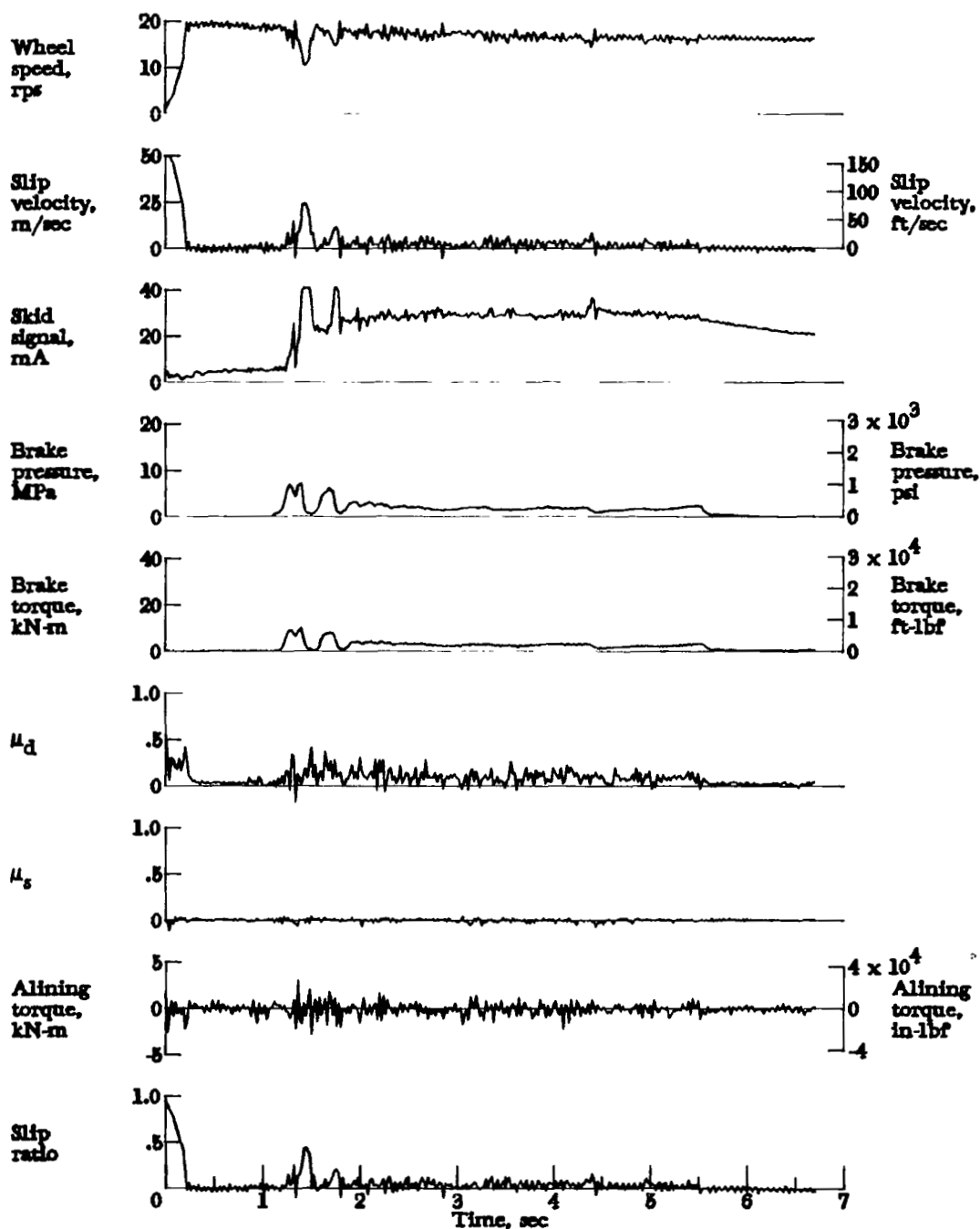


Figure A71.- Time histories for run 71. Nominal carriage speed, 104 knots; vertical load, 87.6 kN (19 700 lbf); yaw angle, 0°; brake supply pressure, 21 MPa (3000 psi); tire condition, worn; surface condition, damp.

APPENDIX

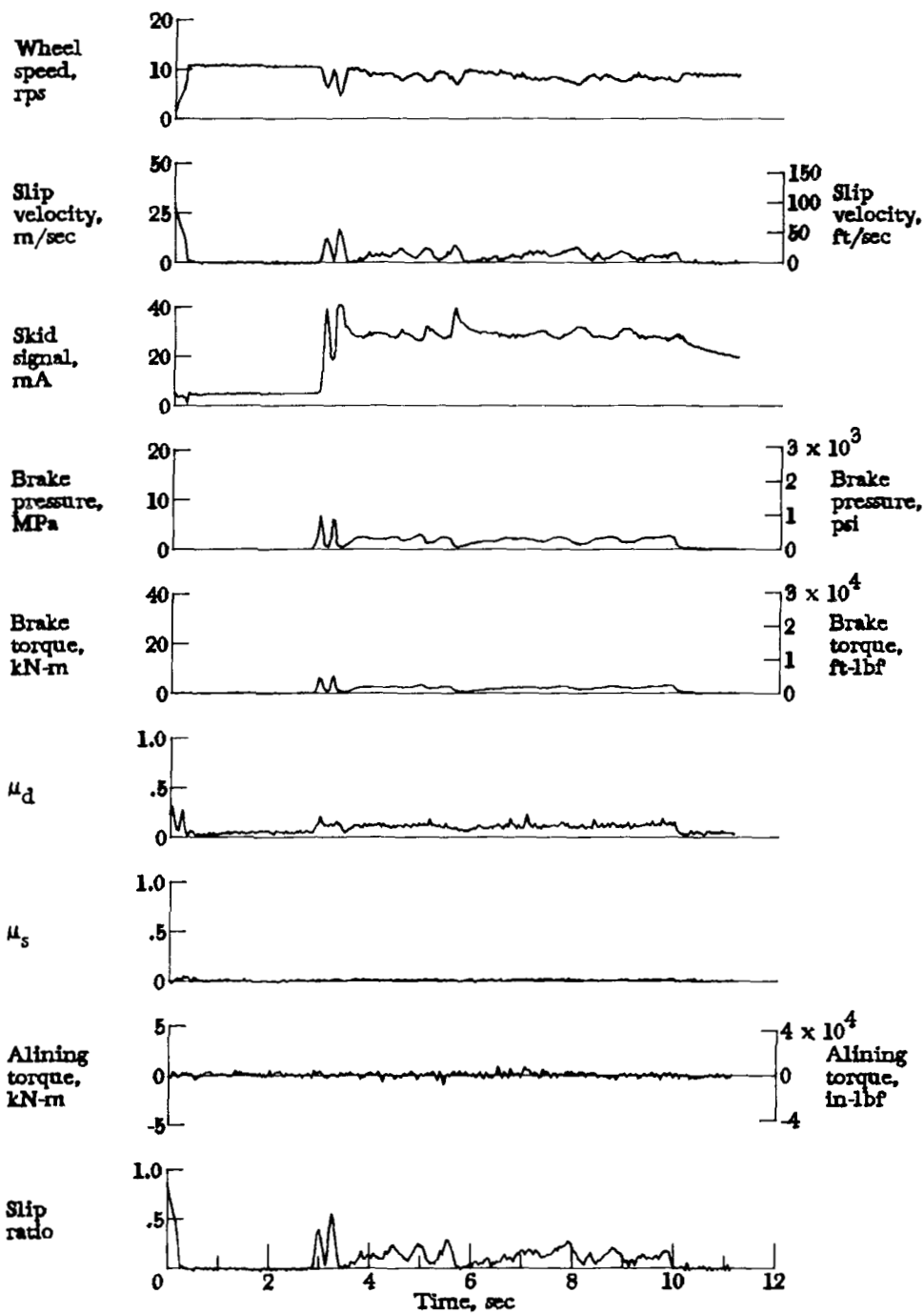


Figure A72.- Time histories for run 72. Nominal carriage speed, 57 knots; vertical load, 72.5 kN (16 300 lbf); yaw angle, 0°; brake supply pressure, 21 MPa (3000 psi); tire condition, worn; surface condition, flooded.

APPENDIX

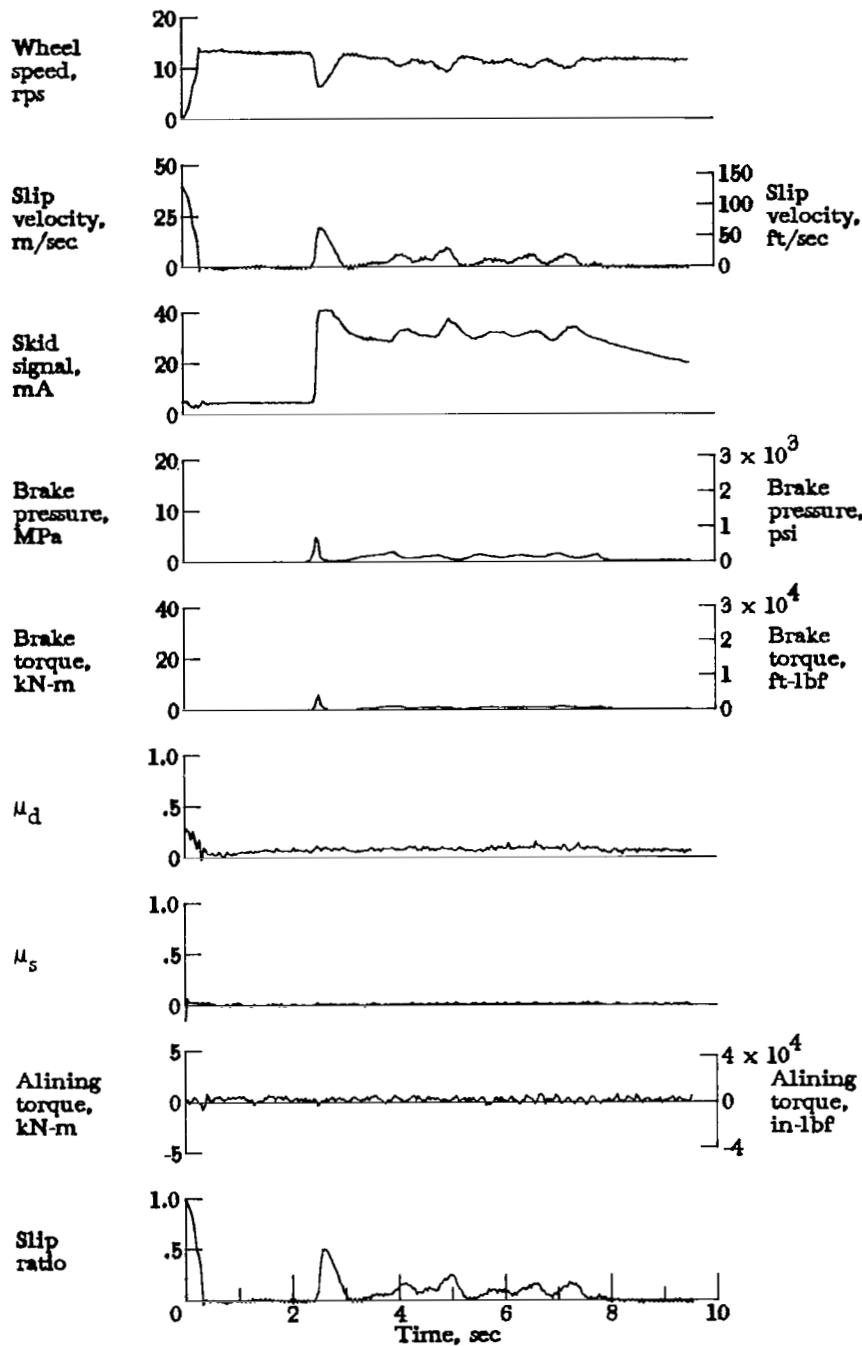


Figure A73.- Time histories for run 73. Nominal carriage speed, 72 knots; vertical load, 72.5 kN (16 300 lbf); yaw angle,  $0^\circ$ ; brake supply pressure, 20 MPa (2900 psi); tire condition, worn; surface condition, flooded.

APPENDIX

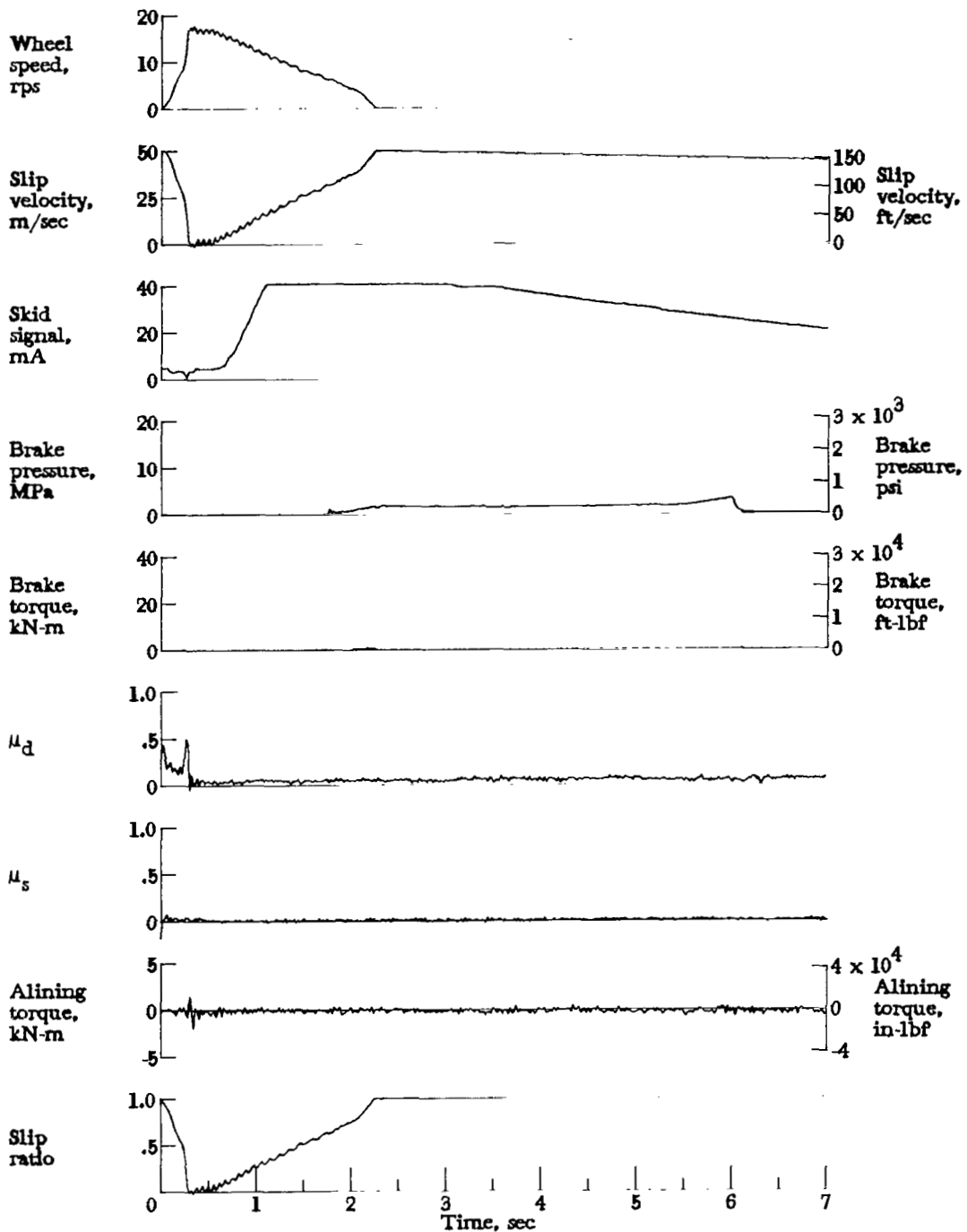


Figure A74.- Time histories for run 74. Nominal carriage speed, 94 knots; vertical load, 72.5 kN (16 300 lbf); yaw angle, 0°; brake supply pressure, 21 MPa (3000 psi); tire condition, worn; surface condition, flooded.

APPENDIX

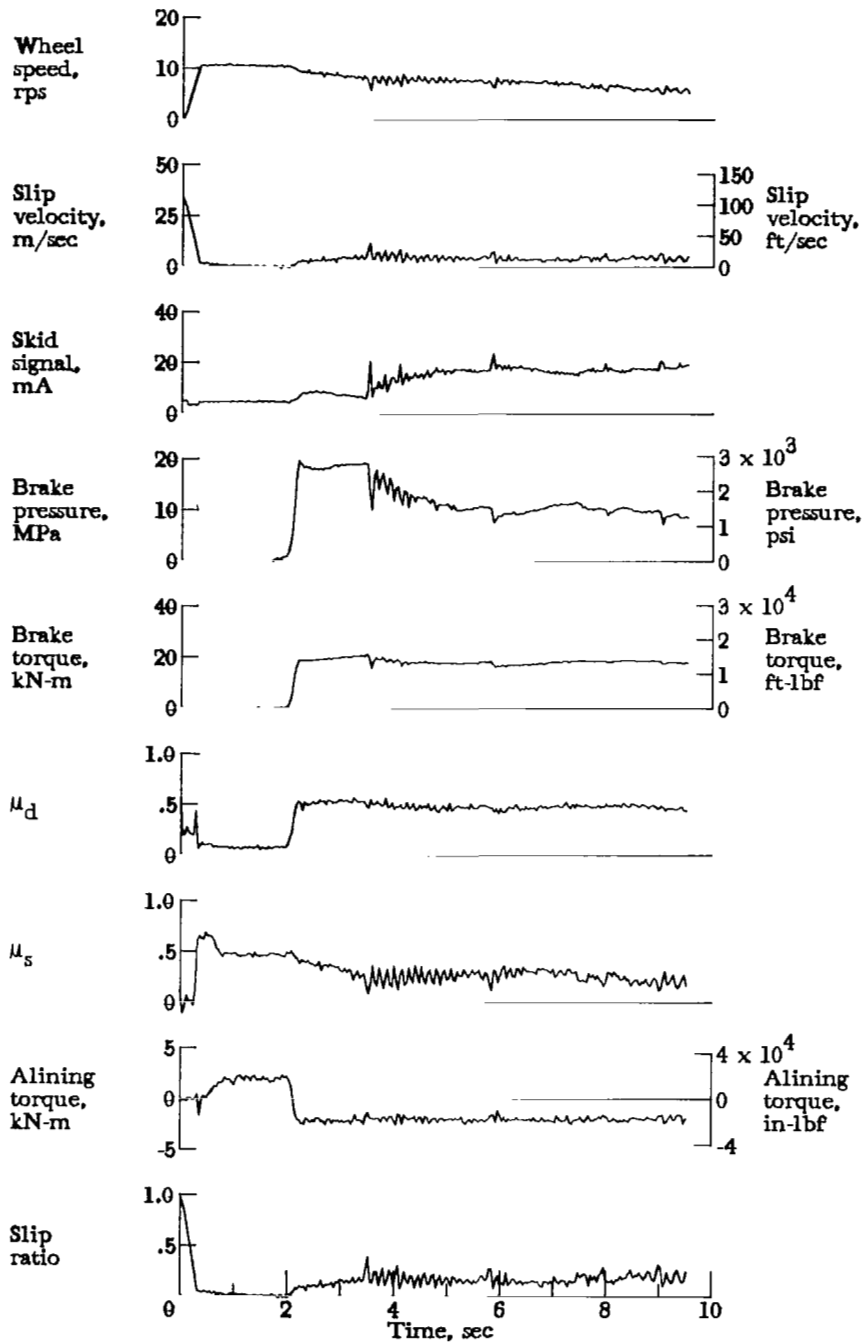


Figure A75.- Time histories for run 75. Nominal carriage speed, 51 knots; vertical load, 84.1 kN (18 900 lbf); yaw angle, 6°; brake supply pressure, 21 MPa (3000 psi); tire condition, worn; surface condition, dry.

# APPENDIX

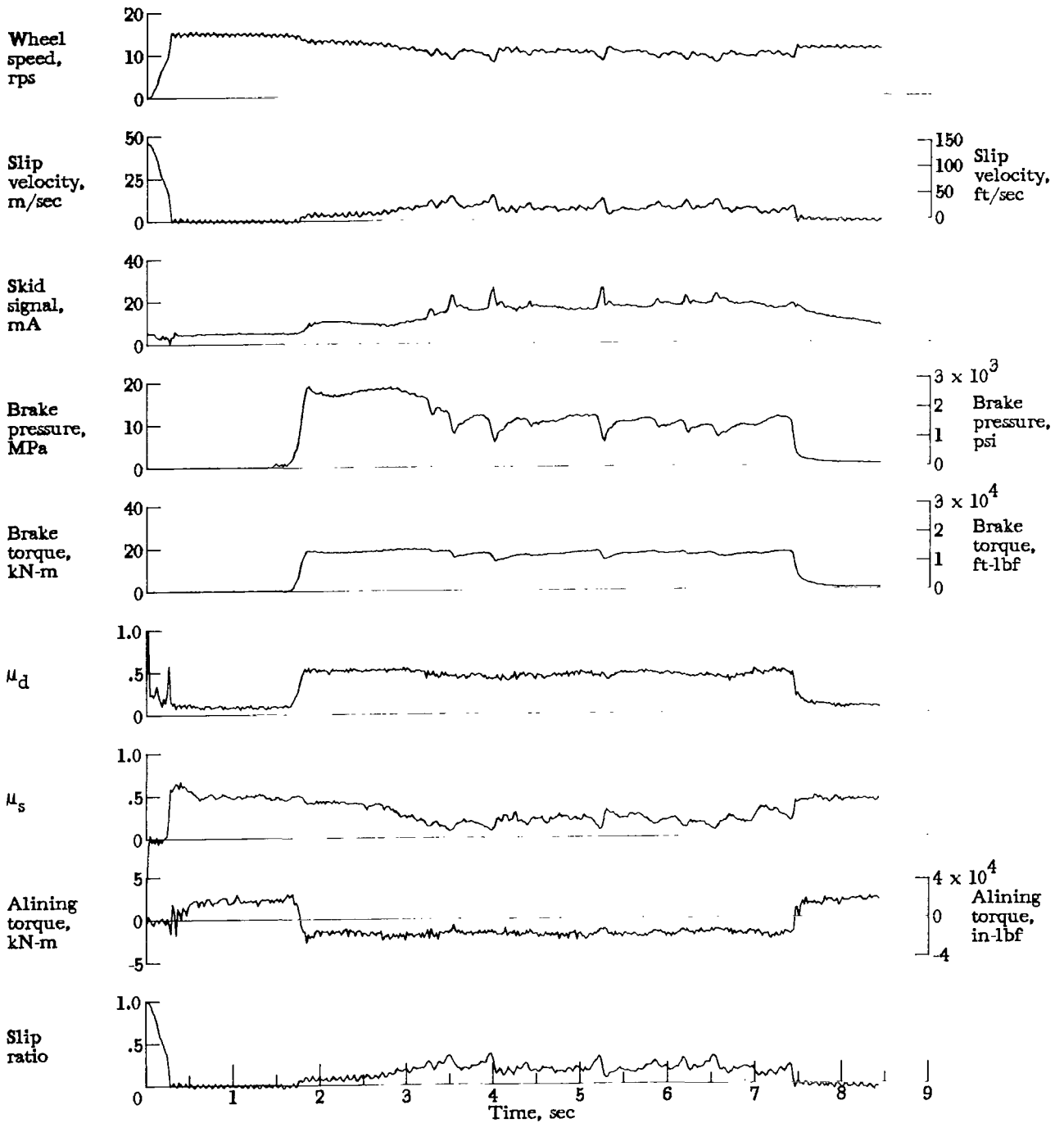


Figure A76.- Time histories for run 76. Nominal carriage speed, 75 knots; vertical load, 84.1 kN (18 900 lbf); yaw angle, 6°; brake supply pressure, 21 MPa (3000 psi); tire condition, worn; surface condition, dry.

APPENDIX

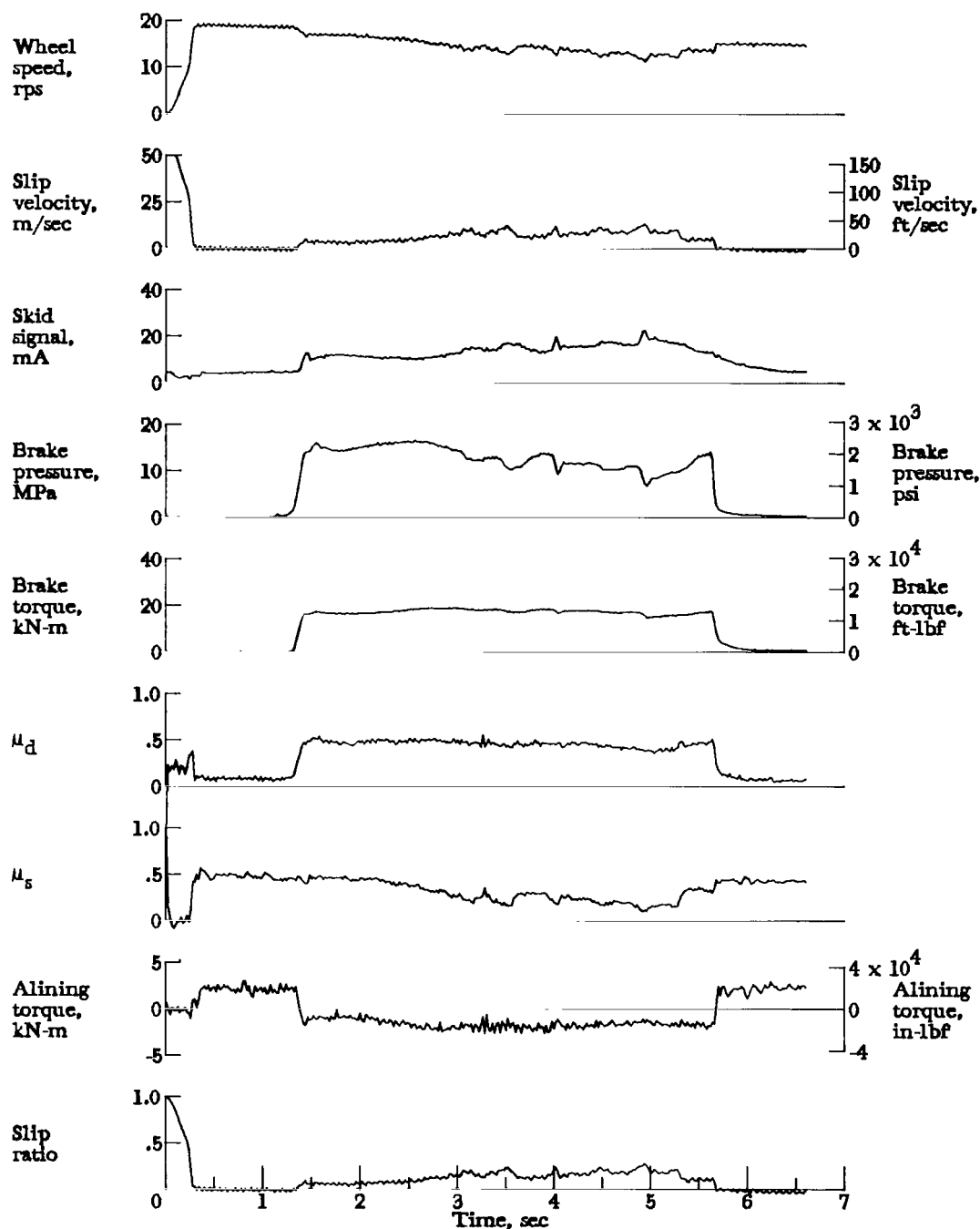


Figure A77.- Time histories for run 77. Nominal carriage speed, 99 knots; vertical load, 85.9 kN (19 300 lbf); yaw angle, 6°; brake supply pressure, 21 MPa (3000 psi); tire condition, worn; surface condition, dry.

APPENDIX

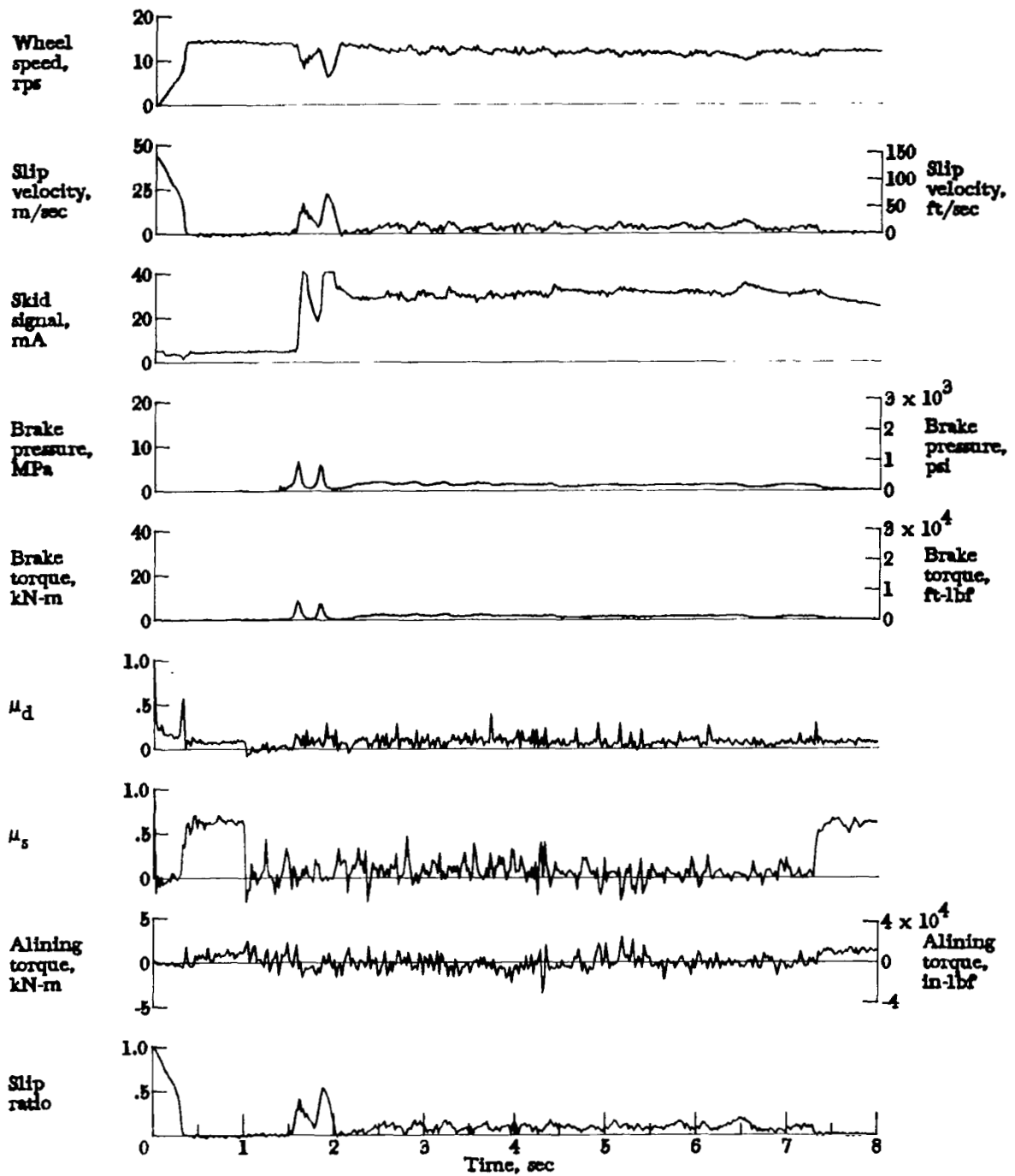


Figure A78.- Time histories for run 78. Nominal carriage speed, 77 knots; vertical load, 58.7 kN (13 200 lbf); yaw angle, 6°; brake supply pressure, 21 MPa (3000 psi); tire condition, worn; surface condition, damp.

APPENDIX

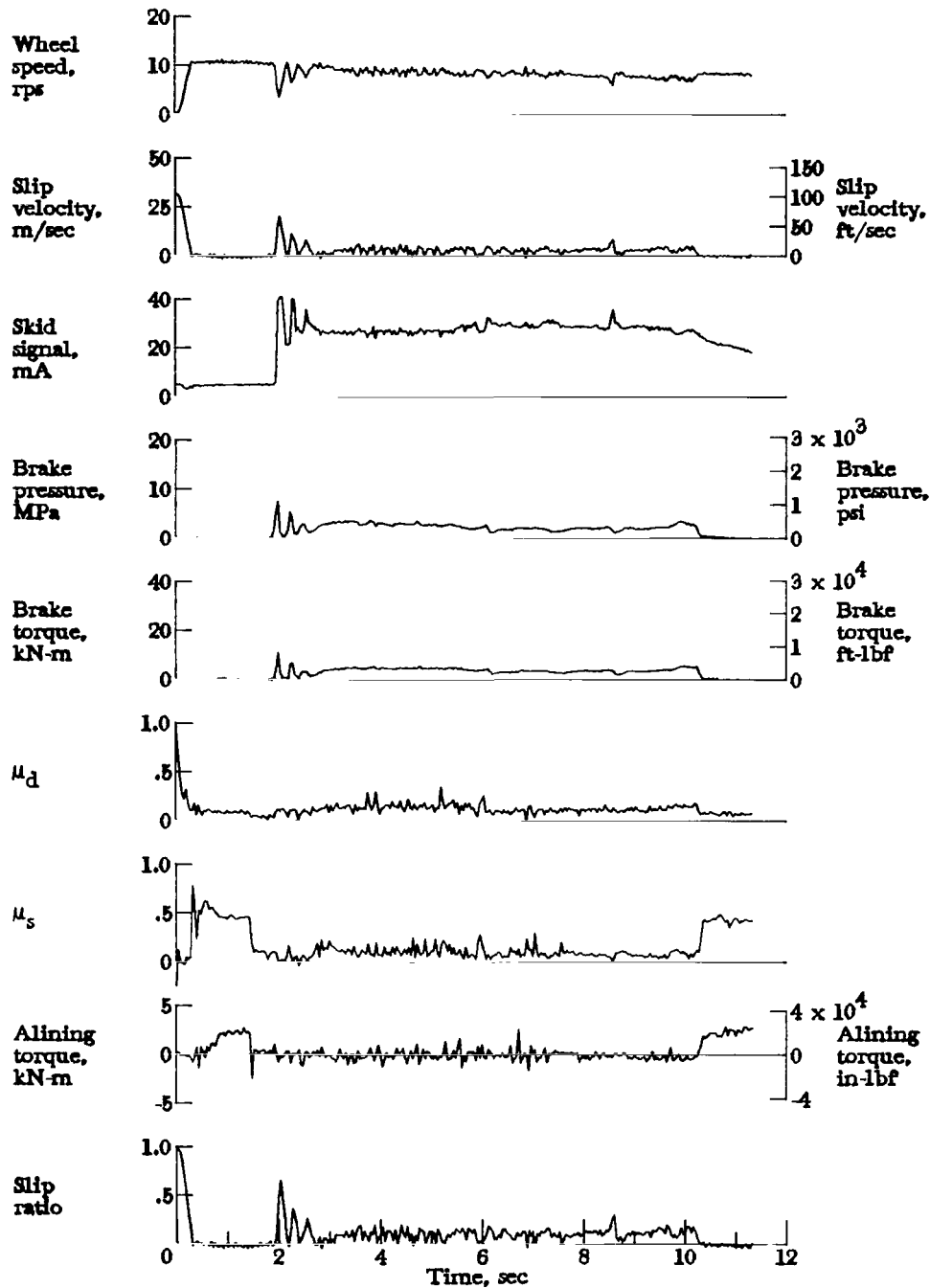


Figure A79.- Time histories for run 79. Nominal carriage speed, 54 knots; vertical load, 87.6 kN (19 700 lbf); yaw angle, 6°; brake supply pressure, 21 MPa (3000 psi); tire condition, worn; surface condition, damp.

APPENDIX

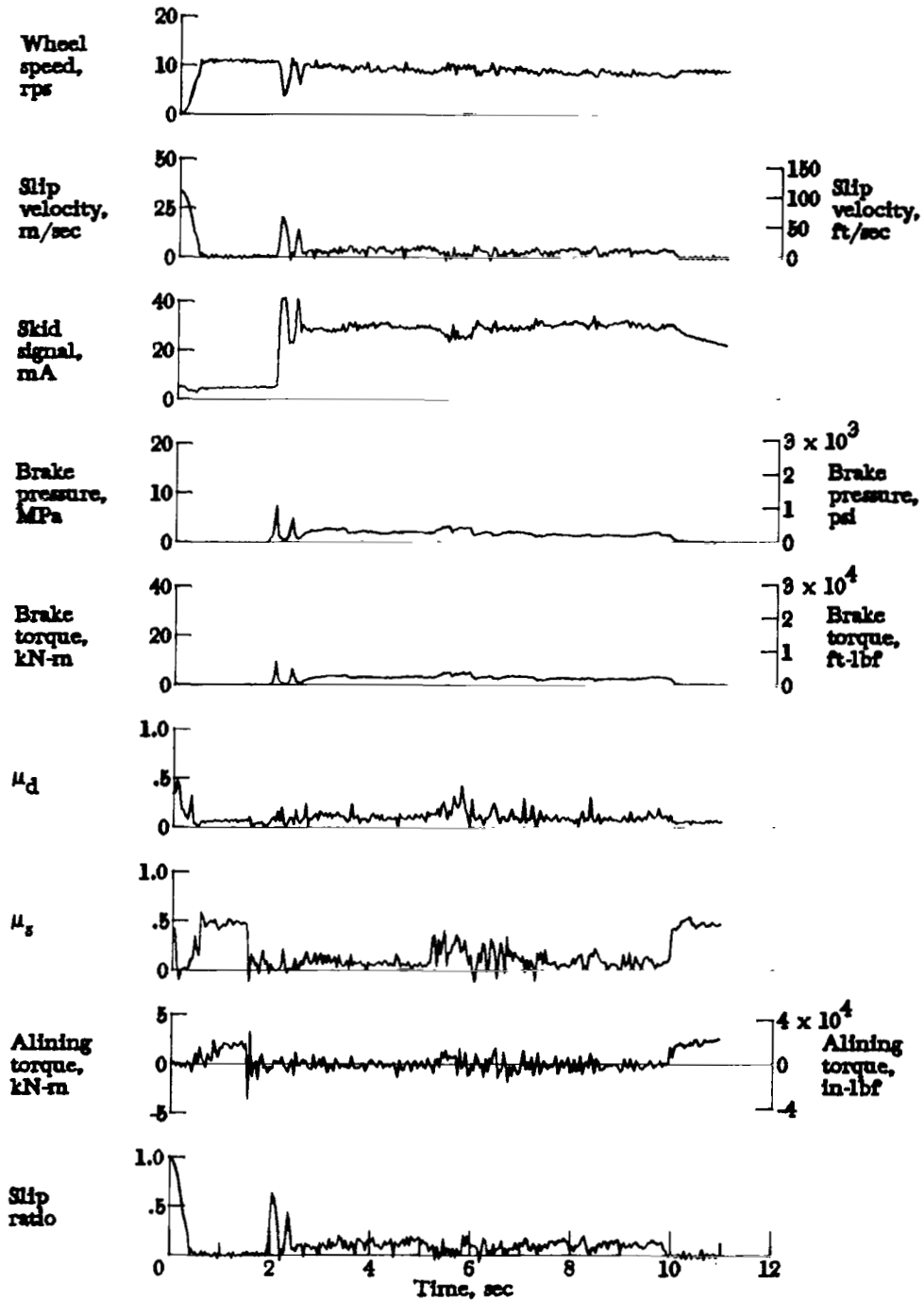


Figure A80.- Time histories for run 80. Nominal carriage speed, 58 knots; vertical load, 79.6 kN (17 900 lbf); yaw angle, 6°; brake supply pressure, 21 MPa (3000 psi); tire condition, worn; surface condition, damp.

APPENDIX

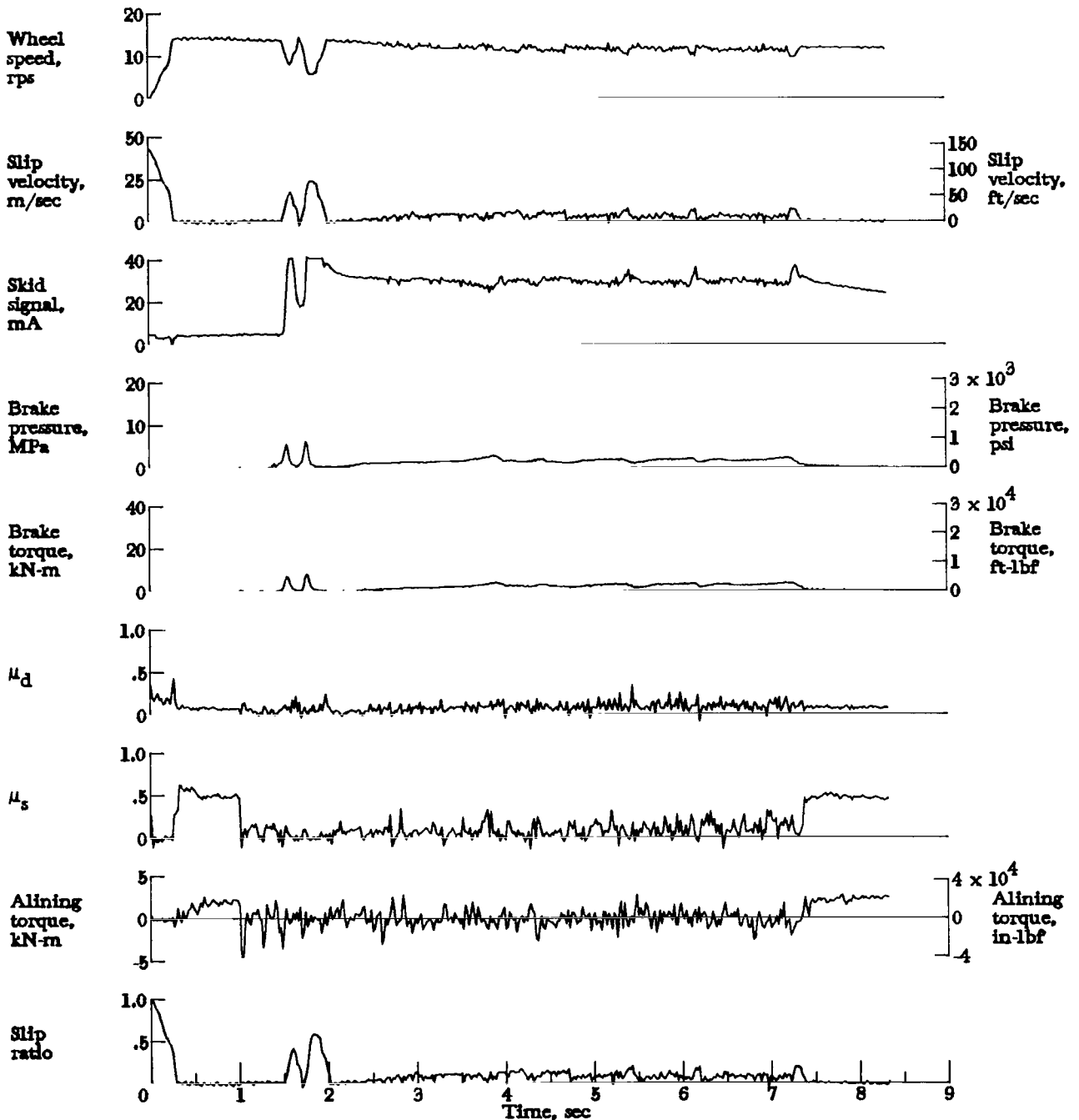


Figure A81.- Time histories for run 81. Nominal carriage speed, 76 knots; vertical load, 81.4 kN (18 300 lbf); yaw angle,  $6^\circ$ ; brake supply pressure, 21 MPa (3000 psi); tire condition, worn; surface condition, damp.

APPENDIX

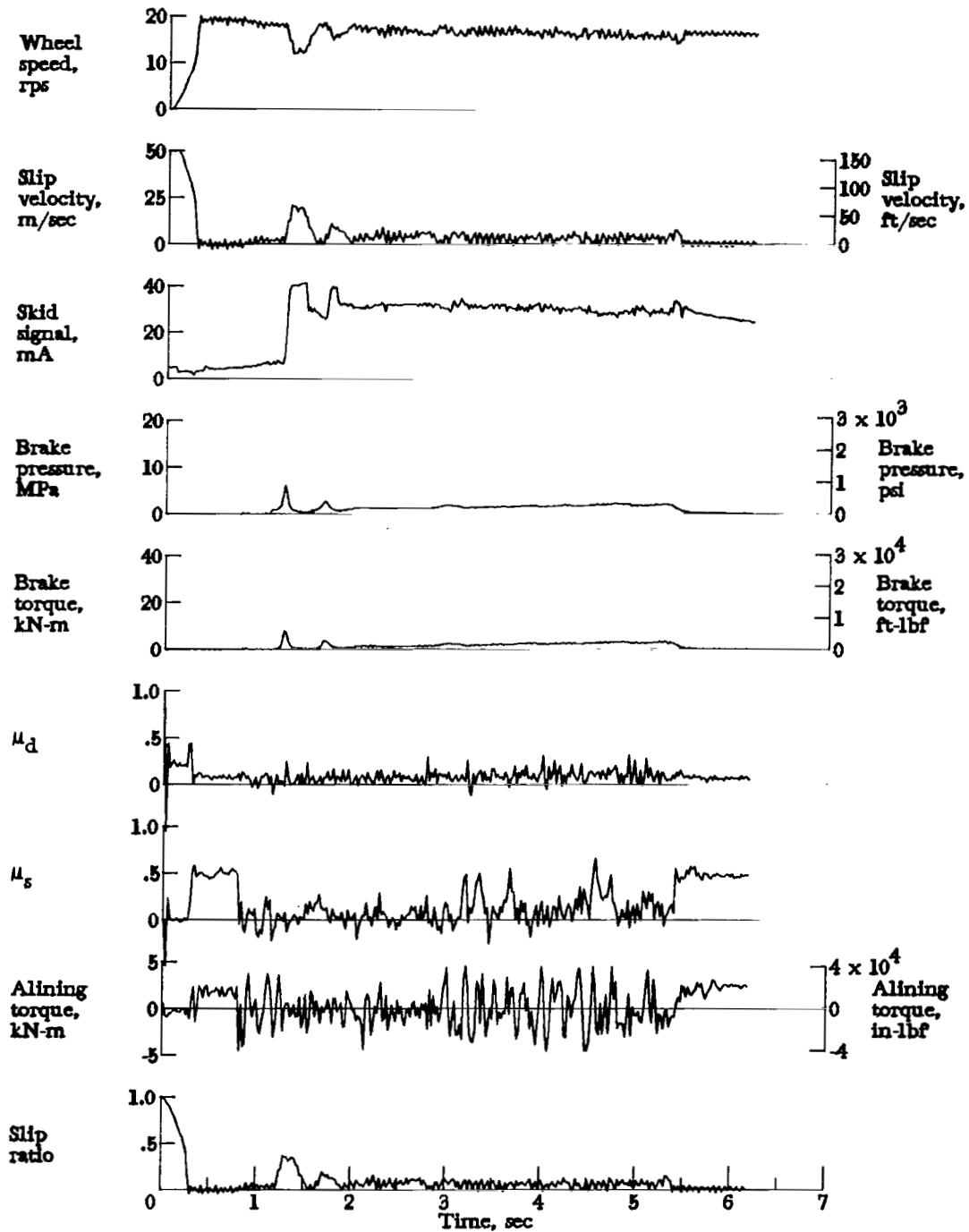


Figure A82.- Time histories for run 82. Nominal carriage speed, 105 knots; vertical load, 79.6 kN (17 900 lbf); yaw angle,  $6^\circ$ ; brake supply pressure, 21 MPa (3000 psi); tire condition, worn; surface condition, damp.

APPENDIX

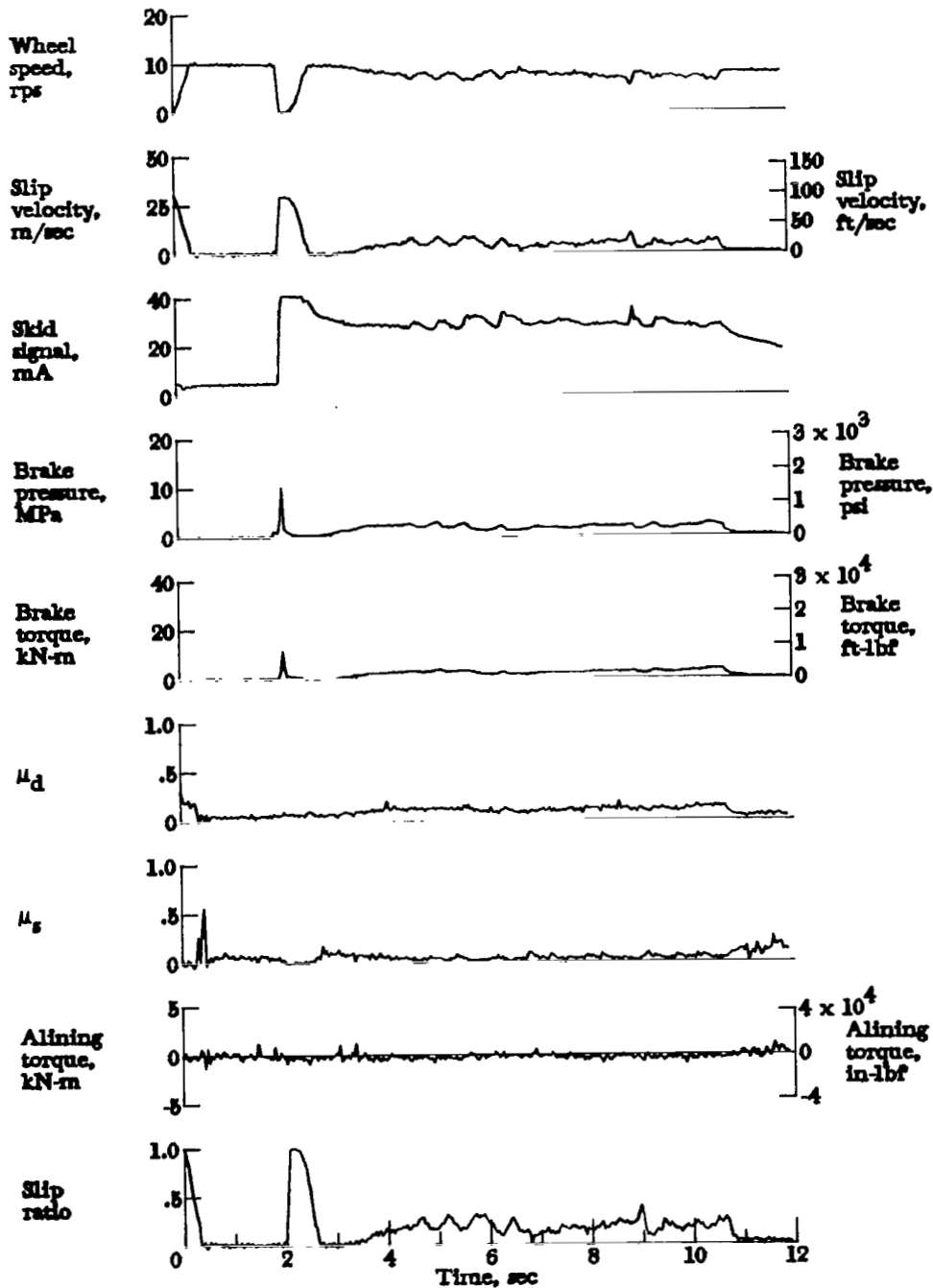


Figure A83.- Time histories for run 83. Nominal carriage speed, 53 knots; vertical load, 78.7 kN (17 700 lbf); yaw angle, 6°; brake supply pressure, 21 MPa (3000 psi); tire condition, worn; surface condition, flooded.

APPENDIX

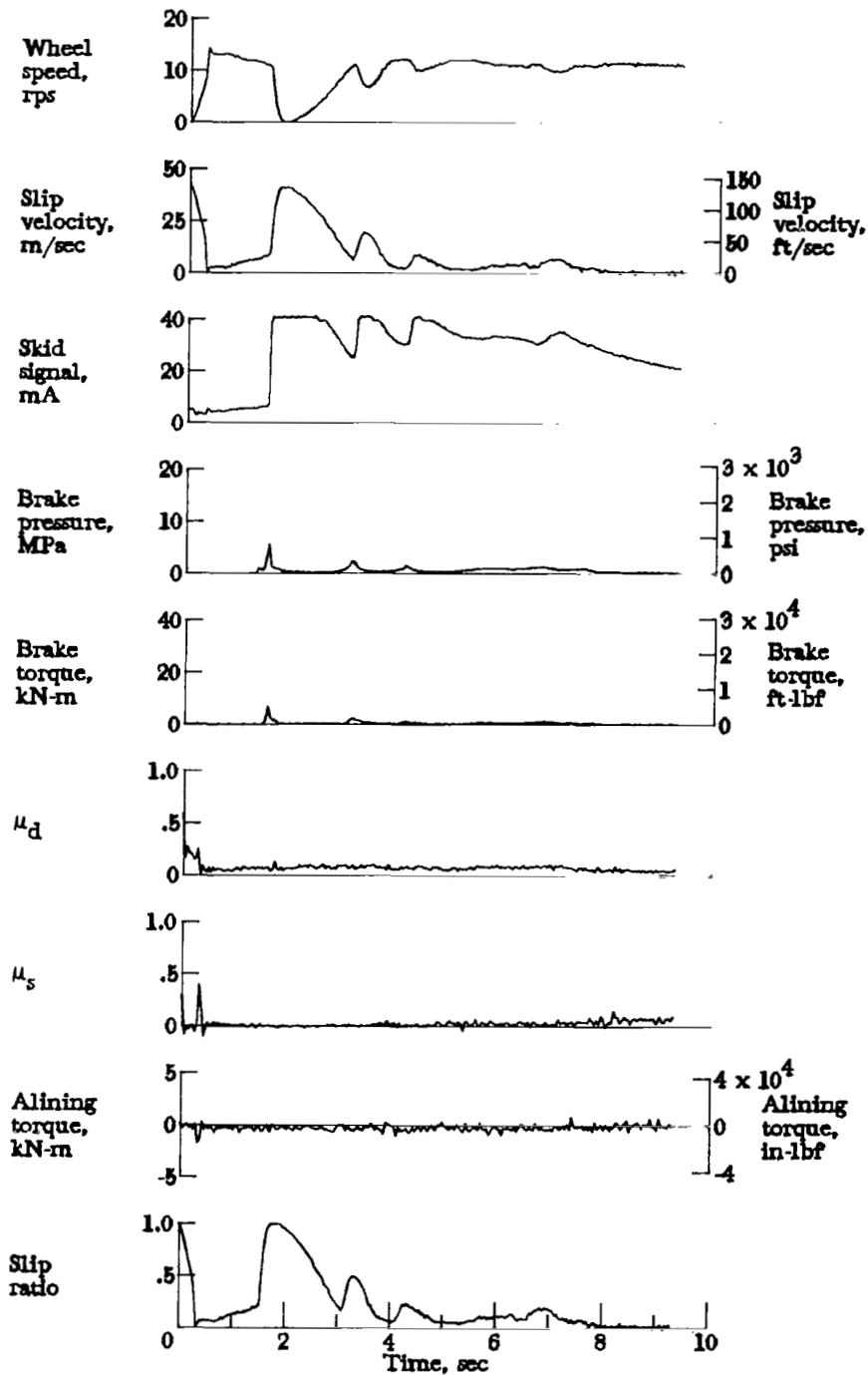


Figure A84.- Time histories for run 84. Nominal carriage speed, 75 knots; vertical load, 77.8 kN (17 500 lbf); yaw angle,  $6^\circ$ ; brake supply pressure, 20 MPa (2900 psi); tire condition, worn; surface condition, flooded.

APPENDIX

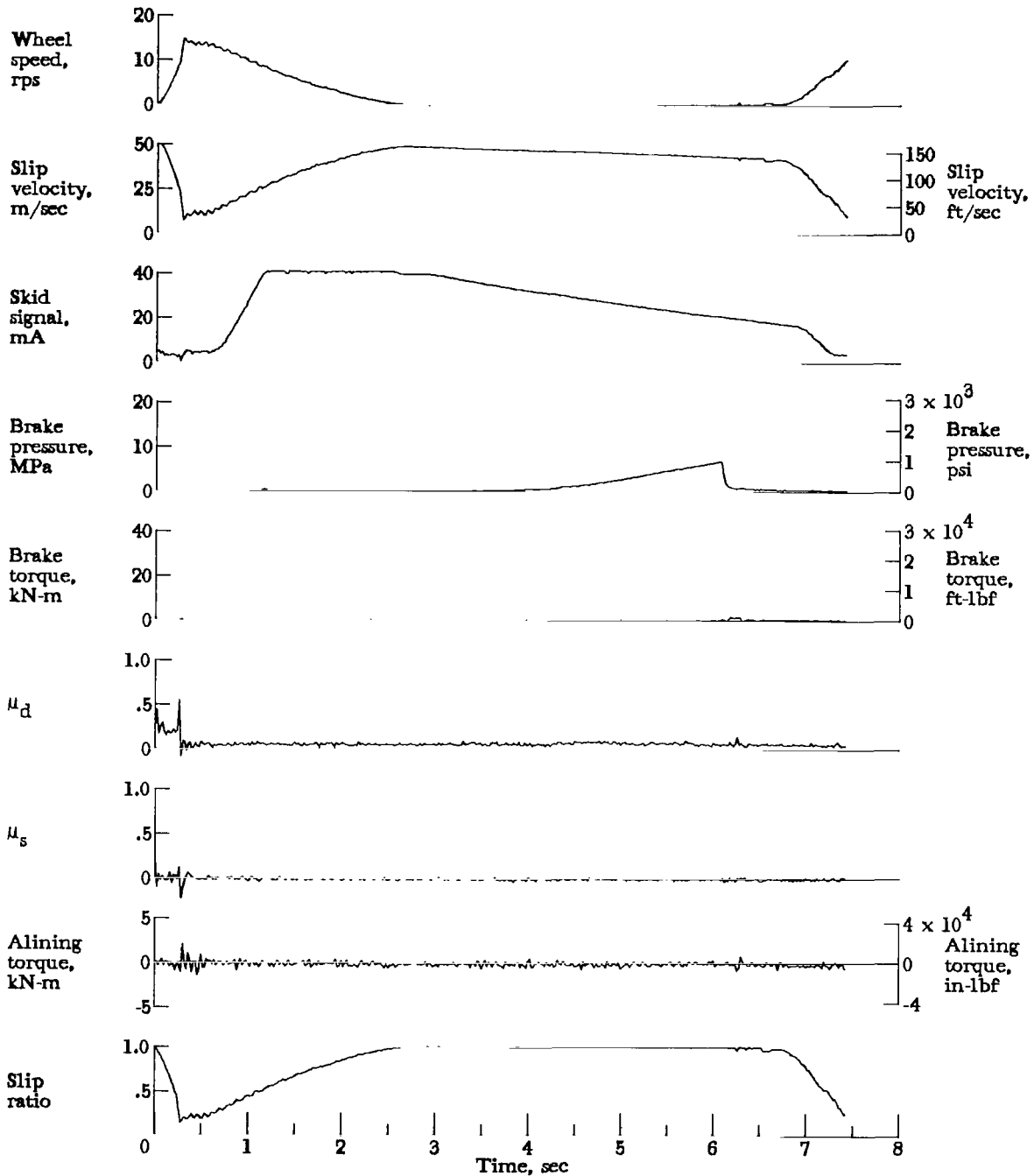


Figure A85.- Time histories for run 85. Nominal carriage speed, 93 knots; vertical load, 78.3 kN (17 600 lbf); yaw angle,  $6^\circ$ ; brake supply pressure, 21 MPa (3000 psi); tire condition, worn; surface condition, flooded.

APPENDIX

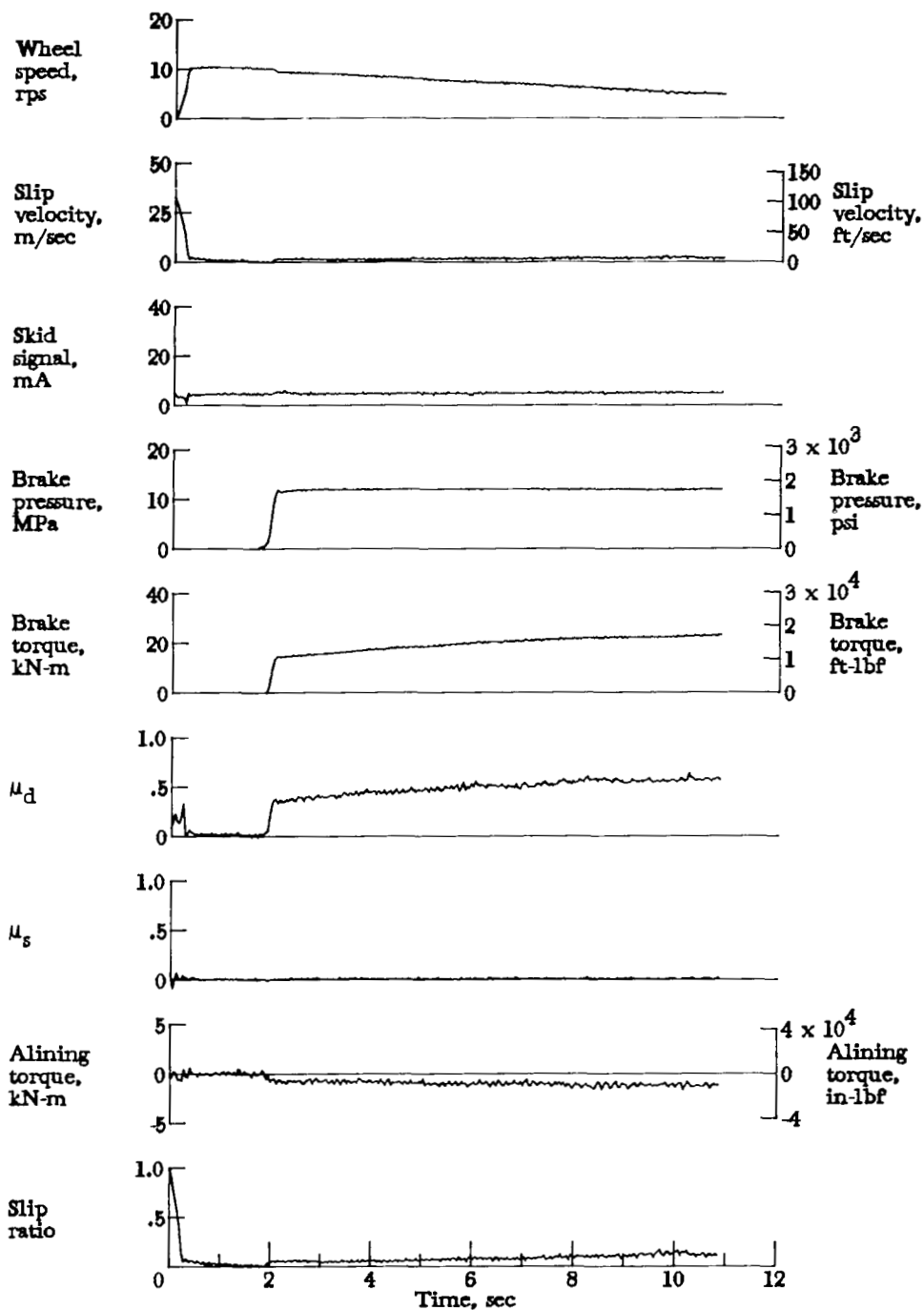


Figure A86.- Time histories for run 86. Nominal carriage speed, 46 knots; vertical load, 83.6 kN (18 800 lbf); yaw angle, 0°; brake supply pressure, 14 MPa (2000 psi); tire condition, new; surface condition, dry.

APPENDIX

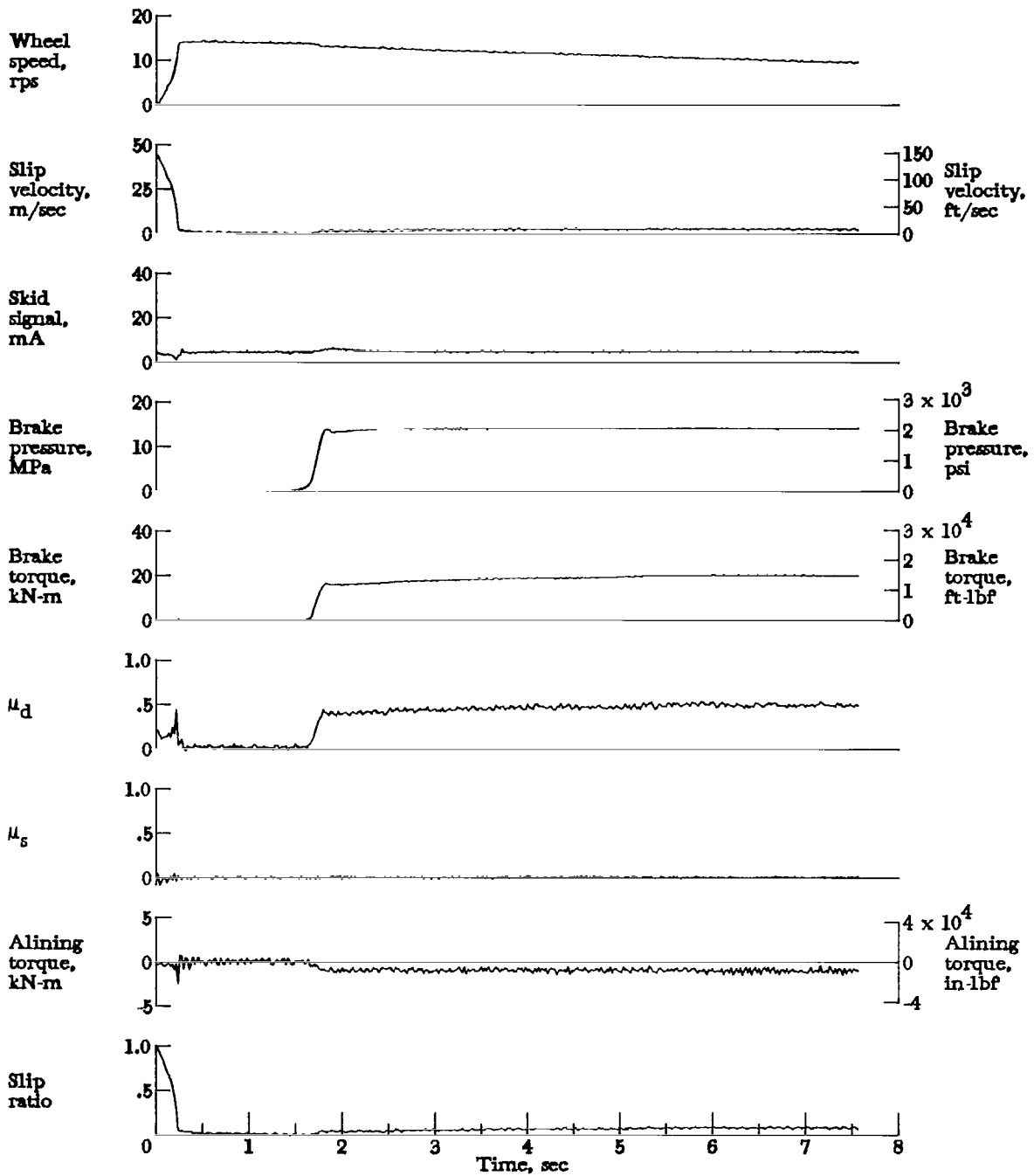


Figure A87.- Time histories for run 87. Nominal carriage speed, 71 knots; vertical load, 84.1 kN (18 900 lbf); yaw angle, 0°; brake supply pressure, 16 MPa (2300 psi); tire condition, new; surface condition, dry.

APPENDIX

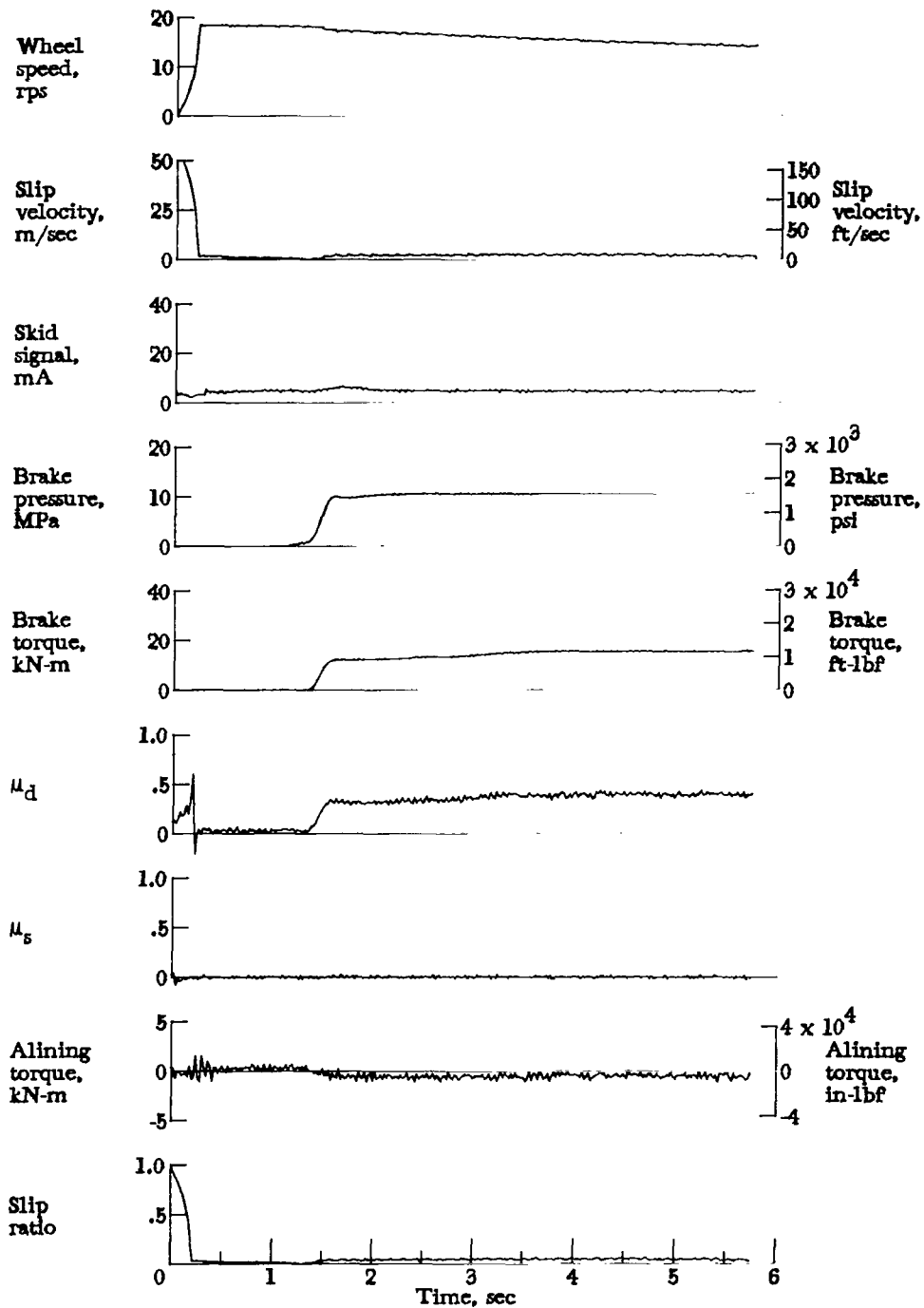


Figure A88.- Time histories for run 88. Nominal carriage speed, 97 knots; vertical load, 84.5 kN (19 000 lbf); yaw angle,  $0^\circ$ ; brake supply pressure, 13 MPa (1900 psi); tire condition, new; surface condition, dry.

APPENDIX

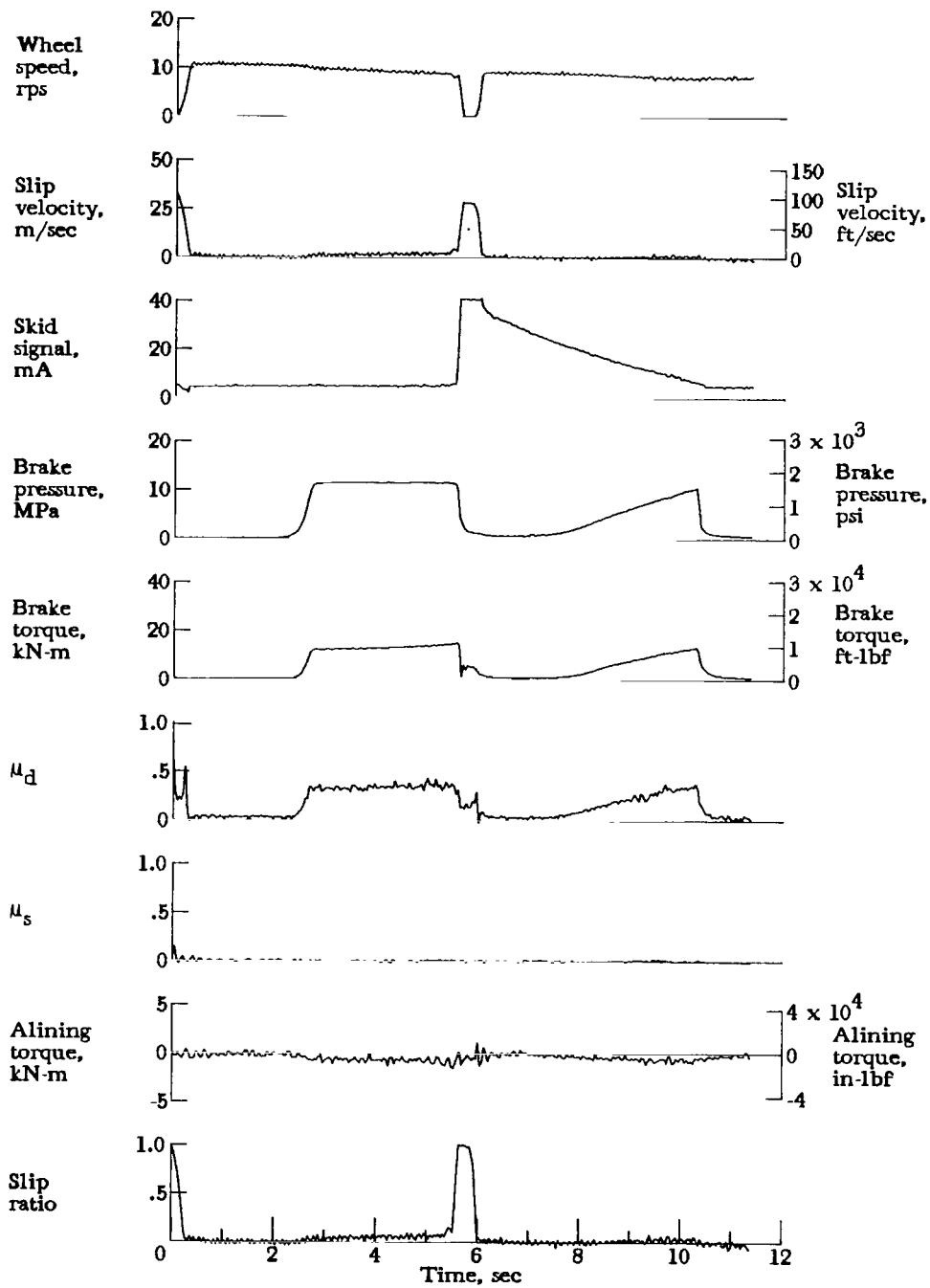


Figure A89.- Time histories for run 89. Nominal carriage speed, 54 knots; vertical load, 82.3 kN (18 500 lbf); yaw angle, 0°; brake supply pressure, 14 MPa (2000 psi); tire condition, new; surface condition, damp.

APPENDIX

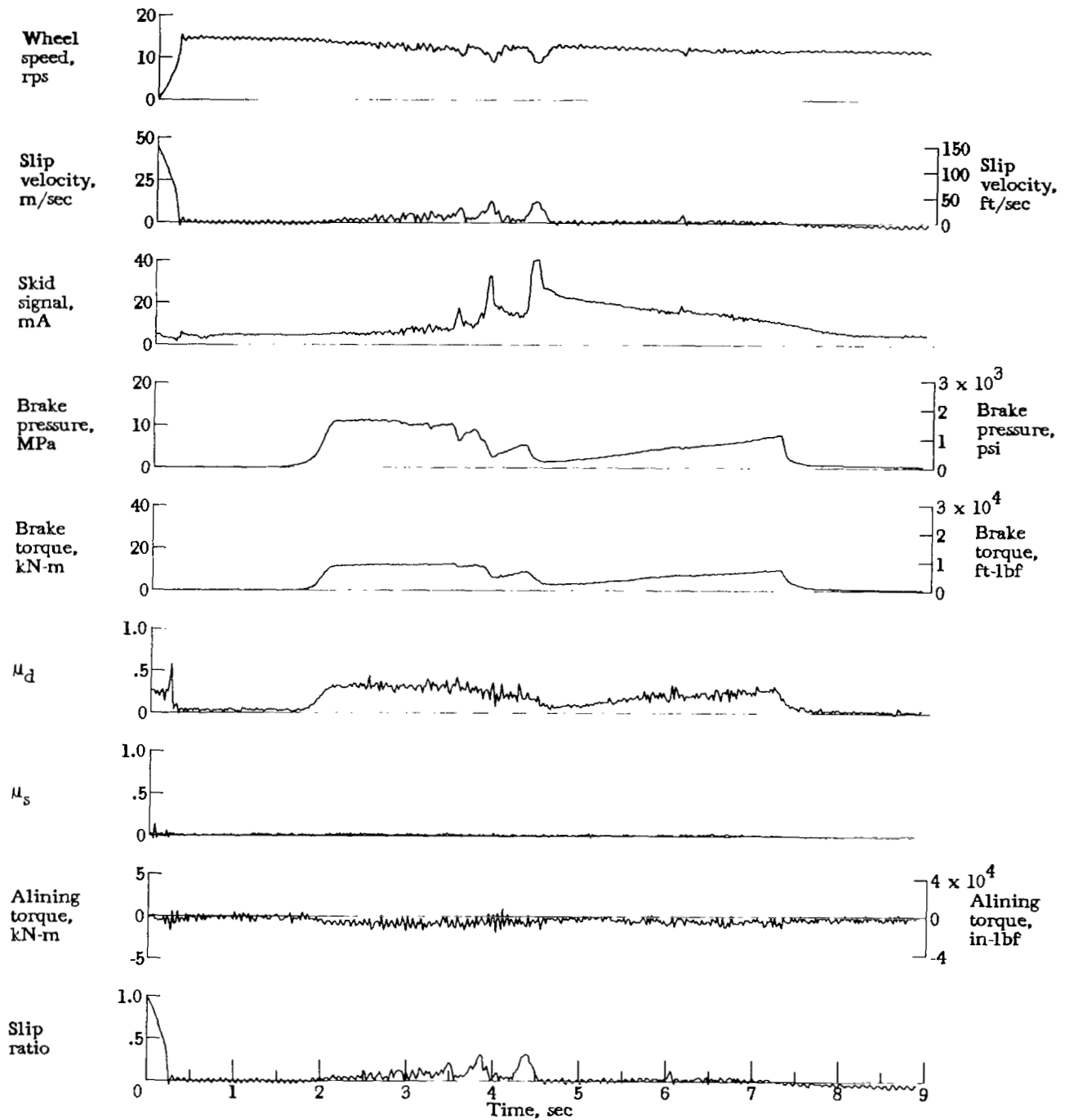


Figure A90.- Time histories for run 90. Nominal carriage speed, 76 knots; vertical load, 81.8 kN (18 400 lbf); yaw angle,  $0^\circ$ ; brake supply pressure, 14 MPa (2000 psi); tire condition, new; surface condition, damp.

APPENDIX

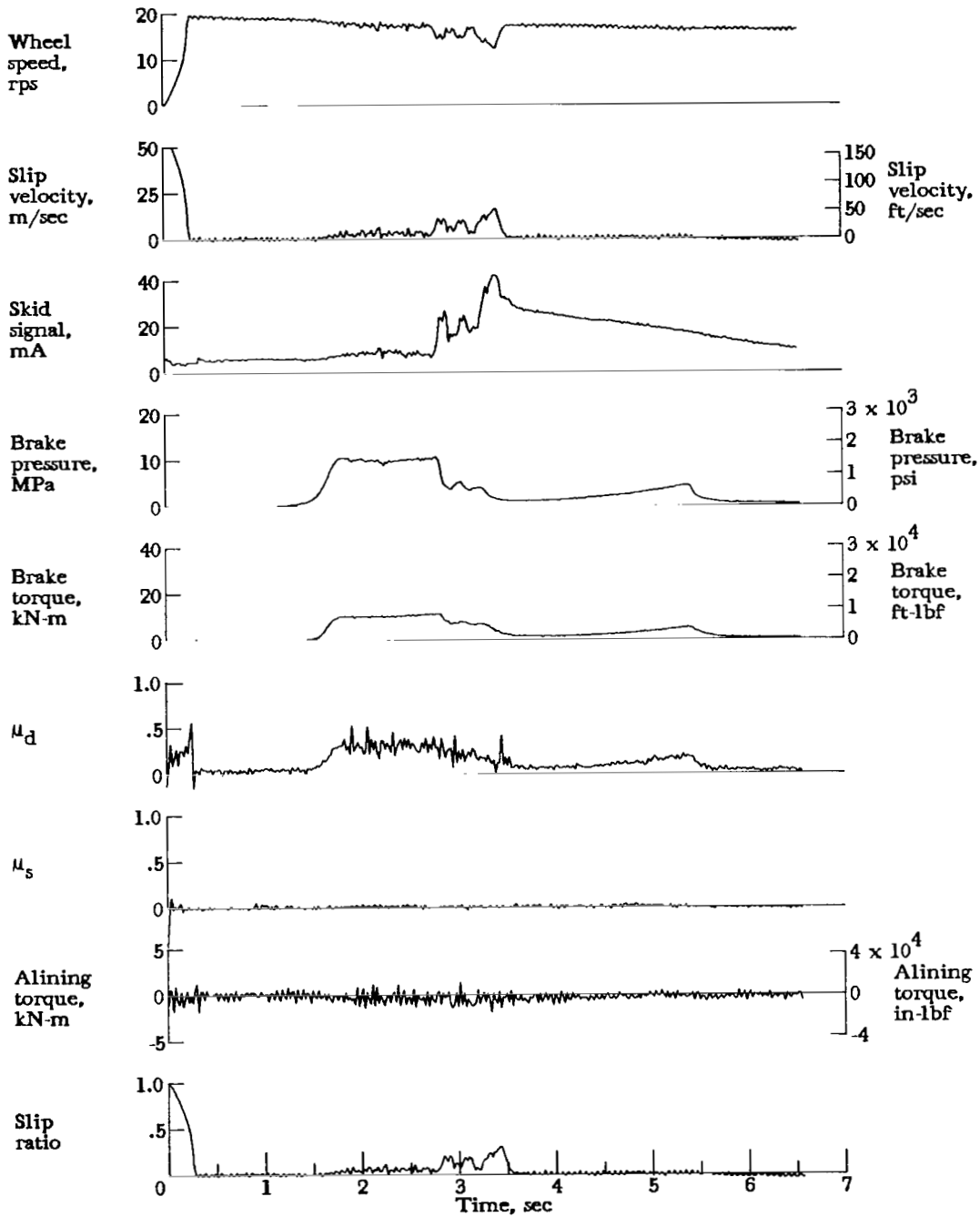


Figure A91.- Time histories for run 91. Nominal carriage speed, 104 knots; vertical load, 81.8 kN (18 400 lbf); yaw angle,  $0^\circ$ ; brake supply pressure, 13 MPa (1900 psi); tire condition, new; surface condition, damp.

APPENDIX

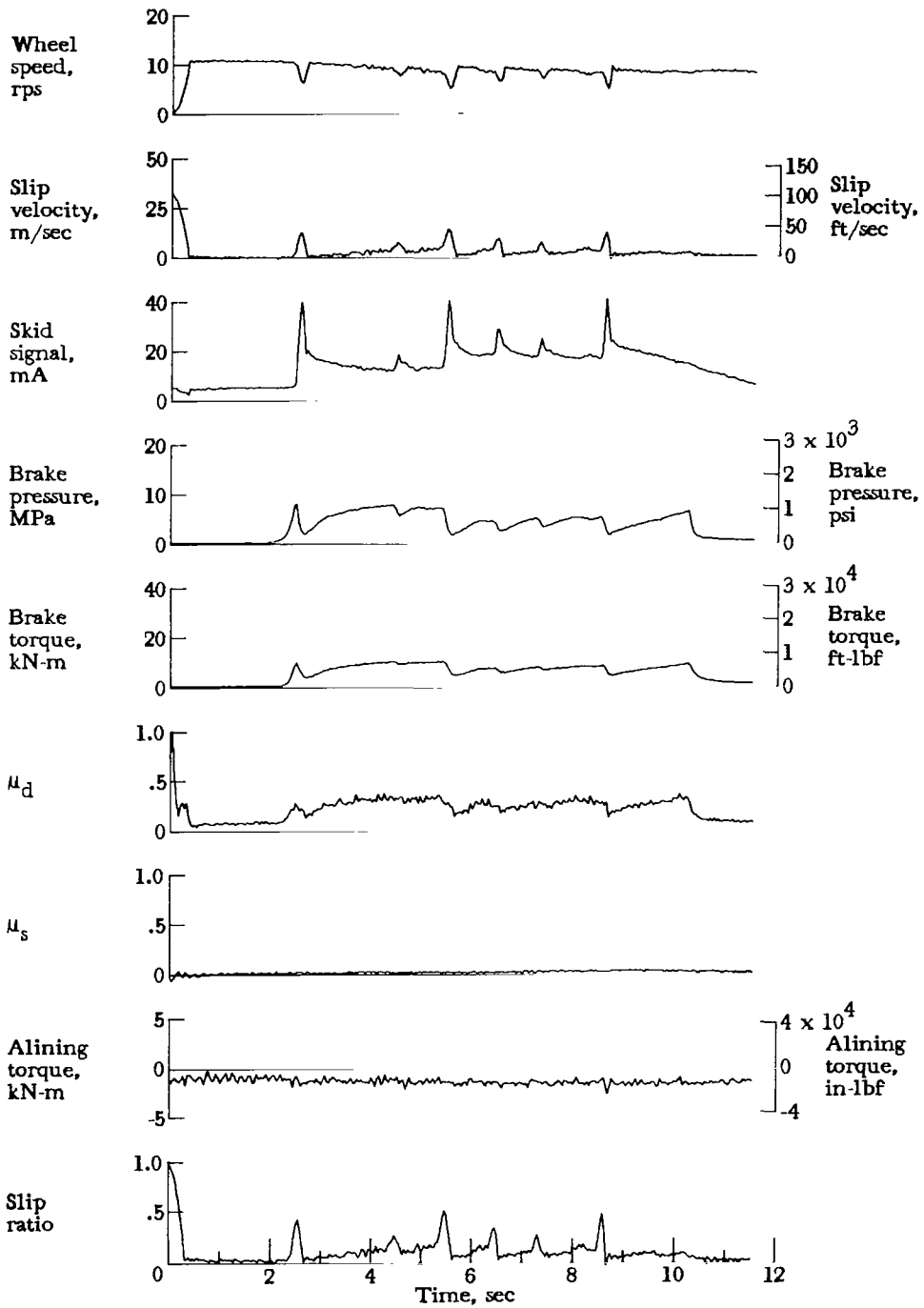


Figure A92.- Time histories for run 92. Nominal carriage speed, 53 knots; vertical load, 82.3 kN (18 500 lbf); yaw angle,  $0^\circ$ ; brake supply pressure, 14 MPa (2000 psi); tire condition, new; surface condition, flooded.

APPENDIX

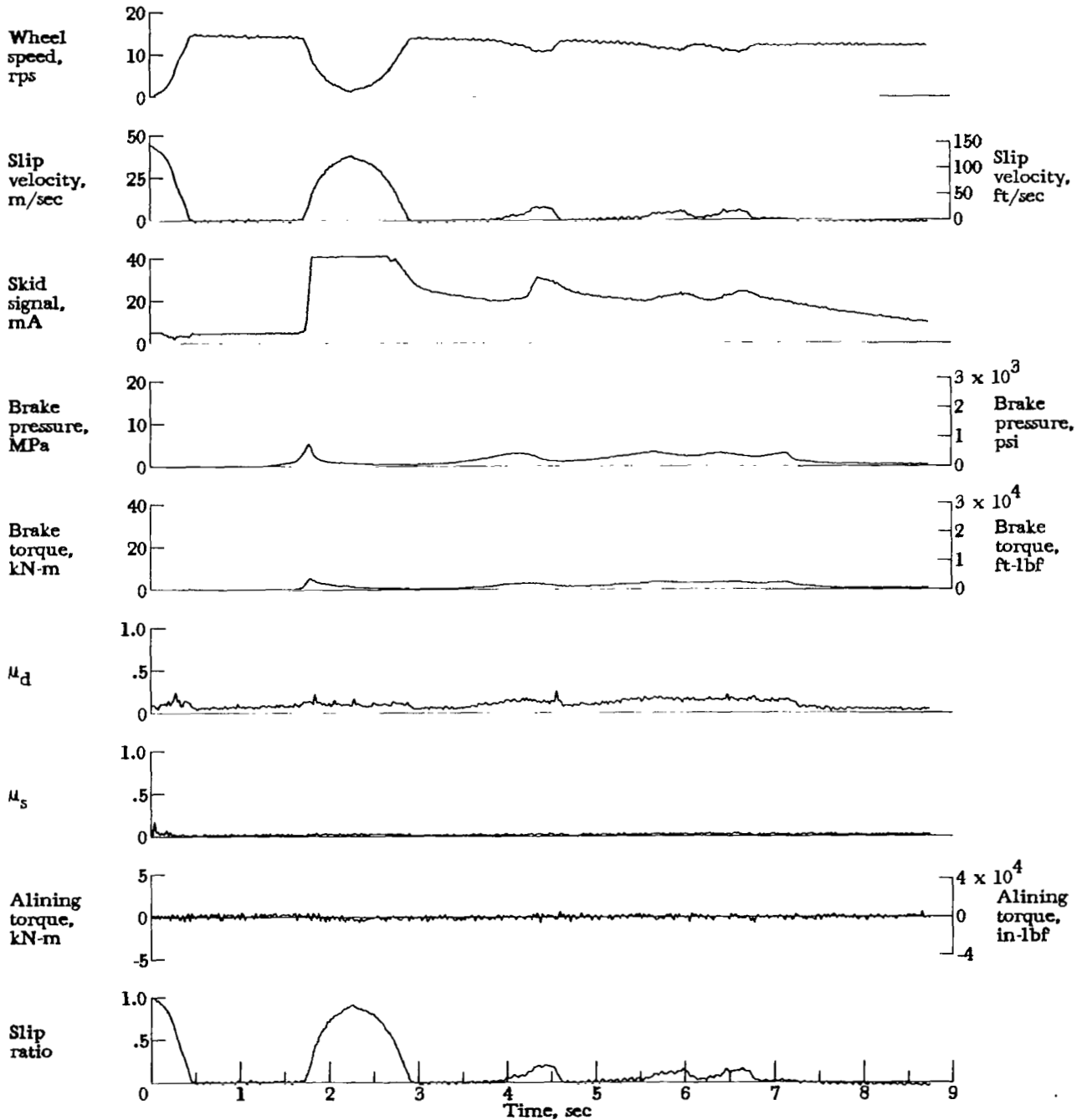


Figure A93.- Time histories for run 93. Nominal carriage speed, 76 knots; vertical load, 81.8 kN (18 400 lbf); yaw angle,  $0^\circ$ ; brake supply pressure, 14 MPa (2000 psi); tire condition, new; surface condition, flooded.

APPENDIX

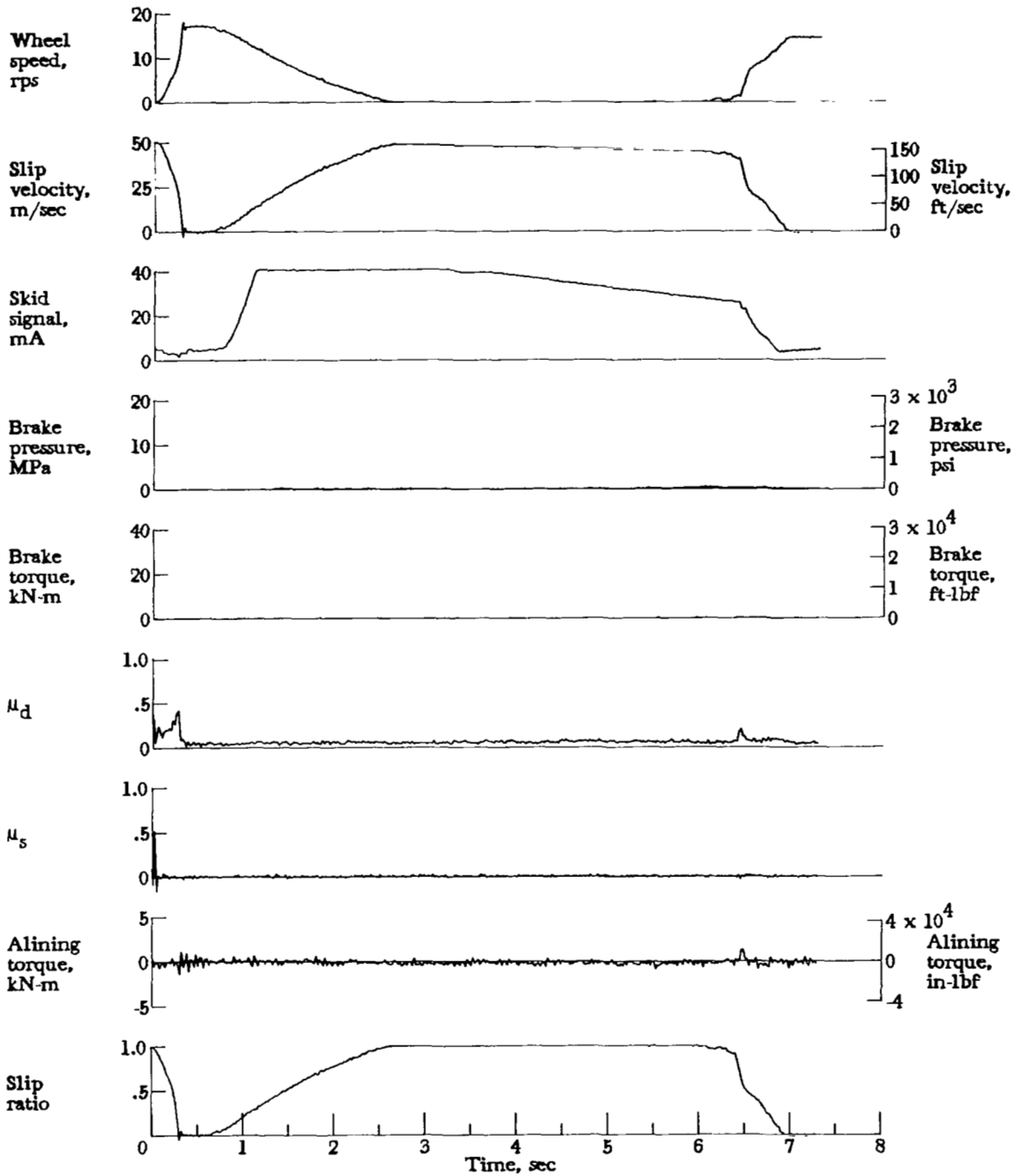


Figure A94.- Time histories for run 94. Nominal carriage speed, 93 knots; vertical load, 80.5 kN (18 100 lbf); yaw angle,  $0^\circ$ ; brake supply pressure, 14 MPa (2000 psi); tire condition, new; surface condition, flooded.

APPENDIX

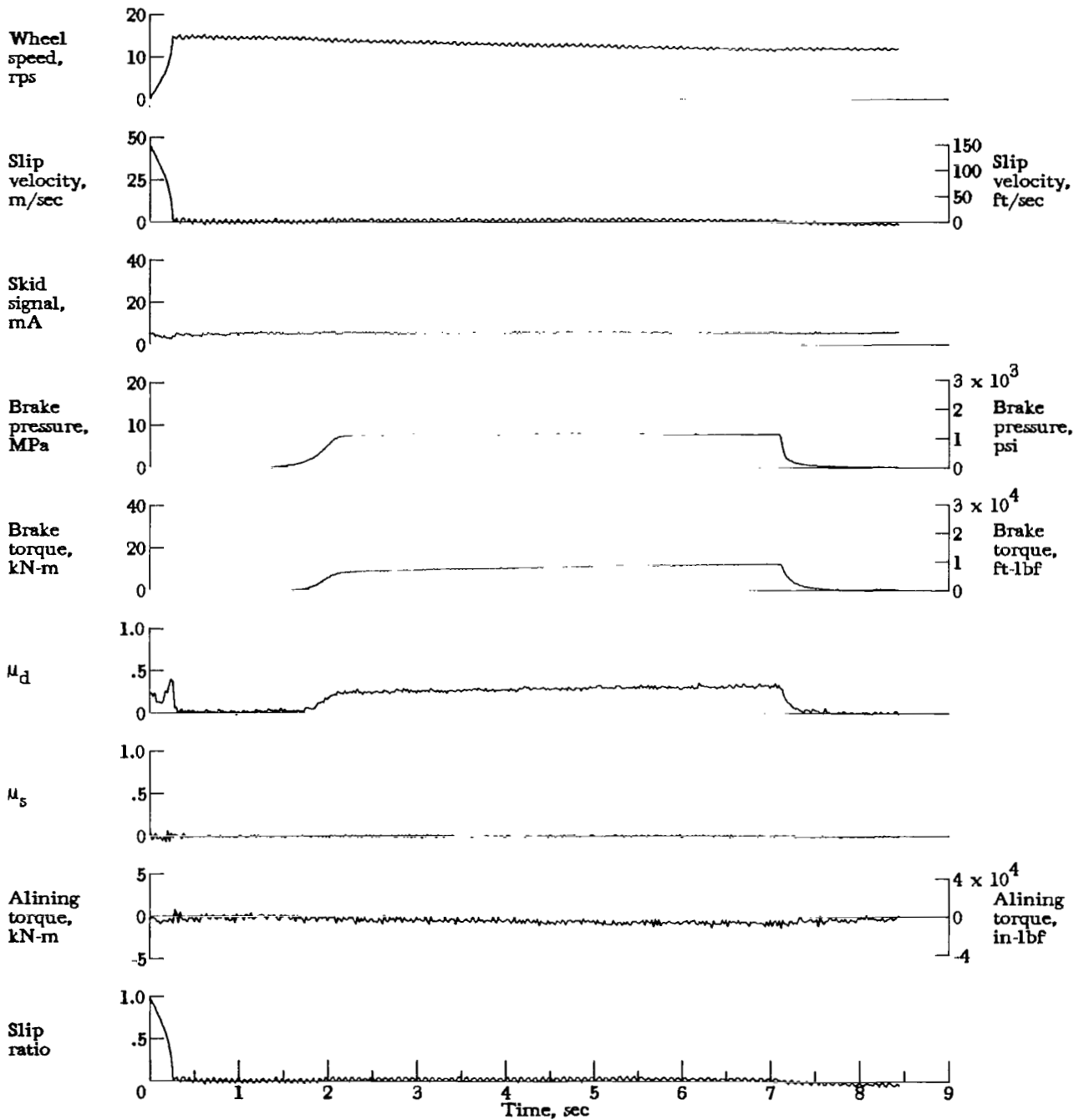


Figure A95.- Time histories for run 95. Nominal carriage speed, 77 knots; vertical load, 83.2 kN (18 700 lbf); yaw angle, 0°; brake supply pressure, 10 MPa (1500 psi); tire condition, new; surface condition, dry.

APPENDIX

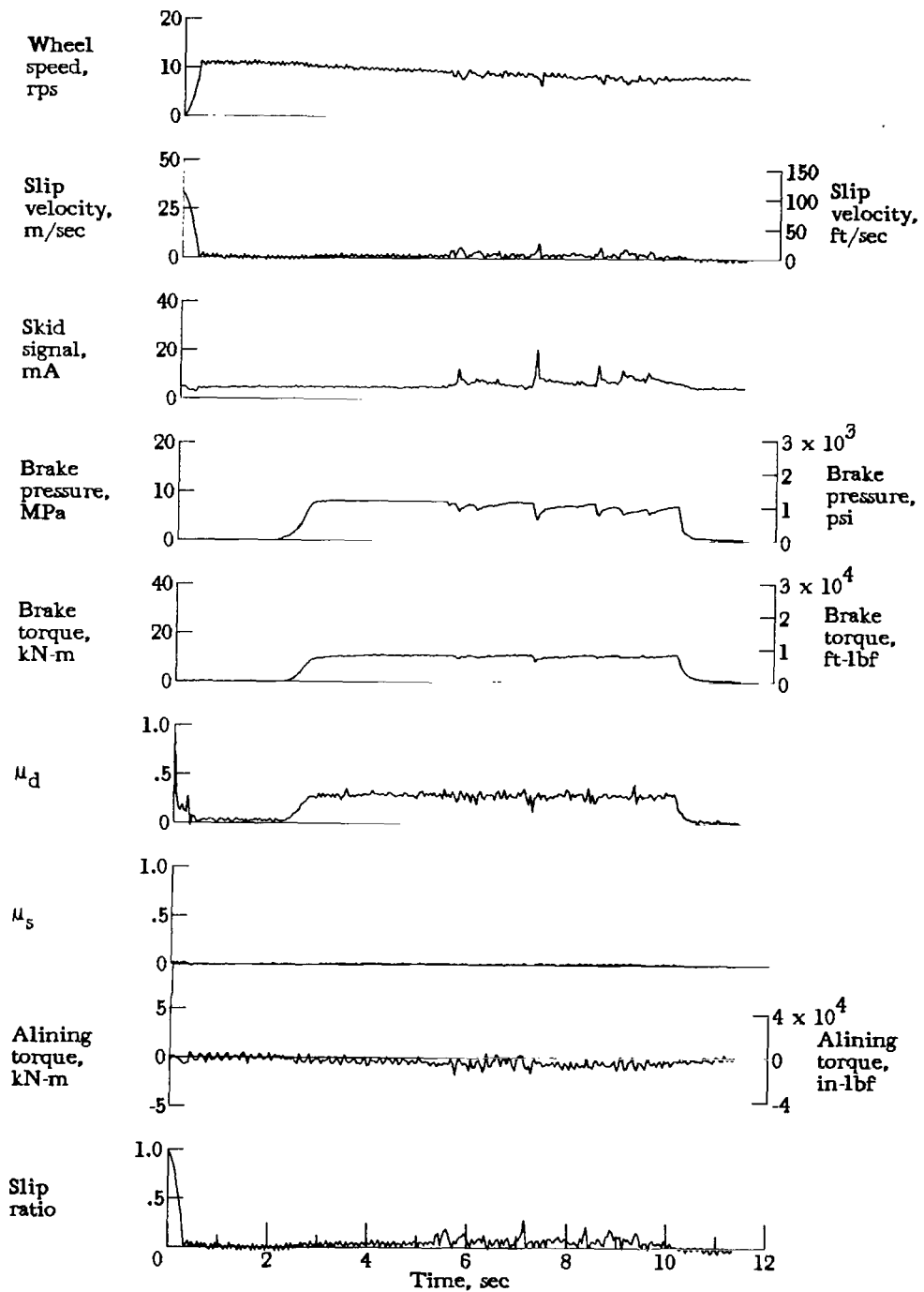


Figure A96.- Time histories for run 96. Nominal carriage speed, 55 knots; vertical load, 81.8 kN (18 400 lbf); yaw angle,  $0^\circ$ ; brake supply pressure, 10 MPa (1500 psi); tire condition, new; surface condition, damp.

APPENDIX

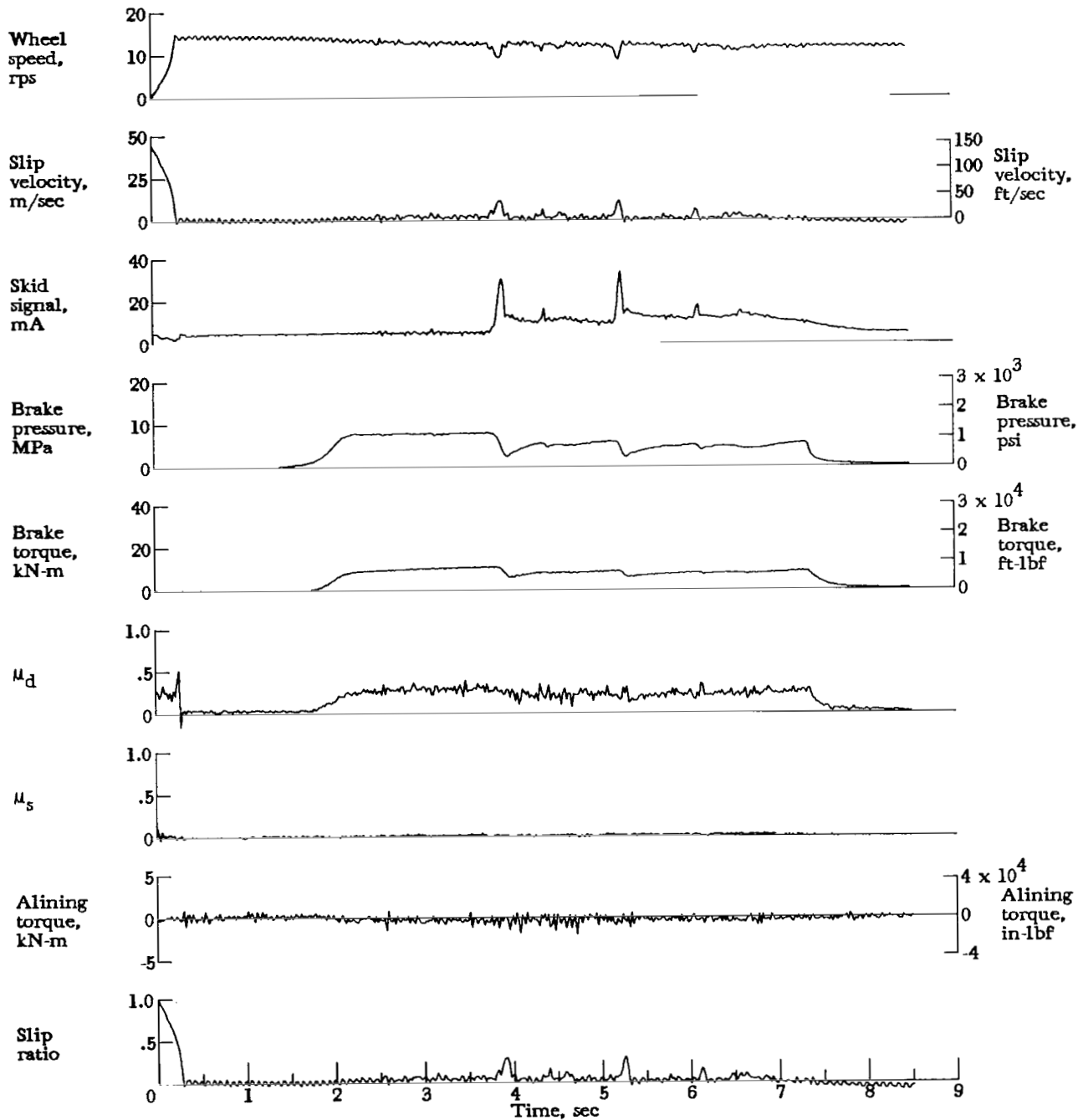


Figure A97.- Time histories for run 97. Nominal carriage speed, 75 knots; vertical load, 82.3 kN (18 500 lbf); yaw angle,  $0^\circ$ ; brake supply pressure, 10 MPa (1500 psi); tire condition, new; surface condition, damp.

APPENDIX

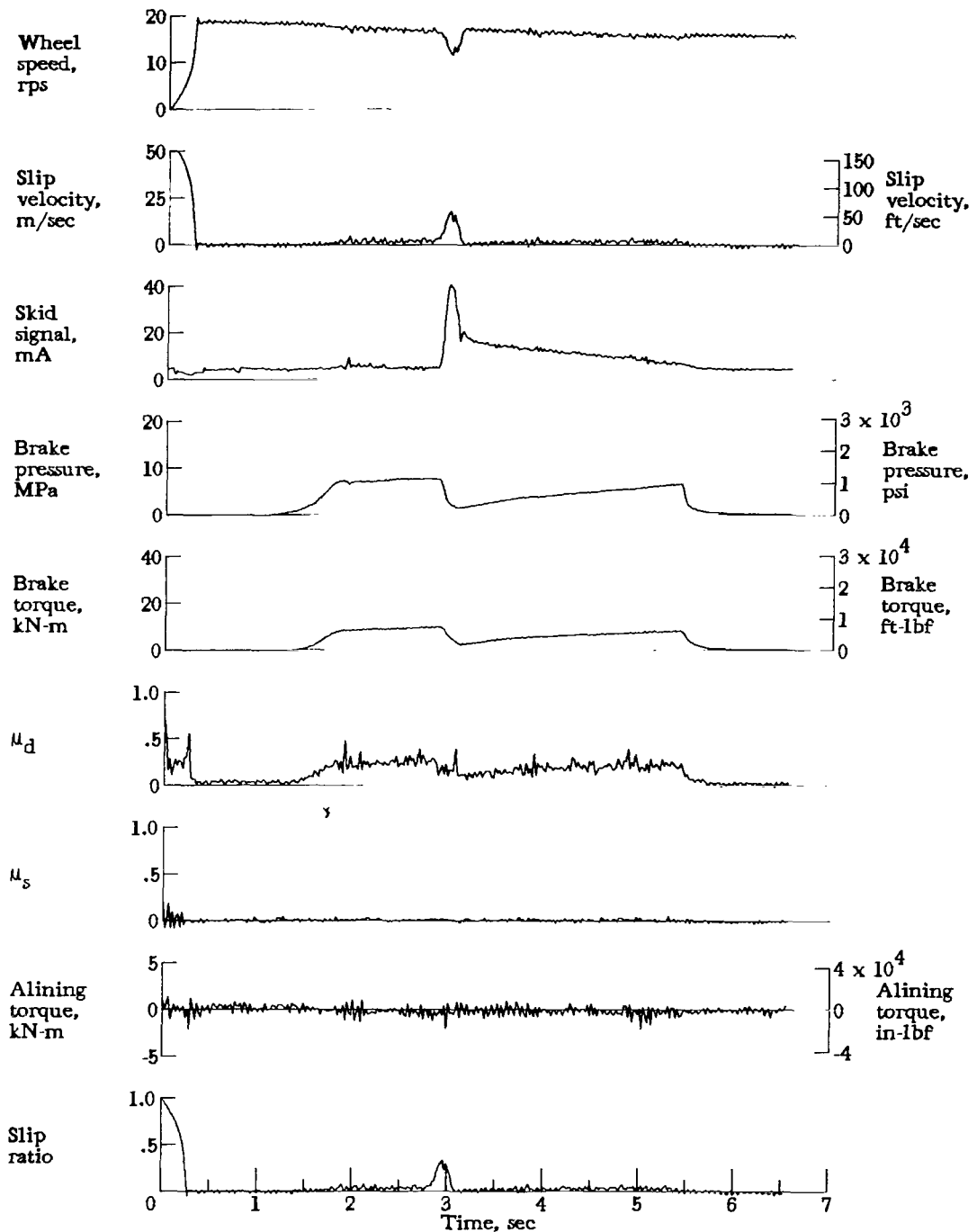


Figure A98.- Time histories for run 98. Nominal carriage speed, 102 knots; vertical load, 83.2 kN (18 700 lbf); yaw angle, 0°; brake supply pressure, 10 MPa (1500 psi); tire condition, new; surface condition, damp.

APPENDIX

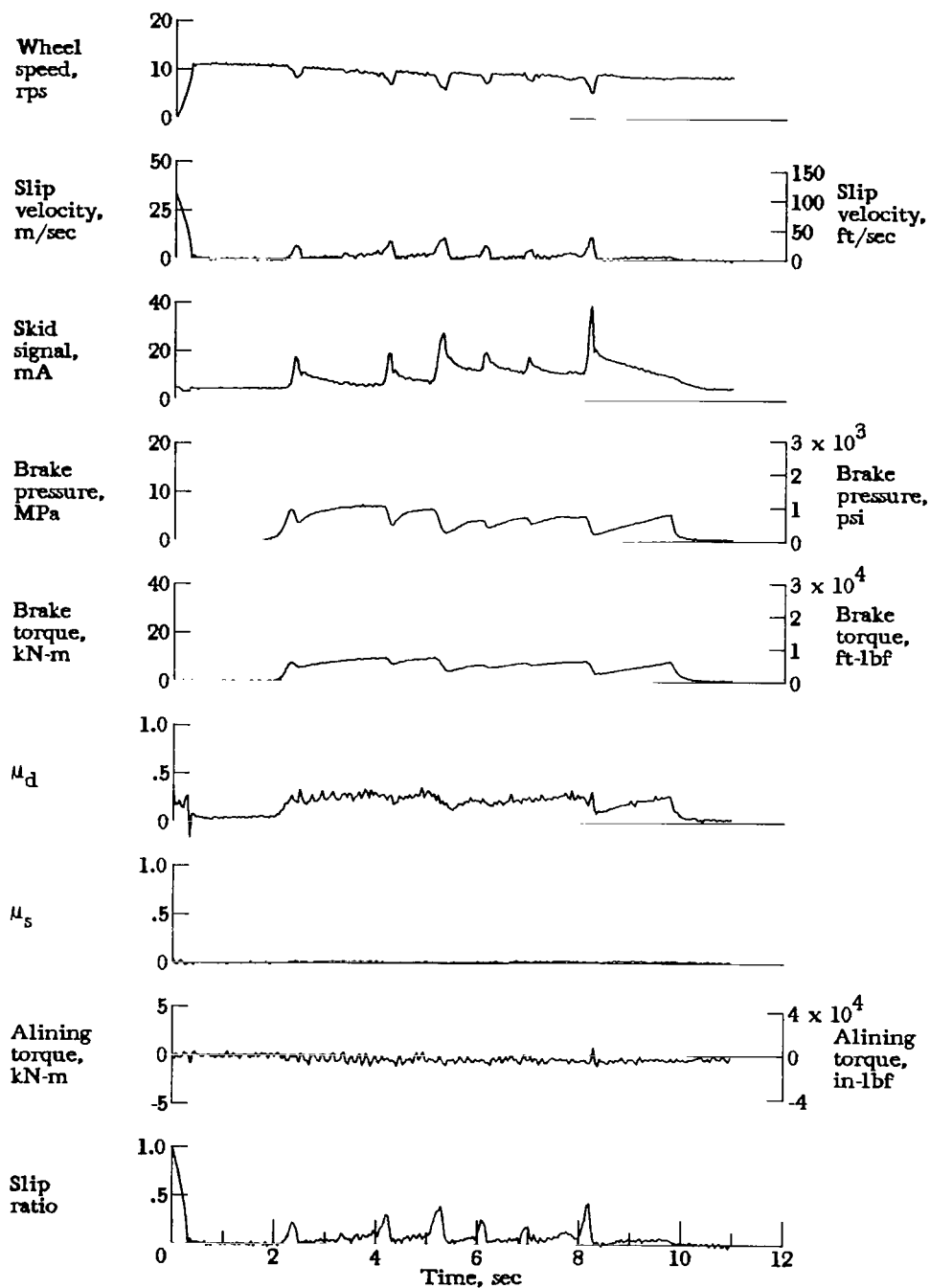


Figure A99.- Time histories for run 99. Nominal carriage speed, 56 knots; vertical load, 82.3 kN (18 500 lbf); yaw angle, 0°; brake supply pressure, 10 MPa (1500 psi); tire condition, new; surface condition, flooded.

APPENDIX

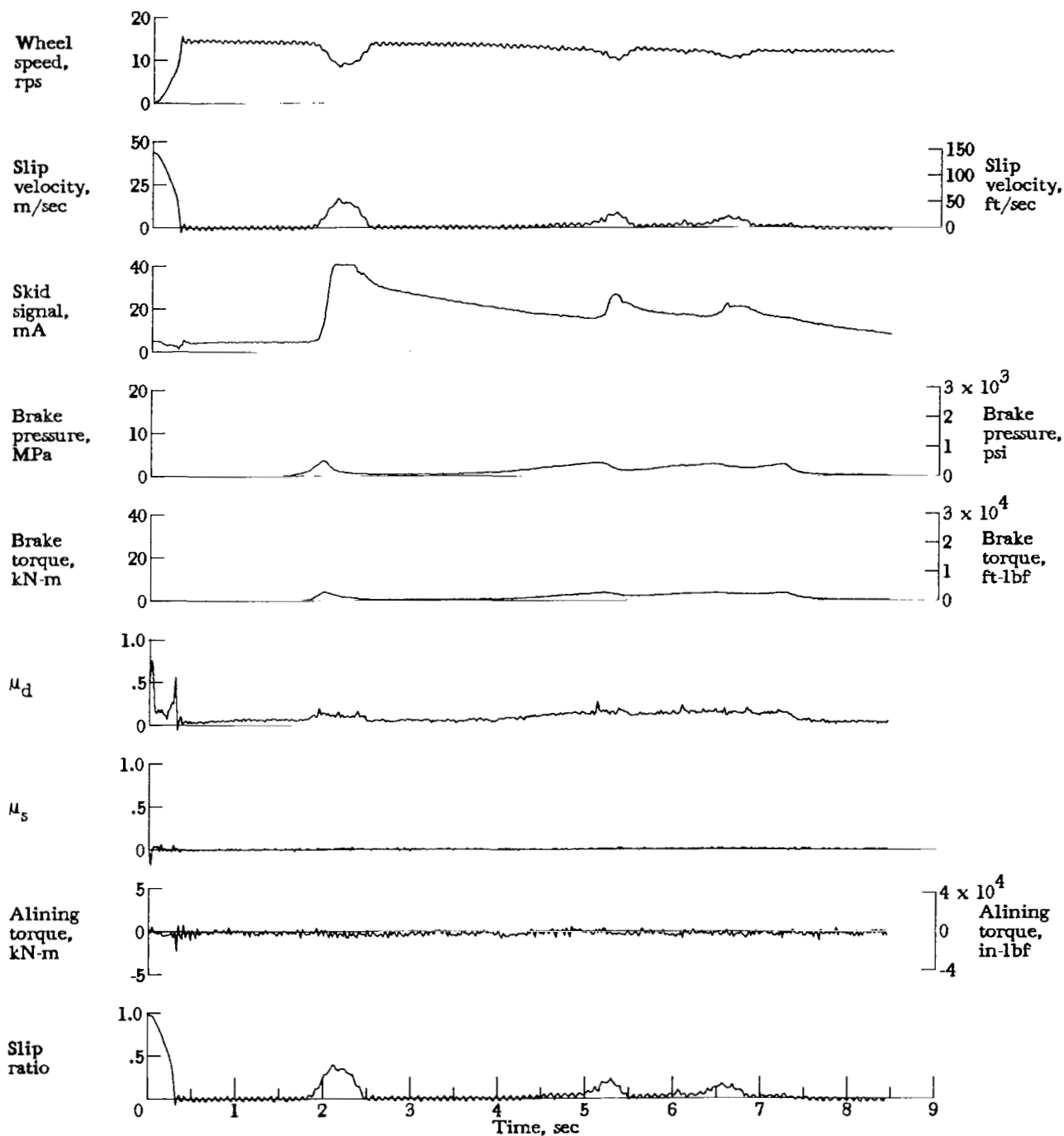


Figure A100.- Time histories for run 100. Nominal carriage speed, 77 knots; vertical load, 81.8 kN (18 400 lbf); yaw angle,  $0^\circ$ ; brake supply pressure, 10 MPa (1500 psi); tire condition, new; surface condition, flooded.

APPENDIX

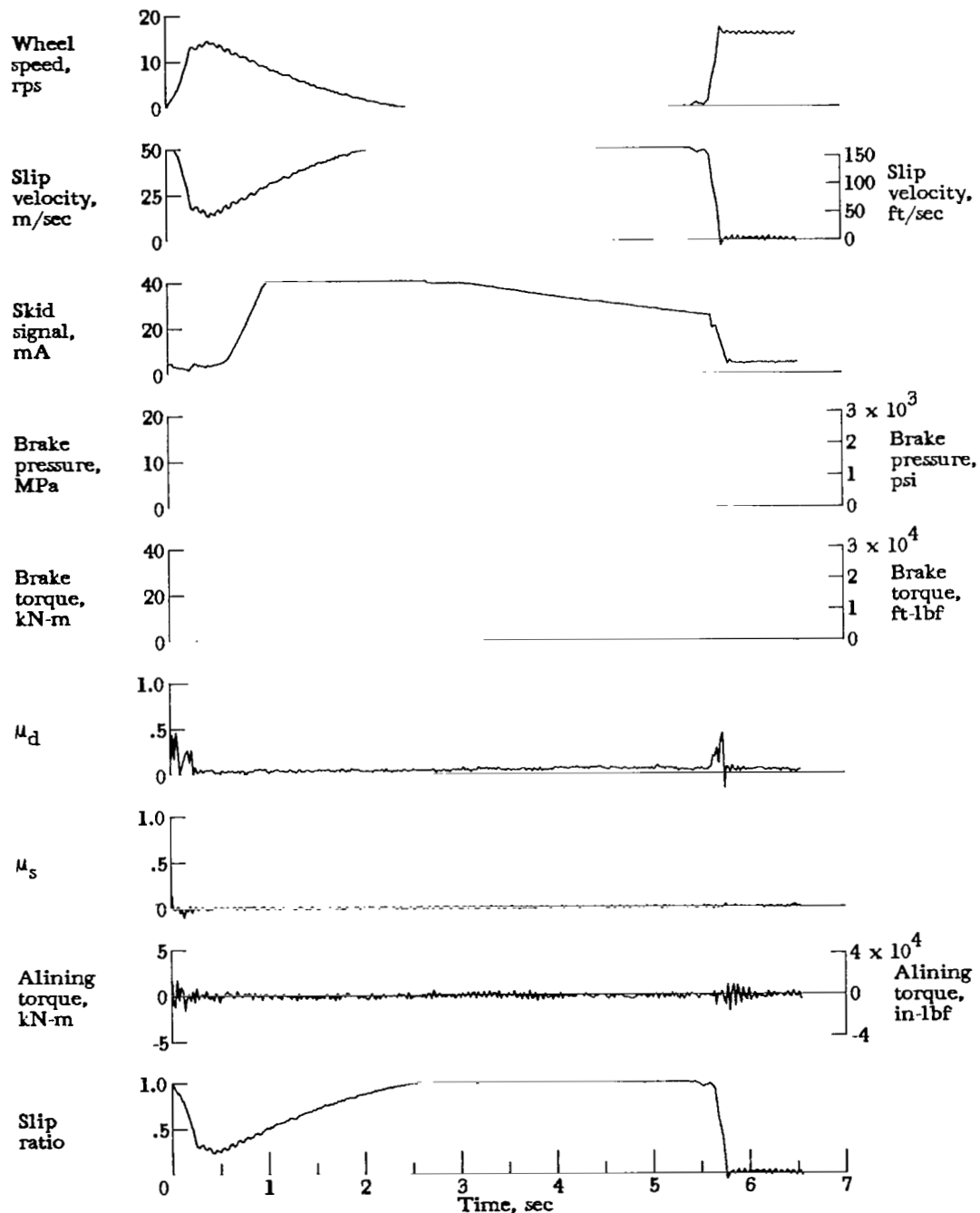


Figure A101.- Time histories for run 101. Nominal carriage speed, 104 knots; vertical load, 81.8 kN (18 400 lbf); yaw angle,  $0^\circ$ ; brake supply pressure, 10 MPa (1500 psi); tire condition, new; surface condition, flooded.

1. Report No. NASA TP-1051		2. Government Accession No.		3. Recipient's Catalog No.	
4. Title and Subtitle BEHAVIOR OF AIRCRAFT ANTISKID BRAKING SYSTEMS ON DRY AND WET RUNWAY SURFACES - A SLIP-VELOCITY-CONTROLLED, PRESSURE-BIAS-MODULATED SYSTEM				5. Report Date December 1979	
				6. Performing Organization Code	
7. Author(s) Sandy M. Stubbs, John A. Tanner, and Eunice G. Smith				8. Performing Organization Report No. L-11760	
9. Performing Organization Name and Address NASA Langley Research Center Hampton, VA 23665				10. Work Unit No. 505-08-33-11	
				11. Contract or Grant No.	
12. Sponsoring Agency Name and Address National Aeronautics and Space Administration Washington, DC 20546				13. Type of Report and Period Covered Technical Paper	
				14. Sponsoring Agency Code	
15. Supplementary Notes					
16. Abstract <p>An experimental investigation was conducted at the Langley aircraft landing loads and traction facility to study the braking and cornering response of a slip-velocity-controlled, pressure-bias-modulated aircraft antiskid braking system. The investigation, conducted on dry and wet runway surfaces, utilized one main gear wheel, brake, and tire assembly of a McDonnell Douglas DC-9 series 10 airplane. The landing gear strut was replaced by a dynamometer. During maximum braking, average braking-behavior indexes based upon brake pressure, brake torque, and drag-force friction coefficient developed by the antiskid system were higher on dry surfaces than on damp and flooded surfaces. The three braking-behavior indexes agreed with one another and may be used interchangeably as a measure of the braking behavior of this antiskid system. However, these braking-behavior indexes are based upon maximum values of pressure, torque, and drag-force friction coefficient which may vary from system to system, and any comparisons between different antiskid systems based solely upon these indexes may be technically misleading. During the transition from a dry to a flooded surface under heavy braking, the wheel entered into a deep skid but the antiskid system reacted quickly by reducing brake pressure and performed normally during the remainder of the run on the flooded surface. The time for brake-pressure recovery following the transition from flooded to dry was 4 sec and was controlled by the decay rate of the residual skid signal built up by the anti-skid system during the initial skid cycles on the first runway surface.</p>					
17. Key Words (Suggested by Author(s)) Cornering Aircraft tires Antiskid braking system			18. Distribution Statement Unclassified - Unlimited		
Subject Category 05					
19. Security Classif. (of this report) Unclassified		20. Security Classif. (of this page) Unclassified		21. No. of Pages 191	22. Price* \$9.00

\* For sale by the National Technical Information Service, Springfield, Virginia 22161

NASA-Langley, 1979

National Aeronautics and  
Space Administration

THIRD-CLASS BULK RATE

Postage and Fees Paid  
National Aeronautics and  
Space Administration  
NASA-451



Washington, D.C.  
20546

Official Business

Penalty for Private Use, \$300

1 1 1U,A, 102679 S00903DS  
DEPT OF THE AIR FORCE  
AF WEAPONS LABORATORY  
ATTN: TECHNICAL LIBRARY (SUL)  
KIRTLAND AFB NM 87117

**NASA**

**S**

POSTMASTER: If Undeliverable (Section 158  
Postal Manual) Do Not Return

---